



UNIVERSITAT DE
BARCELONA

Cell culture interfaces for different organ-on-chip applications: from photolithography to rapid-prototyping techniques with sensor embedding

Roberto Paoli

ADVERTIMENT. La consulta d'aquesta tesi queda condicionada a l'acceptació de les següents condicions d'ús: La difusió d'aquesta tesi per mitjà del servei TDX (www.tdx.cat) i a través del Dipòsit Digital de la UB (diposit.ub.edu) ha estat autoritzada pels titulars dels drets de propietat intel·lectual únicament per a usos privats emmarcats en activitats d'investigació i docència. No s'autoritza la seva reproducció amb finalitats de lucre ni la seva difusió i posada a disposició des d'un lloc aliè al servei TDX ni al Dipòsit Digital de la UB. No s'autoritza la presentació del seu contingut en una finestra o marc aliè a TDX o al Dipòsit Digital de la UB (framing). Aquesta reserva de drets afecta tant al resum de presentació de la tesi com als seus continguts. En la utilització o cita de parts de la tesi és obligat indicar el nom de la persona autora.

ADVERTENCIA. La consulta de esta tesis queda condicionada a la aceptación de las siguientes condiciones de uso: La difusión de esta tesis por medio del servicio TDR (www.tdx.cat) y a través del Repositorio Digital de la UB (diposit.ub.edu) ha sido autorizada por los titulares de los derechos de propiedad intelectual únicamente para usos privados enmarcados en actividades de investigación y docencia. No se autoriza su reproducción con finalidades de lucro ni su difusión y puesta a disposición desde un sitio ajeno al servicio TDR o al Repositorio Digital de la UB. No se autoriza la presentación de su contenido en una ventana o marco ajeno a TDR o al Repositorio Digital de la UB (framing). Esta reserva de derechos afecta tanto al resumen de presentación de la tesis como a sus contenidos. En la utilización o cita de partes de la tesis es obligado indicar el nombre de la persona autora.

WARNING. On having consulted this thesis you're accepting the following use conditions: Spreading this thesis by the TDX (www.tdx.cat) service and by the UB Digital Repository (diposit.ub.edu) has been authorized by the titular of the intellectual property rights only for private uses placed in investigation and teaching activities. Reproduction with lucrative aims is not authorized nor its spreading and availability from a site foreign to the TDX service or to the UB Digital Repository. Introducing its content in a window or frame foreign to the TDX service or to the UB Digital Repository is not authorized (framing). Those rights affect to the presentation summary of the thesis as well as to its contents. In the using or citation of parts of the thesis it's obliged to indicate the name of the author.

Tesis doctoral

Cell culture interfaces for different
organ-on-chip applications:
from photolithography to rapid-
prototyping techniques with sensor
embedding

Roberto Paoli



UNIVERSITAT DE
BARCELONA

Cell culture interfaces
for different organ-on-chip applications:
from photolithography to rapid-prototyping
techniques with sensor embedding

Memoria presentada para optar al grado de Doctor para la
Universitat de Barcelona

Programa de doctorado en Biomedicina

Autor/a: Roberto Paoli

Directors: Prof. Josep Samitier Martí,

Dr. Antoni Homs Corbera

Tutor/a: Prof. Josep Samitier Martí

Departament d'Enginyeria Electrònica i Biomèdica, UB
Institut de Bioenginyeria de Catalunya

Barcelona, 2019



**UNIVERSITAT DE
BARCELONA**

To Laia, Xavi and swingin' out...

...for making this - and much more - possible.

Resumen

A pesar de los avances científicos y tecnológicos de los últimos 60 años en el ámbito de investigación y desarrollo de nuevos fármacos, el número de nuevas moléculas que llegan al mercado por billón de dólares estadounidenses invertido ha ido decayendo constantemente. El escenario actual evidencia la necesidad de nuevos métodos de evaluación que permitan una mejor predicción sobre la eficacia y la seguridad de fármacos en humanos, además de reducir el número de análisis costosos tanto en modelos animales como clínicos.

En los últimos años, para mejorar los modelos actuales, está emergiendo una nueva propuesta desde el campo de la microfluídica. Ésta se basa en el estudio del procesamiento y manipulación de pequeñas cantidades de fluidos en canales de dimensiones micrométricas. Mediante la fusión de cultivos celulares y microfluídica ha nacido un nuevo campo de aplicación denominado “Órgano-en-un-chip” (OOC) donde se recrea un entorno fisiológico a nivel de estímulos fluídicos y mecánicos. La investigación en OOC tiene el objetivo de reproducir unidades funcionales mínimas de diversos órganos del cuerpo humano en dispositivos microfluídicos con el fin de crear nuevos modelos para el estudio de enfermedades o la búsqueda de nuevos fármacos. Un elemento importante para el desarrollo de dispositivos OOC es la reproducción de zonas de interacción entre varios tejidos formados por diferentes tipos celulares

Esta tesis, titulada “Interfaces de cultivo celular para diferentes aplicaciones de OOC: desde fotolitografía a técnicas de prototipado rápido con inclusión de sensores”, tiene como objetivo el diseño, simulación y evaluación de dispositivos para cultivos celulares capaces de reproducir superficies de contacto de tejidos contiguos expuestos a diferentes condiciones de flujo. En particular, el trabajo está enfocado a la exploración de nuevas técnicas de fabricación que permitan el prototipado rápido de dispositivos microfluídicos. La finalidad es conseguir un dispositivo versátil que pueda reducir los costes, el tiempo y la mano de obra asociada con el proceso de fabricación. El objetivo biológico final es demostrar la utilidad de los dispositivos como herramientas de investigación para problemas biológicos, aplicándolos en esta tesis al estudio del túbulo renal y de la barrera hematoencefálica.

Tras una introducción general (Capítulo 1), primero se evalúan las posibilidades para la fabricación de dispositivos OOC utilizando el estándar de fabricación en el ámbito

de la microfluídica, como es la litografía suave de polidimetilsiloxano (PDMS, Capítulo 2). A continuación, se introducen los conceptos de manufacturación digital y prototipado rápido, explorando la posibilidad de su uso para la fabricación de OOC. En particular, se estudian la técnica de manufacturación de objetos por capas — usando dos equipos de manufactura digital (cortadora laser y cortadora de vinilos, Capítulo 4) — y la impresión 3D por estereolitografía para prototipado rápido (Capítulo 4). Posteriormente se procede a la modificación de uno de los diseños, añadiendo funcionalidades como la integración de conectores y una matriz de electrodos para la medición de resistencia eléctrica trans-epitelial. Además, se diseña un sistema compacto para experimentos microfluídicos con control de flujo integrado (Capítulo 5). Finalmente, se aplican las tecnologías desarrolladas a problemas biológicos como el túbulo renal (Capítulo 6) y la barrera hematoencefálica (Capítulo 7).

A través del enfoque clásico de litografía suave, se ha diseñado, simulado y fabricado con éxito un primer dispositivo OOC multicapa en PDMS (OOCv1) capaz de incluir una membrana comercial. El dispositivo se ha generado teniendo en cuenta criterios biomiméticos. Los protocolos de fabricación se han optimizado para obtener dispositivos de mínimo grosor para poder ser inspeccionados utilizando microscopia de alta resolución. Para una segunda versión de OOC (OOCv2), se han definido y optimizado dos protocolos de fabricación con la técnica de manufacturación por capas: uno con cortadora de vinilos y otro con cortadora laser. Esta segunda versión (OOCv2) está fabricada por capas de material termoplástico con calidad óptica superior y adhesivo transparente, ambos biocompatibles. El dispositivo también incluye conectores integrados en una capa de metacrilato para simplificar las conexiones fluídicas y permite una fabricación rápida, de bajo coste y escalable, ideal para el prototipado rápido. Esta misma versión ha sido posteriormente mejorada con la integración de conectores sólidos y electrodos alineados con los canales para realizar las medidas eléctricas. En el ámbito de la fabricación por estereolitografía, tras la puesta a punto y mejora de resolución de una impresora comercial, se ha procedido al diseño y fabricación de dos prototipos de dispositivos diferentes (OOCv3). En un caso, se ha optado por la misma estrategia de integración de una membrana comercial y en el otro por la fabricación de un dispositivo multicapa complejo en PDMS utilizando la estereolitografía como técnica de fabricación rápida de moldes.

Los experimentos biológicos sobre túbulo renal, realizados en los dispositivos OOCv1 y OOCv2, han demostrado la viabilidad de estos dispositivos para cultivos celulares de estudios de la metabolización de ácidos grasos en el riñón relacionados con condiciones diabetogénicas. Se ha observado acumulación de grasas acidas en las células epiteliales de túbulo renal utilizadas. El marcaje de mitocondrias sugiere una diferencia de activación debida a un posible efecto positivo de estimulación por flujo, que estaría de acuerdo con otros estudios sobre la fisiología de la nefrona. Se ha simplificado la configuración experimental utilizando un sistema compacto con fluídica integrada.

Los experimentos biológicos sobre la barrera hematoencefálica han demostrado la viabilidad de OOCv2 para el cocultivo compartimentado de células endoteliales de cerebro y pericitos. La formación y alteración de la barrera tras el tratamiento con manitol, un compuesto hiperosmótico capaz de producir la apertura transitoria de la barrera ha sido investigada utilizando diferentes técnicas, incluyendo observación por microscopia en tiempo real, inmunotinción y análisis por espectroscopía de impedancia. El cocultivo de pericitos y células endoteliales ha resultado en una mejor formación y capacidad de recuperación de la barrera tras la desestabilización de la misma, tanto en términos de confluencia celular como de formación de complejos de uniones. El análisis por espectroscopía de impedancia ha demostrado la repetibilidad de las medidas efectuadas con electrodos integrados. Con estas medidas se ha conseguido desarrollar un modelo de análisis linear discriminatorio para la clasificación de las medidas eléctricas adquiridas en diferentes días experimentales. El modelo final tiene un 100% de exactitud en entrenamiento y un 90% en evaluación. Los resultados son respaldados por datos de microscopía. Gracias a su alta separación entre clases, este modelo basado en la espectroscopía de impedancia tiene potencial para ser aplicado como método de detección no-invasivo y libre de etiqueta (“label-free”) para la estimación de la integridad de la barrera en el modelo in-vitro.

Table of contents

RESUMEN	I
TABLE OF CONTENTS	V
LIST OF FIGURES.....	XI
LIST OF TABLES.....	XV
LIST OF ABBREVIATIONS	XVII
1 GENERAL INTRODUCTION.....	1
1.1 BACKGROUND	1
1.2 GENERAL OBJECTIVES	7
1.3 BRIEF DESCRIPTION AND SPECIFIC OBJECTIVES OF EACH CHAPTER.....	9
1.4 REFERENCES.....	12
2 PDMS SOFT LITHOGRAPHY FOR OOC MICROFABRICATION	15
2.1 BACKGROUND	16
2.1.1 <i>Introduction to Microfluidics</i>	16
2.1.2 <i>Hydrodynamics of fluids inside small channels</i>	17
2.1.2.1 Navier-Stokes equation.....	17
2.1.2.2 Hydraulic Diameter	17
2.1.2.3 Reynolds number	18
2.1.2.4 Poiseuille flow	18
2.1.2.5 Hydraulic resistance.....	19
2.1.2.6 Shear stress in a microfluidic channel.....	20
2.1.2.7 Hess-Murray's Law.....	21
2.1.3 <i>Soft lithography fabrication of microfluidic devices</i>	22
2.1.3.1 Typical soft lithography process by photolithographic master	22
2.1.3.2 PDMS advantages	23
2.1.3.3 Membrane embedding strategies in PDMS devices	24
2.1.4 <i>Microfluidics and cell culture: the birth of OOC</i>	26
2.1.4.1 Lung	27
2.1.4.2 Liver	27
2.1.4.3 Kidney	28
2.1.4.4 Gut	28
2.1.4.5 BBB.....	28
2.1.4.6 Spleen	29
2.1.4.7 Multi-OOC.....	30
2.2 CHALLENGES FOR FABRICATION OF OOC DEVICE USING PDMS SOFT-LITHOGRAPHY TECHNIQUE.	

2.3	MATERIALS AND METHODS.....	31
2.3.1	<i>Materials used</i>	31
2.3.2	<i>Design and simulation of first version OOC (OOCv1)</i>	31
2.3.2.1	Design choices.....	31
2.3.2.2	CAD design and simulation	34
2.3.3	<i>Fabrication of OOCv1</i>	34
2.3.3.1	Photolithography	34
2.3.3.2	Replica molding.....	35
2.3.3.3	Assembly and membrane sealing	36
2.3.4	<i>Characterization</i>	37
2.4	RESULTS	37
2.4.1	<i>Design and simulation</i>	37
2.4.2	<i>Fabrication</i>	38
2.4.3	<i>Assembly</i>	40
2.5	DISCUSSION	41
2.6	CONCLUSIONS	43
2.7	REFERENCES.....	44
3	RAPID PROTOTYPING OF MULTILAYERED OOC DEVICES IN COP	51
3.1	BACKGROUND	52
3.1.1	<i>PDMS and soft-lithography limitations</i>	52
3.1.1.1	Limitations for Cell culture.....	53
3.1.1.2	Limitations in manufacturability for commercialization	54
3.1.2	<i>Digital Manufacturing and Rapid Prototyping in microfluidics</i>	55
3.1.3	<i>Thermoplastics for microfluidics</i>	58
3.1.3.1	Material characteristics.....	58
3.2	CHALLENGES AND SPECIFIC OBJECTIVES	60
3.3	MATERIALS AND METHODS.....	60
3.3.1	<i>Materials</i>	60
3.3.2	<i>Direct Polymer bonding</i>	61
3.3.2.1	APTES functionalization of PC membranes	61
3.3.2.2	Substrate bonding.....	61
3.3.3	<i>COP contact angle measurement</i>	62
3.3.4	<i>OOC design</i>	62
3.3.5	<i>OOC fabrication</i>	63
3.3.5.1	Substrate preparation	63
3.3.5.2	Vinyl cutter.....	63
3.3.5.3	Laser cut.....	64
3.3.5.4	Assembly	64
3.3.5.5	Inspection and Testing	65
3.4	RESULTS	65

3.4.1	<i>Direct Polymer bonding</i>	65
3.4.2	<i>COP contact angle measurements</i>	68
3.4.3	<i>Design and fabrication</i>	68
3.5	DISCUSSION.....	69
3.6	CONCLUSIONS.....	71
3.7	REFERENCES.....	73
4	3D PRINTING FOR MICROFABRICATION	79
4.1	BACKGROUND	80
4.1.1	<i>3D printing</i>	80
4.1.2	<i>SL 3D printing for microfluidics</i>	82
4.1.2.1	Understanding DLP SL process and real 3D resolution	83
4.1.2.2	Main SL applications for LOC and OOC	84
4.1.3	<i>SL printer and previous experience in the lab</i>	87
4.2	CHALLENGES AND SPECIFIC OBJECTIVES OF THIS CHAPTER	88
4.3	MATERIALS AND METHODS.....	90
4.3.0	<i>Materials used</i>	90
4.3.1	<i>Improving a pre-existing SL 3D printer</i>	90
4.3.1.1	Switch to Open Source electronics and tunable freeware software interface ...	90
4.3.1.2	Improving resin vat and build platform	91
4.3.1.3	Switching to UV projector	94
4.3.1.4	Defining printing process	96
4.3.2	<i>Calibration and real resolution assessment</i>	98
4.3.3	<i>Functional LOC printing</i>	98
4.3.4	<i>3D printing OOC applications</i>	100
4.4	RESULTS	103
4.4.1	<i>Improving the printer</i>	103
4.4.2	<i>Calibration and resolution assessment</i>	105
4.4.3	<i>Functional LOCs</i>	107
4.4.4	<i>OOC applications</i>	107
4.5	DISCUSSION	107
4.6	CONCLUSIONS	112
4.7	REFERENCES.....	113
5	AUTOMATING EXPERIMENTAL SET-UP FOR OOC APPLICATIONS: INTEGRATING THE CHIP INTO THE LAB	117
5.1	BACKGROUND	118
5.1.1	<i>Bottlenecks to a broader impact</i>	118
5.1.1.1	World-to-chip connection.....	119
5.1.1.2	Integrated control systems for microfluidics	119
5.1.2	<i>TEER electrodes integration and electrical connections</i>	120

5.2	SPECIFIC OBJECTIVES OF THE CHAPTER	121
5.3	MATERIALS AND METHODS.....	122
5.3.1	<i>Materials and Facilities</i>	122
5.3.2	<i>Improving OOC design (OOC v2.1)</i>	122
5.3.2.1	Adding threaded connector	123
5.3.2.2	Adding media reservoirs	123
5.3.2.3	Custom microscope holders.....	123
5.3.3	<i>Embedded flow control system</i>	124
5.3.3.1	Portable experimental unit	125
5.3.3.2	Small footprint external flow control.....	125
5.3.4	<i>Integrated sensors fabrication (OOC v2.2)</i>	126
5.3.4.1	OOC v2.2 sensor design	126
5.3.4.2	OOC v2.2 manufacturing.....	126
5.3.4.3	Custom holder and adapters.....	128
5.4	RESULTS	129
5.4.1	<i>Improving OOC design</i>	129
5.4.2	<i>Embedded flow control system</i>	129
5.4.2.1	Small footprint flow control system.....	129
5.4.2.2	Portable experimental unit	130
5.4.3	<i>Integrated TEER sensors fabrication</i>	131
5.5	DISCUSSION	132
5.6	CONCLUSIONS	133
5.7	REFERENCES.....	135
6	OOC FOR KIDNEY TUBULAR APPLICATIONS.....	139
6.1	BACKGROUND	140
6.1.1	<i>The Kidney</i>	140
6.1.1.1	Kidney structure and physiological values	140
6.1.1.2	The kidney as a target for new OOC models	142
6.1.1.3	The role of mitochondrial fatty acid β -oxidation (FAO) in DKD.....	142
6.1.2	<i>Kidney-on-chip state of art</i>	143
6.2	MATERIALS AND METHODS.....	149
6.2.0	<i>Materials and general cells seeding protocols</i>	149
6.2.0.1	Materials	149
6.2.0.2	Facilities	149
6.2.0.3	OOCv1 general cells seeding protocol	149
6.2.0.4	OOCv2.1 and OOC v2.2 cells seeding protocol.....	150
6.2.0.5	Organoids culture and cell isolation.....	151
6.2.1	<i>Tubular kidney experiments on OOCv1</i>	151
6.2.1.1	Rationale.....	151
6.2.1.2	Tubular cells seeding in OOCv1 devices	152
6.2.1.3	Open-loop flow experiment.....	152

6.2.1.4	Cell fixation and imaging	152
6.2.2	<i>Tubular kidney experiments on OOCv2.1</i>	153
6.2.2.1	Rationale	153
6.2.2.2	Tubular cells seeding in OOCv2.1 devices	153
6.2.2.3	Recirculating flow experiment	154
6.2.2.4	Static controls	154
6.2.2.5	Cell fixation, staining and imaging	154
6.3	RESULTS	155
6.3.1	<i>Tubular kidney experiments on OOCv1</i>	155
6.3.2	<i>Tubular kidney experiments on OOCv2.1</i>	156
6.4	DISCUSSION	158
6.5	CONCLUSIONS	159
6.6	REFERENCES.....	161
7	OOO FOR BBB APPLICATIONS.....	165
7.1	BACKGROUND	166
7.1.1	<i>BBB physiology</i>	166
7.1.1.1	The role of Tight Junctions (TJ) and Adherens Junctions (AJ) in BBB integrity ..	166
7.1.2	<i>BBB-on-chip state of art</i>	167
7.1.2.1	Design approaches.....	168
7.1.2.2	Electrical barrier assessments.....	169
7.2	SPECIFIC OBJECTIVES OF THE CHAPTER	170
7.3	MATERIALS AND METHODS.....	171
7.3.1	<i>Materials and general cells seeding protocols</i>	171
7.3.1.1	Materials	171
7.3.1.2	Facilities	171
7.3.2	<i>BBB experiments</i>	171
7.3.2.1	Rationale	171
7.3.2.2	BBB cells seeding in OOC v2.1 and OOC v2.2	172
7.3.2.3	Time-lapse experiments.....	173
7.3.2.4	Petri Dish Controls	173
7.3.2.5	Electrical Impedance Spectroscopy (EIS) experiment	173
7.3.2.6	Cell fixation, staining and imaging	174
7.3.2.7	EIS Data Analysis	175
7.4	RESULTS	176
7.4.1	<i>Phase contrast time-lapse</i>	176
7.4.2	<i>Immunostaining</i>	176
7.4.3	<i>Electrical impedance spectroscopy (EIS)</i>	184
7.5	DISCUSSION	187
7.6	CONCLUSIONS	190
8	GENERAL CONCLUSIONS.....	195

List of figures

FIGURE 1-1. EROOM'S LAW. OVERALL TREND IN R&D EFFICIENCY, INFLATION-ADJUSTED.....	1
FIGURE 1-2: EROOM'S LAW. TRENDS IN CAPITALIZED PRE-HUMAN, CLINICAL AND TOTAL COST PER APPROVED NEW DRUG.	2
FIGURE 1-3: QUICK OVERVIEW OF THE MAIN PDMS SOFT LITHOGRAPHY STEPS.....	3
FIGURE 1-4: RAPID PROTOTYPING TECHNIQUES FOR MICROFLUIDICS.	5
FIGURE 2-1: POISEUILLE FLOW PROFILE.	19
FIGURE 2-2: MURRAY LAW HIERARCHICAL BRANCHING NOMENCLATURE.	21
FIGURE 2-3. PDMS SOFT LITHOGRAPHY STEPS.....	23
FIGURE 2-4. PDMS-GLUE BONDING PROTOCOL.	25
FIGURE 2-5. APTES FUNCTIONALIZATION AND PLASMA ACTIVATION BONDING.	26
FIGURE 2-6. LUNG-ON-CHIP FROM INGBER RESEARCH GROUP.	27
FIGURE 2-7. LIVER-ON-CHIP DEVICES.	28
FIGURE 2-8. BBB-ON-CHIP MODELS.	29
FIGURE 2-9. SPLENON-ON-CHIP.	29
FIGURE 2-10. MULTI-ORGAN ON CHIP.....	30
FIGURE 2-11. GENERAL OOCV1 DESIGN.	32
FIGURE 2-12. DETAIL OF OOCV1 SERPENTINE RAMIFICATION AND GENERATION NUMBERING.....	33
FIGURE 2-13. MASK DESIGN TEMPLATE FOR 4" SILICON WAFER.....	35
FIGURE 2-14. WALL SHEAR STRESS DISTRIBUTION IN OOCV1-A AND OOCV1-B.....	38
FIGURE 2-15. CHANNELS DEFORMATION AND OCCLUSION WITH 2.5- μm LAYER OF PDMS-GLUE.....	40
FIGURE 2-16. RESULTS USING 1- μm LAYER OF PDMS-GLUE.....	40
FIGURE 2-17. OOCV1 FINAL ASSEMBLY RESULTS.	41
FIGURE 3-1. XUROGRAPHY LOM FOR MICROFLUIDICS.	57
FIGURE 3-2. LASER CUT LOM FOR MICROFLUIDICS.	57
FIGURE 3-3. THERMOPLASTICS WATER VAPOR PERMEABILITY VS. OXYGEN PERMEABILITY.....	59
FIGURE 3-4. OOCV2.0 DEVICE EXPLODED VIEW.....	63
FIGURE 3-5. OOCV2.0 FABRICATION.....	64
FIGURE 3-6. BEST RESULTS OBTAINED FROM DIRECT POLYMER BONDING.....	66
FIGURE 3-7. CONTACT ANGLE MEASUREMENT OF COP.	68
FIGURE 3-8. OOCV2.0 DEVICE ASSEMBLY.....	69
FIGURE 4-1. MAIN 3D PRINTING TECHNIQUE RELEVANT FOR MICROFLUIDICS.	80
FIGURE 4-2. DIFFERENT PHASES OF PRINTING A CANTILEVER STRUCTURE (I.E. CLOSED CHANNEL).....	83
FIGURE 4-3. MICROFLUIDIC DEVICES PRINTED BY SL.....	85
FIGURE 4-4. APPROACHES FOR MULTI-MATERIAL SL PRINTING OF POROUS MEMBRANE STRUCTURES IN MICROFLUIDIC DEVICES.....	86
FIGURE 4-5. HIGH RESOLUTION DLP SL PRINTING WITH COMMERCIAL PRINTERS.	87
FIGURE 4-6. ILIOS HD FOR RESEARCH SL 3D PRINTER.	88

FIGURE 4-7. OPEN SYSTEM PRINTER CONTROL REPLACEMENT.	91
FIGURE 4-8. VAT ADAPTERS DESIGN	92
FIGURE 4-9. DIFFERENT VATS TESTED.	92
FIGURE 4-10. BUILD PLATFORM DESIGNS THROUGH DIFFERENT ITERATIONS.	93
FIGURE 4-11. VACUUM CIRCUIT SCHEMATIC.....	93
FIGURE 4-12. PROJECTOR MOUNTING.....	96
FIGURE 4-13. RESOLUTION ASSESSMENT TEST DESIGNS.....	99
FIGURE 4-14. FUNCTIONAL 3D PRINTED LOC TEST DEVICES..	100
FIGURE 4-15. OOCV3-A EXPLODED VIEW.	100
FIGURE 4-16. 3D MULTILAYERED COMPARTMENTALIZED DEVICE ASSEMBLY.	102
FIGURE 4-17. PDMS ALIGNING HELPER.	103
FIGURE 4-18. DIFFERENT GENERATION OF BUILD PLATFORMS AND RESIN VATS.	103
FIGURE 4-19. FINAL PRINTER SETUP.	104
FIGURE 4-20. PROJECTOR IRRADIANCE PROFILES.	104
FIGURE 4-21. CLOSED CHANNELS PRINTED USING SPOT HT RESIN AND UV PROJECTOR..	106
FIGURE 4-22. LOC DEVICES PRINTED WITH SPOT HT RESIN AND UV PROJECTOR.....	108
FIGURE 4-23. OOC DEVICES FABRICATED USING SL 3D PRINTER.	109
FIGURE 5-1. CHIP IN A LAB.	118
FIGURE 5-2. INTEGRATED FLOW CONTROL SYSTEMS FOR MICROFLUIDICS.....	120
FIGURE 5-3. NON-PERMANENT ELECTRICAL CONNECTIONS FOR MICROFLUIDIC DEVICES.....	121
FIGURE 5-4. OOC DESIGN V2.1.	123
FIGURE 5-5. CUSTOM MICROSCOPE HOLDER SIZED TO STANDARD MICROTITER PLATE DIMENSIONS.	124
FIGURE 5-6. DESIGN CONCEPT OF THE EMBEDDED FLOW CONTROL SYSTEM.	124
FIGURE 5-7. BASIC SCHEMATIC OF THE ELECTRONIC FLOW CONTROL SYSTEM FOR ONE PUMP.	125
FIGURE 5-8. OOC V2.2 WITH EMBEDDED ELECTRODES FOR TEER MEASUREMENTS.	127
FIGURE 5-9. OKO-LAB INCUBATOR ADAPTER FOR OOC V2.2	128
FIGURE 5-10. OOC V2.1 FABRICATION..	129
FIGURE 5-11. EMBEDDED FLOW CONTROL SYSTEM.	130
FIGURE 5-12. FABRICATED OOC V2.2	131
FIGURE 6-1. THE KIDNEY AND THE NEPHRON STRUCTURE	140
FIGURE 6-2. FABRICATION AND OPERATION OF A MULTI-LAYER MICROFLUIDIC DEVICE (MMD).	145
FIGURE 6-3. DESIGN FOR THE HUMAN KIDNEY PROXIMAL TUBULE-ON-A-CHIP.	146
FIGURE 6-4. RENAL PROXIMAL TUBULES GENERATED IN 3D.....	147
FIGURE 6-5. A FIBRIN-BASED TISSUE-ENGINEERED RENAL PROXIMAL TUBULE FOR BIOARTIFICIAL KIDNEY DEVICES: DEVELOPMENT, CHARACTERIZATION AND IN VITRO TRANSPORT STUDY	148
FIGURE 6-6. FLUORESCENCE IMAGING OF KIDNEY TUBULAR CELLS ON OOCV1.0-B.	155
FIGURE 6-7. MEAN C16 INTENSITY COMPARISON ON FLUORESCENCE IMAGES OF OOCV1-B, NORMALIZED BY BACKGROUND INTENSITY.....	155

FIGURE 6-8. FLUORESCENCE INTENSITY OF C16 AND MITOCHONDRIAL MARKERS IN RENAL TUBULAR EXPERIMENTS IN OOCV2.1, NORMALIZED BY BACKGROUND INTENSITY.	156
FIGURE 6-9. FLUORESCENCE IMAGING OF TUBULAR KIDNEY CELLS IN OOCV2.1.....	157
FIGURE 6-10: FLUORESCENCE INTENSITY C16 AND MITOCHONDRIAL MARKERS IN RENAL TUBULAR EXPERIMENTS IN OOCV2.1, NORMALIZED BY BACKGROUND INTENSITY AND CELL NUMBER.	158
FIGURE 7-1. BBB STRUCTURE.	166
FIGURE 7-2. DESIGN STRATEGIES FOR BBB OOC MODELS.	168
FIGURE 7-3. BBB TEER-EIS EXPERIMENTAL SET-UPS. ⁵	170
FIGURE 7-4. BBBE1 MEASURING CONFIGURATION.	174
FIGURE 7-5. BRIGHT FIELD LIVE IMAGING OF THE BOTTOM CHANNEL OF BBB1 AND BBB2 EXPERIMENTS. .	177
FIGURE 7-6. IMMUNOSTAINING RESULTS OF BBB1 (ECs ONLY), 24 H AFTER MANNITOL TREATMENT.	179
FIGURE 7-7. FLUORESCENCE IMAGES OF ECs CONTROL CULTURE IN PETRI DISHES.....	180
FIGURE 7-8. FLUORESCENCE IMAGES OF PERICYTES CONTROL CULTURE IN PETRI DISHES.....	181
FIGURE 7-9. IMMUNOSTAINING OF THE MEMBRANE.....	182
FIGURE 7-10. IMMUNOSTAINING OF THE BOTTOM OF THE CHANNELS (ECs ONLY) BEFORE (CTRL) AND 24-H AFTER MANNITOL TREATMENT (BBB2).	183
FIGURE 7-11. TYPICAL MEASURED IMPEDANCE SPECTRA ACROSS DIFFERENT TIMEPOINTS.....	185
FIGURE 7-12. UNSUPERVISED AND SUPERVISED EIS CLASSIFICATION.....	186
FIGURE 7-13. IMPROVED EIS SUPERVISED CLASSIFICATION.	188
FIGURE 7-14. IMPROVED EIS MODEL WITH OVERLAY OF BIOLOGICAL DATA INTERPRETATION.	190

List of tables

TABLE 2-1. OOCV1 DESIGN DIMENSIONS RESUME.....	33
TABLE 2-2. AVERAGE WALL SHEAR STRESS DISTRIBUTION ACROSS CHANNEL GENERATIONS.....	37
TABLE 2-3. MEASURED DIMENSIONS RESUME.....	39
TABLE 2-4. AVERAGE WALL SHEAR STRESS DISTRIBUTION ACROSS CHANNEL GENERATIONS CALCULATED USING REAL DIMENSIONS.	39
TABLE 3-1. PDMS-THERMOPLASTICS COMPARISON.....	59
TABLE 3-2. DIRECT POLYMER BONDING RESULTS.....	67
TABLE 3-3. CONTACT ANGLE MEASUREMENTS OF COP, NATIVELY AND AFTER SURFACE TREATMENT.....	68
TABLE 4-1. WINTECH PRO6500 TECHNICAL SPECIFICATION.....	94
TABLE 4-2. PROJECTOR PWM SETTING VS. LED DRIVING CURRENT.....	95
TABLE 4-3. ANALYZED CALIBRATION PRINT JOBS RESUME.....	98
TABLE 4-4. LOC DEVICES PRINTING PARAMETERS.....	99
TABLE 4-5. OOCV3-A PRINTING PARAMETERS.....	101
TABLE 4-6. OOCV3-B PRINTING PARAMETERS.....	101
TABLE 4-7. FEATURE RESOLUTION WITH DIFFERENT MATERIALS AND CONFIGURATIONS.....	105
TABLE 4-8. CHANNEL ARRAY PRINT SUCCESS VS THEORETICAL DIMENSIONS.....	105
TABLE 4-9. CLOSED CHANNEL (CANTILEVER) RESOLUTION ASSESSMENT.....	107
TABLE 5-1. COMPACT EXPERIMENTAL UNIT COST DETAIL.....	131
TABLE 6-1. ANALYSIS OF RAT DIAMETER AND RADIUS VALUES DISTRIBUTION ACROSS RAT KIDNEY BLOOD NETWORK.....	141
TABLE 6-2. EXPERIMENTAL CONDITIONS OVERVIEW FOR TUBULAR KIDNEY CULTURES ON OOCV1.....	152
TABLE 6-3. EXPERIMENTAL CONDITIONS OVERVIEW FOR TUBULAR KIDNEY CULTURES ON OOCV2.1.....	153
TABLE 7-1. EXPERIMENTAL CONDITIONS OVERVIEW FOR BBB EXPERIMENTS.....	172
TABLE 7-2. CONFUSION MATRIX OF PCA-LDA MODEL ON THE WHOLE DATASET.....	184
TABLE 7-3. CONFUSION MATRIX OF LDA MODEL AFTER EXCLUDING LOCATION C.....	184

List of abbreviations

ABBREVIATION	MEANING
μTAS	Micro-Total Analysis Systems
2D	Two-dimensional
3D	Three-dimensional
3T	Three-terminal
ABS	Acrylonitrile butadiene styrene
AC	Alternate current
ADPKD	Autosomal dominant polycystic kidney disease
AJ	Adherens Junctions
APTES	(3-Aminopropyl)triethoxysilane
ATP	Adenosine triphosphate
BBB	Blood Brain Barrier
CAD	Computer-Aided Design
CAM	Computer Aided Manufacturing
CCIT	Centres Científics i Tecnològics
CKD	Chronic kidney disease
CNC	Computer Numerically Controlled
CNR	Italian National Research Center
CO₂	Carbon dioxide
COP	Cyclic Olefin Polymer
DAPI	Diamidino-2-phenylindole
DC	Direct current
DI	Deionized
DIV	Days in vitro
DKD	Diabetic kidney disease
DLP	Digital Light Processing
DM	Digital Manufacturing
DMD	Digital Micromirror Device
DMEM	Dulbecco's Modified Eagle Medium
DoC	Day of Confluence
DXF	Drawing Exchange Format

EC	Endothelial cells
EIS	Electrical Impedance Spectroscopy
ESRD	End-stage renal disease
EtOH	Ethanol
FAO	Fatty acid β -oxidation
FBS	Fetal Bovine Serum
FDM	Fused Deposition Modeling
FEP	Fluorinated ethylene propylene
FOV	Field of View
GPL	GNU Public License
GPIO	General-Purpose Input/Output
HDMI	High-Definition Multimedia Interface
hESC	Human embryonic stem cells
hIPS	Human induced pluripotent stem cells
HK-2	Human renal proximal tubule epithelial cells
HUVEC	Human umbilical vein endothelial cells
I2C	Inter-Integrated Circuit
IBEC	Institute for Bioengineering of Catalonia
IFN	Institute for Photonics and Nanotechnologies
IMCD	Inner medullary collecting duct
IPA	Isopropyl alcohol
IRB	Institute for Research in Biomedicine
LDA	Linear discriminant analysis
LED	Light-emitting diode
LOC	Lab-On-Chip
LOM	Laminated Object Manufacturing
LTL	Lotus tetragonolobus lectin
MCE	Mixed Cellulose Ester
MEMS	Microelectro-mechanical systems
MJM	Multi Jet Modeling
MW	Molecular weight
N₂	Nitrogen
NVU	Neurovascular unit

O₂	Oxygen
OH	Hydroxyl group
OOC	Organ-on-chip
PAMPA	Parallel artificial membrane permeability assays
PBS	Phosphate buffer saline
PC	Polycarbonate
PCA	Principal Component analysis
PCB	Printed Circuit Board
PCR	Polymerase chain reaction
PDMS	Poly(dimethyl-siloxane)
PE	Polyester
PEG-DA	Poly(ethylene glycol) diacrylate
PES	Polyethersulfone
PET	Polyethylene terephthalate
PFA	Paraformaldehyde
PJM	PolyJet Modeling
PLA	Poly(lactic acid)
PMMA	Poly(methyl-methacrylate)
PS	Polystyrene
PSA	Pressure sensitive adhesive
PTFE	Polytetrafluoroethylene
PWM	Pulse Width Modulation
R&D	Research and Development
RC	Regenerated Cellulose
ROI	Region of interest
RP	Rapid Prototyping
RPTCs	Renal proximal tubular cells
RSC	The Royal Society of Chemistry
SBR	Slide Bearing Rails
SEM	Scanning Electron Microscope
SL	Stereolithography
STL	Standard Tessellation Language
TEER	Transepithelial/endothelial electrical resistance
TJ	Tight Junctions

TNF-α	Tumor necrosis factor alpha
UNF	Unified National Fine
USB	Universal Serial Bus
UV	Ultraviolet
UVO₃	Ultraviolet Ozone
WSS	Wall shear stress
ZIF	Zero Injection Force

1 General introduction

1.1	BACKGROUND	1
1.2	GENERAL OBJECTIVES.....	7
1.3	BRIEF DESCRIPTION AND SPECIFIC OBJECTIVES OF EACH CHAPTER.....	9
1.4	REFERENCES	12

1.1 BACKGROUND

The last 60 years have seen major advances in many scientific and technological inputs of drug Research and Development (R&D), both as improvements to existing techniques (combinatorial chemistry, DNA sequencing, X-ray crystallography) or new technologies (High Throughput Screening), computational drug design, transgenic mice, etc.)¹. In contrast, the number of new drugs per billion US dollars of R&D spending has been declined steadily during the same time window^{1,2} (**Figure 1-1**, **Figure 1-2**). Researchers called this decline of R&D efficiency the “Eroom’s law”, as the inverse of the more familiar “Moore’s law” prediction in the electronics field. Eroom’s law describe the decline in number of new approved drugs per billion US dollar R&D spending since 1950, at an approximate halving rate of 9 years, in inflation adjusted terms¹.

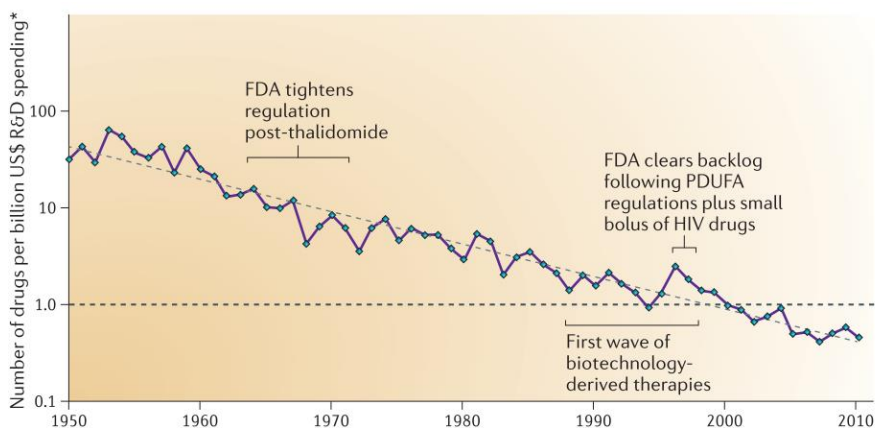


Figure 1-1. Eroom's law. Overall trend in R&D efficiency, inflation-adjusted. The number of US new drugs approved by Food and Drug Administration for 1 billion US dollar R&D spending halves every 9 years. Reprinted by permission from Nature Reviews Drug Discovery: [Scannel et Al, 2012](#)¹.

The current drugs R&D scenario highlights the need for new testing approaches to achieve reliable predictions of drug efficacy and safety in humans, as well as to reduce the number of costly unsuccessful clinical trials³.

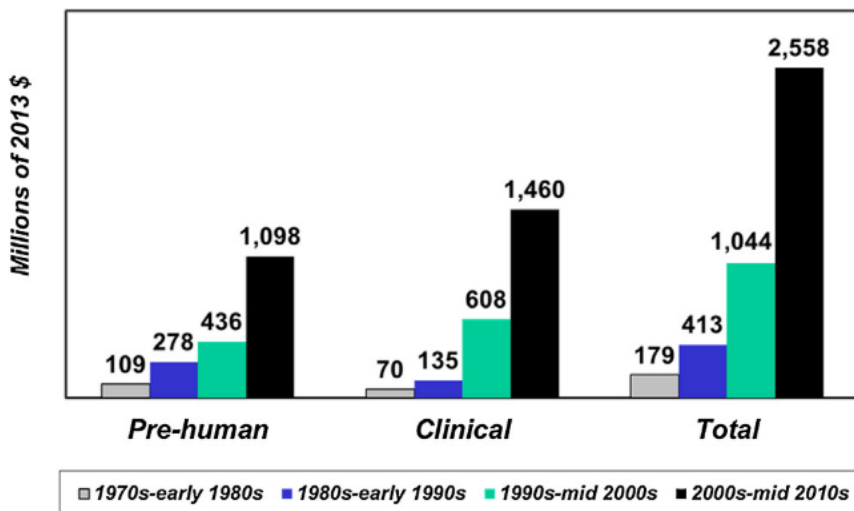


Figure 1-2: Eroom's law. Trends in capitalized pre-human, clinical and total cost per approved new drug. Reproduced with permission from [DiMasi et al., 2016⁴](#).

Pre-clinical trials use two main tools: “*in vitro*” and animal models. “*In vitro*” models include both two-dimensional (2D) and three-dimensional (3D) cell cultures. 2D cell culture had been a milestone in the progress of biomedical science and the basis for cell and tissue engineering⁵. Despite being a well-accepted and useful approach to understand cell behavior, growing evidence now shows that, under some circumstances, the 2D systems can result in cell bioactivities that deviate appreciably the *in vivo* response⁶⁻⁸.

To overcome 2D systems limitations, novel cell culture solutions are being created to better mimic *in vivo* conditions with the usage of microporous, nanofibrous or hydrogel 3D scaffolds⁹. Hydrogels benefit from their high permeability to cell culture medium, nutrients, and waste products generated during the metabolic process.

Furthermore, recent enabled fabrication in customized shaped through controlled 3D printing¹⁰. However, 3D scaffolds still have limitations. On the one hand, it is difficult to monitor cell position and to later harvest cells for functional or biochemical analysis. On the other hand, although 3D scaffolds provide important information about cell homeostasis, they continue to lack the mechanical stimuli

found in true cellular microenvironments (i.e., fluid shear stress, tension and compression)³.

Trying to solve these limitations, a recent emerging approach comes from the field of microfluidics. Microfluidics is the science and technology of systems that process or manipulate small (10^{-9} to 10^{-18} liters) amounts of fluids using channels with dimensions of tens to hundreds of micrometers¹¹. By combining microfluidics with cell culture, biomedical engineers have given rise to so-called Organ-on-chip (OOC) devices. Microfluidic OOCs are advanced platforms designed to mimic physiological structures and continuous flow conditions, thus allowing the culture of cells in a friendlier microenvironment³.

Microfluidic devices are usually built by soft-lithography process, a technique first developed by Bell Labs in the 1970s¹² and later applied to microfluidics and cell culture¹³ (**Figure 1-3**).

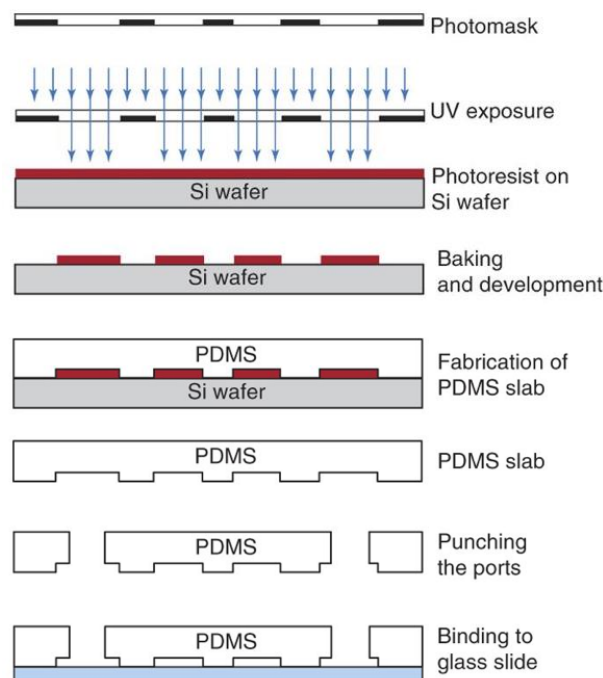


Figure 1-3: Quick overview of the main PDMS Soft lithography steps. From the top: After photomask fabrication, the master substrate is covered with photoresist and exposed through the photomask; Exposed resin is baked and developed to remove unwanted patterns; PDMS mixture is prepared and poured onto the master, degassed and cured; after curing, PDMS is demolded and cut to size; microfluidic ports are then punched into the PDMS device, which is finally bonded to the substrate. Reprinted by permission from Nature: [Mazutis et al, 2013](#)¹⁵.

Soft lithography process usually starts by fabricating negative masters by photolithographic process¹⁴. Masters are usually replica-molded in elastomers -like poly(dimethyl-siloxane) (PDMS) – or thermoplastics -like poly(methyl methacrylate) (PMMA) or polystyrene (PS). Finally, the device is bonded together, and inlets/outlets are connected.

PDMS has a long story in soft-lithography for microfluidics and cell culture, since its first use in 1998¹⁶. PDMS is an optically transparent, gas and vapor-permeable elastomer, which is relatively cheap, can bond reversibly to various materials and enables tuning of surface hydrophilicity¹⁷. Those interesting properties, together with the important contribution to the growth of the microfluidics field, made it become the actual gold standard for microfluidic cell culture applications.

Despite its many advantages, PDMS soft lithography still have many limitations. Some of them emerge in research environment: due to lot of time and money required by the production of masters and masks fabrication, design iteration should be reduced to minimum. Other limitations arise instead when trying to translate research technology to commercial devices. Folch and colleagues clearly highlighted 3 of these major challenges¹⁸: 1) PDMS molding (including PDMS curing, assembly, bonding, and inlet punching) is a largely manual process, very hard to fully automate; 2) user interfaces (inlets/outlets) usually consists in punched or molded holes, prone to leakage; 3) controlling systems required to run flow systems or sensing devices usually requires an engineering expertise which lacks in most biomedical laboratories.

An attempt to answer these challenges is being made in the last years by applying recent digital manufacturing (DM) rapid prototyping (RP) techniques to the problem of microfabrication. DM is a manufacturing process based on computer-assisted technology along all the steps from design to simulation and manufacturing. RP is a term which embraces a range of new technologies for producing accurate parts directly from Computer-Aided Design (CAD) models in a few hours, with little need for human intervention¹⁹. RP techniques may mainly be divided into those involving addition of material (Additive Manufacturing) and the ones involving its removal (Subtractive Manufacturing). Both techniques could significantly save cost and time required for production, as well as enabling easier design revision or customization, while reducing the required manual labor.

Recently particular interest has been shown in two RP techniques: Stereolithography (SL) and laser cut (**Figure 1-4**). SL is a form of 3D printing invented in the 1980s that allows for the assembly-free production of quasi-arbitrary 3D shapes in a single polymeric material from a photosensitive resin precursor by means of a focused laser or a Digital Light Processing (DLP) Projector²⁰. Laser cutting enables precise reproduction of design over a material by selectively vaporizing or melting the substrate. Depending on the combination of material properties and cutting parameters, engraving or clear cuts through the substrate can be achieved.

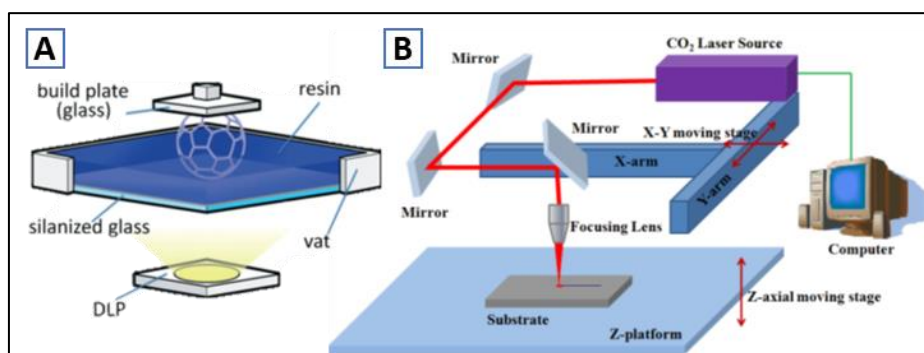


Figure 1-4: Rapid prototyping techniques for Microfluidics. A) In SL DLP setup, 3D object is built layer-by-layer by using selective light exposure to photo-polymerize a precursor resin collected in a vat¹⁸. Image reproduced from [Urrios et al, 2016](#)²⁰ with permission from The Royal Society of Chemistry (RSC); B) In laser cut setup, a substrate is cut or engraved by a laser head mounted on a motorized stage controlled by a computer. Image reproduced from [Hong et al, 2012](#)²¹.

Both previous techniques could be adapted to obtain a versatile fabrication process for OOC devices, adding the general benefits of rapid prototyping techniques. The word “organ” in OOC may be misleading: the goal is not to synthesize the whole organ but to reproduce the minimal part which exhibits tissue- and organ-level functionalities.

From a general design perspective, OOCs share the common background challenge to reproduce the interfaces between different cell types, which is where the most important interchanges happen. To achieve that, a porous membrane is usually required to act as initial support for the growth of two different cell types.

The first systems developed consisted of a single cell type cultured in a single perfused chamber with the aim to mimic the functions of a given tissue³. Later on, researchers focused on reproducing interfaces between distinct tissues to mimic complex organ-level responses²². Researchers have published studies on OOC

devices mimicking -among others- lung²², liver^{23,24}, kidney^{8,25,26}, gut²⁷, Blood Brain Barrier (BBB)²⁸⁻³⁰ and spleen³¹ functionalities. Among them, kidney and BBB mimicking receive particular interest in drug R&D. Kidney have particular relevance in pharmacokinetic studies due to its major role in drug excretion³² and relevance of nephrotoxicity in all stages of clinical trials³³. BBB accurate *in vitro* models are necessary for understanding how the BBB forms and functions, as well as for evaluating drug and toxin penetration across the barrier³⁴.

Following a pioneering study by Shuler and coworkers³⁵, the latest advances are trying to study multiple OOC interconnections. Combination of different organ-type models have been achieved, both as a single device^{36,37} and by interconnecting different bioreactors^{38,39}. Khademhosseini and colleagues recently reported on the use of elastomeric free-form blood vessels to interconnect OOC systems⁴⁰.

OOC technology aims to offer new tools and approaches to research in medicine, biology, and pharmacology, among others⁴¹. In order to achieve that, some challenges still need to be overcome regarding materials, cellular fidelity, multiplexing, sensing, scalability and validation⁴². Particularly, successful translation of OOCs from proof of concept in the laboratory to commercial screening platforms will require the identification and optimization of new low-cost materials and fabrication strategies suitable for their mass production and integration into existing infrastructures in the pharmaceutical industry⁴³. In that sense, OOC technology could benefit a lot integrating DM and RP techniques already at the laboratory proof-of-concept stage. DM and RP early stage integration will not only simplify a possible future technology translation, but also bring immediate additional benefits to proof-of-concept design, fabrication and revisions.

1.2 GENERAL OBJECTIVES

This thesis, entitled

“Cell culture interfaces for different organ-on-chip applications: from photolithography to rapid-prototyping techniques with sensor embedding”,

aims to design, simulate, fabricate and test microfluidic devices for cell co-culturing to replicate the interface between two different cell types under flow conditions.

Being a thesis in the Biomedical Engineering research area, it conjugates both technological and biological challenges. Technological objectives need to be met first in order to reach the complex goal of their application to biological problems.

The thesis has a strong technological focus on the exploration of novel fabrication techniques which could enable rapid prototyping of microfluidic OOC devices. The main technological goal is to achieve a versatile device for OOC applications which could lower costs, time and human labor associated to fabrication process.

Secondary technological goal is the simplification of the complex and often costly microfluidic setup which nowadays still prevents a broader public of biologist researchers to adopt microfluidics and OOC as an extra tool for their experiments.

Final biological objective is to demonstrate the suitability of the developed devices as research tools, applying them the investigation of two relevant biological interface problems. Tubular kidney and BBB physiological systems were chosen due to their particular relevance in drug R&D.

Specific objectives are:

1. To design a microfluidic membrane-embedded device;
2. To design a versatile device, capable of:
 - embedding membranes as a base structure of the cell-cell interface;
 - performing different type of experiments on the same device (static vs flow condition);
 - modifying the device in order to mimic different cell-cell interface without excessive additional costs or manufacturing time;
 - including electrodes for sensing and electrical measurements;
 - providing easy and solid interfacing of fluidic and electrical network to the macro world.

3. To investigate different fabrication methods for the microfluidic device in order to meet objective 2;
4. To integrate the fluidic setup in a portable platform;
5. To design and fabricate electrodes which allows integration with rapid prototyping fabrication;
6. To test the developed device to investigate biological problems.

1.3 BRIEF DESCRIPTION AND SPECIFIC OBJECTIVES OF EACH CHAPTER

This thesis articulates across different chapters, each one addressing one or more of the general objectives, inside the general framework aimed at the main general objective. Each chapter comprehends a thorough introduction to situate the reader on the current state of art, followed by an experimental section describing the material and methods applied. Results are then presented and discussed to arrive to independent conclusions for each chapter.

Chapter 2 mainly addresses specific objective 1; it focuses on developing a microfluidic membrane-embedded device to mimic cell culture interfaces using soft-lithography process (*OO v1*). Specific objectives of the chapter are:

- 2.1. to design and simulate a microfluidic device able to embed membranes;
- 2.2. to fabricate the device using photolithographic process.

Chapter 3 and 4 address general objective 3, by exploring the use of some rapid prototyping techniques for the fabrication of microfluidic devices.

Chapter 3 will focus on two similar subtractive techniques, using a plotter cutter and a laser cutter machine. Specific objectives of the chapter are:

- 3.1. to select suitable materials for OOC applications, compatible with RP techniques described in the chapter;
- 3.2. to design a versatile OOC device (*OOC v2.0*), integrating standard connectors, to be fabricated using RP techniques previously presented;
- 3.3. to optimize the fabrication protocol and to fabricate the devices;
- 3.4. to fabricate and test the new devices.

Chapter 4 will conversely focus on an additive manufacturing technique: SL 3D printing. Specific objectives of the chapter are:

- 4.1. to improve an existing commercial SL DLP printer for microfabrication;
- 4.2. to fabricate transparent and functional microfluidic devices using SL 3D printing;

4.3. to fabricate a 3D printed membrane embedded device for mimicking of cell culture interfaces (*OOCv3-A*) using SL 3D printing;

4.4. to fabricate “real 3D” complex multi-layered OOC device (*OOCv3-B*) using PDMS soft-lithography with SL-printed masters.

Chapter 5 addresses specific objectives 4 and 5, studying solutions to “integrate the chip in the lab”. Specific objectives of the chapter are:

5.1. to address the fluidic world-to-chip interface problem fluidic interface of *OOCv2.0* with a versatile solution which is compatible with the DM process illustrated in Chapter 3 (*OOCv2.1*);

5.2. to design and fabricate electrodes for transepithelial electrical resistance (TEER) measurements compatibles with the fabrication techniques seen in Chapter 3 (*OOC v2.2*) and providing easy and non-permanent electrical interfacing solution;

5.3. to design and fabricate a portable fluidic setup which could be embedded in a portable platform, aimed to simplify laboratory setups and experimental procedures.;

Chapter 6 and 7 addresses general objective 6, presenting the application of all the previously developed technology to two different biological problems, involving epithelial tubular kidney and the BBB.

Specific objectives of chapter 6 are:

6.1. to verify the viability of fabricated devices (*OOCv1*, *OOCv2.1*) for culturing of tubular kidney epithelial cells under flow condition;

6.2. to verify the viability of the portable fluidic setup developed in chapter 5 as a tool to simplify fluidic setup;

6.3. to adapt immunostaining protocols “on-chip”;

6.4 to study both cellular activity and metabolism of fatty acids in healthy vs pathological condition.

Specific objectives of chapter 7 are:

7.1. to verify the viability of fabricated device (OOCv2.1, OOCv2.2) for co-culturing of different cells under flow condition;

7.2. to verify repeatability of electrical measurements using electrodes in OOCv2.2;

7.3. to adapt immunostaining protocols “on-chip”;

7.4. to assess BBB formation and recovery after a disruptive treatment using various techniques;

Finally, **Chapter 8** presents the overall achievements and the general conclusions of this work.

1.4 REFERENCES

1. Scannell, J. W., Blanckley, A., Boldon, H. & Warrington, B. Diagnosing the decline in pharmaceutical R&D efficiency. *Nat. Rev. Drug Discov.* **11**, 191–200 (2012).
2. Munos, B. Lessons from 60 years of pharmaceutical innovation. *Nat. Rev. Drug Discov.* **8**, 959–968 (2009).
3. Paoli, R. & Samitier, J. Mimicking the kidney: A key role in organ-on-chip development. *Micromachines* **7**, (2016).
4. DiMasi, J. A., Grabowski, H. G. & Hansen, R. W. Innovation in the pharmaceutical industry: New estimates of R&D costs. *J. Health Econ.* **47**, 20–33 (2016).
5. Ziółkowska, K., Kwapiszewski, R. & Brzózka, Z. Microfluidic devices as tools for mimicking the in vivo environment. *New J. Chem.* **35**, 979 (2011).
6. Duval, K. *et al.* Modeling Physiological Events in 2D vs. 3D Cell Culture. *Physiology* **32**, 266–277 (2017).
7. Bachmann, K. & Ghosh, R. The Use of In Vitro Methods to Predict In Vivo Pharmacokinetics and Drug Interactions. *Curr. Drug Metab.* **2**, 299–314 (2001).
8. Jang, K.-J. *et al.* Human kidney proximal tubule-on-a-chip for drug transport and nephrotoxicity assessment. *Integr. Biol.* **5**, 1119 (2013).
9. Tibbitt, M. W. & Anseth, K. S. Hydrogels as extracellular matrix mimics for 3D cell culture. *Biotechnol. Bioeng.* **103**, 655–663 (2009).
10. Stanton, M. M., Samitier, J. & Sánchez, S. Bioprinting of 3D hydrogels. *Lab Chip* **15**, 3111–3115 (2015).
11. Farré, M., Kantiani, L. & Barceló, D. Microfluidic Devices: Biosensors. in *Chemical Analysis of Food: Techniques and Applications* 177–217 (Academic Press, 2012). doi:10.1016/B978-0-12-384862-8.00007-8
12. Aumiller, G. D., Chandross, E. A., Tomlinson, W. J. & Weber, H. P. Submicrometer resolution replication of relief patterns for integrated optics. *J. Appl. Phys.* **45**, 4557–4562 (1974).
13. Masuda, S., Washizu, M. & Nanba, T. Novel Method Of Cell Fusion In Field Constriction Area In Fluid Integrated Circuit. *IEEE Trans. Ind. Appl.* **25**, 732–737 (1989).
14. Moreau, W. M. *Semiconductor Lithography: Principles, Practices, and Materials.* Springer US (1988). doi:10.1007/978-1-4613-0885-0

15. Mazutis, L. *et al.* Single-cell analysis and sorting using droplet-based microfluidics. *Nat. Protoc.* **8**, 870–91 (2013).
16. Duffy, D. C., McDonald, J. C., Schueller, O. J. A. & Whitesides, G. M. Rapid prototyping of microfluidic systems in poly(dimethylsiloxane). *Anal. Chem.* **70**, 4974–4984 (1998).
17. Sackmann, E. K., Fulton, A. L. & Beebe, D. J. The present and future role of microfluidics in biomedical research. *Nature* **507**, 181–189 (2014).
18. Bhattacharjee, N., Urrios, A., Kang, S. & Folch, A. The upcoming 3D-printing revolution in microfluidics. *Lab on a Chip* **16**, 1720–1742 (2016).
19. Gault, R. & Pham, D. . A comparison of rapid prototyping technologies. *Int. J. Mach. Tools Manuf.* **38**, 1257–1287 (1998).
20. Urrios, A. *et al.* 3D-printing of transparent bio-microfluidic devices in PEG-DA. *Lab Chip* **16**, 2287–2294 (2016).
21. Hong, T.-F. *et al.* An Integrated Microfluidic Chip for Rapid Methanol Detection. *Int. J. Autom. Smart Technol.* **2**, 21–27 (2012).
22. Huh, D. *et al.* Reconstituting Organ-Level Lung Functions on a Chip. *Science (80-.)*. **328**, 1662–1668 (2010).
23. Bavli, D. *et al.* Real-time monitoring of metabolic function in liver-on-chip microdevices tracks the dynamics of mitochondrial dysfunction. *Proc. Natl. Acad. Sci.* **113**, E2231–E2240 (2016).
24. Nakao, Y., Kimura, H., Sakai, Y. & Fujii, T. Bile canaliculi formation by aligning rat primary hepatocytes in a microfluidic device. *Biomicrofluidics* **5**, (2011).
25. Jang, K.-J. & Suh, K.-Y. A multi-layer microfluidic device for efficient culture and analysis of renal tubular cells. *Lab Chip* **10**, 36–42 (2010).
26. Musah, S. *et al.* Mature induced-pluripotent-stem-cell-derived human podocytes reconstitute kidney glomerular-capillary-wall function on a chip. *Nat. Biomed. Eng.* **1**, (2017).
27. Kim, H. J., Huh, D., Hamilton, G. & Ingber, D. E. Human gut-on-a-chip inhabited by microbial flora that experiences intestinal peristalsis-like motions and flow. *Lab Chip* **12**, 2165–2174 (2012).
28. Adriani, G., Ma, D., Pavesi, A., Goh, E. L. K. & Kamm, R. D. Modeling the Blood-Brain Barrier in a 3D triple co-culture microfluidic system. *Proc. Annu. Int. Conf. IEEE Eng. Med. Biol. Soc. EMBS* **2015-Novem**, 338–341 (2015).
29. Booth, R. & Kim, H. Characterization of a microfluidic in vitro model of the

- blood-brain barrier (μ BBB). *Lab Chip* **12**, 1784 (2012).
30. Xu, H. *et al.* A dynamic in vivo-like organotypic blood-brain barrier model to probe metastatic brain tumors. *Sci. Rep.* **6**, 36670 (2016).
 31. Rigat-Brugarolas, L. G. *et al.* A functional microengineered model of the human splenon-on-a-chip. *Lab Chip* **14**, 1715 (2014).
 32. Morrissey, K. M., Stocker, S. L., Wittwer, M. B., Xu, L. & Giacomini, K. M. Renal transporters in drug development. *Annu. Rev. Pharmacol. Toxicol.* **53**, 503–29 (2013).
 33. Arrowsmith, J. & Miller, P. Trial watch: phase II and phase III attrition rates 2011-2012. *Nat. Rev. Drug Discov.* **12**, 569 (2013).
 34. Brown, J. A. *et al.* Recreating blood-brain barrier physiology and structure on chip: A novel neurovascular microfluidic bioreactor. *Biomicrofluidics* **9**, (2015).
 35. Viravaidya, K., Sin, A. & Shuler, M. L. Development of a Microscale Cell Culture Analog To Probe Naphthalene Toxicity. *Biotechnol. Prog.* **20**, 316–323 (2004).
 36. Imura, Y., Yoshimura, E. & Sato, K. Micro Total Bioassay System for Oral Drugs: Evaluation of Gastrointestinal Degradation, Intestinal Absorption, Hepatic Metabolism, and Bioactivity. *Anal. Sci.* **28**, 197 (2012).
 37. Wagner, I. *et al.* A dynamic multi-organ-chip for long-term cultivation and substance testing proven by 3D human liver and skin tissue co-culture. *Lab Chip* **13**, 3538–47 (2013).
 38. Vozzi, F. *et al.* A flexible bioreactor system for constructing in vitro tissue and organ models. *Biotechnol. Bioeng.* **108**, 2129–2140 (2011).
 39. Iori, E. *et al.* Glucose and fatty acid metabolism in a 3 tissue in-vitro model challenged with normo- and hyperglycaemia. *PLoS One* **7**, e34704 (2012).
 40. Zhang, W. *et al.* Elastomeric Free-Form Blood Vessels for Interconnecting Organs on Chip Systems. *Lab Chip* **16**, 1579–1586 (2016).
 41. Sosa-Hernández, J. E. *et al.* Organs-on-a-Chip Module: A Review from the Development and Applications Perspective. *Micromachines* **9**, 536 (2018).
 42. Zhang, B., Korolj, A., Lai, B. F. L. & Radisic, M. Advances in organ-on-a-chip engineering. *Nat. Rev. Mater.* **3**, 257–278 (2018).
 43. Esch, E. W., Bahinski, A. & Huh, D. Organs-on-chips at the frontiers of drug discovery. *Nat. Rev. Drug Discov.* **14**, 248–260 (2015).

2 PDMS soft lithography for OOC microfabrication

2.1	Background	16
2.1.1	INTRODUCTION TO MICROFLUIDICS.....	16
2.1.2	HYDRODYNAMICS OF FLUIDS INSIDE SMALL CHANNELS	17
2.1.3	SOFT LITHOGRAPHY FABRICATION OF MICROFLUIDIC DEVICES	22
2.1.4	MICROFLUIDICS AND CELL CULTURE: THE BIRTH OF OOC	26
2.2	Challenges for fabrication of OOC device using PDMS soft-lithography.	30
2.3	Materials and methods	31
2.3.1	MATERIALS USED.....	31
2.3.2	DESIGN AND SIMULATION OF FIRST VERSION OOC (OOCv1)	31
2.3.3	FABRICATION OF OOCv1.....	34
2.3.4	CHARACTERIZATION	37
2.4	Results	37
2.4.1	DESIGN AND SIMULATION	37
2.4.2	FABRICATION.....	38
2.4.3	ASSEMBLY.....	40
2.5	Discussion	41
2.6	Conclusions	43
2.7	References.....	44

PDMS soft lithography, the gold standard of microfabrication, is the natural starting point to explore microfabrication techniques for OOC applications.

Aim of this chapter is the development of membrane-embedded OOC devices using PDMS soft lithography. We will call this first design version OOCv1.

The background section presents a proper introduction to the world of microfluidics, PDMS soft lithography and its OOC applications. Afterwards, a biologically inspired design template is defined and customized selecting two different values of channels dimensions and aspect ratios. After verifying the wall shear stress distribution of the selected final designs through computer simulations, PDMS devices are fabricated and different strategies for membrane embedding are evaluated.

Functional devices are finally obtained, and results are discussed together with some considerations on possible improvements.

2.1 BACKGROUND

This chapter will be dedicated to design and fabrication of OOC devices using traditional PDMS soft lithography techniques. Thus, this section will start with a brief introduction to microfluidics, its main concept and fundamental laws, whose knowledge is a necessary starting point for the design of OOC devices. Later on, we will introduce PDMS soft lithography process and the current state of art to embed membranes in PDMS devices. Finally, a brief overview of OOC state of art is exposed.

2.1.1 Introduction to Microfluidics

The run to technology miniaturization has reached nowadays impressive levels which would have sounded impossible just a few years ago. All started in December 1959, when Nobel prize physicist Richard P. Feynman had a visionary speech in which he foresaw the possibility to manipulate matters at the micro- and nano-scale¹. In the talk, Feynman challenged the audience offering \$1000 to the first person able to make an operating micro-electric motor. First fulfillment of that vision arrived in 1965, when Nathanson conceived the Microelectronic frequency selective apparatus, to serve as a tuner for microelectronic radios, marking the birth of a new field of study: microelectro-mechanical systems (MEMS)². More complex devices followed from the 70's to the 90's, like the first pressure sensors, airbag activations systems, ink-jet and the first micromotor³.

The first isolated microsystem applicated to the manipulation of fluid dates back to 1979⁴, but only during the 1990s MEMS devices started to be fabricated for chemical, biological and biomedical applications³. The study of fluid flows operating under unusual and unexplored conditions inside those devices, naturally led to the birth of a new field: microfluidics³.

Microfluidics is defined as the science and technology of systems that process or manipulate small (10^{-9} to 10^{-18} L) amounts of fluids using channels with dimensions of tens to hundreds of micrometers⁵. The escalation of miniaturization together with the ability of manipulating tiny quantities of fluid paved the way towards the idea of Micro-Total Analysis Systems (μ TAS), miniaturized devices that automate and include all necessary steps for a chemical analysis of a sample^{6,7}. The concept was later expanded by the term "Lab-On-a-Chip" (LOC) to indicate a microdevice which integrates one or several laboratory functions with the aim to achieve automation and high-throughput screening. Both terms, μ TAS and LOC, are often used as synonyms. Through miniaturization, on the one hand LOC devices

enables to reduce sample volume, reagents and overall cost, processing time and equipment footprint considerably^{5,8}. On the other hand, thanks to microfluidics, LOC offers new capabilities to manipulate the sample and interacting with it⁵, exploiting physical laws and phenomena which are not valid at the macroscale.

2.1.2 Hydrodynamics of fluids inside small channels

Microfluidics enable to investigate and make us of some laws and phenomena which are only valid at the microscale. Here we introduce the main concepts and physical laws which we consider fundamental to understand the general aspects of hydrodynamics inside small channels and are important for cell culture in microfluidics device.

2.1.2.1 Navier-Stokes equation

The motion of viscous fluid substances is described in physics by the Navier–Stokes equations, named after Claude-Louis Navier and George Gabriel Stokes. For flows in microfluidic devices, fluids (primarily water and aqueous solutions) are well approximated as incompressible^{9,10}, which implies that their density is uniform. In particular, for incompressible uniform-viscous Newtonian fluids the Navier-Stokes describing flow velocity are reduced to:

$$\rho \frac{\partial \vec{\mu}}{\partial t} = -\rho \vec{\mu} \nabla \vec{\mu} - \nabla P + \mu \nabla^2 \vec{\mu} \quad (2-1)$$

where $\vec{\mu}$ is the velocity field [$m \ s^{-1}$]; ρ is the fluid density [$kg \ m^{-3}$]; P is the pressure [Pa]; μ is the viscosity [Pa s].

2.1.2.2 Hydraulic Diameter

Most hydrodynamic laws have general formulations for circular channels. To generalize some of that formulations to non-circular channels, we introduce the concept of hydraulic diameter D_H , defined as

$$D_H = \frac{4A}{P} \quad (2-2)$$

where $A [m^2]$ is the cross-sectional area and $P [m]$ is the wetted perimeter.

Particularly, for rectangular channels, the hydraulic diameter is equal to

$$D_H = \frac{4A}{P} = \frac{4wh}{2(w+h)} = \frac{2wh}{w+h} \quad (2-3)$$

where w is the width of the channel and h is the height.

D_H makes it possible in some cases to calculate hydraulic characteristics of the flow in channels of various geometrical shapes by the formulas derived for a circular pipe¹¹.

2.1.2.3 Reynolds number

To characterize the fluidic behavior in channels, we introduce a dimensionless parameter called Reynolds number (Re), which is conventionally defined as the ratio of inertial forces to viscous forces⁹:

$$Re = \frac{(\text{inertia force})}{(\text{viscous force})} = \frac{\rho VD}{\mu} \approx \frac{\rho UD_H}{\mu} \quad (2-4)$$

Where V is the characteristic velocity [m s^{-1}]; U is the area-averaged velocity [$\text{m}\cdot\text{s}^{-1}$]; D is the characteristic length [m] and D_H the hydraulic diameter of the channel [m].

At low Reynolds numbers viscous forces are dominant and laminar flow occurs ($Re < 2300$ for straight and smooth channels^{9,12}). In laminar flow layers of liquid slide by one another in a direction that is parallel to the surface containing the liquid¹³. Fluid flows in microchannels typically occurs at low Re , because of the small geometries, and the common usage of low flow rates.

2.1.2.4 Poiseuille flow

Poiseuille flow can be defined as a pressure-driven laminar flow in a long circular channel. Its velocity field is unidirectional and laminar and there is no acceleration of the fluid⁹. Based on that assumptions, Navier-Stokes equation can be simplified as following:

$$\nabla P = \mu \nabla^2 \vec{u} \quad (2-5)$$

Due to geometric simplification and no-slip boundary condition (velocity $\mu = 0$ on the walls), the velocity profile of Poiseuille flow inside a channel of radius R [m] is parabolic across a diameter (**Figure 2-1**)

$$u = \frac{R^2 - r^2}{4\mu} \left(-\frac{dP}{dx} \right) = u_{max} \left(1 - \frac{r^2}{R^2} \right) \quad (2-6)$$

where r [m] is the radial distance (cylindrical polar coordinates), and $u_{max} = \frac{R^2}{4\mu} \left(-\frac{dP}{dx} \right)$ is the maximum velocity in the center of the channel ($r = 0$)⁹.

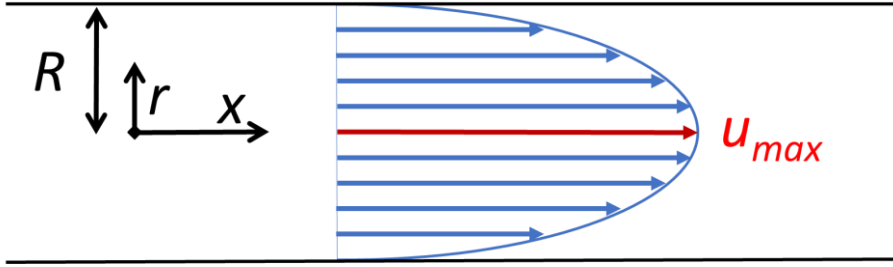


Figure 2-1: Poiseuille flow profile. Maximum velocity at center of the channel.

Total volumetric flow rate Q [$m^3 \cdot s^{-1}$] in a circular channel is obtained through spatially integrate contributions from Equation (2-6), obtaining:

$$Q = \frac{\pi}{8\mu} \left(-\frac{dP}{dx} \right) \quad (2-7)$$

If i) $L \gg R$ and ii) $\frac{L}{R} \gg Re$ laminar flow in a long narrow channel can be assumed fully developed and we can assume a uniform pressure gradient across the length of the channel⁹, so we can simplify to

$$Q = \frac{\pi R^4 \Delta P}{8\mu L} \quad (2-8)$$

where ΔP is the pressure difference [Pa] across the channel length L .

2.1.2.5 Hydraulic resistance.

In analogy with electrical circuits, we can define the Hydraulic resistance R_H of a microchannels as

$$R_H = \frac{Q}{\Delta P} = \frac{8\mu L}{\pi R^4} \quad (2-9)$$

where R is the radius of a circular channel. It should be noted that equation (2-9) can be applied to non-circular channels by replacing the radius R with the hydraulic radius of the microchannel ($r_H = \frac{D_H}{2}$), obtaining

$$R_H = \frac{8\mu L}{\pi R^4} \approx \frac{8\mu L}{\pi r_H} \quad (2-10)$$

The exact formula for hydraulic resistance of a rectangular microchannel¹⁴ is

$$R_H = \frac{12\eta L}{wh^3 \left(1 - \frac{h}{w} \left(\frac{192}{\pi^5} \sum_{n=1,3,5}^{\infty} \frac{1}{n^5} \tanh \left(\frac{n\pi w}{2h} \right) \right) \right)} \quad (2-11)$$

but in general equation (2-10) can be applied to non-circular channels using their respective hydraulic radius⁹, resulting in a valid, much easier to calculate approximation for design purposes.

2.1.2.6 Shear stress in a microfluidic channel

When a fluid is in motion, shear stresses are developed due to the inner movement of its forming particles. In laminar flow, shear stresses develop at the interface between layers moving at different speeds; particularly, as no-slip condition dictates zero velocity of the fluid at the boundary, wall shear stresses develops at the solid-liquid interfaces.

For a Newtonian fluid, shear stress at a distance y from a stationary wall is

$$\tau(y) = \mu \frac{\partial u}{\partial y} \quad (2-12)$$

where μ [$Pa \cdot s$] is the dynamic viscosity of the fluid and $\frac{\partial u}{\partial y}$ [s^{-1}] is the velocity gradient across the boundary.

Under fully developed laminar flow conditions, shear stress acting on the walls of a circular pipe is

$$\tau_w = \frac{8\mu\bar{u}}{d} \quad (2-13)$$

while the one acting on a rectangular microchannel with $w > h$ is

$$\tau_w \approx \frac{h \Delta P}{2 L} = \frac{6\mu Q}{wh^2} \quad (2-14)$$

Many cell types in their natural environment are surrounded by moving fluids which generates shear stress. Wall shear stress is a relevant input to mechano-adaptation, which regulates cell decision events, such as cell growth and proliferation, apoptosis, differentiation, and shape modulation¹⁵. Aa very wide range of cellular phenomena are recognized as being influenced by fluid shear, including both mechano-reception (e.g., plasma membrane receptors, ion channels, integrins/focal adhesions, protein kinase signaling) and response (e.g., intracellular calcium, nitric oxide, prostacyclin, cytoskeletal remodeling)¹⁵⁻¹⁷. Precise control over shear stress is required. Too high values of shear stress might result in cell detachment or affect physiological functions of cells while physiological values can exert positive effects¹⁸. For example, various studies on the renal epithelial cells demonstrated the role of wall shear stress

(WSS) as a modulator of cellular signal transduction, organization of cytoskeleton, junctional complex and expression of tight and adherens junction, amongst others¹⁹.

2.1.2.7 Hess-Murray's Law

Since organisms have developed over time optimized structures thanks to natural selection, an entire new research field -called bio-mimetics- has developed to understand these "natural" optimal design strategies²⁰. A fascinating example are the biomimetic design principle found in mammals cardiovascular and respiratory system, arranged into hierarchical structures²¹. Mathematical modeling of these structures can be traced back to 1926, when Murray²² used the principle of minimum work to derive a relationship between the diameter of the parent vessel and the optimum diameters of the daughter vessels in a branching network²⁰.

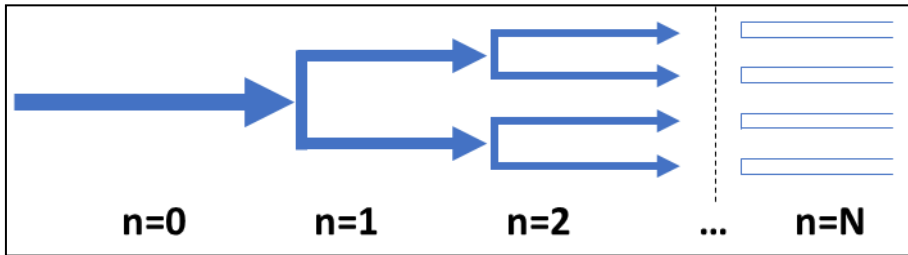


Figure 2-2: Murray Law hierarchical branching nomenclature.

Considering a hierarchical branching of vessels as in **Figure 2-2**, we obtain the *Hess-Murray law*, or *third power law*

$$d_0^3 = d_{1A}^3 + d_{1B}^3 \quad (2-15)$$

For symmetrical systems, where $d_1 \equiv d_{1A} = d_{1B}$, equation (2-15) becomes

$$d_0^3 = 2d_1^3 \quad (2-16)$$

It has been demonstrated that the Hess-Murray law can be generalized introducing a branching parameter X to modify the rate at which the channel dimensions diminish in size^{20,21,23} :

$$X = \frac{d_0^3}{2d_1^3} \quad (2-17)$$

When $X = 1$, equation (2-17) represent the symmetrical case of the *third power law* as in (2-16) and the parent/daughter branching obeys the principle of minimum work²⁰.

As volumetric flow rate halves at each bifurcation i.e. $Q_n = 2^{-n}Q_0$, the mean velocity in each ramification is

$$\bar{u}_n = \bar{u}_0 \left[\frac{1}{2} X^2 \right]^{-\frac{n}{3}} \quad (2-18)$$

Average residence time of fluid in the n -th generation can be defined as the ratio between length of the channel L_n and the average velocity \bar{u}_n . If the length of an individual segment is considered proportional to its diameter through a constant k , the average residence t_n time in the n -th generation is

$$t_n = \frac{L_n}{\bar{u}_n} = \frac{k d_n}{\bar{u}_n} = \frac{k d_0}{\bar{u}_0 X^n} = \frac{L_0}{\bar{u}_0 X^n} = \frac{t_0}{X^n} \quad (2-19)$$

Values of $X \neq 1$ can be used to design micro-vasculature with specific residence time distribution.

Substituting (2-17) and (2-18) into (2-13), we obtain the formula for wall shear stress for each generation

$$\tau_{W,n} = \tau_{W,0} \cdot X^n \quad (2-20)$$

For $X = 1$, we obtain a constant shear stress value across all generations. Using a value of $X < 1$, the shear stress value decreases toward the finest branches of the vasculature; this configuration may be especially useful in tissue-engineering applications in order to increase the probability of cells binding to the walls, and also to increase the residence time of the biofluid to enhance the diffusion of nutrients into the tissue culture²⁰.

2.1.3 Soft lithography fabrication of microfluidic devices

Most used fabrication method for microfluidics is called soft lithography and is derived from lithographic process of microelectronics.

2.1.3.1 Typical soft lithography process by photolithographic master

Typical soft lithography process consists of a series of steps (Figure 2-3). First a mask has to be designed using a CAD program and printed on a transparent support. High resolution masks are generally plates of quartz on which patterns are reproduced through deposits of chrome³. Chrome masks fabrication is expensive and time consuming²⁴; a much cheaper alternative, made on transparent polymer sheet using a high resolution printer, has been around since 1996 and enables reproduction of patterns down to $20 \mu m$ ²⁴. Obviously is not possible to obtain a microstructure with

a precision superior to that of the mask, but many microfluidics applications are fine with that resolution. The surface of the substrate of choice (usually silicon or glass) has to be cleaned to eliminate impurities. A height-controlled layer of photosensitive resin is applied on top of the substrate. This operation can be done both by laminating dry-film resist on top of the substrate or by spin-coating liquid resin and successively baking it. The deposited resin layer is then brought in contact with the mask and exposed to UV light. The luminous flux initiates physico-chemical reactions in the polymer, modifying its solubility in certain solvents³. Depending on the polarity of the resist, positive or negative, the exposed zones become respectively soluble or insoluble. Finally, after a developing step, we obtained the three-dimensional negative of our structure. At this point, replica-molding in elastomers - like poly(dimethyl-siloxane) (PDMS) – or thermoplastics -like poly(methyl-methacrylate) (PMMA) or polystyrene (PS) is performed. At this point ports usually need to be punched, and the replica needs to be bonded to a flat surface (usually glass or the same polymer).

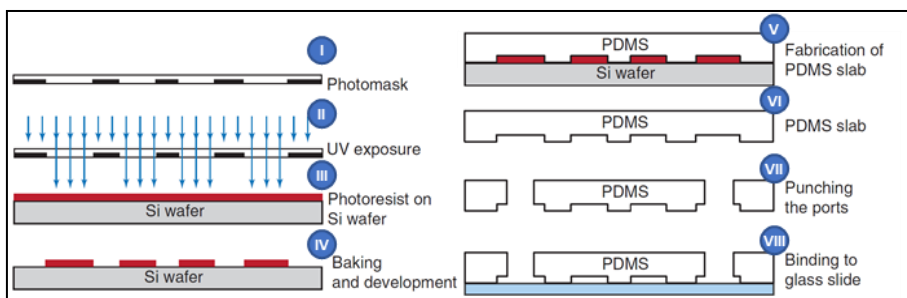


Figure 2-3. PDMS soft lithography steps. Image Reprinted by permission from Nature: Mazutis et al, 2013²⁵.

2.1.3.2 PDMS advantages

In the late 1990's the field of biomicrofluidics exploded^{5,26,27} with the introduction of PDMS, an optically transparent, soft elastomer ideal for biological applications on the small scale²⁸. PDMS quickly became the standard for fabrication of microfluidics devices in research environment, especially the ones involving cell culture. PDMS is relatively low cost and can be replicated repeatedly against photolithographic masters using extremely simple—albeit difficult to automate—procedures²⁹. Mold releasing is facilitated by its low surface energy (typical 0.02 J m^{-2}) and low Young modulus (typical $\sim 750 \text{ kPa}$)^{30–32}. Low surface energy also enables reversible sealing to materials. Low Young modulus further enables fabrication of active elements like valves^{31,32}. Its high transparency enables microscope observation in the range of

240~1100 nm³² and it is impermeable to liquid water. Finally, its high gas permeability and biocompatibility made it the ideal candidate for cell cultures.

2.1.3.3 Membrane embedding strategies in PDMS devices

The use of membranes in microfluidics has been a topic of growing interest for its various possible applications³³, including the use of biocompatible or biodegradable membranes as a scaffold for cell cultures which is a key point in this thesis. Hereafter we describe membrane embedding strategies, focusing on PDMS devices and cell culture applications.

We can define a membrane as a semi-permeable barrier³³. Cell culture applications usually need low selectivity membranes, in order to not limit substances interchange while retaining cells in their corresponding channel before adhesion. Membrane embedding strategies for PDMS devices mainly consists of three different approaches: design pores or small channels in the PDMS replica, add a channel to be filled with porous hydrogel or embed commercial membranes. Also, we will differentiate between horizontal vs vertical separation approach, if the different culture channels (or chambers) separated by the membrane are located - respectively- on the same plane or one on top of the other.

Make a membrane out of PDMS features is possibly one of the neatest solutions, enabling to use a single material for the fabrication and avoiding the need for additional bonding strategies. Two different approaches are available in this case, with vertical or horizontal separation. The first one consists using a multilayer device, where two layers of channels are separated by a thin membrane layer where pores are obtained by replicating a master with an array of micropillars. Main limitations of this approach come from the soft-lithography process involved, both in terms of minimum pores size as well as aspect ratio. Additionally, difficulty in handling thin layers of PDMS before their bonding makes the process delicate and dependent on user dexterity. The second one consists of adding porosity to the wall separating two channels on the same layer, by adding slits. While being much easier to implement, this options limits membrane surface areas.

Second strategy consist in adding an intermediate channel which is filled with a hydrogel before the seeding and polymerize it (usually by temperature change) so it could later act as a barrier. This approach is widely used in the literature, especially in various works from Kamm et colleagues³⁴⁻³⁶. In this case like in any horizontal approach, microscope observation is easier as the device bottom layer could be

directly a microscope coverslip. Even if a strategy to generate the inner collagen wall using laminar flow has been published³⁷, most approaches make use of columns to contain the hydrogel, limiting effective membrane surface area.

Finally, another versatile solution reported in literature consists in embedding commercial membranes in the devices, sandwiching it between two layers of PDMS. The largest advantages of directly incorporating membranes are the simplicity of the process and the wide choice of membrane materials and morphologies³³. One major problem in this approach is the sealing step. Clamping of the membrane is not a valid solution: due to capillary forces liquid is pulled at the interface between the two layers. A complete sealing is thus required. Although PDMS can readily bond substantially with another silicon-based material such as glass, silicon wafer, and quartz through simple surface oxidation and thermal curing^{38–40}, its ability to form robust and irreversible chemical bonds with non-silicon-based materials such as plastics, metals, alloys, and ceramics in the assembly process is hampered^{5,41}.

One solution is sealing the assembly using glue, though the procedure is not easy as the glue could be easily sucked inside the channels due to capillary force. Glass slides spin-coated with PDMS/Toluene mixture was used to deposit a very thin layer of uncured PDMS over PDMS microstructures, which were later assembled and cured to obtain leakage free devices with channel sections down to $40 \times 100 \mu\text{m}$ ⁴² (**Figure 2-4**). Another solution, when possible, consists in modifying the material surface with a silane composite which could be later oxidized exposing hydroxyl groups (OHs) (**Figure 2-5**)^{41,43}.

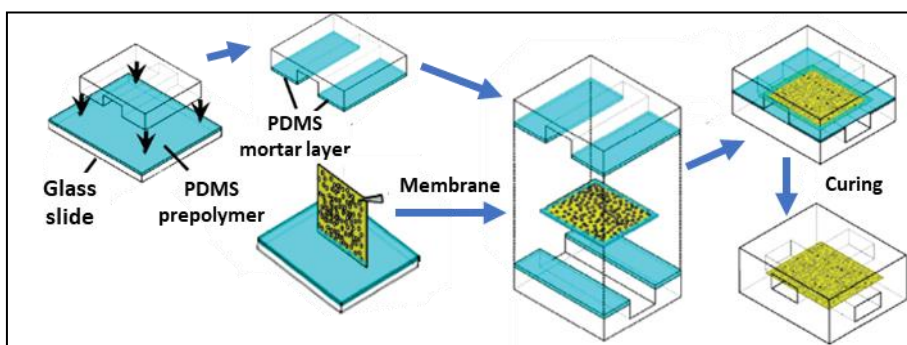


Figure 2-4. PDMS-glue bonding protocol. Image adapted with permission from [Chueh et al, 2007](#)⁴². Copyright (2007) American Chemical Society.

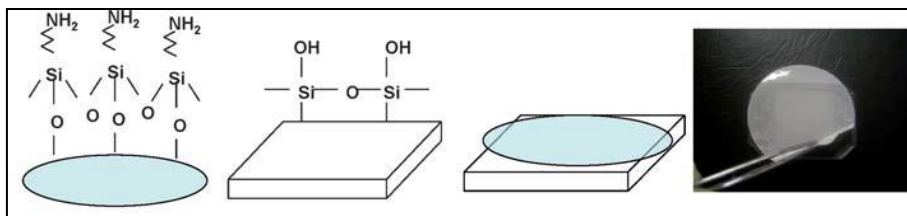


Figure 2-5. APTES functionalization and plasma activation bonding. From left: Membrane functionalized with APTES; PDMS surface after plasma treatment; the membrane bonded to PDMS and a photo of the assembly. Reproduced from [Aran et al, 2010](#)⁴³, by RSC permission.

2.1.4 Microfluidics and cell culture: the birth of OOC

The increasing cost for drug R&D that pharmaceutical industries are facing⁴⁴ highlights the need for new strategies to improve R&D productivity⁸. Microfluidics researchers tried to address this problem proposing new tools aimed at reducing the costs of drug R&D. These devices, named OOC, aim at mimicking the cellular microenvironment. The word “Organ” refers to the aim of mimicking the smaller functional unit which exhibit specific tissue- and organ-level functionality. On the other hand, the word “chip” refers to the main fabrication technique, photolithographic etching process, borrowed from the electronic microchip manufacturing industry⁴⁵.

In general, cell lines cultured *in vitro* have been largely inactivated and lack physiological functions^{46,47}. Traditional cell culture in a semi-static environment differ from *in vivo* cells conditions, which obtain oxygen and nutrients via blood flow, as well as receive chemical stimulation and physical stimulation, such as stretching and shear stress, from the surrounding environment⁴⁷. OOC technology tries to fill this gap, which might be the reason for loss or deactivation of cellular functions in culture⁴⁷.

Furthermore, while in traditional drug screening approaches, organ-specific effects and the toxicity of a drug are examined using a homogeneous population of specific cells, human organs are based on intricate interactions between various specialized cell types arranged in precise geometries and interacting with specific microenvironments²⁸. These interactions often occur at well-defined tissue-tissue interfaces, enabling organ function²⁰.

The concept of mimicking the organ-level function of human physiology or disease using cells inside a microfluidic chip was first published in 2004, when Michael Shuler

and colleagues^{48,49} first demonstrated a cell culture analogue system that captured the systemic interaction between lung and liver on a one square inch silicon chip²⁸.

During the last decade, researchers developed many solutions to recapitulate different organs. Here we present a brief overview of the state of the art, with focus on fabrication; for a more detailed state of art of Kidney and BBB OOC devices, please refer to chapter 6.1.

2.1.4.1 Lung

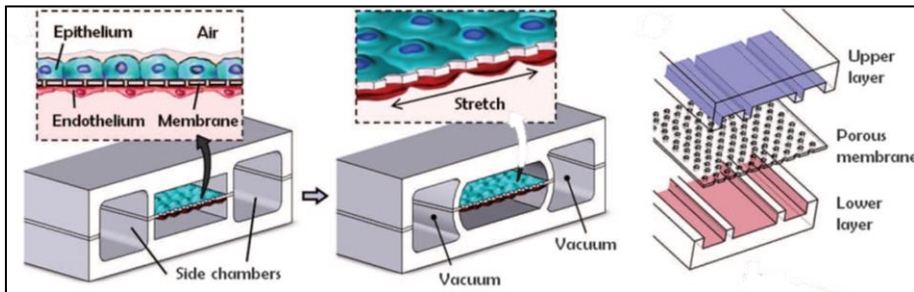


Figure 2-6. Lung-on-chip. Reproduced from [Huh et al, 2010](#)⁵⁰ with permission from Science.

The most known OOC is the lung-on-chip developed in by Ingber research group⁵⁰ in 2010 (**Figure 2-6**). The entire device is fabricated in PDMS and consists of two-layer of channels separated vertically by a porous membrane. Additionally, two side chambers running parallel to the channels enabled stretching and contraction of the membrane by changing air pressure. They cultured alveolar epithelial cells and vascular endothelial cells on upper and the lower surface of the membrane, respectively. They flew air and culture medium, respectively, in the upper and lower channel. They reproduced inflammatory reactions to tumor necrosis factor (TNF- α) and bacteria, conducted a toxicity test using nanoparticles and, in a later study⁵¹, created a disease model recapitulating symptoms of pulmonary edema.

2.1.4.2 Liver

The liver, with its high metabolic activity, is crucial to life and its tissue usually suffers major damage from chronic diseases and viral infections⁵². Bavli et al⁵³ fabricated a perfusion bioreactor made of two circular PMMA supports with glass bottom to fit PDMS inserts with microwells (**Figure 2-7-A**). Kimura et al⁵⁴ designed a device to mimic liver hepatic cords structures, which led to the formation of bile canaliculi (**Figure 2-7-B**). The device, entirely in PDMS, consisted of small cell culture area separated by the adjacent medium flow channel (width: 100 μm , height: 30 μm) by a series of square slits (width, height: 2 μm) through a 30 μm wall.

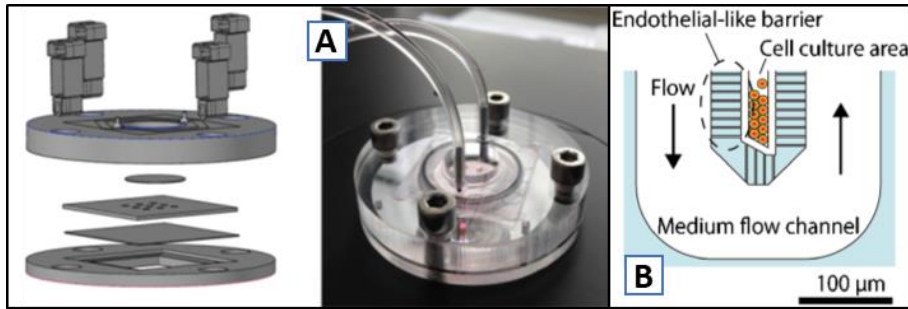


Figure 2-7. Liver-on-chip devices. A) Perfusion biorreactor. Reprinted from [Bavli et al⁵³](#); B) Hepatic lobules model. Reprinted from [Kimura et al⁵⁴](#), with permission from AIP Publishing.

2.1.4.3 Kidney

In 2009 Jang et al⁵⁵ fabricated a multilayer microfluidic device for culturing of primary rat inner medullary collecting duct cells and. The device consisted of a microfluidic channel (width: 1 mm, height: 100 μm) and a reservoir, both in PDMS, separated by a polyester (PE) membrane. The system was bonded using O_2 plasma. The same device was later used to culture human proximal tubule renal cells⁵⁶. Musah et al⁵⁷ used a slight modification of the lung-on-chip⁵⁰ to culture and differentiate human induced pluripotent stem cells (hIPS) into renal podocytes. Ingber group⁵⁷ applied the “lung-on-a-chip” device to replicate the glomerulus structure by combining hIPS podocytes with human glomerular endothelial cells, under shear stress and cyclic strain stimuli. Cells responded producing glomerular basement-membrane collagen and recapitulating the natural tissue–tissue interface of the glomerulus, achieving differential clearance of albumin and insulin⁵⁷.

2.1.4.4 Gut

The “lung-on-chip” device developed by Ingber group⁵⁰ found another application to mimic human intestine⁵⁸. Mechanical stimulation through air pressure change in adjacent channels was used to mimic peristaltic movement. Many biological gut-on-chip application followed, like effects on villus differentiation⁵⁹ or pathophysiologic studies on the effects of bacteria⁶⁰, virus⁶¹ or radiations⁶².

2.1.4.5 BBB

Booth and Kim⁶³ fabricated an hybrid PDMS-glass devices to replicate the BBB and include electrodes (**Figure 2-8-A**). A polycarbonate membrane separates the intersection between two 200 μm high PDMS channels. Upper and lower channels (width 2 mm and 5 mm, respectively) are bonded to glass slides where electrodes have been fabricated. Membrane is sealed using PDMS-glu stamping.

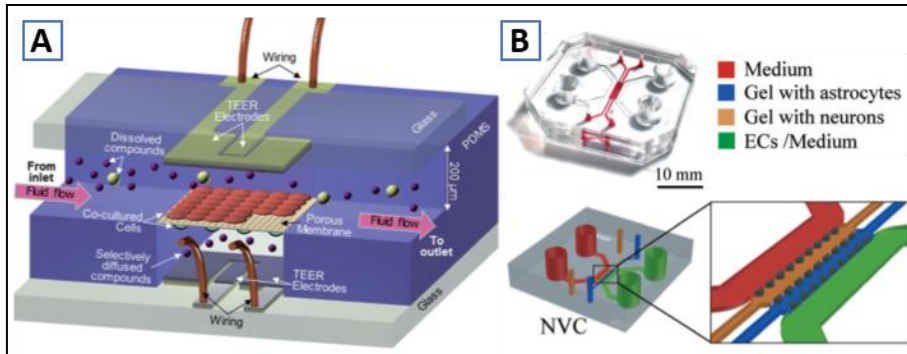


Figure 2-8. BBB-on-chip models. A) PDMS device including electrodes (Reproduced from [Booth and Kim, 2012](#)⁶³, by permission of RSC); B) PDMS multichannel hydrogel device (Adapted from [Adriani et al, 2017](#)⁶⁴, by permission of RSC).

Kamm et colleagues^{35,36,65} fabricated PDMS device with coverslip glass bottom consisting of 4 adjacent microchannels (height: $190\ \mu\text{m}$, **Figure 2-9-B**). The 2 inner hydrogel channels (width: $580\ \mu\text{m}$) are separated from the outer media channels (width: $920\ \mu\text{m}$) from trapezoidal structures who helps retaining the hydrogel during filling. Primary rat astrocytes and neurons together with human cerebral microvascular endothelial cells were cultured inside the device. Similar approach is followed by other groups⁶⁶.

2.1.4.6 Spleen

Recently our group⁶⁷ developed the first micro-engineered model mimicking the hydrodynamic forces and the physical properties of the splenon, the minimal functional unit of the red pulp able to maintain filtering functions (**Figure 2-9**). The device consisted of a PDMS device reproducing the fast and slow flow channel. Slow flow channel featured filter-like structure with a pillar matrix and small micro-slits.

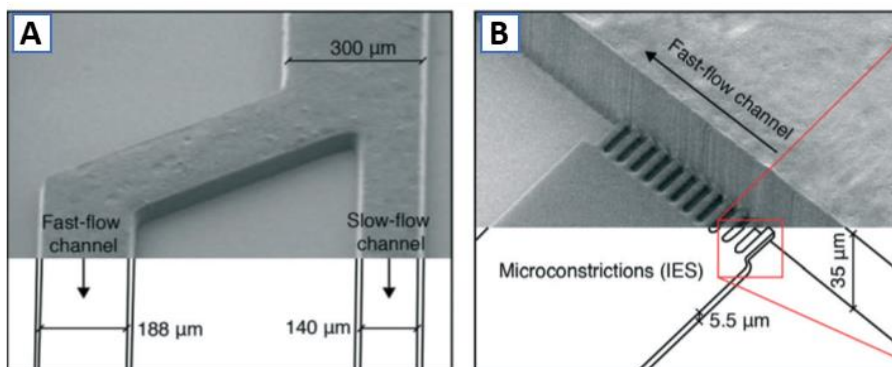


Figure 2-9. Splenon-on-chip. A) Flow division zone; B) Micro-constrictions representing the inter-endothelial slits. Image reproduced from [Riqat et al, 2014](#)⁶⁷, with permission from RSC.

2.1.4.7 Multi-OOC

The Shuler research group has been a pioneer in studies involving the concept of body-on-a-chip since the 2000s^{48,68–70} using their hybrid PDMS-Polycarbonate (PC) system able to include different commercial membranes.

Similar approach has been followed by another recent multi-organ-on-chip device⁷¹. In a standard microscope slide, the device includes four interconnected compartments to culture liver, intestine, kidney and skin tissues (**Figure 2-10**). The chambers are interconnected by a microfluidic channel for surrogate blood flow which overlaps in the tubular region with a second microfluidic circuit of fluid excreted by renal epithelial cells. The channels and the two integrated peristaltic micropumps are in PDMS. PE membrane is glued. Intestine and liver cells proceed from primary source, while skin and kidney ones are from immortalized cell lines.

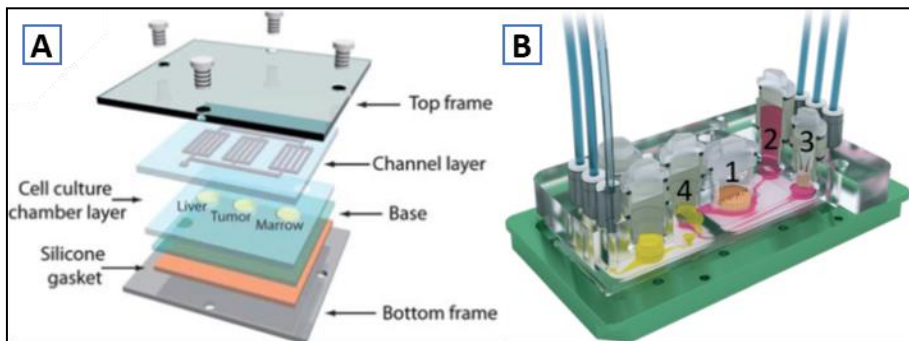


Figure 2-10. Multi-organ on chip. A) Device from Shuler group, featuring culturing of liver, bone marrow and tumor cells (image reproduced from [Sung et al., 2010](#)⁶⁹ with permission from RSC); B) Four organ on chip device, featuring intestine (1), liver (2), skin (3) and kidney (4) cells culture (image reproduced from [Maschmeyer et al., 2015](#)⁷¹, published by RSC).

2.2 CHALLENGES FOR FABRICATION OF OOC DEVICE USING PDMS SOFT-LITHOGRAPHY TECHNIQUE.

One of the limitations emerging from the background section is the relative big size of microchannels (hundreds of micra) compared to the real physiological dimensions of arterioles, capillaries and small ducts presents in the different organs (tens of micra)^{72–76}. Taking advantage of the high resolution of PDMS soft-lithography technique, our OOCv1 design aims at achieving an OOC device with more physiological dimensions.

In parallel, taking into consideration the relevance of shear stress in cell cultures, we aim at controlling wall shear stress distribution.

We will particularly address the following specific objectives:

1. to design and simulate a microfluidic device able to embed membranes;
2. to fabricate the device using PDMS soft lithography based in traditional photolithographic process.

2.3 MATERIALS AND METHODS

2.3.1 Materials used

All solvents and chemical were from Sigma-Aldrich Co. (St Louis, MI USA), unless otherwise specified. SU-8 photoresists and developer were from MicroChem (Newton, MA, USA).

Cyclic Olefin Polymer (COP) sheets (Zeonor[®] 1420R, thickness 180 μm) are from Zeon Corporation (Tokyo, Japan).

PDMS (Sylgard 184) was from Dow Corning (Midland, MI USA). Transparent Polyethylene terephthalate (PET) membranes (24 mm diameter, 10 μm thickness, 0.4 μm pore size) were cut from from Transwell[®] inserts (CLS3450) obtained from Corning[®] Inc. (Corning, NY USA); PC membranes (Whatman[®] 7091-4710, 47 mm diameter, 10 μm thickness, 1 μm pore size) were from GE Healthcare Bio-Sciences (Pittsburgh, PA USA).

(3-Aminopropyl)triethoxysilane (APTES, $\geq 98\%$, A3648), Ethanol (EtOH, 96 %, ACS grade) and Isopropyl alcohol (IPA, ACS grade) was from Sigma Aldrich (St. Louis, MO USA). Deionized (DI) water was obtained from MilliQ purification system (Meck Millipore, Burlington, MA USA). Polylactic acid (PLA) filament (Primavalue, 1.75 mm diameter) used to 3D print aligners and tools was from 3D Prima (Malmö, Sweden).

2.3.2 Design and simulation of first version OOC (OOCv1)

2.3.2.1 Design choices

The OOCv1 design concept consists of two nets of channels (named respectively top and bottom layer) and a commercial membrane sandwiched in between (**Figure**

2-11). The channels layers are fabricated in PDMS (10:1), different membrane materials have been tested (PC and PET).

The design choice is a compromise between ideal mimicking of the physiological unit (smaller size), higher interchange surface and limitation of the hydraulic resistance of the channel. The latter two factors are important to easily manipulate the samples. In order to increase the membrane interchange surface while maintaining controlled hydraulic resistance and pressure drop across the channel, we opted for a multi-generation microfluidic network, as suggested by the theoretical work *Damiri et colleagues*⁷⁷.

We considered (hydraulic) diameter values coherent with the literature, particularly regarding the BBB and tubular kidney vessel, which appear to be in a similar range. Diameter of the renal tubule was estimated in the range of 22~50 μm ⁷⁸⁻⁸⁰; human BBB micro-vasculature in vivo was reported to range from 7~10 μm (capillaries) to 20~90 μm (arterioles and venules)^{76,81}.

After creating a parametric design of OOCv1 (**Figure 2-12**), two different channel sizes were selected for fabrication, resulting in two final designs: OOCv1-A and OOCv1-B (See **Table 2-1**).

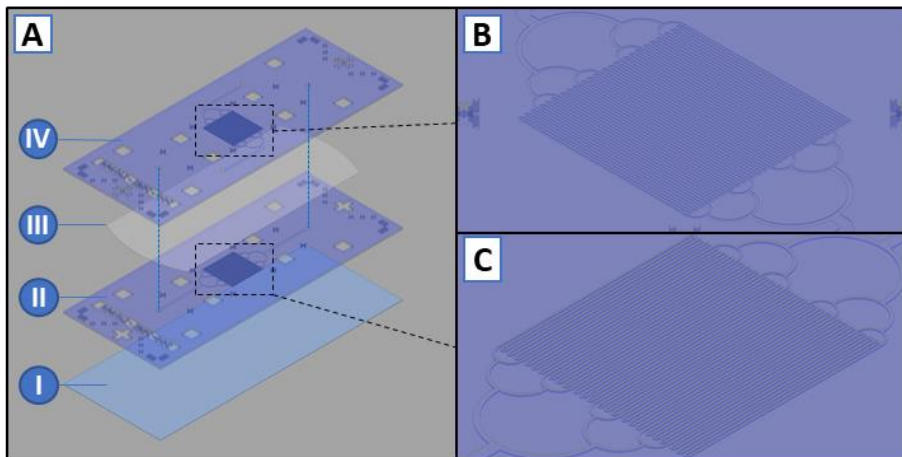


Figure 2-11. General OOCv1 design. A) Exploded view of the device, consisting of lower coverslip (I), lower PDMS channels layer (II), porous membrane (III) and upper PDMS channel layer; B) Detail of the upper layer parallel serpentine; C) Detail of the lower layer parallel serpentine.

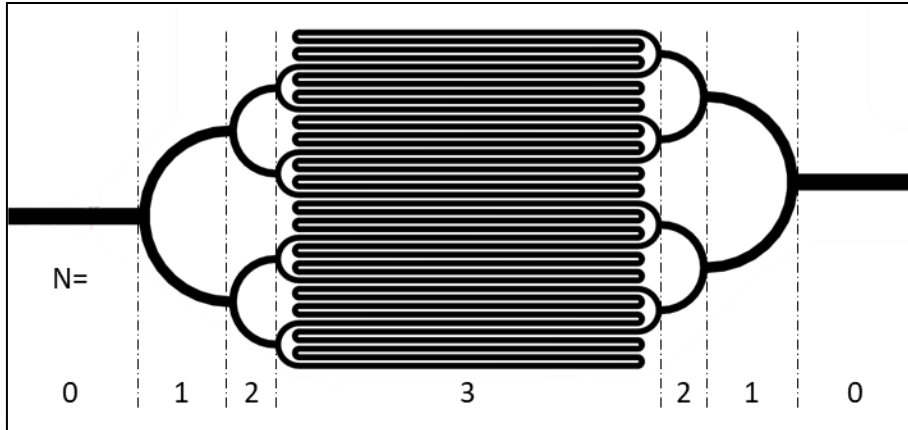


Figure 2-12. Detail of OOCv1 serpentine ramification and generation numbering.

Table 2-1. OOCv1 design dimensions resume.

Channel generation n	OOCv1-A				OOCv1-B			
	Design width	Design depth	Hydraulic diameter	Branching factor	Design width	Design depth	Hydraulic diameter	Branching factor
	w_n^A [μm]	h_n^A [μm]	$D_{H,n}^A$ [μm]	X_n^A [#]	w_n^B [μm]	h_n^B [μm]	$D_{H,n}^B$ [μm]	X_n^B [#]
0 -Inlet	120	40	60	0.75	525	37.5	70	0.7
1	76		52.4		189		55.93	
2	53.5		45.8		110		62.57	
3-Small	40		40		75		50	

First, the cross section of the smaller generation ($n=3$) was fixed according to literature ($D_{H,3}^A = 40 \mu\text{m}$; $D_{H,3}^B = 50 \mu\text{m}$). Different aspect ratios ($\alpha^A = 1$, $\alpha^B < 1$) were chosen. Aspect ratio smaller than unity ($w^B = 75 \mu\text{m}$, $h^B = 38 \mu\text{m}$, $\alpha^B \approx 0.5$) increases surface area in contact with the membrane. A branching parameter lower than 1 ($X^A = 0.75$; $X^B = 0.7$) was chosen to ensure a progressive decrease of shear stress moving toward the finest branches, in order to increase the probability of cells binding to the walls and also to enhance the diffusion of nutrients into the tissue culture²⁰.

2.3.2.2 CAD design and simulation

OOC layers were designed in AutoCAD® (Autodesk, Inc. San Rafael, CA, USA). Microchannel geometry could fit inside standard microscope coverslip ($24 \times 60 \text{ mm}$). Each layer includes a double cutting-guide, both for microscope slide ($75 \times 25 \text{ mm}$) or for coverslip ($24 \times 60 \text{ mm}$), and two groups of alignment marks. Masks were designed for 4" wafers, accommodating 3 microscope slides in each wafer. Masks were exported in Drawing Exchange Format (DXF). 2-D flow simulations were performed in COMSOL MultiPhysics, importing the mask designs. Flow simulations also considered data from the literature. WSS within the renal tubule system was estimated in the range of $0.02 \sim 2 \text{ Pa}^{80,82}$, with *In vivo* WSS in BBB capillaries is estimated between $0.1 \sim 0.5 \text{ Pa}^{83}$. A value of 0.2 Pa was chosen for the calculations.

2.3.3 Fabrication of OOCv1

2.3.3.1 Photolithography

Transparency masks were printed in high resolution (minimum feature size: $10 \mu\text{m}$) through a web service (CAD/Art Services Inc, Oregon, USA). All the following procedures were carried out in the MicroFabSpace facility of the Institute for BioEngineering of Catalonia (IBEC), in a clean room environment. All plasma processing described were performed using a Harrick Plasma Cleaner PDC-002-CE with Oxygen (O_2) gas; pressure and gas flow were controlled using Harrick PlasmaFlow.

Two masters -one for top and one for bottom layer respectively- were obtained through photolithography on 4" silicon wafers. In order to achieve reproducible low thickness replicas, each layer master was fabricated using a two-steps lithographic process in order to achieve two resist heights: one for the channels and a taller one for the squared pillars which act as spacers (**Figure 2-13**).

The substrate was previously cleaned using 3 subsequent solvent baths of acetone, ethanol and isopropanol. Then, after dehydration, surface was cleaned using energy O_2 plasma (20 min , 7.2 W , 0.2 Torr).

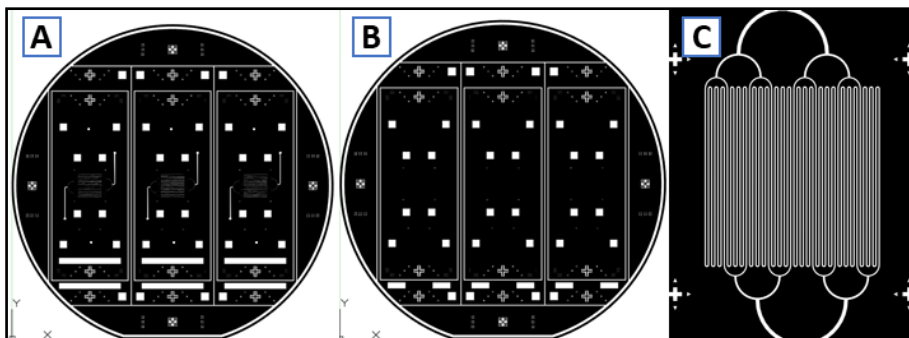


Figure 2-13. Mask design template for 4" silicon wafer. A) First step photolithography mask (with channels); B) Second step photolithography mask (only columns and alignment marks); C) Detail of the serpentine.

For each master, the substrate was first spin-coated with a $40\ \mu\text{m}$ layer of SU-8 2050 photoresist, soft-baked according to datasheet and exposed with an energy of $160\ \text{mJ cm}^{-2}$ in a MJB4 manual mask aligner (SÜSS Microtec, Germany). After post-exposure bake according to datasheet (1 min at $65\ ^\circ\text{C}$, 6 min at $95\ ^\circ\text{C}$), the substrate was developed in SU-8 developer for 5 minutes. After rinsing in IPA, drying with nitrogen (N_2) gas stream and dehydration ($95\ ^\circ\text{C}$, 6 min), the master was ready for the second step.

Peripheral alignment marks on the substrate were covered using adhesive tape; this is an added step to improve visibility during alignment. Peeling off the adhesive tape and the freshly deposited resist from the alignment mark area improve the otherwise low contrast across a thick layer of resist.

After masking the alignment marks with adhesive tape, the substrate was spin-coated with a $110\ \mu\text{m}$ layer of SU-8 2050. Adhesive tape was removed during soft bake, after 5 min at $65\ ^\circ\text{C}$ and before starting the 20 min at $95\ ^\circ\text{C}$. Mask was manually aligned with the substrate before the exposure ($240\ \text{mJ cm}^{-2}$). Post-bake was performed (5 min at $65\ ^\circ\text{C}$, 10 min at $95\ ^\circ\text{C}$) before developing unexposed resist (10 min in SU-8 developer) and finally rinsing the substrate with IPA and drying with N_2 .

2.3.3.2 Replica molding

Replica molding is achieved using COP layer as substrate for the thin PDMS layer, to add rigidity and avoid deformation during demolding. A COP sheet was cut in circular shape ($130\ \text{mm}$ diameter), washed using EtOH and dried with N_2 , without removing its protective layer on one of its sides. The COP substrate was then activated with O_2

plasma (29.6 W, 1 min, 0.2 Torr). After venting the plasma chamber, the COP substrate was inserted in a big petri dish (140 mm diameter) with protective film facing down and immediately covered with a previously degassed mixture of PDMS (prepolymer-curing agent 10: 1). On another support (i.e. Petri cover) the bottom layer master was covered with the same mixture of PDMS. Both the substrates were degassed under vacuum for 15 min, then the master was flipped 180 ° and pushed against the COP substrate (~500 g weight). The PDMS was left to cure on a leveled bench overnight and finished to cure at 60 °C for 2~3 h. Similar procedure was used for the top layer replica, except that pre-drilled glass slides are used instead of COP substrate and are kept in place using a custom aligner 3D printed in PLA.

Once completely cured, the PDMS replica were demolded from the masters. In the case of COP-PDMS replica, protective layer was removed after demolding, ensuring no PDMS remains attached to the bottom side of the COP. COP-PDMS replicas were finally cut to coverslip size (24 × 60 mm) using a scalpel, with the help of the guiding lines replicated in PDMS.

2.3.3.3 Assembly and membrane sealing

Different types of membranes were tested. PET membranes (24 mm diameter, 10 μm thickness, 0.4 μm pore size) were cut from Transwell inserts using a surgical scalpel, while commercial PC membranes were used (47 mm diameter, 10 μm thickness, 1 μm pore size).

Two different strategies have been explored: PDMS-glue sealing and silane functionalization. Glue sealing was performed according to Chueh *et al.*⁴². A mixture of PDMS-toluene (1: 2) was spin-coated on top of glass substrate to obtain a ~1 μm thick layer of uncured PDMS. PDMS replicas were stamped on top of the PDMS thin layer, and membrane borders were touched against it. Membrane and PDMS were sandwiched together.

Silane functionalization was performed using an adapted protocol from Aran *et al.*⁴³. Top and bottom layers of the device were cleaned using ethanol, dried using N₂ gas and dehydrated. A solution of 5 % APTES in DI water was pre-heated at 80 °C on a hotplate and covered to prevent evaporation. The membrane was activated using O₂ plasma (1 min, 29.6 W, 0.2 Torr) and immediately submersed in the solution afterwards. After 20 min, the membrane was washed thoroughly using DI water and deposited on top of a Polytetrafluoroethylene (PTFE) flat substrate. Performing this step with the membrane still humid is fundamental

improve membrane flat adhesion to the PTFE base. Top layer of the device was activated using O₂ plasma (1 min, 29.6 W, 0.2 Torr) and put in contact with the membrane. The PTFE-Membrane-Top layer sandwich was left 5 min under pressure on a hotplate at 95 °C to evaporate extra water. The part of membrane exceeding the device surface was cut away using a scalpel to prevent involuntary sticking during the next steps. Pass-through inlets/outlets were punched using a biopsy tool (Harris Uni-Core). Bottom layer was activated using O₂ plasma as in previous step. Top and bottom layer were finally manually aligned and brought into contact and left to cure at 60 °C overnight under pressure (500 g weight per slide).

2.3.4 Characterization

Lithography masters were characterized using Dektak 6M Stylus Surface Profilometer (Veeco Instruments, NY, USA), Wyko NT1100 Optical Profiling System (Veeco Instruments, NY, USA) and an Olympus BX51RF upright microscope.

2.4 RESULTS

2.4.1 Design and simulation

OOCv1 has been successfully designed with a decreasing distribution of fluid shear stress. Two different version of the design with different channels dimensions was completed, OOCv1-A and OOCv1-B (See **Table 2-1** for dimensions details). Computer fluidic simulations confirmed a decreasing distribution of shear stress towards the smaller ramifications of the device (**Table 2-2**). Wall shear stress in the smaller ramifications is 0.2 Pa for a total flow of $Q^A = 1.2 \mu\text{L} \cdot \text{min}^{-1}$, $Q^B = 2.2 \mu\text{L} \cdot \text{min}^{-1}$, respectively.

Table 2-2. Average Wall Shear Stress distribution across channel generations.

	Generation <i>n</i>	OOCv1-A ($Q_0^A = 1.2 \mu\text{L} \cdot \text{min}^{-1}$)	OOCv1-B ($Q_0^B = 2.2 \mu\text{L} \cdot \text{min}^{-1}$)
Average Wall Shear Stress $\bar{\tau}_n$ [Pa]	0- Inlet	0.395	0.216
	1	0.379	0.292
	2	0.285	0.260
	3-Small	0.205	0.201

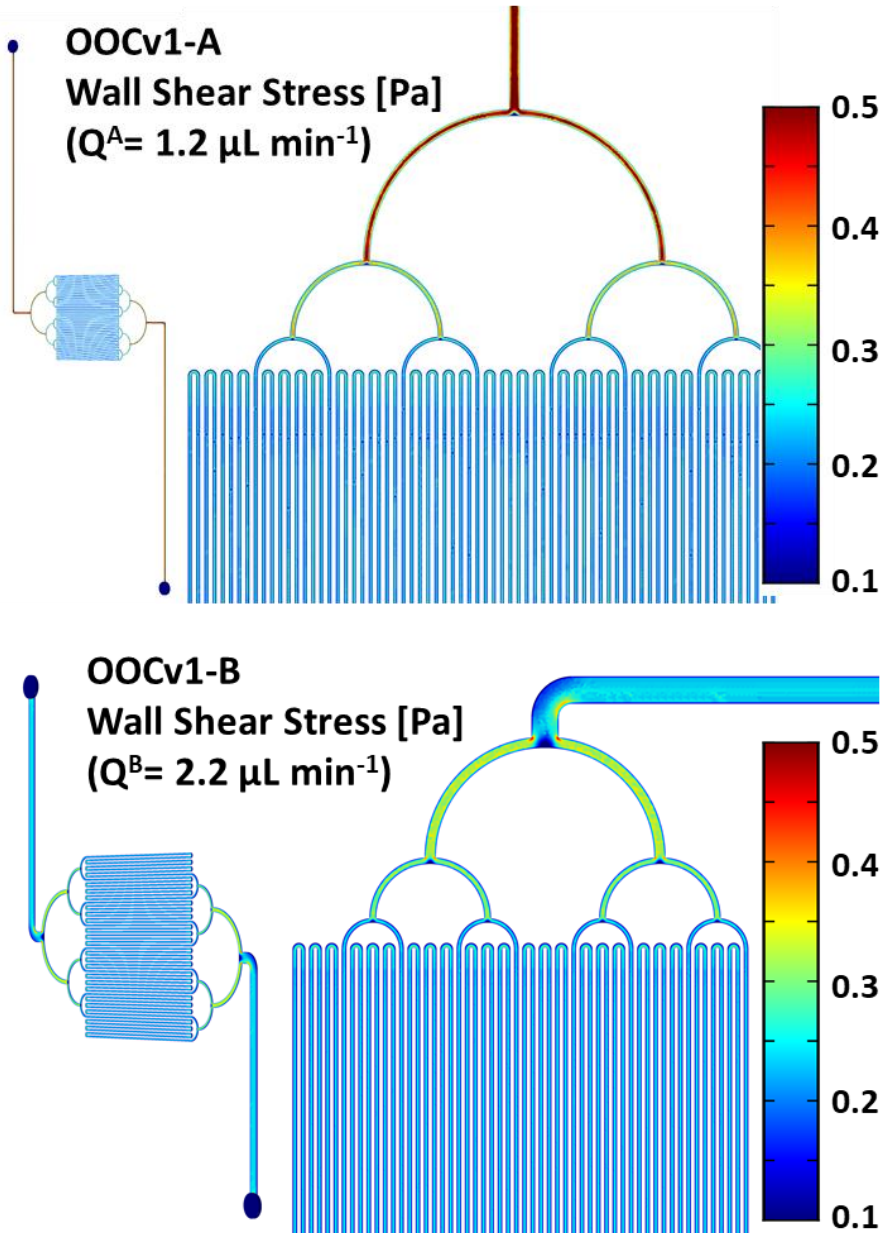


Figure 2-14. Wall shear stress distribution in OOCv1-A and OOCv1-B. Total flowrates of $Q^A = 1.2 \mu\text{L min}^{-1}$ $Q^B = 2.2 \mu\text{L min}^{-1}$. Simulation performed using COMSOL® Multiphysics. Scale is in [Pa].

2.4.2 Fabrication

Multistep SU-8 masters were successfully fabricated using photolithography. A resume of physical characterization is reported in **Table 2-3**.

Table 2-3. Measured dimensions resume.

Channel generation n	OOCv1-A				OOCv1-B			
	Actual width	Actual depth	Hydraulic diameter	Branching factor	Actual width	Actual depth	Hydraulic diameter	Branching factor
	w_n^A [μm]	h_n^A [μm]	$\overline{D_{H,n}^A}$ [μm]	$\overline{X_n^A}$ [#]	w_n^B [μm]	h_n^B [μm]	$\overline{D_{H,n}^B}$ [μm]	$\overline{X_n^B}$ [#]
0-Inlet	119.7 ± 0.5	46.6 ± 3.9	67.1	0.758	525.1 ± 0.7	42.3 ± 3.3	78.3	0.727
1	78.2 ± 0.6		58.4	0.793	188.8 ± 0.6		69.1	0.726
2	54.1 ± 0.4		50.1	0.793	109.5 ± 0.7		61.0	0.719
3-Small	39.8 ± 0.3		42.9	-	74.9 ± 0.5		54.1	-

As measured dimensions results in an increase in height respect to design both for OOCv1-A and OOCv1-B ($\Delta h^A = +16.5\%$, $\Delta h^B = +12.8\%$), Simulations were recalculated using the real devices dimensions. Required flowrates to achieve desired wall shear stress ($\overline{\tau_{n=3}} = 0.2 \text{ Pa}$) are $Q_0^A = 1.6 \mu\text{L min}^{-1}$ and $Q_0^B = 2.8 \mu\text{L min}^{-1}$.

Table 2-4. Average Wall Shear Stress distribution across channel generations calculated using real dimensions.

Average Wall Shear Stress $\overline{\tau_n}$ [Pa]	Generation n	OOCv1-A ($Q_0^A = 1.6 \mu\text{L min}^{-1}$)	OOCv1-B ($Q_0^B = 2.8 \mu\text{L min}^{-1}$)
		0- Inlet	0.398
	1	0.380	0.293
	2	0.289	0.264
	3-Small	0.203	0.203

2.4.3 Assembly

PDMS replicas were successfully obtained for both masters and were inspected at microscope. Assembly using PDMS-gluе strategies were not successful. Using 2 μm layer of PDMS-gluе, uncured PDMS get sucked into the channels resulting in their deformation or occlusion (**Figure 2-15**).

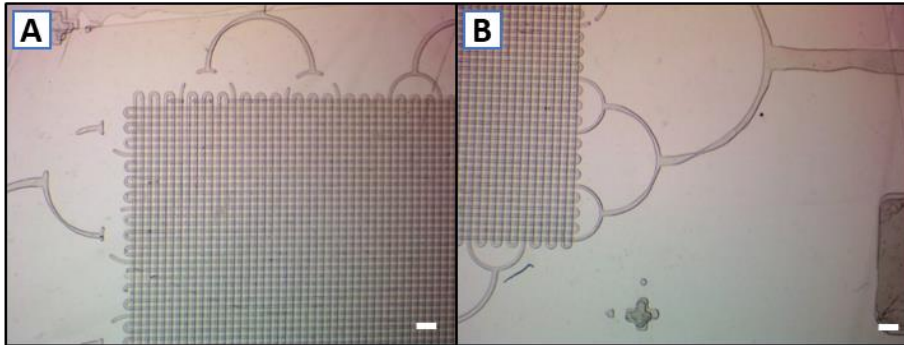


Figure 2-15. Channels deformation and occlusion with 2.5- μm Layer of PDMS-gluе.

Reducing the PDMS-gluе layer to 1 μm , the occlusions and deformations disappeared. Nonetheless, even applying extra quantity of gluе locally, 1- μm gluе resulted in insufficient sealing across the border of the membrane and consequent leaking between the layers, bypassing the membrane.

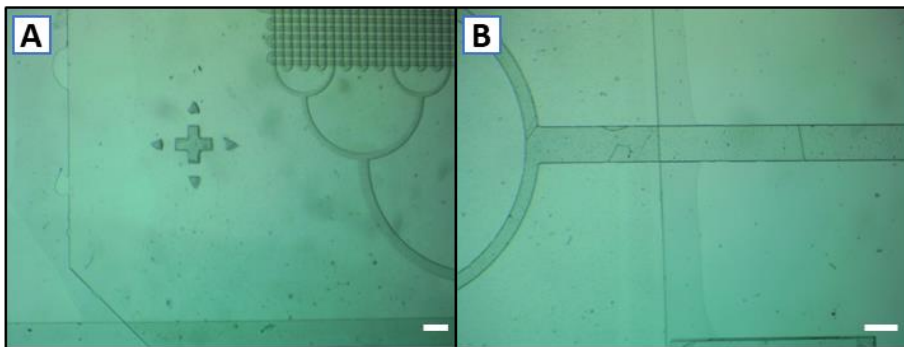


Figure 2-16. Results using 1- μm layer of PDMS-gluе. Channels are not obstructed and perfectly sealed (A) but insufficient sealing is obtained at the border of the membrane (B). Scale bars are 400 μm .

Using the APTES functionalization approach, we obtained irreversible bonding of the substrates. Using small membranes (i.e. from Transwell® inserts) we again encountered problems of poor local bonding along the membrane border, due to its thickness preventing conformal bonding. The problem was later solved finding

membranes with larger diameter, achieving complete, irreversible, leakage-free bonding.

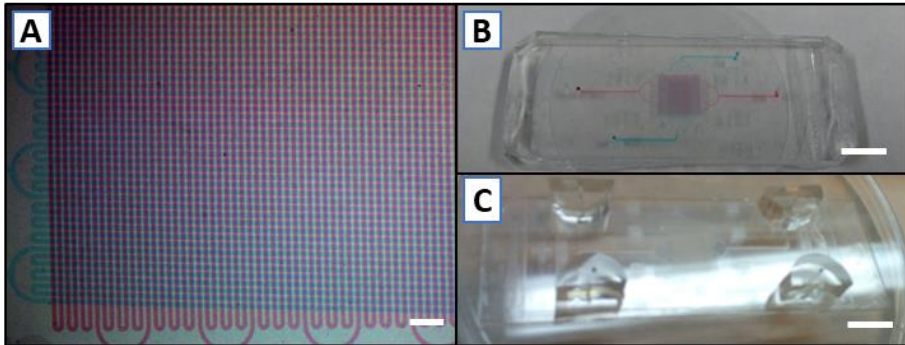


Figure 2-17. OOCv1 final assembly results. A) Fluidics test using blue and red aqueous ink solutions (scale bar: 400 μm); B) Assembled PDMS device filled with ink solutions (scale bar: 1 mm); C) Assembled low profile OOCv1 device (scale bar: 1 mm).

Devices were tested fluidically for 24 h with a flowrate 10 times bigger than the one required by experimental conditions. ($Q_{TEST}^A = 10 \cdot Q_0^A = 18 \mu\text{L} \cdot \text{min}^{-1}$, $Q_{TEST}^B = 10 \cdot Q_0^B = 27.5 \mu\text{L} \cdot \text{min}^{-1}$) and showed no leakage (**Figure 2-17**).

2.5 DISCUSSION

Using a generalized version of Hess-Murray law, we were able to design two devices with a WSS distribution tailored to improve cell adhesion in the membrane interchange area. Computer simulations confirmed a decreasing shear stress distribution across the channel generations, with an average value in the interchange area ($n=3$) in the 0.2 Pa range. This value is inside physiological range of most organs (i.e. kidney^{80,82}, BBB⁸³), resulting in good cell adhesion as will be shown later by experiments in Chapter 7. Furthermore, adequacy of the range was confirmed during some cell culture experiments (not reported) when, due to a malfunctioning of the pump, flowrate was suddenly increased by ~ 15 times, causing a proportional increase in WSS ($\tau_{W,3} \cong 3 \text{ Pa}$) which resulted in renal tubular cells detachment from the device.

As a first consideration, OOCv1-B design (aspect ratio $\alpha^B \approx 0.5$) resulted both in increased surface area as well as easier manipulation during the demolding and sealing steps compared to OOCv1-A. The parallel design choice was a compromise between increasing total flowrate and total chip volume while maintaining channel dimensions in a physiologic range. This appear to be useful for example when flowing

different concentrations of substances on each side, in filtration/diffusion studies. If it is true that one key advantages of microfluidics it's the reduction of sample sizes, standard analysis systems available in a biolab often still require a minimum sample volume. Under same wall shear stress conditions ($\tau_{n=3} = 0.2 \text{ Pa}$), running a single channel ramification would result in a flow $Q_3^B = \frac{Q_0^B}{8} = \frac{2.8}{8} = 0.35 \mu\text{L} \cdot \text{min}^{-1}$, leading to a sample collection each hour of about $21 \mu\text{L}$ against the $168 \mu\text{L}$ collected by our configuration of 8 parallel channels. When analysis does not take place *in-situ* on the device, dead volumes must be accounted both for the connectors as well as the tubing outlet. Just as an example, as low as 5 cm of tubing we typically use in the lab (Inner Diameter $ID = 0.5 \text{ mm}$) adds a dead volume of $\sim 10 \mu\text{L}$.

The two-step master fabrication process enabled the inclusion of spacer columns in the master to enable reproducible thickness of PDMS replicas. After process optimization, channel dimensions were obtained with a height error of $+12\sim 16 \%$. Computer simulations have been repeated to adjust shear stress distribution to the measured channel dimensions, modifying the flowrate accordingly.

Low thickness layers replica protocol has been improved. Low thickness layers of PDMS can break or deform during demold, so it is necessary to couple PDMS to a more rigid support material. Our initial choice was using glass coverslips; though we could successfully obtain working replicas, the process was very delicate due to the glass fragility and rigidity. Furthermore, glass coverslip needed to be aligned one by one against the master. COP appeared as the natural alternative, because it has optical characteristics close to the glass while being flexible, not fragile and easy to cut after demolding. As a result, demolding process reliability drastically increased. It is important to note that, whenever for applications requirements glass bottom is required, COP might yet be replaced if the plasma activation step of the protocol is not performed; this way COP-PDMS bonding remain reversible.

Assembly and sealing protocol also went through various iteration. While it worked fine with big features, we could not reach a reliable success rate of PDMS-glue approach when working with channels smaller than $100 \mu\text{m}$. The process was very delicate and highly dependent on user fine manipulation. After a proper tuning of processing times, we found APTES functionalization approach much more robust. The process is versatile, as it enables the integration of a vast variety of commercially available membranes.

Even after such improvements, we would like to point out how the whole process is quite long and laborious, both for the replica and assembly process, requiring a lot of precision manipulation from the user as well as overnight steps both in the replica and assembly process.

2.6 CONCLUSIONS

In this chapter we explored traditional soft lithography approach for OOC device fabrication. The channel design was realized considering generalized Hess-Murray law and its effects on wall shear stress distribution, which has been verified through computational finite elements analysis. Simulations of WSS resulted in overall values inside physiological range. WSS distribution decrease toward the center of the device to promote cell adhesion and increase residence time inside the membrane area.

SU-8 masters were fabricated using two-step photolithography process. Reproducible thin layer PDMS replica were successfully obtained thanks to spacers embedded in the master design. After exploring different sealing strategies, a robust membrane embedding protocol has been chosen. Use of COP as lower substrate resulted in improved reliability of the process, while maintaining superior optical properties.

A membrane-embedded membrane device was successfully fabricated. The fabricated devices have dimensions in the physiological range of small body vessels, while maintaining a good compromise with minimum flowrate.

2.7 REFERENCES

1. Feynman, R. 'There's Plenty of Room at the Bottom'. *J. MicroElectroMechanics Syst.* **1**, 60–66 (1959).
2. Nathanson, H. C. & Wickstrom, R. A. A resonant-gate silicon surface transistor with high-q band-pass properties. *Appl. Phys. Lett.* **7**, 84–86 (1965).
3. Tabeling, P. Introduction to Microfluidics. (2003).
4. Terry, S. C., Herman, J. H. & Angell, J. B. A Gas Chromatographic Air Analyzer Fabricated on a Silicon Wafer. *IEEE Trans. Electron Devices* (1979). doi:10.1109/T-ED.1979.19791
5. Whitesides, G. M. The origins and the future of microfluidics. *Nature* **442**, 368–373 (2006).
6. Manz, A., Grabner, N. & Widmer, H. M. Minutuarized total chemical analysis systems: A novel approach for chemical sensing. *Sens. Actuat. B* **1**, 244–248 (1990).
7. Gaudin, V. Advances in biosensor development for the screening of antibiotic residues in food products of animal origin – A comprehensive review. *Biosens. Bioelectron.* **90**, 363–377 (2017).
8. Sackmann, E. K., Fulton, A. L. & Beebe, D. J. The present and future role of microfluidics in biomedical research. *Nature* **507**, 181–189 (2014).
9. Oh, K. W., Lee, K., Ahn, B. & Furlani, E. P. Design of pressure-driven microfluidic networks using electric circuit analogy. *Lab Chip* **12**, 515–45 (2012).
10. Kir. *Micro- and Nanoscale Fluid Mechanics: Transport in Microfluidic Devices*. (Cambridge University Press, 2010).
11. Ibragimov, M. K. HYDRAULIC DIAMETER. in *A-to-Z Guide to Thermodynamics, Heat and Mass Transfer, and Fluids Engineering* (Begellhouse). doi:10.1615/AtoZ.h.hydraulic_diameter
12. Koo, J. & Kleinstreuer, C. Liquid flow in microchannels: experimental observations and computational analyses of microfluidics effects. *J. Micromechanics Microengineering* **13**, 568–579 (2003).
13. Li, D. *Encyclopedia of microfluidics and nanofluidics. Mechanical Engineering* **1**, (2008).
14. Cornish, R. J. Flow in a Pipe of Rectangular Cross-Section. *Proc. R. Soc. A Math. Phys. Eng. Sci.* (1928). doi:10.1098/rspa.1928.0175

15. Shemesh, J. *et al.* Flow-induced stress on adherent cells in microfluidic devices. *Lab Chip* (2015). doi:10.1039/c5lc00633c
16. Davies, P. F. Flow-mediated endothelial mechanotransduction. *Physiol. Rev.* **75**, 519–560 (1995).
17. Thomas D, B. Techniques for mechanical stimulation of cells in vitro: a review. *J. Biomech.* **33**, 3–14 (2000).
18. Huber, D., Oskooei, A., Casadevall, X. & Kaigala, G. V. Hydrodynamics in Cell Studies. *Chem. Rev.* **118**, 2042–2079 (2018).
19. Wilmer, M. J. *et al.* Kidney-on-a-Chip Technology for Drug-Induced Nephrotoxicity Screening. *Trends Biotechnol.* **34**, 156–170 (2016).
20. Barber, R. W. & Emerson, D. R. Biomimetic design of artificial micro-vasculatures for tissue engineering. *ATLA Alternatives to Laboratory Animals* **38**, 67–79 (2010).
21. Barber, R. W. & Emerson, D. R. Optimal design of microfluidic networks using biologically inspired principles. *Microfluid. Nanofluidics* **4**, 179–191 (2008).
22. Murray, C. D. The physiological principle of minimal work. I. The vascular system and the cost of blood volume. *Proc. Natl. Acad. Sci.* **12**, 207–214 (1926).
23. Emerson, D. R., Cieřlicki, K., Gu, X. & Barber, R. W. Biomimetic design of microfluidic manifolds based on a generalised Murray’s law. *Lab Chip* (2006). doi:10.1039/b516975e
24. Qin, D., Xia, Y. & Whitesides, G. M. Rapid prototyping of complex structures with feature sizes larger than 20 μm . *Adv. Mater.* **8**, 917–919 (1996).
25. Mazutis, L. *et al.* Single-cell analysis and sorting using droplet-based microfluidics. *Nat. Protoc.* **8**, 870–91 (2013).
26. Duffy, D. C., McDonald, J. C., Schueller, O. J. A. & Whitesides, G. M. Rapid prototyping of microfluidic systems in poly(dimethylsiloxane). *Anal. Chem.* **70**, 4974–4984 (1998).
27. Xia, Y. & Whitesides, G. M. Soft Lithography. *Annu. Rev. Mater. Sci.* **28**, 153–184 (1998).
28. Zhang, B., Korolj, A., Lai, B. F. L. & Radisic, M. Advances in organ-on-a-chip engineering. *Nat. Rev. Mater.* **3**, 257–278 (2018).
29. Naderi, A., Bhattacharjee, N. & Folch, A. Digital Manufacturing for Microfluidics. *Annu. Rev. Biomed. Eng.* **21**, 325–364 (2019).

30. Chaudhury, M. K. & Whitesides, G. M. Direct Measurement of Interfacial Interactions between Semispherical Lenses and Flat Sheets of Poly(dimethylsiloxane) and Their Chemical Derivatives. *Langmuir* (1991). doi:10.1021/la00053a033
31. Unger, M. A., Chou, H. P., Thorsen, T., Scherer, A. & Quake, S. R. Monolithic microfabricated valves and pumps by multilayer soft lithography. *Science* (80-.). (2000). doi:10.1126/science.288.5463.113
32. McDonald, J. C. & Whitesides, G. M. Poly(dimethylsiloxane) as a material for fabricating microfluidic devices. *Acc. Chem. Res.* **35**, 491–499 (2002).
33. de Jong, J. *et al.* Membranes and microfluidics: a review. *Lab Chip* **6**, 1125 (2006).
34. Shin, Y. *et al.* Microfluidic assay for simultaneous culture of multiple cell types on surfaces or within hydrogels. *Nat. Protoc.* **7**, 1247–1259 (2012).
35. Adriani, G., Ma, D., Pavesi, A., Goh, E. L. K. & Kamm, R. D. Modeling the Blood-Brain Barrier in a 3D triple co-culture microfluidic system. *Proc. Annu. Int. Conf. IEEE Eng. Med. Biol. Soc. EMBS* **2015-Novem**, 338–341 (2015).
36. Adriani, G., Ma, D., Pavesi, A., Kamm, R. D. & Goh, E. L. K. A 3D neurovascular microfluidic model consisting of neurons, astrocytes and cerebral endothelial cells as a blood-brain barrier. *Lab Chip* **17**, 448–459 (2017).
37. Wong, A. P., Perez-Castillejos, R., Christopher Love, J. & Whitesides, G. M. Partitioning microfluidic channels with hydrogel to construct tunable 3-D cellular microenvironments. *Biomaterials* **29**, 1853–1861 (2008).
38. Wu, W., Trinh, K. T. L. & Lee, N. Y. Hand-held syringe as a portable plastic pump for on-chip continuous-flow PCR: Miniaturization of sample injection device. *Analyst* **137**, 983–990 (2012).
39. Wu, W., Kang, K. T. & Lee, N. Y. Bubble-free on-chip continuous-flow polymerase chain reaction: Concept and application. *Analyst* **136**, 2287–2293 (2011).
40. Wu, W., Loan Trinh, K. T. & Lee, N. Y. Flow-through PCR on a 3D qiandu-shaped polydimethylsiloxane (PDMS) microdevice employing a single heater: Toward microscale multiplex PCR. *Analyst* **137**, 2069–2076 (2012).
41. Wu, W., Wu, J., Kim, J.-H. & Lee, N. Y. Instantaneous room temperature bonding of a wide range of non-silicon substrates with poly(dimethylsiloxane) (PDMS) elastomer mediated by a mercaptosilane. *Lab Chip* **15**, 2819–2825 (2015).
42. Chueh, B. H. *et al.* Leakage-free bonding of porous membranes into layered

- microfluidic array systems. *Anal. Chem.* **79**, 3504–3508 (2007).
43. Aran, K., Sasso, L. A., Kamdar, N. & Zahn, J. D. Irreversible, direct bonding of nanoporous polymer membranes to PDMS or glass microdevices. *Lab Chip* **10**, 548 (2010).
 44. DiMasi, J. A., Grabowski, H. G. & Hansen, R. W. Innovation in the pharmaceutical industry: New estimates of R&D costs. *J. Health Econ.* **47**, 20–33 (2016).
 45. Paoli, R. & Samitier, J. Mimicking the kidney: A key role in organ-on-chip development. *Micromachines* **7**, (2016).
 46. Rodríguez-Antona, C. *et al.* Cytochrome P450 expression in human hepatocytes and hepatoma cell lines: molecular mechanisms that determine lower expression in cultured cells. *Xenobiotica* **32**, 505–520 (2002).
 47. Kimura, H., Sakai, Y. & Fujii, T. Organ/body-on-a-chip based on microfluidic technology for drug discovery. *Drug Metab. Pharmacokinet.* **33**, 43–48 (2018).
 48. A., S. *et al.* The Design and Fabrication of Three-Chamber Microscale Cell Culture Analog Devices with Integrated Dissolved Oxygen Sensors. *Biotechnol. Prog.* **20**, 338–345 (2004).
 49. K., V., A., S. & M.L., S. Development of a Microscale Cell Culture Analog to Probe Naphthalene Toxicity. *Biotechnol. Prog.* **20**, 316–323 (2004).
 50. Huh, D. *et al.* Reconstituting Organ-Level Lung Functions on a Chip. *Science (80-.)*. **328**, 1662–1668 (2010).
 51. Huh, D. *et al.* A human disease model of drug toxicity-induced pulmonary edema in a lung-on-a-chip microdevice. *Sci. Transl. Med.* **4**, 159ra147 (2012).
 52. Sosa-Hernández, J. E. *et al.* Organs-on-a-Chip Module: A Review from the Development and Applications Perspective. *Micromachines* **9**, 536 (2018).
 53. Bavli, D. *et al.* Real-time monitoring of metabolic function in liver-on-chip microdevices tracks the dynamics of mitochondrial dysfunction. *Proc. Natl. Acad. Sci.* **113**, E2231–E2240 (2016).
 54. Nakao, Y., Kimura, H., Sakai, Y. & Fujii, T. Bile canaliculi formation by aligning rat primary hepatocytes in a microfluidic device. *Biomicrofluidics* **5**, (2011).
 55. Jang, K.-J. & Suh, K.-Y. A multi-layer microfluidic device for efficient culture and analysis of renal tubular cells. *Lab Chip* **10**, 36–42 (2010).
 56. Jang, K.-J. *et al.* Human kidney proximal tubule-on-a-chip for drug transport and nephrotoxicity assessment. *Integr. Biol.* **5**, 1119 (2013).

57. Musah, S. *et al.* Mature induced-pluripotent-stem-cell-derived human podocytes reconstitute kidney glomerular-capillary-wall function on a chip. *Nat. Biomed. Eng.* **1**, (2017).
58. Kim, H. J., Huh, D., Hamilton, G. & Ingber, D. E. Human gut-on-a-chip inhabited by microbial flora that experiences intestinal peristalsis-like motions and flow. *Lab Chip* **12**, 2165–2174 (2012).
59. Kim, H. J. & Ingber, D. E. Gut-on-a-Chip microenvironment induces human intestinal cells to undergo villus differentiation. *Integr. Biol. (United Kingdom)* **5**, 1130–1140 (2013).
60. Kim, H. J., Li, H., Collins, J. J. & Ingber, D. E. Contributions of microbiome and mechanical deformation to intestinal bacterial overgrowth and inflammation in a human gut-on-a-chip. *Proc. Natl. Acad. Sci.* **113**, E7–E15 (2016).
61. Villenave, R. *et al.* Human gut-on-a-chip supports polarized infection of coxsackie B1 virus in vitro. *PLoS One* **12**, 1–17 (2017).
62. Jalili-Firoozinezhad, S. *et al.* Modeling radiation injury-induced cell death and countermeasure drug responses in a human Gut-on-a-Chip article. *Cell Death Dis.* **9**, (2018).
63. Booth, R. & Kim, H. Characterization of a microfluidic in vitro model of the blood-brain barrier (μ BBB). *Lab Chip* **12**, 1784–1792 (2012).
64. Adriani, G., Ma, D., Pavesi, A., Kamm, R. D. & Goh, E. L. K. A 3D neurovascular microfluidic model consisting of neurons, astrocytes and cerebral endothelial cells as a blood–brain barrier. *Lab Chip* **17**, 448–459 (2017).
65. Adriani, G., Bai, J., Wong, S., Kamm, R. D. & Thiery, J. P. M2a macrophages induce contact-dependent dispersion of carcinoma cell aggregates. *Macrophage* 1–5 (2016). doi:10.14800/macrophage.1222
66. Xu, H. *et al.* A dynamic in vivo-like organotypic blood-brain barrier model to probe metastatic brain tumors. *Sci. Rep.* **6**, 36670 (2016).
67. Rigat-Brugarolas, L. G. *et al.* A functional microengineered model of the human splenon-on-a-chip. *Lab Chip* **14**, 1715 (2014).
68. Sung, J. H. & Shuler, M. L. A micro cell culture analog (CCA) with 3-D hydrogel culture of multiple cell lines to assess metabolism-dependent cytotoxicity of anti-cancer drugs. *Lab Chip* **9**, 1385–1394 (2009).
69. Sung, J. H., Kam, C. & Shuler, M. L. A microfluidic device for a pharmacokinetic-pharmacodynamic (PK-PD) model on a chip. *Lab Chip* **10**, 446–455 (2010).

70. Sung, J. H. *et al.* Using physiologically-based pharmacokinetic-guided “body-on-a-chip” systems to predict mammalian response to drug and chemical exposure. *Exp. Biol. Med.* **239**, 1225–1239 (2014).
71. Maschmeyer, I. *et al.* A four-organ-chip for interconnected long-term co-culture of human intestine, liver, skin and kidney equivalents. *Lab Chip* **15**, 2688–2699 (2015).
72. Alpern, R. J., Moe, O. W. & Caplan, M. *Seldin and Giebisch’s The Kidney - Physiology & Pathophysiology*. (Academic Press, 2013).
73. Bell, R. D. & Zlokovic, B. V. Neurovascular mechanisms and blood-brain barrier disorder in Alzheimer’s disease. *Acta Neuropathologica* (2009). doi:10.1007/s00401-009-0522-3
74. Braverman, I. M. The cutaneous microcirculation. in *Journal of Investigative Dermatology Symposium Proceedings* (2000). doi:10.1046/j.1087-0024.2000.00010.x
75. Wong, A. D. *et al.* The blood-brain barrier: An engineering perspective. *Frontiers in Neuroengineering* (2013). doi:10.3389/fneng.2013.00007
76. Campisi, M. *et al.* 3D self-organized microvascular model of the human blood-brain barrier with endothelial cells, pericytes and astrocytes. *Biomaterials* **180**, 117–129 (2018).
77. Damiri, H. S. & Bardaweel, H. K. Numerical design and optimization of hydraulic resistance and wall shear stress inside pressure-driven microfluidic networks. *Lab Chip* **15**, 4187–4196 (2015).
78. Chou, C. L., Sands, J. M., Nonoguchi, H. & Knepper, M. A. Concentration dependence of urea and thiourea transport in rat inner medullary collecting duct. *Am. J. Physiol. - Ren. Fluid Electrolyte Physiol.* (1990).
79. DiGiovanni, S. R., Nielsen, S., Christensen, E. I. & Knepper, M. A. Regulation of collecting duct water channel expression by vasopressin in Brattleboro rat. *Proc. Natl. Acad. Sci. U. S. A.* (1994). doi:10.1073/pnas.91.19.8984
80. Cai, Z., Xin, J., Pollock, D. M. & Pollock, J. S. Shear stress-mediated NO production in inner medullary collecting duct cells. *Am. J. Physiol. - Ren. Physiol.* **279**, 270–274 (2000).
81. Zlokovic, B. V. Neurovascular pathways to neurodegeneration in Alzheimer’s disease and other disorders. *Nature Reviews Neuroscience* (2011). doi:10.1038/nrn3114
82. Jang, K.-J. *et al.* Fluid-shear-stress-induced translocation of aquaporin-2 and reorganization of actin cytoskeleton in renal tubular epithelial cells. *Integr.*

Biol. (Camb). **3**, 134–41 (2011).

83. Cucullo, L., Aumayr, B., Rapp, E. & Janigro, D. Drug delivery and in vitro models of the blood-brain barrier. *Current Opinion in Drug Discovery and Development* **8**, 89–99 (2005).

3 Rapid prototyping of multilayered OOC devices in COP

3.1	BACKGROUND	52
3.1.1	PDMS AND SOFT-LITHOGRAPHY LIMITATIONS	52
3.1.2	DIGITAL MANUFACTURING AND RAPID PROTOTYPING IN MICROFLUIDICS.....	55
3.1.3	THERMOPLASTICS FOR MICROFLUIDICS	58
3.2	CHALLENGES AND SPECIFIC OBJECTIVES	60
3.3	MATERIALS AND METHODS	60
3.3.1	MATERIALS	60
3.3.2	DIRECT POLYMER BONDING.....	61
3.3.3	COP CONTACT ANGLE MEASUREMENT	62
3.3.4	OOC DESIGN	62
3.3.5	OOC FABRICATION	63
3.4	RESULTS	65
3.4.1	DIRECT POLYMER BONDING.....	65
3.4.2	COP CONTACT ANGLE MEASUREMENTS	68
3.4.3	DESIGN AND FABRICATION.....	68
3.5	DISCUSSION	69
3.6	CONCLUSIONS	71
3.7	REFERENCES	73

After exploring PDMS soft lithography capabilities for OOC device fabrication in the previous chapter, we will now enter the world of Rapid Prototyping (RP) techniques. This chapter aims to explore Digital Manufacturing (DM) RP techniques for fabrication of a membrane-embedded OOC, focusing on subtractive manufacturing techniques. Pure additive manufacturing will be explored in the next chapter. After an evaluation of the main limitations of PDMS soft-lithography strategy. DM and RP concepts are introduced and their main applications to microfluidics are presented. Different material options are also reviewed, and various bonding strategies considered.

Finally, a new OOC device (OOCv2.0) is designed and protocols for its fabrication in COP using two different RP technologies are defined. Functional devices are finally obtained, and results are discussed.

Collaborations: The work presented in this chapter was achieved in collaboration with PhD student Davide Di Giuseppe and his supervisor Prof. Eugenio Martinelli, from Sensors group of Rome Tor Vergata University.

3.1 BACKGROUND

From last chapter emerged how, even after protocol optimization, OOCv1 fabrication was yet a long laborious process, partly user dependent. Furthermore, the time and money required for master fabrication process, which is required at any design upgrade, is yet elevated.

This chapter will introduce the concepts of Digital Manufacturing (DM) and Rapid Prototyping (RP) for microfluidics application, proposing a solution to this and other limitations of PDMS soft lithography fabrication. Particularly, the chapter will focus on the use of subtractive DM techniques for OOC applications. Main available thermoplastics for microfluidics are also presented to have an initial overview of possible material choices.

3.1.1 PDMS and soft-lithography limitations

As already introduced in the previous chapter, in the last two decades, the vast majority of microfluidic systems have been built in PDMS by soft lithography, a technique based on PDMS micromolding¹. PDMS features some key properties that have made it become the material of choice for rapid prototyping in microfluidics. PDMS is 1) easy to mold; 2) elastomeric; 3) biocompatible; 4) transparent; 5) gas-permeable; 6) impermeable to water; 7) inexpensive; 8) copyright-free; and 9) can mold at very high resolution¹. As long as aspect ratio is not too elevated, resulting in collapsed microstructures, it is possible to replicate tiny structures like $6 \mu m \times 6 \mu m$ Quake valves² or $2 \mu m \times 5.5 \mu m$ microchannels arrays³.

Nevertheless, in the last few years a number of limitations have started to emerge, raising concerns about PDMS as an appropriate material for future manufacturing of OOC. Limitations usually undermine two different key features an ideal material for OOC technology should possess: on the one hand, suitability for cell-culture and, on the other end, manufacturability for commercialization.

3.1.1.1 *Limitations for Cell culture*

Though being central in the development in microfluidics in the last decades, PDMS raised concerns about its suitability for cell-based studies. One of the main concerns is bulk absorption of small molecules in PDMS, compared to surface-only adsorption of glass and thermoplastics. PDMS has been reported to absorb and deplete both estrogens in the media⁴ and administered drugs⁵, altering their effectiveness. This can affect not only fundamental biology studies, but also drug discovery and high-throughput screening applications that rely on platform materials that are inert to absorption⁶

Another important point is leaching. PDMS in cured form contains residual uncross-linked polymer chains that can freely diffuse within the bulk material. When in contact with solution, these uncross-linked oligomers can leach out of the bulk and into solution. Leached oligomers had been reported to incorporate into the membranes of culture cells⁴. The issue had received small attention to date, however, is expected to become more evident as microfluidic systems become more popular for studies of cell membranes⁶, like in OOC applications.

Evaporation is another challenge to consider working with PDMS. Evaporation is inherently present in regular macroscale cell cultures as well, but the phenomenon becomes more dominant at the microscale where small amounts of evaporation can significantly shift volumes, concentrations, chemical balances, critical gradients and other factors⁶⁻⁹. Furthermore, evaporation in microchannels can cause significant loss of liquid volume, which can lead to bubbles that propagate, block flow, and lyse cells in microchannels, causing dramatic, detrimental effects that can lead to loss of data or result in experiments ending prematurely⁶.

PDMS high oxygen permeability is often reported as a great benefit of the material; nonetheless hyperoxic microenvironment has been reported to cause cell stress^{10,11}. A brief analysis of oxygen permeabilities shows that the oxygen supply through a thin microfluidic PDMS device can be much higher than that in cell culture flasks or Petri dishes containing a height of culture media of 1~4 mm⁶.

3.1.1.2 Limitations in manufacturability for commercialization

In the medium-long term, OOCs aim at becoming widespread tools for biological researchers. Though that scenario is often referred to the future, it is already a proper time to start thinking the best path and tools to get there. In order to maximize diffusion and impact, technology requires to be manufacturable at low cost. Manufacturability should not be confused with high-throughput fabrication; a device is easily manufacturable when it can be brought to market at a low cost (including resources and development) using a reliable process^{1,12}. PDMS and soft lithography presents a series of limitations regarding manufacturability. To start with, PDMS molding (including PDMS curing, assembly, bonding, and inlet punching) is a largely a manual process, which is slow and hard to fully automate¹³. If slowness of the process might be counteracted -at a cost- with huge parallelization, lack of automation will make the process too expensive and too prone to human-error to be reliable.

Easy integration of user-friendly and leakage-free user interfaces (inlets/outlets) has been for years another Achille's heel of PDMS devices¹. Doctors and biologist are used to intuitive connectors, like industry standards Luer-Lock, but their inclusion usually requires extra steps making the process more complex.

Also, the control systems required to run microfluidic valves (ranging from the computer, pressure sources, software, etc.), or even to connect relatively simple chips, involve engineering expertise and equipment not present in most biomedical laboratories¹. This aspect will be further addressed in Chapter 5.

Finally, moving from a PDMS working prototype to commercialization of the device usually requires developing a plastic-molding process that is entirely different from the original soft lithographic one¹³. New manufacturing process usually means new challenges and need for new designs, duplicating all the efforts. Additionally, at present, a single engineer designs most of the PDMS-based microfluidic platforms often from scratch, in a non-standardized and non-modular way¹. In contrast, in other older and more evolved industries, like automotive and electronics, teams of engineers digitally design parts and functional units according to common standards, being able to digitally review and improve previous designs. To achieve that change, an understanding and application of DM and RP concepts is required.

3.1.2 Digital Manufacturing and Rapid Prototyping in microfluidics

Thanks to the rapid evolution of science and technology since the middle of the 20th century, society witnessed the birth of new concepts, new theories, new technologies, new ideas and new methods having information technology as its core¹⁴. After digitalization of information, our society is undergoing similar digitalization of the manufacturing industry and processes.

DM is a manufacturing process which is based on customer demand thanks to the support of digital technologies -such as CAD, Simulations and Rapid Prototyping through Computer Aided Manufacturing (CAM)¹⁴. With DM, designs can be digitally inspected and adjusted, annotated, and cloud-shared with collaborators, resulting in better design turnaround time, cost, and performance¹⁵. The pressure to shift manufacturing to DM comes from society's push to increase efficiency (and thus decrease cost), rather than from a purely technological advantage¹⁵. Similar shift is desirable in microfluidics and OOC, where standardization and digitalization of fabrication processes could benefit design workflow for a vast universe of different applications. Nonetheless, microfluidics scenario seems to slowly reluctantly adapt to this ongoing revolution. DM techniques are usually regarded as technically inferior by many microfluidic engineers as they still present the ongoing challenge to achieve resolution and biocompatibility comparable to those of micro-molding gold standard¹⁵.

As a result, microfluidics devices are often still designed using non-DM methods (largely from scratch each time), precursor materials have to be mixed and poured into a mold, and the resulting 2D layers must be manually aligned and bonded to form the final device¹⁵. Even if use of basic CAD design and simulation of structures is quite diffused, there is still room for improvement both in rapid prototyping and CAM.

RP are a set of techniques able to quickly fabricate a physical part from 3D CAD data. Those are usually divided into additive or subtractive manufacturing techniques, depending if the final part is obtained joining material together, usually layer by layer, or subtracting material from a bulk block. All DM methods share (a) the ability to produce a physical device from a digital design file and (b) the ability to encode the fabrication process as a set of parameters;

importantly, both the design file and the process parameters can be electronically sent to distant collaborators operating a similar machine in order to produce a replica of the same device¹⁵. This chapter will focus on microfluidic applications of subtractive manufacturing; additive manufacturing will be described more in detail in the following chapter.

Subtractive manufacturing techniques has been implemented in microfluidics since the very beginning, when the first devices were produced using subtractive (etching) methods in silicon and glass, derived from methods used to make microelectronic chips¹⁵⁻¹⁷. Nonetheless etching cannot be labelled as RP or DM techniques, as design are usually 2D. Computer Numerically Controlled (CNC) micromilling^{18,19} was probably the first example of a more proper DM technique, though it has some drawbacks. Milling microchannels requires small tools with high rotational speeds ($> 10000\text{ rpm}$), so longevity of the tools might be an issue²⁰. Also, highly skilled operators are required, manufacturing time can be relatively long (hours) for high quality and complexity microfluidic devices and the process is hardly scalable to mass production²⁰.

Other techniques stand at the intersection of additive and subtractive manufacturing. Subtractive techniques, like laser-cut or xurography, are used as part of an additive process where the final part is obtained by joining together different layers of laminates previously cut to shape. The process is often referred as Laminated Object Manufacturing (LOM) or sheet lamination.

In 2005, borrowing a technology used in the sign industry to cut adhesive graphics, a new RP technique to fabricate microstructure was introduced, called Xurography (from Latin: "Razor writing")²¹. The technique simply required a vinyl cutter, a CNC machine similar to a printer where movement of a razor blade -instead of a printing nozzle- over a sheet of material is controlled by a computer. The technique made possible to fabricate structure with widths down to $6\ \mu\text{m}$ and thickness of $25\ \mu\text{m}$ in a matter of minutes without need for masks²¹. Across the years, different techniques were used to bond different layers, like heat press²², heat lamination²¹, Pressure Sensitive Adhesive (PSA) layers^{23,24} or solvent bonding²⁵ (**Figure 3-1**).

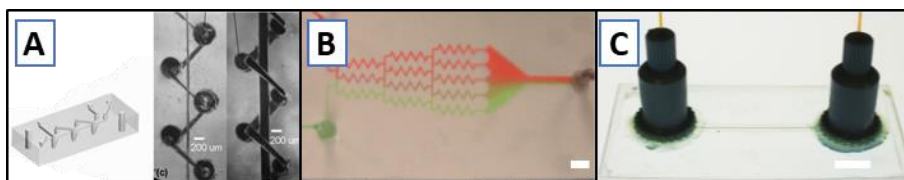


Figure 3-1. Xurography LOM for microfluidics. A) 3D coiled channel surrounding a straight channel using heat lamination (Scale bar: 200 μm , ©2005 IEEE. Reprinted, with permission, from [Bartholomeusz et al.](#)²¹); B) 3D serpentine microchannel mixer using PSA xurography (total device thickness: 400 μm , scale bar: 500 μm , reproduced from [Yuen et al., 2010](#)²³ by permission of RSC); C) COP microfluidic device fabricated using xurography and solvent bonding (Scale bar: 5 mm, from [Azouz et al., 2014](#)²⁵).

Similar application of LOM makes use of laser cutting instead of xurography. Laser cutting machines work by scanning a high-power laser across a two-dimensional material surface, locally heating the material which melts, burns or vaporize. Different kind of laser source might be used, but all laser cutting machines share the same general working principle. Through lenses or fiber optics, a laser beam is routed to a lens in a moving laser head which focuses the laser on the material surface. Laser excitation and XY laser head movement are controlled by the computer. Most works in the literature make use of carbon-dioxide (CO_2) laser. CO_2 laser ablation for fabrication of microfluidics channels has been used with different materials, like PMMA²⁶, PDMS²⁷, Mylar^{28–33} and recently PLA^{22,34} (**Figure 3-2**). Bonding is mostly done through surface activation or solvent bonding.

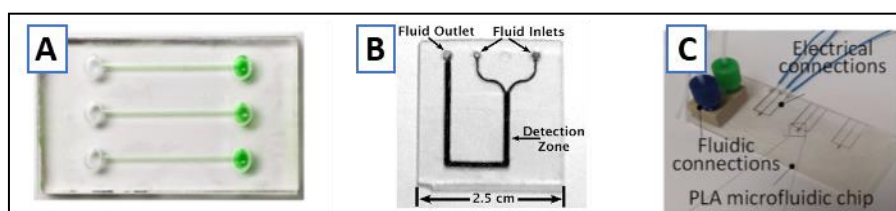


Figure 3-2. Laser cut LOM for microfluidics. A) PMMA microchannels (Reproduced from [Mohammed et al., 2015](#)²⁶); B) Diffusion immunoassay in a T-sensor laser cut in Mylar (Reprinted by permission from Springer Nature: [Hatch et al., 2001](#)²⁸); C) Laser cut PLA microfluidic device (Reprinted with permission from [Ongaro et al., 2018](#)²². Copyright (2018) American Chemical Society).

CO_2 laser ablation brings many benefits of a proper DM technique, such as rapid turnaround time for manufacture (1~3 min/chip), low operational costs, mask/cast-less process, agile design processing through interface with CAD software, ability to process a wide variety of low cost substrates (e.g. polymers) and scalability to large scale mass manufacturing²⁶.

3.1.3 Thermoplastics for microfluidics

In this section we explore some thermoplastics alternatives to PDMS for microfabrication. Particularly, we pre-selected PC, PS, PMMA and Zeonor® 1420R COP because of their biocompatibility.

3.1.3.1 *Material characteristics*

One important drawback of PDMS is its absorption of hydrophobic molecules⁶. PS and COP may be more desirable materials for microfluidic devices because they do not undesirably absorb hydrophobic drugs⁵. Mild plasma treatment on PS and COP (final contact angle of 19~36 °) can achieve cell growth properties as good as commercial tissue culture plastics, while no improvement has been found in PMMA³⁵. While PS has become a standard in cell culture, it has been found to exert biological effects on the samples³⁶⁻³⁸. To cite some examples, monocyte-derived macrophages exhibited spontaneous secretion of interleukin-1 β and tumor necrosis factor- α when cultured on tissue culture-grade PS regardless of the presence of pre-adsorbed serum proteins³⁷. Also, U937 cells on PS released nearly 25% of their acid phosphatase and exhibited activated intracellular monocyte-specific and cholesteryl esterases³⁶. On the contrary, COP has been repeatedly reported to have high biological inertness^{19,39,40}. COP ultra-low water vapor permeability (< 0.01 % in 24 h) is beneficial to ensure excellent dimensional stability despite changes of the environmental conditions. Moreover, COP is highly transparent in the visible and near ultraviolet regions of the spectrum¹⁹ and has low autofluorescence⁴¹. Furthermore, COP allow long-term stable surface treatments. Finally, COP favors culture of respiring cells while limiting sample evaporation, thanks to its relatively low permeability to water vapor compared to other gases such as oxygen^{38,42} (**Figure 3-3**). As can be observed in **Table 3-1**, all thermoplastics have similar range of Elasticity Modulus.

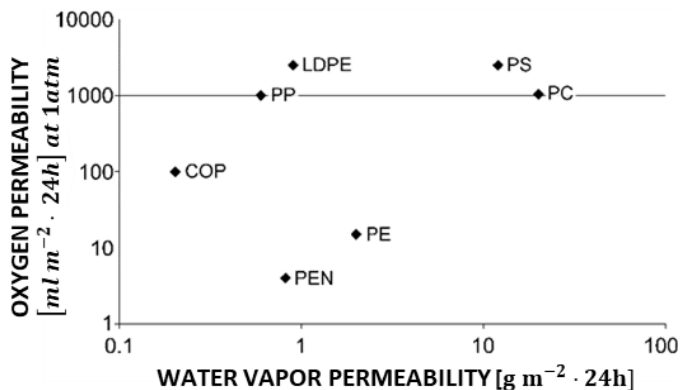


Figure 3-3. Thermoplastics water vapor permeability vs. oxygen permeability. Oxygen permeability was measured for 80 μm -thin sheets of the indicated material, and water vapor permeability was measured for 0.3 mm thick sheets by JIS Z 0280 (Japanese mechanical measurement standard). COP, Zeonor 1420R; PP, polypropylene; PEN, polyethylene naphthalate; LDPE, low-density polyethylene; PE, polyethylene; PS, polystyrene; PC, polycarbonate. Image reproduced from [Niles, Coassin, 2008](#)³⁸

Table 3-1. PDMS-thermoplastics comparison. Unless otherwise referenced, data is sourced from Tsao, 2016⁴³.

POLYMER	PDMS	THERMOPLASTICS			
		PC	PMMA	PS	COP
MECHANICAL PROPERTY	Elastomer	Rigid	Rigid	Rigid	Rigid
YOUNG MODULUS [MPa]	1.32-2.97 ⁴⁴	2300-2400 ⁴⁵	2400-3300 ⁴⁵	2300-4100 ⁴⁵	2200 ⁴⁶
THERMAL PROPERTY [°C]	~80	140~150	100~125	90~100	70~155
SOLVENT RESISTANCE	Poor	Good	Good	Poor	Excellent
ACID/BASE RESISTANCE	Poor	Good	Good	Good	Good
OPTICAL TRANSMISSIVITY	Excellent	Excellent	Excellent	Excellent	Excellent
BIO-COMPATIBILITY	Good	Good	Good	Good	Good
MATERIAL COST [\$/kg]	~150	<3	2~4	<3	20~25
WATER ABSORPTION [%] (24 h)	0.2 ⁴⁷	0.1 ⁴⁵	0.2 ⁴⁵	<0.4 ⁴⁷	<0.01 ⁴⁶

3.2 CHALLENGES AND SPECIFIC OBJECTIVES

As evidenced through the background section, in order for OOC technology to have real and widespread impact on future research, there is a need to overcome limitation of current PDMS gold standard, both regarding suitability for cell culture as well as manufacturability.

Our previously developed OOCv1 shared many of these limitations, particularly regarding the high initial cost of each design, the long and laborious fabrication process, and the lack of integration for standard, solid fluidic connections.

Aim of this chapter is to explore LOM techniques to overcome such limitations. Specific objectives of this chapter will be:

- 3.1. to select suitable materials, compatible with LOM RP technique. Materials should: i) be suitable for cell cultures; ii) enable efficient bonding between layers, to achieve leakage-free devices;
- 3.2. to design a versatile OOC device (*OOC v2.0*) to be fabricated using LOM RP techniques previously presented;
- 3.3. to optimize the fabrication protocols;
- 3.4. To fabricate and test the new devices.

We will consider 4 polymers as possible base material and investigate different bonding strategies. Based on bonding results and material properties, we will select our chosen materials and bonding method, design and fabricate the device optimizing the process. We will try both xurography and laser cutting for the fabrication of layers.

3.3 MATERIALS AND METHODS

3.3.1 Materials

COP sheets (Zeonor[®] 1420R, thickness 180 μm) are from Zeon Corporation (Tokyo, Japan). PC and PS (thickness 1 mm) were from Goodfellow (Huntingdon, England). PMMA (clear, thickness 3 mm) was from Trotec Laser

Inc. (Marchtrenk, Austria). Cyclohexane (28920), Trichloromethane (02487) , (3-Aminopropyl)triethoxysilane (APTES, $\geq 98\%$, A3648) and PC membranes (Whatman 9100-4710, pore size $1\ \mu\text{m}$, thickness $10\ \mu\text{m}$) were from Sigma Aldrich (St. Louis, MO USA). Double sided biocompatible pressure sensitive adhesive ARSeal® 8026 was from Adhesive Research (Glen Rock, PA USA). Adhesive transfer tape 467MP was from 3M™ (Maplewood, MN USA).

3.3.2 Direct Polymer bonding

Different bonding strategies were explored, particularly O_2 plasma bonding, Ultraviolet Ozone (UVO_3), solvent bonding and adhesive. Different bulk materials were tested: COP, PC, PS, PMMA. Apart from bulk materials, testing of bonding against PC membranes was performed. For plasma and UVO_3 , both pristine and APTES functionalized PC membranes were used.

3.3.2.1 APTES functionalization of PC membranes

APTES functionalized PC membranes were prepared following similar protocol as described in Chapter 2. A solution of 5 % APTES in DI water was pre-heated in a glass Petri dish at $80\ ^\circ\text{C}$ on a hotplate and covered with another Petri dish to prevent evaporation. The membrane was activated using O_2 plasma (1 min, 29.6 W, 0.2 Torr) and immediately submerged in the solution afterwards. After 20 minutes, the membrane was washed thoroughly using DI water, deposited on top of a PTFE flat substrate and dried using a gentle N_2 gas stream.

3.3.2.2 Substrate bonding

Under fume hood, samples of each material were rinsed in IPA and dried using gentle N_2 gas stream. Specific steps of each bonding method were according to the following subparagraphs. Qualitative bonding test was performed by manually gently pulling the samples apart.

O_2 Plasma treatment

All plasma processing described were performed in the MicroFabSpace facility of the IBEC, in a clean room environment, using a Harrick Plasma Cleaner PDC-002-CE (Harrick Plasma, Ithaca, NY USA) with O_2 gas; pressure and gas flow were controlled using Harrick PlasmaFlow (Harrick Plasma, Ithaca, NY USA). Bonding of each bulk material was tested against itself as well as against pristine and APTES functionalized PC membranes. After cleaning, the samples were treated with O_2 plasma ($t = [1, 2, 5]\ \text{min}$, 29.6W, 0.2 Torr).

After plasma treatment, samples were brought into contact and left under pressure (500 g weight) at 65 °C for at least 10 minutes.

UVO₃ treatment

Bonding of each bulk material was tested against itself as well as against pristine and APTES functionalized PC membranes. After cleaning, samples were treated with UVO₃ using UV/Ozone Cleaner (BioForce Nanoscience, Ames, IA USA, $t = [2, 10, 20] \text{ min}$). After treatment, samples were brought into contact and left under pressure (500 g weight) at 65 °C for at least 15 minutes.

Solvent bonding

The following material combinations were tested: 1) COP on COP, 2) COP on PC membrane, 3) PC on PC membrane, 4) PMMA on PC, 5) PS on PS, 6) PS on PC membrane. Solvent used was Cyclohexane for COP and Tricloromethane for all other materials. The substrates were suspended on top of a glass petri dish filled with solvent to a level 2~3mm below the substrate surface. Another glass petri dish was flipped on top to form a vapor exposure chamber. The whole assembly was placed in over a hotplate to maintain a constant temperature of 65 °C. After exposing to vapors, the substrates were pressed together and heated at 65 °C.

3.3.3 COP contact angle measurement

Contact angle measurements of COP samples were performed on native material and after treatment with O₂ plasma ($t = [1, 2, 5] \text{ min}$, 29.6W, 0.2 Torr) and UVO₃ ($t = [10, 20] \text{ min}$). Measurements were performed using OCA15 Pro system from DataPhysics (Filderstadt, Germany). After focusing the sample, a small 2- μL drop of de-ionized water was released on top of the surface and digital image captured. Contact angle measurement was performed using SCA 20 software from DataPhysics.

3.3.4 OOC design

Using Autodesk Inventor®, we designed a multilayered device assembled using LOM technique. Different layers were exported in DXF format. The design consists of a PC membrane sandwiched between two networks of 4 parallel microfluidic channels (**Figure 3-4**). Flow is distributed to the parallel channels (layers II and IV) thanks to a fluidic splitter layer (V). Double-sided Pressure

sensitive adhesive (PSA) is used as bonding method between layers. Cross section of the parallel channels is $2\text{ mm} \times 180\ \mu\text{m}$, length is 20 mm .

Taking advantage of CAD technology, the design includes Mini Luer fluidic ports in a 3-mm PMMA layer (VII), in order to simplify OOC interfacing using standard connectors. This is aimed to avoid extra fabrication steps, as the assembly uses the same technique.

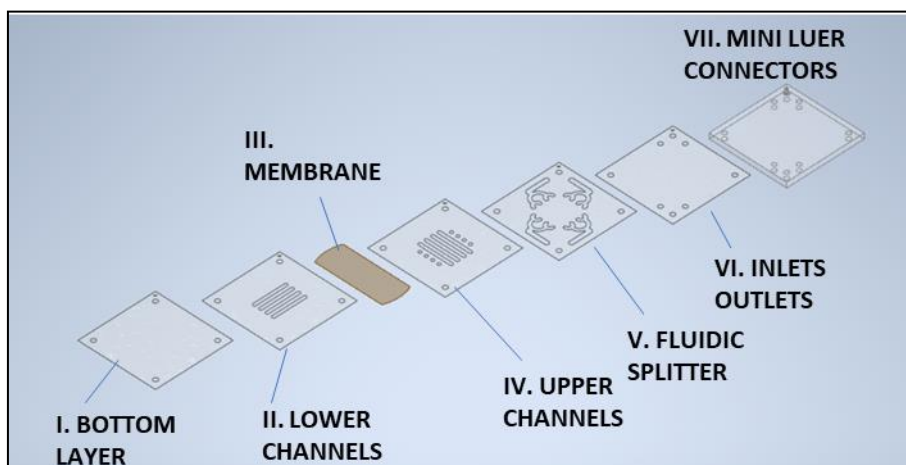


Figure 3-4. OOCv2.0 device exploded view. From left (bottom) to right (top): I) bottom layer (COP); II) lower channels layer (COP); III) porous membrane (PC); IV) upper channels layer (COP); V) flow splitters (COP); VI) inlets/outlets layer (COP); VII) Mini Luer ports layer (PMMA).

3.3.5 OOC fabrication

3.3.5.1 Substrate preparation

A $180\text{-}\mu\text{m}$ thick COP sheet was pre-cut to A4 size using a guillotine paper cutter. After removing the protective release liner, substrate was rinsed in IPA and dried using N_2 gas stream. Double sided PSA was laminated on the COP and PMMA substrates with the help of a hand-roller, avoiding bubble formations.

3.3.5.2 Vinyl cutter

After importing DXF designs, layers were cut from prepared substrate using Graphtec® CE-5000-40 vinyl cutter (Graphtec Corporation, Tokyo, Japan). Substrates were attached to cutting mat and blade length was regulated according to material substrate thickness. Cutting was performed using 2 passes at a speed of 30 mm s^{-1} . After cutting, unused parts were mechanically removed using tweezers.

3.3.5.3 Laser cut

A Trotec Speedy 100 laser cutter (Trotec Laser Inc., Marchtrenk, Austria) was used for laser cut fabrication. COP substrates were positioned on top of 2-mm PMMA sheet in the cutter bed and laser head was brought into focus (**Figure 3-5**). After importing DXF designs, layers were cut using 2-mm lens (40 W, 5000 Hz, speed: 0.15 m s^{-1}). Thick layers of PMMA were cut with adhesive side facing up. Unused parts were mechanically removed using tweezers. $\frac{1}{4}$ -28 UNF threads were formed using a threading plug tap.

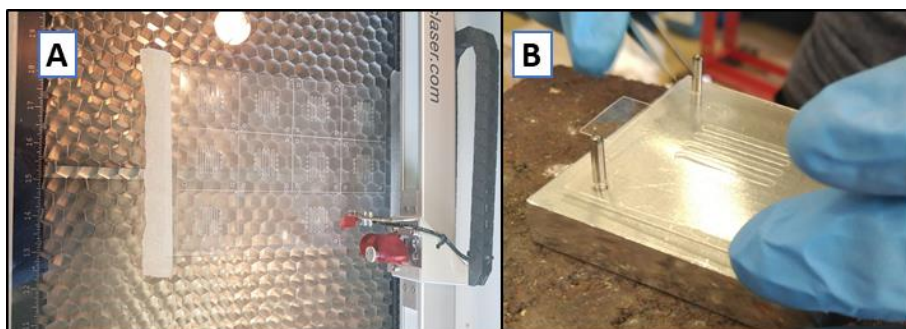


Figure 3-5. OOCv2.0 Fabrication. A) Array of COP layers being cut in the Trotec Speedy-100; B) Layers assembly using the aluminum aligner.

3.3.5.4 Assembly

Assembly was performed with the help of a custom-made aluminum aligner consisting of a thick base ($60 \times 60 \times 10 \text{ mm}$) with 4 press-fitted steel dowel pins and a thick cover with 4 holes ($60 \times 60 \times 10 \text{ mm}$). Each layer design included 4 alignment holes at the corners, each one matching the corresponding dowel pin for accurate alignment. Layers located below the membrane plane were sequentially placed in the aligner base after removing all the release liners but last one (**Figure 3-5**). Aligner cover was added on top and the whole stack was pressed using an Atlas T8 hydraulic press (Specac Ltd, Orpington, UK) at $2 \cdot 10^3 \text{ kg}$ for 30 seconds. After pressing, the assembled layers were removed from the alignment block and the procedure was iterated for the layers located above the membrane. Membrane was manually cut to size using a template and, after removing release liner from one of the previously assembled part, it was positioned with the help of tweezers. Finally, the other pre-assembled part was used to close the sandwich after removing its own release layer. Everything was pressed again using the same conditions.

Finally, after removing release liners, a thicker PMMA layer with mechanized Mini-Luer® ports was added and pressed to obtain the complete device.

3.3.5.5 Inspection and Testing

After assembly, devices were inspected using optical microscope and tested for leakage using a flow of 2 mL min^{-1} .

3.4 RESULTS

3.4.1 Direct Polymer bonding

Effective bonding between various layers of the device is fundamental to avoid liquid leakages which would compromise the entire device functionality. We tested different materials using Plasma treatment, UVO₃ treatment and solvent bonding. Results are summarized in **Table 3-2**.

O₂ plasma and UVO₃ gave generally poor bonding or no-bonding results. Using O₂ plasma to seal two samples of the same bulk polymer failed with all materials. UVO₃ treatment gave almost the same result, with exception of COP-COP bonding. Good strength COP-COP bonding was obtained with higher UVO₃ exposure times and thermal post-curing. Both surface activation methods failed to bond pristine PC membranes to bulk materials. Good results using both surface activation techniques were obtained between COP and APTES-functionalized PC membranes. Sandwiching between two COP layer was not possible, as one of the layers always showed poor bonding. Similar results were obtained using UVO₃, but with easy reversible bonding.

Solvent bonding gave stronger results between most same-material combinations (COP, PS, PMMA). As can be observed in some examples of **Figure 3-6**, optical quality of such results was poor, with lot of residual bubbles (D,F) or material opacification (E). Using solvent bonding, we were unable to obtain bonding to PC membranes.

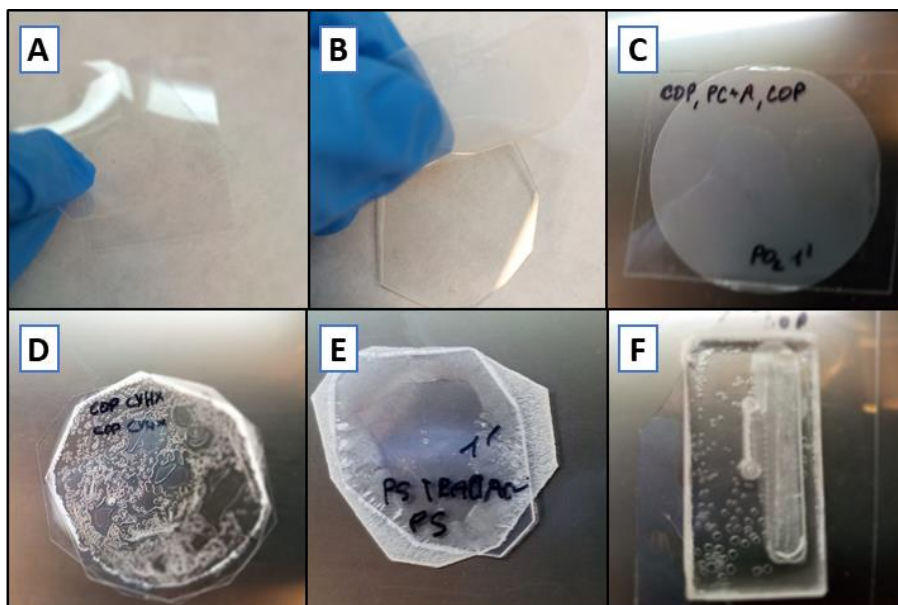


Figure 3-6. Best results obtained from direct polymer bonding. A) Poor, reversible COP-COP bonding after 10 minutes UVO_3 treatment; B) Poor reversible COP-pristine PC membrane bonding after O_2 plasma treatment; C) Irreversible bonding of COP-APTES functionalized membrane after O_2 plasma treatment; D) Irreversible solvent bonding of COP-COP; E) Irreversible solvent bonding of PS-PS; F) Irreversible solvent bonding of COP sheet to a thicker COP block with milled microchannel. All solvent methods resulted in poor optical properties, due to residual bubbles (D, F) or opacification (E).

Table 3-2. Direct polymer bonding results. *) low optical quality; **) Good results only on one side of the membrane, unable to obtain a proper polymer-PC membrane-polymer sandwich; -) not tested.

Method	1 st material	2 nd material	COP			PS			PMMA		PC				
			COP	PC	APTES -PC	PS	PC	APTES -PC	PMMA	PC	PC				
Method			O ₂ Plasma	1 min	None	None	None	-	-	-	None	None	None		
				2 min	None	None	Good **	None	-	None	None	None	None	None	
				10 min	None	Poor	Good **	None	None	None	None	None	None	None	
				5 min	None	None	None	None	None	None	None	None	None	None	
				UVO ₃	10 min	Poor	None	Poor	None	-	None	None	None	None	None
					20 min	Good	None	Poor	None	None	None	None	None	None	None
			Solvent		Good *	None	-	Good *	None	-	Good *	None	Poor		

3.4.2 COP contact angle measurements

Contact angles measurements were performed on Native COP and after O₂ plasma or UVO₃ treatment. Results are exposed in **Table 3-3**. As illustrated also in **Figure 3-7**, in both cases contact angle is significantly reduced.

Table 3-3. Contact angle measurements of COP, natively and after surface treatment. (Mean values and standard deviations for N = 3 samples).

Treatment	Native	UVO ₃		O ₂ Plasma		
Time [min]	-	10	20	1	5	10
C. A. [°]	98.4 ± 1.53	32.83 ± 1.18	24.41 ± 0.99	28.6 ± 2.23	8.03 ± 0.78	9.13 ± 1.31

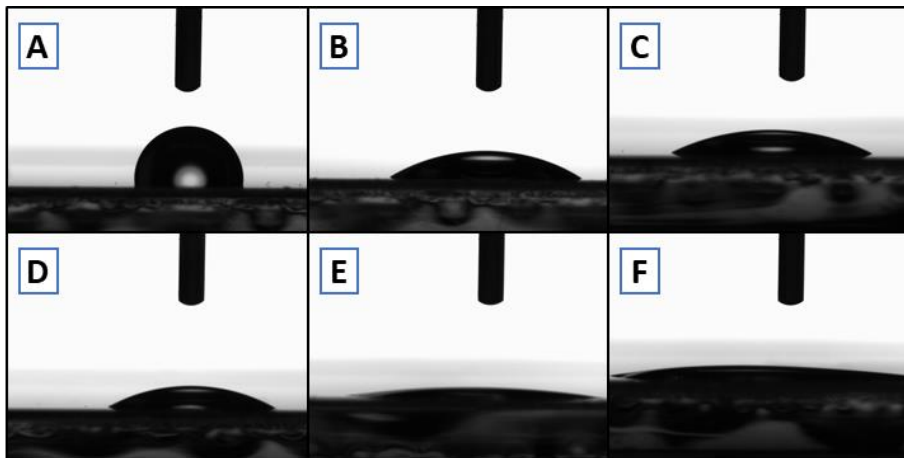


Figure 3-7. Contact angle measurement of COP. A) Native; B-C) after UVO₃ surface treatment (10 and 20 minutes, respectively); D, E, F) after O₂ plasma treatment (1, 5 and 10 minutes, respectively).

3.4.3 Design and fabrication

We designed and fabricated a multilayer device consisting of two networks of channels. Once selecting COP as main material, we first fabricated various layers through xurography and later translated the process to laser cut. Initial adhesive bonding proof of concept was performed using 467MP adhesive. Assembly was successful, though optical quality was poor. Use of biocompatible optical clear ARSeal® 8026 resulted in superior quality (**Figure 3-8**).

Final assembled devices were successfully tested against leakage for 24h.

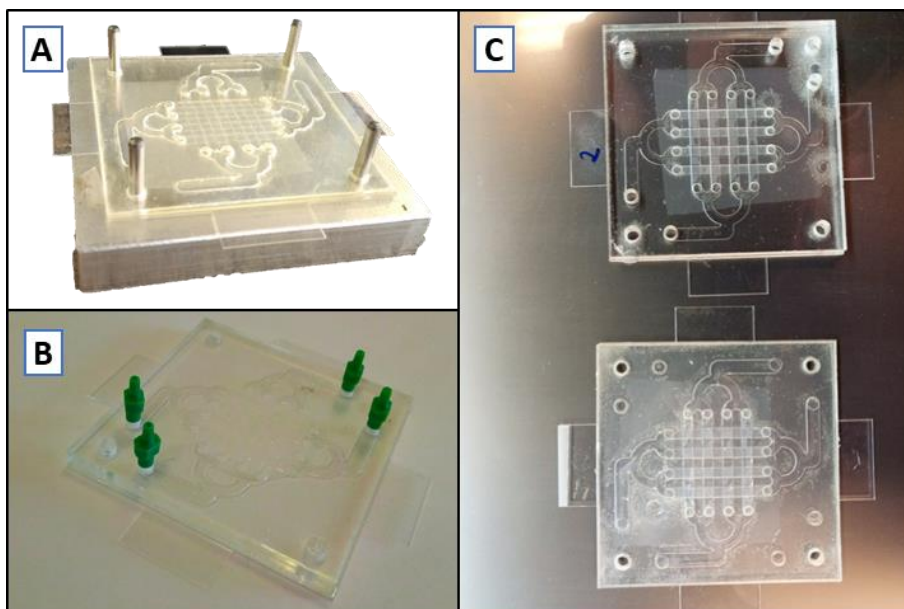


Figure 3-8. OOCv2.0 device assembly. A) OOC in the alignment block during the assembly process; B) Final OOC device assembled with green Mini-Luer® connectors; C) Optical clarity comparison between ARSeal 8026 PSA (Top) and 467MP (Bottom).

3.5 DISCUSSION

The work presented in this chapter was focused on exploring digital manufacturing technologies for OOC device fabrication. Particularly, our focus was on LOM techniques that make use of vinyl cutter (readily available in our laboratory) and a CO_2 laser cutter (to which we had access thanks to a collaboration with University of Rome Tor Vergata, Italy). After identifying possible material candidates thanks to their favorable biocompatible characteristics, we further refined our selection after testing possible bonding strategies. We started with direct bonding strategies, with the idea to maintain the use of PC membranes. We could not achieve irreversible, solid bonding using O_2 plasma on any pristine material. We suspect this might be due to relative low energy of the plasma equipment at our disposal or to the lack of proper thermocompression equipment to achieve optimal annealing conditions. Particularly, PMMA bonding with UVO_3 and O_2 plasma was previously reported⁴⁸, but higher plasma power and pressures ($0.2\sim 1 Pa$) were used. Plasma bonding of PC membranes was successful to COP only after APTES treatment, but we could achieve irreversible bonding only to one side of the membrane. UVO_3 and solvent bonding results of COP-COP were

encouraging. Nonetheless, optimizing the bonding quality and uniformity across the sample would have required a hot-press equipment in a clean environment and irreversible bonding to PC membranes could not be achieved. For that reasons, we decided to abandon direct bonding strategies for a more versatile adhesive bonding solution. Nonetheless we suggest direct bonding solutions could be considered for further research or even for a future translation into a commercial product.

After a series of considerations on materials properties, we decided to use COP for device layers fabrication. We discarded PC due to its known flammability when exposed to CO_2 laser processing. COP was preferred over PS and PMMA for its superior optical properties, biocompatibility, low water vapor permeability and ease of sourcing in thin films. PS was discarded as being reported exerting biological effects and being difficult to process using CO_2 laser. COP was also preferred to PMMA for its top-grade cell culture properties after mild plasma treatment (contact angle in $19\sim 36^\circ$ range)³⁵. Our contact angle measurements confirmed that we can achieve similar surface activation after 1-minute O_2 plasma or 10-20 minutes UVO_3 treatment.

We decided to maintain PMMA as a material for the fluidic connections layer, having greater young modulus and being the gold standard plastic in CO_2 laser processing of thicker layers.

Both LOM fabrication strategies described in this process bring the benefits of rapid prototyping into microfluidics fabrication. Throughput is improved both by reduction of process duration as well as by removal of intermediate steps, such as mold fabrication. The latter further reduces the overall process cost and especially costs connected to future modifications of the device, enabling easier and faster iteration of the design. Once cutting parameters are optimized for each material, time from initial design to finally assembled device is drastically reduced. We find adhesive bonding to be a versatile solution for rapid prototyping in research environment, as it enables to extend the process to different membrane materials. On the contrary, solvent or surface activation strategies might limit the process to a smaller range of compatible materials or might require adding chemical functionalization to achieve bonding of different materials.

Use of 3D design software and renderings allows for easier control and revision of all the phases of the process. Inclusion of standard microfluidic ports since the design enables easy interfacing of the device to the outer lab environment, without need of manual and time-consuming bonding of ports to each outlet. Embedding of standard connectors is subject to further improvements later discussed on Chapter 5.

Few works can be found in the microfluidics literature regarding processing COP with cutting plotter^{25,49} or laser cutters⁵⁰, and even a LOC device fabricated in COP using cutting plotter and PSA with embedded membrane⁵¹. Nonetheless, the cited work⁵¹ used white polyester adhesive, while our device embeds a transparent membrane using optically-clear biocompatible adhesive. Furthermore, our device -which is designed for OOC applications - is also fabricable entirely by laser ablation, features embedded auto-aligning standard Mini Luer[®] connectors.

3.6 CONCLUSIONS

We successfully designed and developed biocompatible membrane-integrated OOC devices using two different subtractive RP techniques. The assembled device integrates standard microfluidics ports for easier handling by the final user. Fabrication process is rapid (1~2 *h* from scratch to final device) and low cost. Compared to traditional soft-lithography, the fabrication process also requires less steps and no mask nor master fabrication. Particularly, laser cutting option is also less dependent on user dexterity and can be scaled up to achieve higher throughput.

We investigated direct bonding polymer for COP, PC, PMMA and PS. Though results were not satisfactory for our application, some partially positive results might be further investigated and considered for possible applications in which introduction of PSA layers is not desirable.

The fabrication process developed overcome most of the limitations of PDMS. Thanks to the material choice, the produced device present excellent optical characteristics, minimum evaporation, no small molecules absorption, no uncross-linked oligomers leakage and low autofluorescence. The developed process is rapid, easier, low cost and enables easy modifications of the design, connectors embedding and scalability.

To the best of our knowledge, we found no previous works in the literature where an optically-clear membrane-embedded OOC device with embedded auto-aligning Mini Luer® fluidic connectors was fabricated in COP using laser cutting technique.

3.7 REFERENCES

1. Bhattacharjee, N., Urrios, A., Kang, S. & Folch, A. The upcoming 3D-printing revolution in microfluidics. *Lab on a Chip* **16**, 1720–1742 (2016).
2. Araci, I. E. & Quake, S. R. Microfluidic very large scale integration (mVLSI) with integrated micromechanical valves. *Lab Chip* (2012). doi:10.1039/c2lc40258k
3. Rigat-Brugarolas, L. G. *et al.* A functional microengineered model of the human splenon-on-a-chip. *Lab Chip* **14**, 1715 (2014).
4. Regehr, K. J. *et al.* Biological implications of polydimethylsiloxane-based microfluidic cell culture. *Lab Chip* **9**, 2132–2139 (2009).
5. Su, X. *et al.* Microfluidic cell culture and its application in high-throughput drug screening: Cardiotoxicity assay for hERG channels. *J. Biomol. Screen.* **16**, 101–111 (2011).
6. Berthier, E., Young, E. W. K. & Beebe, D. Engineers are from PDMS-land, Biologists are from Polystyrenia. *Lab Chip* **12**, 1224–37 (2012).
7. Berthier, E., Warrick, J., Yu, H. & Beebe, D. J. Managing evaporation for more robust microscale assays : Part 1. Volume loss in high throughput assays. *Lab Chip* **8**, 852 (2008).
8. Berthier, E., Warrick, J., Yu, H. & Beebe, D. J. Managing evaporation for more robust microscale assays : Part 2. Characterization of convection and diffusion for cell biology. *Lab Chip* **8**, 860 (2008).
9. Scott Lynn, N., Henry, C. S. & Dandy, D. S. Evaporation from microreservoirs. *Lab Chip* **9**, 1780 (2009).
10. Gewandter, J. S., Staversky, R. J. & Reilly, M. A. O. Free Radical Biology & Medicine Hyperoxia augments ER-stress-induced cell death independent of BiP loss. *Free Radic. Biol. Med.* **47**, 1742–1752 (2009).
11. Tang, Y. *et al.* CYP1B1 and endothelial nitric oxide synthase combine to sustain proangiogenic functions of endothelial cells under hyperoxic stress. (2019). doi:10.1152/ajpcell.00153.2009.
12. Barclay, I. & Dann, Z. *Concurrent Engineering: Contemporary issues and modern design tools.* *Concurrent Engineering* (Springer US, 1993). doi:10.1007/978-1-4615-3062-6
13. Au, A. K., Lee, W. & Folch, A. Mail-order microfluidics: evaluation of stereolithography for the production of microfluidic devices. *Lab Chip* **14**, 1294–1301 (2014).

14. Zhou, Z., Xie, S. & Chen, D. *Fundamentals of Digital Manufacturing Science*. (Springer London, 2012). doi:10.1007/978-0-85729-564-4
15. Naderi, A., Bhattacharjee, N. & Folch, A. Digital Manufacturing for Microfluidics. *Annu. Rev. Biomed. Eng.* **21**, 325–364 (2019).
16. Manz, A. *et al.* Planar chips technology for miniaturization and integration of separation techniques into monitoring systems. *J. Chromatogr. A* **593**, 253–258 (1992).
17. Harrison, D. J. *et al.* Micromachining a miniaturized capillary electrophoresis-based chemical analysis system on a chip. *Science (80-.)*. (1993). doi:10.1126/science.261.5123.895
18. Okagbare, P. I., Emory, J. M., Datta, P., Goettert, J. & Soper, S. A. Fabrication of a cyclic olefin copolymer planar waveguide embedded in a multi-channel poly(methyl methacrylate) fluidic chip for evanescent excitation. *Lab Chip* **10**, 66–73 (2010).
19. Nunes, P. S., Ohlsson, P. D., Ordeig, O. & Kutter, J. P. Cyclic olefin polymers: Emerging materials for lab-on-a-chip applications. *Microfluidics and Nanofluidics* **9**, 145–161 (2010).
20. Mohammed, M. I., Zainal Alam, M. N. H., Kouzani, A. & Gibson, I. Fabrication of microfluidic devices: Improvement of surface quality of CO₂ laser machined poly(methylmethacrylate) polymer. *J. Micromechanics Microengineering* **27**, (2017).
21. Bartholomeusz, D. A., Boutte, R. W. & Andrade, J. D. Xurography: rapid prototyping of microstructures using a cutting plotter. *J. Microelectromechanical Syst.* **14**, 1364–1374 (2005).
22. Ongaro, A. E. *et al.* Laser Ablation of Poly(lactic acid) Sheets for the Rapid Prototyping of Sustainable, Single-Use, Disposable Medical Microcomponents. *ACS Sustain. Chem. Eng.* **6**, 4899–4908 (2018).
23. Yuen, P. K. & Goral, V. N. Low-cost rapid prototyping of flexible microfluidic devices using a desktop digital craft cutter. *Lab Chip* **10**, 384–387 (2010).
24. Islam, M., Natu, R. & Martinez-Duarte, R. A study on the limits and advantages of using a desktop cutter plotter to fabricate microfluidic networks. *Microfluid. Nanofluidics* **19**, 973–985 (2015).
25. Azouz, A. Ben, Murphy, S., Karazi, S., Vázquez, M. & Brabazon, D. Fast Fabrication Process of Microfluidic Devices Based on Cyclic Olefin Copolymer. *Mater. Manuf. Process.* **29**, 93–99 (2014).

26. Mohammed, M. I. *et al.* Improved Manufacturing Quality and Bonding of Laser Machined Microfluidic Systems. *Procedia Technol.* **20**, 219–224 (2015).
27. Wang, L. *et al.* Prototyping chips in minutes: Direct Laser Plotting (DLP) of functional microfluidic structures. *Sensors Actuators, B Chem.* **168**, 214–222 (2012).
28. Hatch, A. *et al.* A rapid diffusion immunoassay in a T-sensor. *Nat. Biotechnol.* **19**, 461–465 (2001).
29. Schilling, E. A., Kamholz, A. E. & Yager, P. Cell Lysis and Protein Extraction in a Microfluidic Device with Detection by a Fluorogenic Enzyme Assay. *Anal. Chem.* **74**, 1798–1804 (2002).
30. Fu, E., Ramsey, S. A., Kauffman, P., Lutz, B. & Yager, P. Transport in two-dimensional paper networks. *Microfluid. Nanofluidics* **10**, 29–35 (2011).
31. Macounová, K., Cabrera, C. R., Holl, M. R. & Yager, P. Generation of natural pH gradients in microfluidic channels for use in isoelectric focusing. *Anal. Chem.* **72**, 3745–3751 (2000).
32. Garcia, E., Kirkham, J. R., Hatch, A. V, Hawkins, K. R. & Yager, P. Controlled microfluidic reconstitution of functional protein from an anhydrous storage depot. *Lab Chip* **4**, 78–82 (2004).
33. Munson, M. S., Cabrera, C. R. & Yager, P. Passive electrophoresis in microchannels using liquid junction potentials. *Electrophoresis* **23**, 2642–2652 (2002).
34. Ongaro, A. E. *et al.* Polylactic acid, a sustainable, biocompatible, transparent substrate material for Organ-On-Chip, and Microfluidic applications. *bioRxiv* 647347 (2019). doi:10.1101/647347
35. Johansson, B., Larsson, A., Ocklind, A. & Öhrlund, Å. Characterization of air plasma-treated polymer surfaces by ESCA and contact angle measurements for optimization of surface stability and cell growth. *J. Appl. Polym. Sci.* **86**, 2618–2625 (2002).
36. Matheson, L. A., McBane, J. E., Malowany, J. I., Santerre, J. P. & Labow, R. S. Is cell culture stressful? Effects of degradable and nondegradable culture surfaces on U937 cell function. *Biotechniques* (2007). doi:10.2144/000112460
37. Bonfield, T. L., Colton, E. & Anderson, J. M. Plasma protein adsorbed biomedical polymers: Activation of human monocytes and induction of interleukin 1. *J. Biomed. Mater. Res.* (1989).

doi:10.1002/jbm.820230602

38. Niles, W. D. & Coassin, P. J. Cyclic olefin polymers: innovative materials for high-density multiwell plates. *Assay Drug Dev. Technol.* **6**, 577–90 (2008).
39. Bhattacharyya, A. & Klapperich, C. M. Thermoplastic microfluidic device for on-chip purification of nucleic acids for disposable diagnostics. *Anal. Chem.* (2006). doi:10.1021/ac051449j
40. Choi, S. H., Kim, D. S. & Kwon, T. H. Microinjection molded disposable microfluidic lab-on-a-chip for efficient detection of agglutination. *Microsyst. Technol.* (2009). doi:10.1007/s00542-008-0689-x
41. Piruska, A. *et al.* The autofluorescence of plastic materials and chips measured under laser irradiation. *Lab Chip* **5**, 1348–1354 (2005).
42. Corp, Z. *Zeonex and Zeonor Technical Data Supplement.* (2006).
43. Tsao, C. W. Polymer microfluidics: Simple, low-cost fabrication process bridging academic lab research to commercialized production. *Micromachines* **7**, (2016).
44. Johnston, I. D. Mechanical characterization of bulk Sylgard 184 for microfluidics and microengineering. (2014). doi:10.1088/0960-1317/24/3/035017
45. Ltd., G. C. Good Fellow materials catalogue. Available at: <http://www.goodfellow.com/catalogue/GFCatalogue.php>. (Accessed: 20th April 2019)
46. Corp, Z. Zeonor® 1020R Polymer Datasheets. Available at: http://www.zeonex.com/applications_bio-diagnostic.asp.
47. Blau, A., Neumann, T., Ziegler, C. & Benfenati, F. Replica-moulded polydimethylsiloxane culture vessel lids attenuate osmotic drift in long-term cell cultures. *J. Biosci.* **34**, 59–69 (2009).
48. Shinohara, H. Low-temperature Direct Bonding of Poly (methyl methacrylate) for Polymer Microchips. 301–306 (2007). doi:10.1002/tee.20157
49. Do, J., Zhang, J. Y. & Klapperich, C. M. Maskless writing of microfluidics: Rapid prototyping of 3D microfluidics using scratch on a polymer substrate. *Robot. Comput. Integr. Manuf.* **27**, 245–248 (2011).
50. Cai, J. *et al.* Rapid prototyping of cyclic olefin copolymer based microfluidic system with CO₂ laser ablation. *Microsyst. Technol.* **23**,

5063–5069 (2017).

51. Lanfranco, R., Saez, J., Di Nicolò, E., Benito-Lopez, F. & Buscaglia, M. Phantom membrane microfluidic cross-flow filtration device for the direct optical detection of water pollutants. *Sensors Actuators, B Chem.* **257**, 924–930 (2018).

4 3D printing for microfabrication

4.1	BACKGROUND	80
4.1.1	3D PRINTING.....	80
4.1.2	SL 3D PRINTING FOR MICROFLUIDICS	82
4.1.3	SL PRINTER AND PREVIOUS EXPERIENCE IN THE LAB	87
4.2	CHALLENGES AND SPECIFIC OBJECTIVES OF THIS CHAPTER	88
4.3	MATERIALS AND METHODS	90
4.3.0	MATERIALS USED	90
4.3.1	IMPROVING A PRE-EXISTING SL 3D PRINTER	90
4.3.2	CALIBRATION AND REAL RESOLUTION ASSESSMENT	98
4.3.3	FUNCTIONAL LOC PRINTING.....	98
4.3.4	3D PRINTING OOC APPLICATIONS	100
4.4	RESULTS.....	103
4.4.1	IMPROVING THE PRINTER	103
4.4.2	CALIBRATION AND RESOLUTION ASSESSMENT	104
4.4.3	FUNCTIONAL LOCs	107
4.4.4	OOC APPLICATIONS.....	107
4.5	DISCUSSION	107
4.6	CONCLUSIONS	112
4.7	REFERENCES	113

After RP laser cut approach presented in the previous chapter, we will explore 3D printing DM techniques – particularly SL 3D printing- for OOC fabrication.

The work here presented starts optimizing a commercial SL 3D printer to enable microfluidics applications. A series of upgrades are presented, and their benefits explained. Then, after characterizing upgraded printer resolution, a couple of example LOCs are printed to verify their functionality.

Finally, two solutions for fabrication of OOC are proposed. On the one hand, a hybrid 3D printing-laser cut technique is presented which to easily embed commercial membranes (OOCv3-A). On the other hand, SL is proposed as a faster, cheaper and more automated tool for PDMS multilayered soft lithography. A device for mimicking neuro-muscular junction is designed and fabricated (OOCv3-B).

Collaborations: The work presented in this chapter was achieved in collaboration with PhD student Davide Di Giuseppe and his supervisor Prof. Eugenio Martinelli, from Sensors group of Rome Tor Vergata University, and PhD student Maider Badiola Mateos, from Nanobioengineering group of IBEC.

4.1 BACKGROUND

4.1.1 3D printing

In the last chapter we introduced DM and RP technologies, with a special emphasis on subtractive techniques. Here we introduce with more details Additive Manufacturing, generally known as 3D printing. “3D-printing” refers to a set of additive manufacturing techniques, which can create solid 3D objects layer-by-layer under precise digital control¹. Of these techniques, the ones that are most relevant to microfluidic device, fused deposition modeling (FDM) Photopolymer based inkjet printers (Multi Jet/PolyJet Modeling ,MJM/PJM) and fabrication are stereolithography (SL) (**Figure 4-1**).

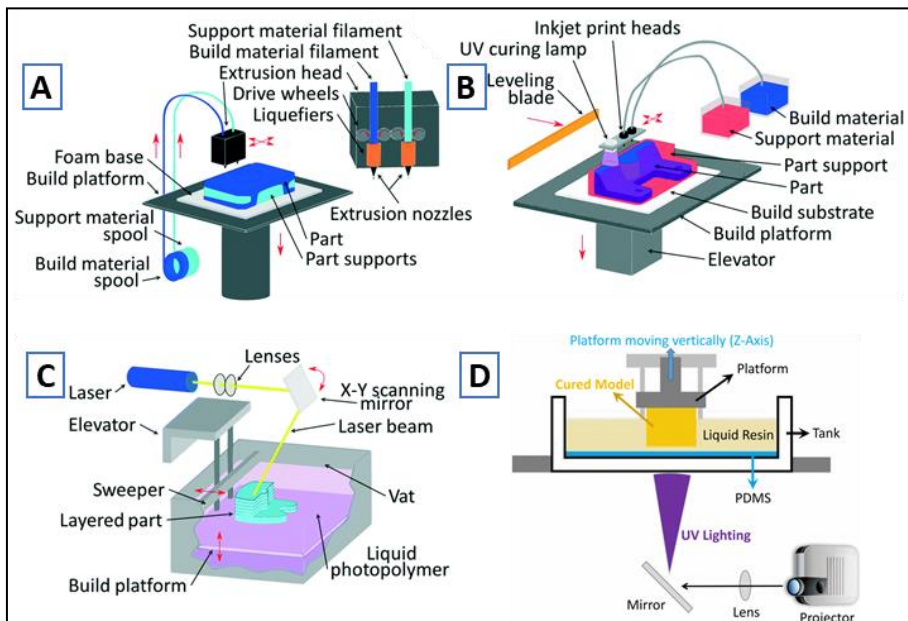


Figure 4-1. Main 3D printing technique relevant for microfluidics. A) FDM; B) MJM/PJM; C) Laser-based SL; D) DLP-based SL. Images A, B, C adapted from [Bhattacharjee et al. 2016¹](#), by permission of RSC; Image D ©2016 IEEE. Reprinted, with permission, from [Wu et al, 2016²](#).

Fused Deposition Modeling (FDM)

FDM, also known as thermoplastic extrusion, is nowadays the most know 3D printing technology between general publics. First invented by Crump in 1989³, it works extruding heated thermoplastic material from a nozzle head which can be displaced in controlled manner in across the axis. When the material cools down after being extruded, it solidifies again. While resolution in FDM still presents a challenge, the technique's biocompatibility and multi-material versatility are unparalleled⁴. FDM materials are sold in convenient filament rolls of inexpensive and biocompatible thermoplastic polymers such as acrylonitrile butadiene styrene (ABS), poly- lactic acid (PLA), polycarbonate, polyethylene terephthalate glycol-modified, thermoplastic elastomers, thermoplastic polyurethane, PMMA, polypropylene, nylon, polyamide, and polystyrene, among others⁴.

Photopolymer based inkjet printers (MJM/PJM)

Photopolymer based inkjet printers use an array of inkjet print heads to deposit tiny drops of the build- and support- material to form the object in a layer-by-layer fashion⁵. The build material is typically an acrylate-based photopolymer and includes monomers, oligomers, and a photo-initiator to cure each layer with an ultraviolet (UV) source⁵. Commercial manufacturers, such as Objet Geometries Ltd and Stratasys use DoD technology, termed PJM, while 3D Systems use MJM. In both cases, the print head has many small holes that jets droplets of build material and support material simultaneously, to build 3D structure.

Stereolithography (SL)

SL was the first form of 3D printing to be invented in the 1980s. Though nowadays Hull⁶ is considered the first inventor of SL, a patent was previously filed in 1984 by three French inventors⁷. SL allows for the assembly-free simultaneous production of quasi-arbitrary 3D shapes in a single polymeric material from a liquid photo-resin precursor by means of a focused laser or a digital light processing (DLP) projector⁴. In laser approach a 3D object is built either by scanning the laser in a 3D path or layer by layer⁴. In layer-by-layer approach, the platform is lowered a few microns into the resin-filled vat at each layer and the laser is sequentially scanned on the resin surface across all the pixels of the image representing a section of the model. In modern desktop systems, the laser is substituted by a (more affordable) DLP⁸ projector, and the

fluid to be exposed is squeezed into a thin layer by a motorized build plate. The DLP projector forms the projected image using a Digital Micromirror Device (DMD), a rectangular array of micromirrors which can be rotated individually. Compared to laser approach, DLP 3D printers results in more homogenous layer surfaces and reduced printing time, projecting each layer as a whole. In DLP-based SL, the XY-resolution is limited by the size of the projected pixels, and the Z-resolution is determined in part by the resolution of the Z-motor⁴.

4.1.2 SL 3D printing for microfluidics

Though all presented 3D printed approaches have been applied to the microfluidics field, the first two currently show some major limitations.

On the one hand, microchannel fabrication with FDM has presented a challenge for several reasons: (a) The sizes of the extruded filaments are larger than typical channels used in microfluidics; (b) from a topological consideration, it might not be possible to lay down the walls of any arbitrary channel layout in the form of extruded filaments, especially at channel intersections, where joining filament ends can cause leaks; (c) the lack of structural integrity between the layers can result in weak seals^{4,9}; and (d) the creation of rough surfaces, which create disturbance in the flow within the channels⁵.

On the other hand, research in MJM/PJM applications for OOC are mainly limited by proprietary and expensive inkjet formulations used, which suppresses innovation⁴. Furthermore, there is concern about poor cytocompatibility, and bio-functionality studies with mammalian systems are lacking, so most MJM/PJM microfluidic researchers have focused on non-biological applications⁴. Clearly, MJM/PJM will have a bright future when the patents expire, and academic developers can start innovating open-source biocompatible and functional resins⁴.

SL, on the other hand, is already seeing a lot of research application to microfluidics and many works trying to establish open formulations for resin materials. Achievable surface quality is also usually superior in terms of roughness to other techniques¹⁰.

4.1.2.1 Understanding DLP SL process and real 3D resolution

DLP SL process

In DLP SL printing process, the printed object is generated upside-down, hanging from a build platform that can be displaced across the Z (vertical) axis. The process starts lowering the platform and submerging it in a resin filled vat with a transparent bottom (usually glass). Through precise motion, only a thin, few-microns-thick layer of photocurable resin is left between the platform and the vat bottom. After exposing, the platform is then moved up and down again, to the level of the next layer. To avoid the object to detach from the platform during the lift process, usually a gradient of adhesion between the bottom and the platform is required. This is sometime achieved increasing roughness of the platform (not an option for microfluidics) or facilitate the release from the vat using some hydrophobic coating (i.e. PDMS, flexible film of fluorinated compound). Also, the movement speed of the Z-axis plays a role, though reducing this parameter affect the printing speed. Finally, a few first layers, called burn-in layers, are usually exposed with higher dose, to ensure a good adhesion of the printer through the process. Other parameters might also need tuning when changing material viscosity, like how much to lift the platform at each cycle or how much time to wait for the resin to settle before exposing the layer. Finally, exposure dose (D) can be regulated through two parameters: projector irradiance (E_e) and exposure time (Δt).

$$D = E_e \cdot \Delta t \quad (4-1)$$

Real DLP SL 3D resolution

To understand SL resolution, we should first differentiate between dimensional accuracy when printing simple features or cantilever-like structures (i.e. closed channels).

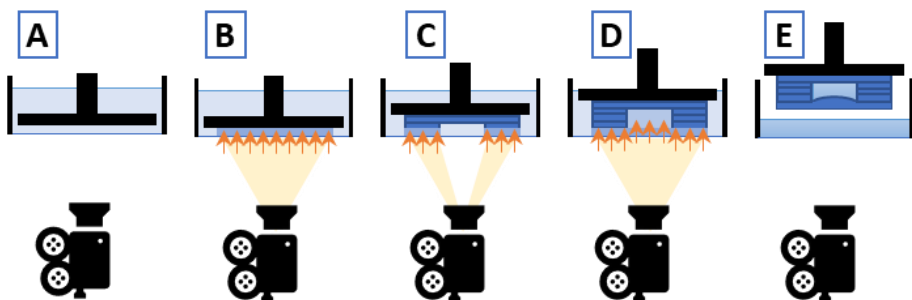


Figure 4-2. Different phases of printing a cantilever structure (i.e. closed channel).

As seen before, when speaking of simple features, XY resolution is mainly limited by the projected pixel size, while Z resolution is limited by the minimum step size which the build platform can achieve. Printing of cantilever structures, instead, becomes more challenging. When printing the roof of a cantilever structure, light tends to penetrate across the resin to the previous layers, affecting in particular the Z-resolution. Furthermore, the minimum cross-sectional area of a microchannel that is attainable by SL depends not only on the laser spot size or pixel resolution but also on the type and viscosity of the resin, which has to be effectively drained from the channels post printing^{4,11}. In both laser-based and DLP-based setups, the minimum feature size that is achievable by SL is dependent on the pixel/laser spot size, the absorption spectra of the photoresin, and the diffusivity of the reactants^{4,12}. Recent SL printers incorporate high-intensity focused light-emitting diode (LED) light sources in the visible wavelength^{4,8}. Nonetheless, for microfluidics a transparent resin is desirable, so an UV source becomes necessary⁴. Transparent resins feature low absorption (and thus poor resolution) in the visible range^{4,13}. Also, the penetration depth of resins under blue LEDs is larger than that under UV light^{14–16}.

4.1.2.2 Main SL applications for LOC and OOC

The first SL-printed microfluidic device, credited to the Renaud group¹⁷ in 2001, was a 3D fluidic mixer⁴ (**Figure 4-3-A**). DLP SL has been used to create hollow, ~1 mm long micro-needles (with a bore diameter of 375 μm) that could penetrate cadaveric porcine skin (**Figure 4-3-B**)^{1,18}. Lately, various microfluidic devices for immunomagnetic separation of bacteria¹⁹, separation of cells by using helical channels with trapezoid cross-sections²⁰ (**Figure 4-3-C**), gradient generation²¹ (**Figure 4-3-D**), emulsion droplet generators^{21–24}, DNA assembly²⁵ and an oxygen control insert for a 24-well dish²⁶, to name a few, have been designed and fabricated using SL¹.

Between the main advantages of SL, stands the possibility of printing a complete device, with embedded fluidic connectors and automation.

As we will see more in detail in the next chapter, the absence of standardization in interfacing PDMS microdevices with the peripherals has been a major bottleneck in the widespread adoption of LOC technologies¹. 3D printing of devices with integrated connectors has been demonstrated and is

believed to help facilitating standardization of interfaces and also to promote user-friendly design in microfluidics^{1,11,26,27}.

Various approach had been taken towards printing of integrated microvalves, various formulations of absorbers and activators. Improvements has been made both in size and transparency^{28–34}, with latest record of 300 μm diameter transparent valves^{4,35}.

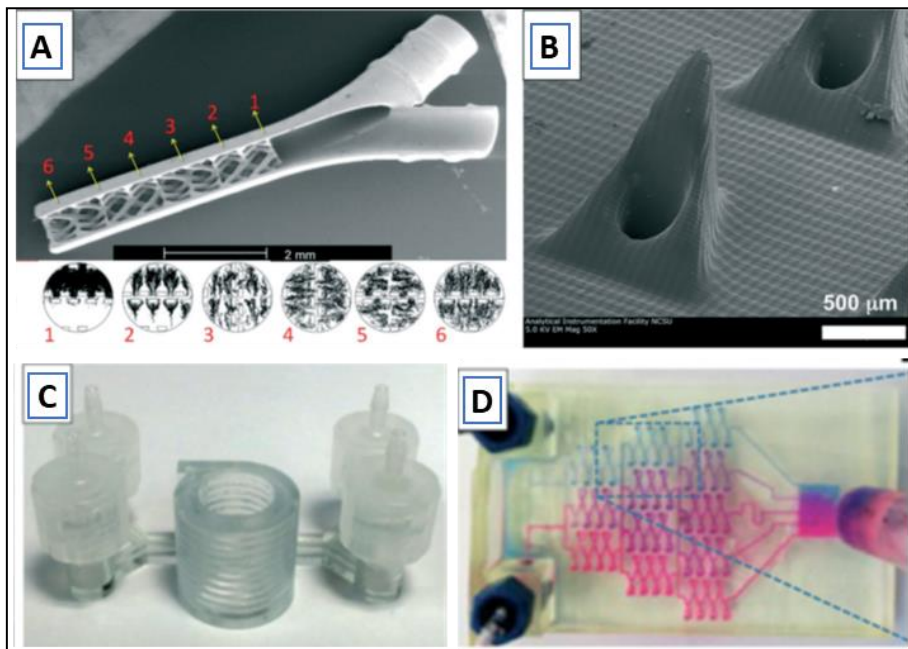


Figure 4-3. Microfluidic devices printed by SL. A) SEM micrograph of the first microfluidic device (micro-mixer) printed with SL. (below) numerical simulations of fluid mixing at the indicated cross-sections of the device (Reprinted from [Bertsch et al., 2001](#)¹⁷, by permission of RSC); B) SEM of hollow micro-needles fabricated in e-Shell-200 by DLP-SL (Reprinted from [Miller et al., 2011](#)¹⁸, with the permission of AIP Publishing); C) Spiral microchannel with trapezoid cross-section (printed with Watershed) used for size-selective separation of bacterial cells (Reproduced from [Lee et al., 2015](#)²⁰); D) A complex microfluidic mixer and gradient generator printed with a commercial desktop SL system (Reprinted with permission from [Shallan et al., 2014](#)²¹. Copyright (2014) American Chemical Society.

Printing microvalves is just one example of the important role of material research in future SL development. Main requirements for microfluidics-ready SL resins are being transparent, high resolution, biocompatible and widely available (possibly open source formulations). The field of restorative dentistry is being a fertile ground for SL engineers because of its great interest in developing biocompatible high resolution photopolymerizable resins⁴. Though

various certified biocompatible resins exist in the market, only one transparent commercial SL resin, Watershed 11122 XC, has been reviewed for cell culture compatibility. Cells can be exposed to Watershed for short periods of time^{19,20,30}, but not for longer durations¹, and the resin is not permeable to gases⁴.

Some research groups started to search for new open materials. Main candidate to date is Poly(ethylene glycol) diacrylate (PEG-DA) with molecular weight (MW) of 258 *Da*, which can achieve high resolution, transparent devices which sustained cell cultures¹³. Folch's group also recently published the formulation of a SL resin which shares all the positive properties of Sylgard 184 PDMS³⁶; nonetheless printing resolution is still low for use in microfluidics. The same group also published the first work featuring two-materials SL printing. The work achieved inclusion of porous membrane-like structure inside a 3D printed device using different formulations of PEG-DA with different MW³⁷ (**Figure 4-4**).

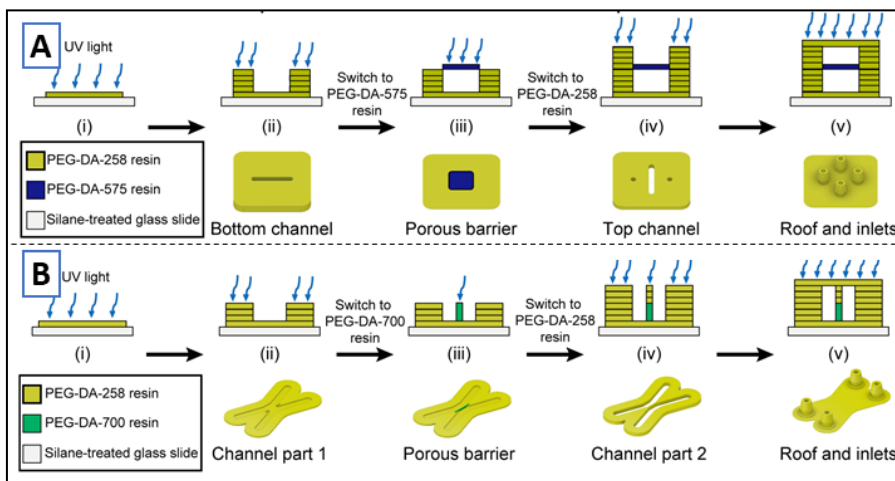


Figure 4-4. Approaches for multi-material SL printing of porous membrane structures in microfluidic devices. Horizontal (A) and vertical (B) membranes are fabricated on top of a silane treated glass slide (white) using pausing printing process and switching between different MW PEG-DA formulations (258 *Da* in yellow and 700 *Da* in green). Images reproduced from [Kim et al, 2018](#)³⁷.

Recently, Folch's group achieved the highest resolution to date using a commercial UV DLP 3D printer³⁸. Using their PEG-DA based resin formulation and 385-*nm* UV light source, they achieved single pixel resolution (**Figure 4-5**) and printed an array of high aspect ratio (37:1) single-pixel wide microchannels

($27\ \mu\text{m}$), separated by $54\text{-}\mu\text{m}$ wide walls. The same device was later demonstrated for the straightforward injection of hydrogel barriers in microchannels³⁹.

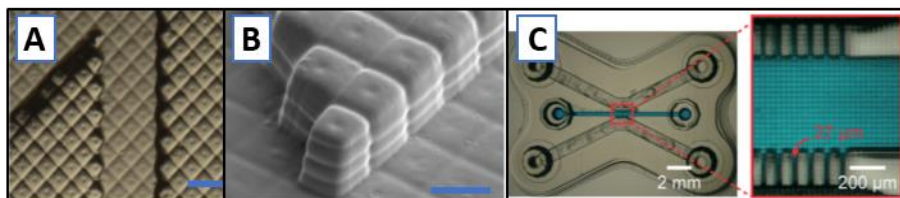


Figure 4-5. High resolution DLP SL printing with commercial printers. A) Microscope image and B) SEM image of test motives with high precision reproduction of single pixel structures (scale bars: $100, 50\ \mu\text{m}$, reprinted from [Kuo et al, 2019](#)³⁸ with permission); C) 3D printed microfluidic device for hydrogel partitioning of microchannels, with detail of single-pixel microchannels array (reprinted from [Kim et al, 2019](#)³⁹ by permission of RSC).

Few studies feature SL as a rapid prototyping technique of masters for PDMS soft-lithography^{40,41}. To the best of our knowledge, only simple planar structure have been reported, while more complex multilayer devices have been only obtained replicating masters rapid-prototyped with MJM/PJM⁴².

4.1.3 SL printer and previous experience in the lab

Our laboratory owned a SL 3D printer “Ilios HD Custom Kit” from Ilios 3D systems (Cyprus). It was the first in-situ approach of our lab to 3D printing and no particular expertise had been developed before. The device consisted of a big, solid structure assembled with pre-cut aluminum extruded profiles. A large vat (approx. $35 \times 35\ \text{cm}$, named as V0 vat) is suspended over the base plane with a spring-loaded mechanism. The original build platform (V0) is fixed to a horizontal profile (Z-gantry) which is displaced vertically using two high resolution stepper motors (one on each side) to provides fine control of positioning (resolution: $12.5\ \mu\text{m}$; maximum deviation on positioning repeatability: $< 2\ \mu\text{m}$). A visible light DLP projector (Optoma HD20, 1080p) with removed color wheel is used as light source with lower approximate wavelength of $405\ \text{nm}$; the projector has a resolution of $1920 \times 1080\ \text{pixels}$ with variable focus which enable to reach a minimum projected pixel size of about $30 \times 30\ \mu\text{m}$, with a Field of View (FOV) of $57.6 \times 32.4\ \text{mm}$. The system is controlled through proprietary software running on an embedded Raspberry Pi which is accessible through a web interface to load previously sliced files and start the printing process. The Raspberry Pi

communicates through a serial port to a proprietary control board which drives all the electronics. A separate slicing software had to be installed in a Microsoft Windows computer to prepare the files for printing. Both the slicer program as well as the web interface has only few customizable settings (i.e. exposure time and layer thickness).

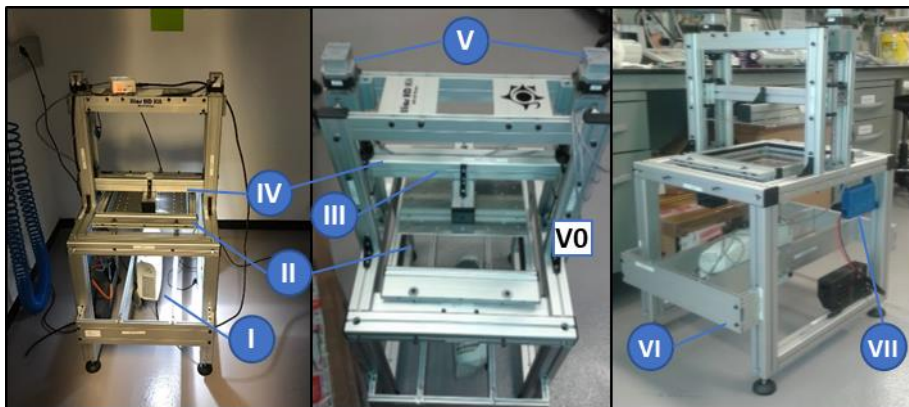


Figure 4-6. Ilios HD for Research SL 3D printer. The original Optoma HD visible projector (I) exposed the image over the resin V0 vat; II) Z-axis moving gantry; the V0 build platform (III) is secured to an horizontal gantry which moves across the Z-axis thanks to two high precision stepper motors (V); the projector stands on a fixed, manually aligned support; all motion control is performed by proprietary electronics (VII).

4.2 CHALLENGES AND SPECIFIC OBJECTIVES OF THIS CHAPTER

This chapter will explore fabrication of LOC and OOC devices using SL 3D printing.

On the one hand, room for improvements emerges from the current state of art. Particularly – despite being an interesting feature for OOC application – only one work has been recently reported about embedding membranes in 3D printed devices. Furthermore, no complex structure has been realized using masters printed with SL. Finally, development of new materials is still an open research subject which just started to gain attention.

The Ilios SL 3D printer shows a list of limitations. To start with, besides being called “Ilios for Research”, there is limited control over the whole set of printing parameters and the printing sequence. Proprietary software and hardware are a huge limitation to the possibility of modifying protocols for non-standard material as well as adding features to the printer. The software

also offers no option to set projector pixel size nor to modify the predefined sequence of actions performed during the printing process.

Projector positioning and alignment is a manual operation which inherently lacks accuracy. Projector support structure must be loosened from the four anchoring points, manually positioned and retightened to a precise height while holding the structure in place counteracting gravity force. Any misalignment of the projector support plane does results in projected image distortion. Visible light projector is also a limitation itself, as resolution improves reducing the wavelength. Light sources in the UV range are preferred. Furthermore, it has no physical shutter and the background luminosity of black pixels is high, causing undesired exposure. Vat and build platform are oversized for microfluidic application and desired FOV, resulting in waste of material. Vat positioning system relying on spring-loaded support results in variations of first layer thickness each time the vat is removed for cleaning or replacement of PDMS layer. Two-motor Z-axis configuration with a single mechanical end-stop also results in lack of accuracy. On the one hand, the mechanical end-stop used is subject to high hysteresis and can easily result in variations of hundreds of microns of the home positions. On the other hand, each time stepper motors are power cycled, they could randomly shift one step. Being independent, the two Z-axis motors could then shift in opposite directions and accumulating steps difference over time, requiring manual realignment after few power-cycles.

Specific objectives of this chapter are the following:

- 4.1. to improve the existing commercial SL DLP printer for microfabrication;
- 4.2. to fabricate transparent and functional microfluidic devices;
- 4.3. to fabricate a 3D printed membrane embedded device for mimicking of cell culture interfaces (*OOCv3*);
- 4.4 to fabricated “real 3D” complex multi-layered OOC device using PDMS soft-lithography with SL-printed masters.

4.3 MATERIALS AND METHODS

4.3.0 Materials used

Unless stated otherwise, all aluminum machining had been performed with CNC tools by the mechanical workshop of Centres Científics i Tecnològics (CCIT) of the University of Barcelona. Ilios HD for Research had been previously purchased from Ilios3D (Cyprus). Spot HT resin was from Spot-A Materials (Barcelona, Spain). Sample of biocompatible Detax Medicalprint® clear UV was supplied from Detax GmbH & Co. KG (Ettlingen, Germany). Build platform and vat V1 were purchased from FlexVAT (Olympia Fields, IL USA). Vat V2 was replacement for Anycubic Photon 3D printer, purchased from Shenzhen Anycubic Technology Co. (Shenzhen, China).

4.3.1 Improving a pre-existing SL 3D printer

4.3.1.1 *Switch to Open Source electronics and tunable freeware software interface*

First step toward achieving granular control over printing parameters consisted in getting rid of proprietary hardware and software of the machine. Component choice prioritized open-source solution when available and community backed solutions open to customization. Compatibility with previous components as well as modularity and possibility of future expansion was also considered. On the hardware side, the new open system consists of two parts: a Raspberry Pi®⁴³ embedded computer and the open-source Reprap Universal Mega Board with Allegro driver (RUMBA) controller board. RUMBA board was released under GNU Public License (GPL) v2.0⁴⁴ by reprapdiscount.com. Raspberry Pi® runs NanoDLP⁴⁵ front-end and control software. The software enables customization of the whole printing process while providing a slicer and a remotely accessible web interface. The software communicates with the open-source Marlin firmware⁴⁶ which runs on the RUMBA board and controls axis movements. Marlin firmware is released under GPL v3.0⁴⁷. Marlin firmware was configured to control the two Z-axis through two different motors and two optical end-stops based on tcst2103 sensor, which replaced the single mechanical end-stop for reliable alignment at each power-cycle. Marlin is normally used to control FDM printers, where the overall printing process – including control of the nozzle heating – is entirely managed by the electronics board (i.e. RUMBA). As SL requires

integration with a video source – externally controlled by NanoDLP software – synchronization is required. To achieve it, original Marlin code was modified to send a notification back to NanoDLP when the last requested movement terminated correctly. The code has been resubmitted to the Marlin codebase, according to GPL requirements, and is now available in current releases. Adapters for end-stops mounting were 3D printed in PLA at 0.1 mm resolution to ensure stable and precise positioning.

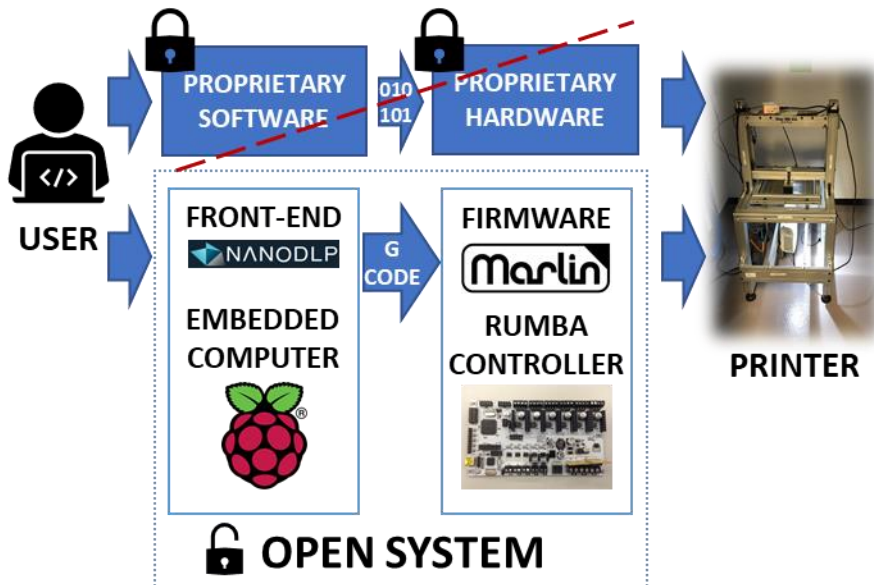


Figure 4-7. Open system printer control replacement. Original Ilios system functioned using closed-source software and proprietary hardware, which communicated using proprietary protocol. Replacement open system control and front-end software (NanoDLP⁴⁵) runs on Raspberry Pi^{®43} embedded computer. Hardware controller is an open-source RUMBA board running open-source Marlin firmware⁴⁶, which is controlled through a derivative of standard G-Code. (Raspberry Pi[®] and the Raspberry Pi logo are trademarks of the Raspberry Pi Foundation⁴³).

4.3.1.2 Improving resin vat and build platform

Printer vat and build platform went through a couple of prototype iterations. First requirements to simplify removal and installation of both vat and build platform with repeatability of positioning was the design of two adapters. Vat adapter consisted of a flat aluminum sheet (6 mm thickness) anchored to the main structure of the printer through preexisting mounting holes with an open window in the center (**Figure 4-8**). Aluminum vat adapter was designed in Autodesk Inventor[®] and manufactured at CCIT.

Build platform adapter was designed in Autodesk Inventor® and 3D printed in PLA (0.1 mm Z-resolution). It anchors to the Z-gantry using the same mounting holes of the pre-existing platform and features a fast unlocking mechanism for the build platform, with an M8 screw and four pins for easy alignment (**Figure 4-9**).

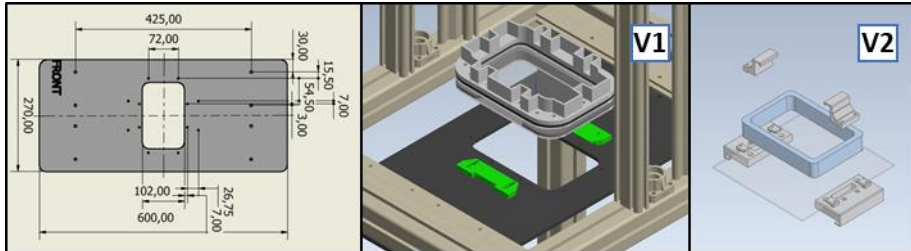


Figure 4-8. Vat adapters design. The new vat adapter (Design with dimensions on the left) integrates with the original structure and support the new vats. V1 is fixed using a sliding clamp mechanism, V2 features a fixed glass bed and removable clamps to secure and align the vat centered respect with the window.

Vat improvements

Two different commercial vat were chosen and adapted to the printer (**Figure 4-9**). Both solutions present a flexible vat, were the bottom of the pool is formed using a pre-tensed fluorinated ethylene propylene (FEP) film. First design was a mix of 3D printed and machined aluminum parts. FEP film was suspended at 20 mm from the base of the vat structure and the vat was secured/removed using a 3D printed sliding clamp. Second design was made of metal parts, with FEP film aligned with the bottom of the platform. This model is intended to work against a rigid glass surface, so we added a flat borosilicate glass and a series of 3D printed adapters, both to hold the glass in place as well to easily secure/remove the vat in place.

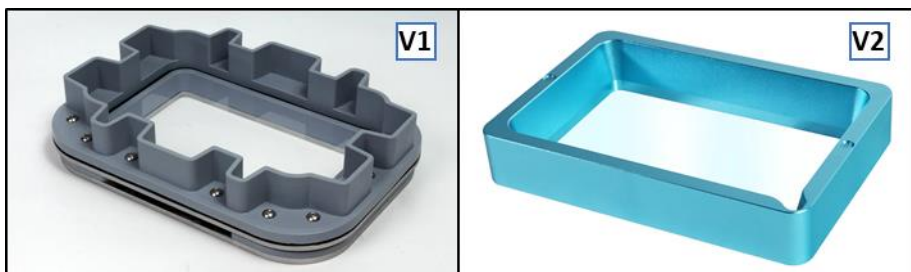


Figure 4-9. Different vats tested. Both V1 and V2 version consisted of flexible FEP film bottom. V1 version is an assembly of 3D printed ABS parts and aluminum; V2 is made of anodized metal parts only.

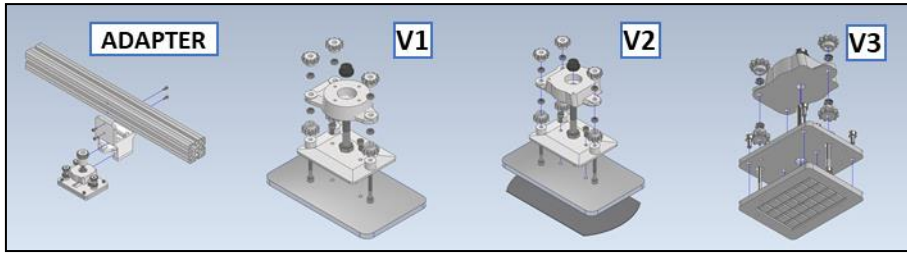


Figure 4-10. Build platform designs through different iterations. Adapter had been designed to fit V1 alignment system and printer Z-gantry. Leveling system consisting of three knobs in all build platforms is inspired to V1 design. V2 improved the alignment system using smaller dimensional tolerances for the alignment slots and added a silicon wafer glued to the platform. V3 added a vacuum chuck with recessed 2-mm channel grid and alignment pins.

Build platform improvements

Three different new build platforms were tried (**Figure 4-10**). First model was the commercial system obtained from Flexvat (Olympia Fields, IL USA) together with the first vat version. It featured 3 knobs to level the platform with the vat base and four recessed holes for alignment pins. Second revision took inspiration from the first design, maintaining the 3-knob system while improving the alignment pins system. Flatness of the platform was also improved by fixing a pre-cut silicon wafer to the aluminum build platform. Third design introduced a vacuum chuck with alignment pins into the platform, for use of standard $50 \times 75 \text{ mm}$ glass slides as low cost replaceable printing substrate. Connection to the vacuum system was performed through a pneumatic quick connection coupling, screwed to the plate. Low/high vacuum pressure switching was performed by opening/closing a secondary exhaust valve connect the vacuum circuit to ambient pressure (**Figure 4-11**). A pressure gauge dial was included in the circuit in order to verify the pressure level.

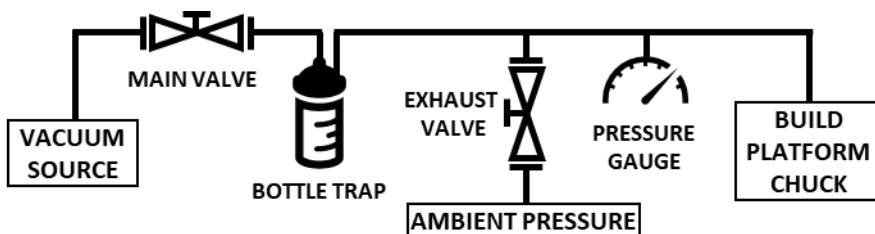


Figure 4-11. Vacuum circuit schematic. Circuit was connected to the vacuum source through the main valve. Secondary exhaust valve regulated low/high vacuum delivery to the build platform chuck, as well as depressurization of the system. Bottle trap was used to avoid resin reaching the vacuum source in case of any malfunctioning. Pressure gauge allowed easy visual feedback of vacuum pressure.

4.3.1.3 Switching to UV projector

Another point of improvement was replacement of the DLP projector. Candidate for replacement was Wintech PRO6500 based on DLP6500 Digital Micromirror Device (DMD) by Texas Instruments® (Dallas, TX USA). It is an UV DLP LED system with 1920 x 1080 resolution and a projected pixel size of 50 μm at fixed working distance. It features an all glass 0 % offset optics, optimized for 381~650 nm transmission. Peak wavelength is 384 nm . The projector is equipped with standard High-Definition Multimedia Interface (HDMI) and DisplayPort connectors for video input and Universal Serial Bus (USB) and Inter-Integrated (I2C) ports for projector control.

Table 4-1. Wintech PRO6500 technical specification.

UV Wavelength	Minimum System Power	Lens Working Distance	Resolution	Projected Pixel Size	FOV
[nm]	[mW]	[mm]	[px]	[μm]	[mm]
384	1100	150	1920 x 1080	50	96 x 54

Projector programming

Being a dedicated device, the projector works slightly differently from a general-purpose multimedia projector. Desired startup setting (video source, LED status and power) must be programmed in a proprietary Texas Instruments® macro language. Further live control of projector status and parameters can be performed using USB or I2C interface. We preset the macro to switch off the LED and select HDMI input at startup. After testing, USB connection was chosen over I2C, being less prone to interferences which could result in the loss of control of the projector. A custom program was written to control projector LED status and intensity over USB protocol. The program was configured in the frontend (NanoDLP). Valid values for Pulse Width Modulation (PWM) setting are reported in **Table 4-2**.

Additional Safety Measures

Wintech projector peak wavelength is 384 nm , so extra safety measures were added to the printer design. Beside adding an enclosure to limit accidental exposure of the user, the system was configured to activate the projector LED

only during the printing process and to switch it off at the end of the print. Additionally, a custom mechanical shutter add-on for the projector has been designed in Autodesk Inventor and printed in PLA (0.3 mm Z-resolution). A 5V micro servo motor (MG90S, TowerPro) was used as the shutter actuator and interface to a General-Purpose Input/Output (GPIO) pin of the Raspberry Pi® and configured into NanoDLP. Finally, a camera was connected to the Raspberry Pi® and mounted using a custom 3D printed adapter to check the printing process without entering the yellow-light room.

Table 4-2. Projector PWM setting Vs. LED driving current.

PWM	0	15	20	25	30	35	40	45	50
LED Current	0	3.6	4.4	5.2	6.4	7.2	8.4	9	9.6

PWM	60	70	80	90	100	120	140	150	155
LED Current	10.6	11.9	13.1	13.8	14.4	16	17.2	17.9	18.1

Projector mounting and motorized focus calibration system

A new system to mount the new projector and control its alignment was designed using Autodesk Inventor® (**Figure 4-12**). The base, consisting of two 6mm thick aluminum sheet separated by 8 columns, provides a solid structure parallel to the XY-plane, mechanically coupled to printer. The projector support is coupled to the base through two 16-mm slide bearing rails (SBR) linear shafts and four SBR16UU bearing blocks which enable the projector to slide across the Y-axis. Movement is controlled by a third stepper motor (repurposed from the old tilt mechanism) coupled to a SFU1204 ball screw. A third optical end-stop was added to the design to enable recognition of zero position.

A 75 × 75 mm UV enhanced aluminum mirror was mounted at 45° angle below the vat to redirect the projector light. All custom supports were printed in PLA (0.3 mm Z resolution). Aluminum parts were machined at CCIT from a 6 mm aluminum sheet. Stepper motor was configured as X-axis in Marlin firmware, optical end-stop offset was calibrated using digital caliper.

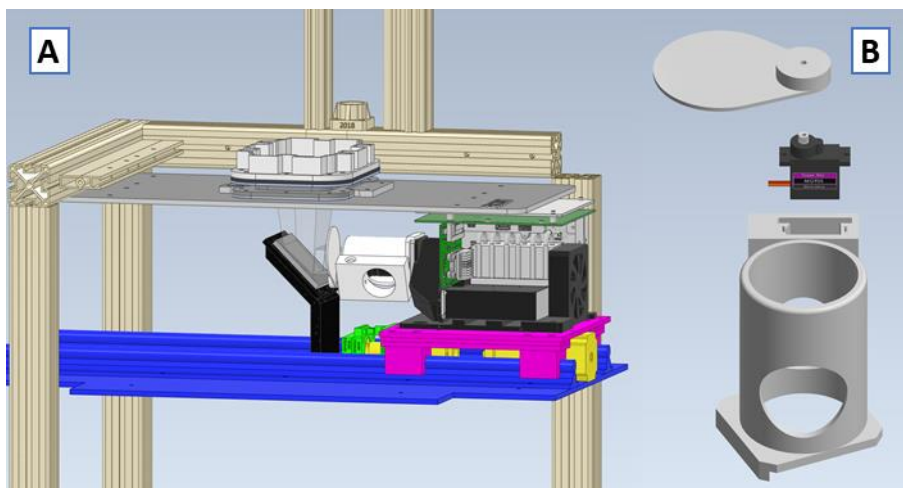


Figure 4-12. Projector mounting. A) Projector support (blue) with projector carriage (magenta), linear transmission system (yellow) and optical end-stop used to control focus position (Black and grey); a mirror tilted at 45° is fixed to a 3D printed support (black) just below the vat; Part of the original structure is removed for visibility purpose; B) exploded view of the mechanical shutter.

Projector irradiance calibration

Projector irradiance was measured using a Power and Energy meter USB interface with S302C Thermal Power Sensor (Bandwidth: 190~2500 nm, Maximum 2 W, Sensor diameter 12 mm) from Thorlabs (Newton, NJ USA). The sensor was fixed to the build platform adapter of the printer at brought at focus distance. Measurements were performed at different projector PWM setting value ($PWM = 20, 45, 50, 70, 100, 150$). Irradiance was calculated for 4 different configurations: i) no vat installed, ii) old V0 vat with new, freshly replaced PDMS layer, iii) old V0 vat with used PDMS layer (10 print jobs) and iv) V2 vat with new FEP film and v) V2 vat with used FEP film (10 print jobs).

4.3.1.4 Defining printing process

Printing process was redefined from scratch. Here follows a description of the general printing protocol performed by the user as well the sequence of action performed by the printer.

General Printing Protocol

Print substrate (glass or aluminum plate) was cleaned by washing it sequentially in acetone and ethanol, and dried using N_2 gas stream. The build platform was mounted to the printer and realigned with the vat plane if

necessary. If glass slide is used, both vacuum valves were opened to pre-pressurize the chuck. Glass slide was put in place and the secondary vacuum valve (exhaust) was closed to pressurize the chuck. Minimum target pressure needs to be achieved before proceeding further. The vat was placed in the printer and secured using the knobs/screws. From this point, all the steps were performed under yellow light to avoid exposure of the resin. Vat was filled with the required resin. The minimum sufficient amount depended on the print job, being 3-*mm* height a mean value for LOC device. The projector power supply was connected, and the print job was launched from outside the room using the web interface. Once the job finished, the build platform was unlocked from its support and left dripping in a tilted position to remove and recover extra unexposed resin. If vacuum was used, starting from the main one, both vacuum valves were toggled to depressurize the system and remove the glass slide. The print substrate was then washed in IPA. After detaching, the printed model was sonicated twice in IPA (3 *min*) and dried using N₂ gas stream. If the printed model feature printed channels, extra flow of IPA using a disposable syringe. Post-curation was performed by exposing the printed object 30 *min* on each side with a wide spectrum UV fluorescent light (bandwidth 300~400 *nm*, peak wavelength 365 *nm*).

Print job process

The sequence of action performed by the printer had been programmed into NanoDLP configuration. Different profiles can be defined for different materials or configurations (projector intensity, vat type, etc.). Profiles enable to customize printing process in depth, including the sequence of action performed before and after exposing each layer. In our application we limited customizations to Z-axis speed, number of burn-in layers, exposure or resin settle times. The general print job executed by the printer consisted of the following steps:

1. Build platform reached end-stops home position (top of Z-axis);
2. Projector was brought in focus;
3. Build platform moved to the current layer Z position (starting at $z =$ layer height);
4. Mechanical shutter was opened, and current slice image was projected for required time;

5. Mechanical shutter was closed and build platform started to slowly lift, detaching the polymerized layer from the bottom of the vat;
6. Steps 2-4 were repeated for the remaining layers;
7. Build platform was elevated again to the top of Z-axis for user removal.

4.3.2 Calibration and real resolution assessment

Calibration models were designed in Autodesk Inventor® (**Figure 4-13**) and exported to Standard Tessellation Language (STL) file format. Feature resolution test models consisted of an array of protruding and hollowing rectangular features of different width. Cantilever resolution test models consisted of an array of closed channels, with one side open for easier measurement. Most relevant tests performed are reported in **Table 4-3**. Printed feature models were inspected using Dektak profilometer. Printed cantilever models were inspected using Scanning Electron Microscope (SEM) imaging.

4.3.3 Functional LOC printing

We printed two different kind of functional LOC devices (**Figure 4-14**). The STL model of a serpentine-like channel with $1 \times 1 \text{ mm}$ cross-section was downloaded from the supplementary information of a previously published work¹³. A spiral-shaped device for particle separation was designed by student Miguel Mir Garcia of Biomedical Engineering BSc degree (University of Barcelona)⁴⁸. The devices were printed using the parameters reported in **Table 4-4**.

Table 4-3. Analyzed calibration print jobs resume.

Resin		Spot HT	Spot HT	Spot HT	MP
Build platform		V1	V2	V2	V3
Resin vat		V0 (PDMS)	V1	V2	V2
Test Model		Feature	Feature	Cantilever	Feature
Z-layer Thickness	$[\mu\text{m}]$	50	50	50	50
PWM LED	$[\#]$	25	20	20	30

Burn-in layers	[#]	10	10	6	6
Burn-in exposure	[s]	25	12	12	15
Normal Exposure	[s]	3	0.5	0.5	0.75
Z speed	[$m s^{-1}$]	0.125	0.125	0.125	0.125
Z retraction	[mm]	3	3	3	3

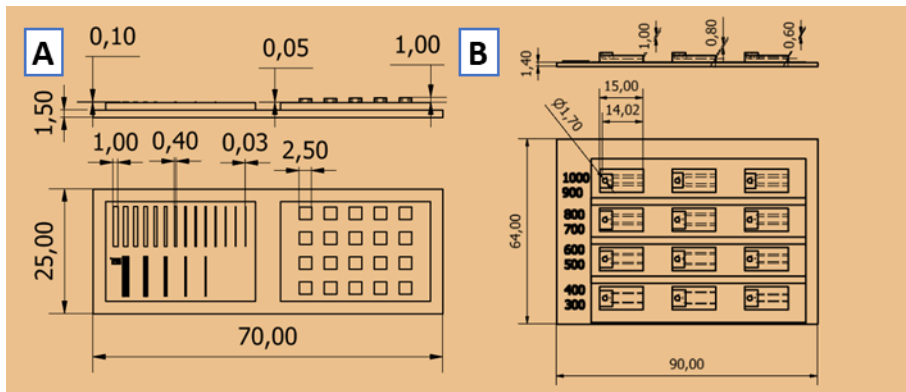


Figure 4-13. Resolution assessment test designs. A) Feature resolution test model; B) Closed channels resolution test model.

Table 4-4. LOC devices printing parameters. The devices were printed using resin vat V1 and build platform V2.

Resin	Z resolution	LED PWM	Burn-in layers	Burn-in exposure	Normal exposure	Z speed
	[μm]	[#]	[#]	[s]	[s]	[$mm s^{-1}$]
Spot HT	50	20	5	15	0.5	0.125

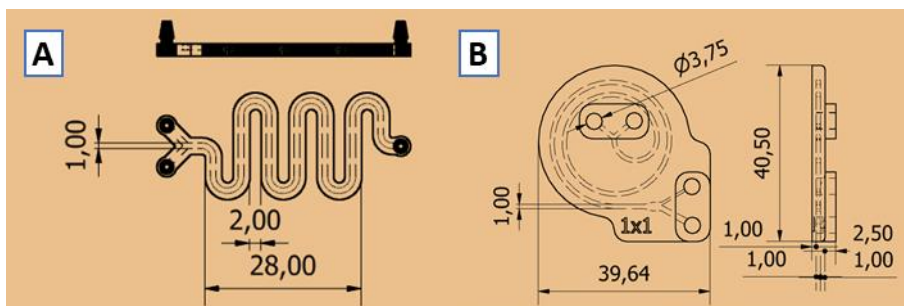


Figure 4-14. Functional 3D printed LOC test devices. A) Laminar flow serpentine (as published by Urrios et al, 2016¹³; B) Particle separating spiral device⁴⁸.

4.3.4 3D printing OOC applications

Membrane enclosed solution (OOCv3-A)

A design similar to OOCv2 was realized using Autodesk Inventor®. The device consists of two nets of parallel channels sandwiched across a commercial membrane.

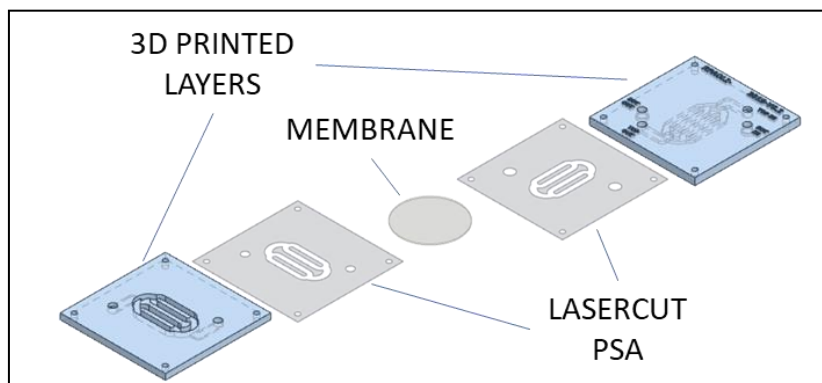


Figure 4-15. OOCv3-A exploded view.

The two layers were printed using Spot HT resin and the printing parameters reported in **Table 4-5**. A layer of ARSeal biocompatible adhesive, previously laser cut to size, was applied to the sides in contact with the membrane. The membrane was later sandwiched between the two adhesive-backed parts which were aligned and compressed using the same alignment block used for OOCv2. The assembled device was connected to a flow system using the embedded Mini-Luer® connectors and tested for leakage.

Table 4-5. OOCv3-A printing parameters. The device was printed using resin vat V2 and build platform V3.

Resin	Z resolution	LED PWM	Burn-in layers	Burn-in exposure	Normal exposure	Z speed
	$[\mu\text{m}]$	$[\#]$	$[\#]$	$[\text{s}]$	$[\text{s}]$	$[\text{mm s}^{-1}]$
Spot HT	50	20	5	15	1	0.125

interconnected on different levels by microchannels. The device was formed by three PDMS layers, assembled together using O_2 plasma bonding (**Figure 4-16**). After designing the device in Autodesk Inventor, three separated masters for PDMS replica molding have been derived from the design and exported to STL format. Each master was printed in Medicalprint[®] resin using printing parameters reported in **Table 4-6**. After post-processing, controlled thickness PDMS replica molding was obtained by pouring degassed 10:1 mixture of PDMS over the masters and curing it overnight against a standard glass slide ($75 \times 50 \text{ mm}$) on a hotplate at 70°C . After demolding the three layers where activated using O_2 plasma (1 min, 29.6 W, 0.2 Torr) and sequentially aligned and brought into contact.

Table 4-6. OOCv3-B printing parameters. The device was printed using resin vat V2 and build platform V3.

Resin	Z resolution	LED PWM	Burn-in layers	Burn-in exposure	Normal exposure	Z speed
	$[\mu\text{m}]$	$[\#]$	$[\#]$	$[\text{s}]$	$[\text{s}]$	$[\text{mm s}^{-1}]$
Deta x MP	50	30	5	6	0.75	0.125

To simplify alignment procedure, an aligner helper was designed in Autodesk Inventor[®] and fabricated laser cutting 6-mm thick PMMA. The device used 2- and 2.5-mm stainless-steel pins to align with holes replicated in the PDMS from the masters (**Figure 4-17-A**). After aligning the pins, the thin layer of PDMS was brought into contact with the previous layer through a sliding mechanism (**Figure 4-17-C**).

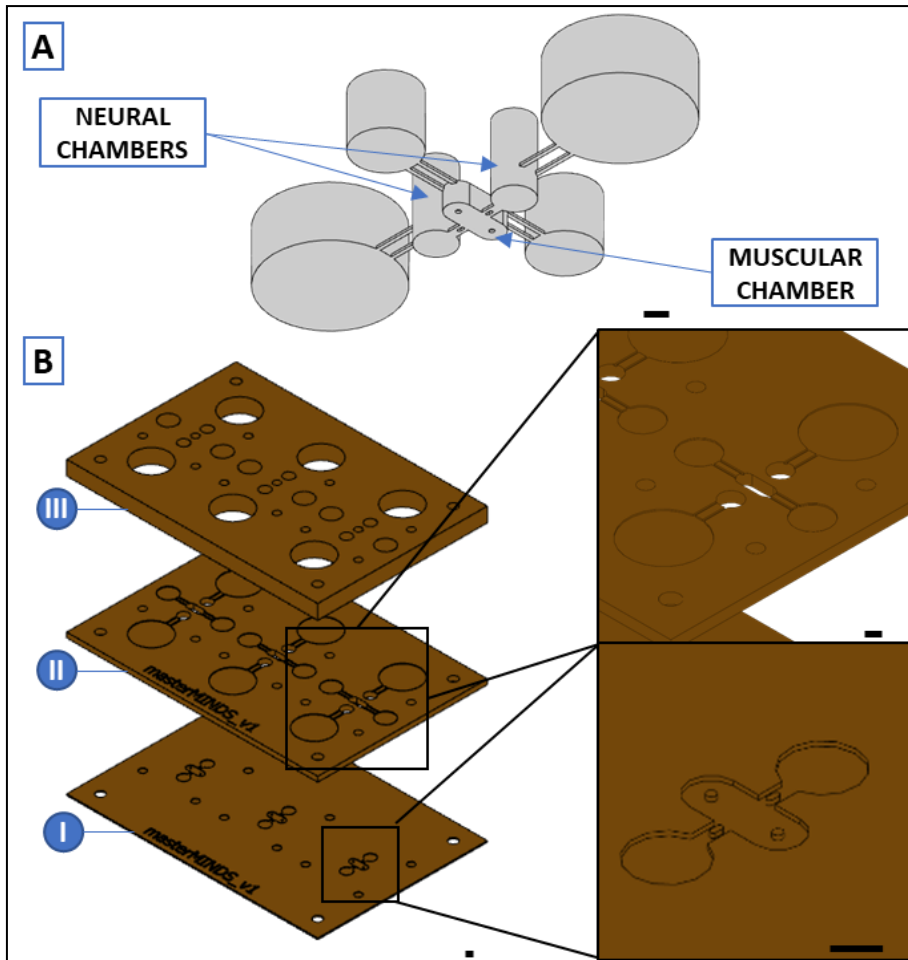


Figure 4-16. 3D multilayered compartmentalized device assembly. A) Fluidic 3D structure (interior of the channels) consisting of 2 neuronal chambers connected to a central muscular chamber with 2 PDMS posts for muscular cells alignment. Each chamber is connected to media reservoirs through microchannels located at an upper level; B) Exploded view of the three layers of PDMS forming the device. I) Lower level, including the interconnection of the channels and PDMS posts; II) Intermediate level, containing the interconnection between each chamber and its media reservoir; III) Upper level containing extra height for the media reservoirs. All scale bars are 2 mm.



Figure 4-17. PDMS aligning helper. After demolding, the PDMS layer was aligned with the stainless-steel pins (A) and flipped on top of previous PDMS layer, using the pins to align (B). Rigid PMMA layer is finally slid down (C) to bring the surface into contact without misalignment.

4.4 RESULTS

4.4.1 Improving the printer

After hardware and software modification to the 3D printer control system, all parameters involved in the printing process were accessible for inspection and modification. User web-interface enabled to change the parameter as well as to define new actions. Camera live streaming included in the interface enabled to check the active print job remotely and safely, as well as to check projector alignment and focus using test patterns. Thermocouples attached to the RUMBA board enabled to have feedback about printer parts (i.e. projector, resin).

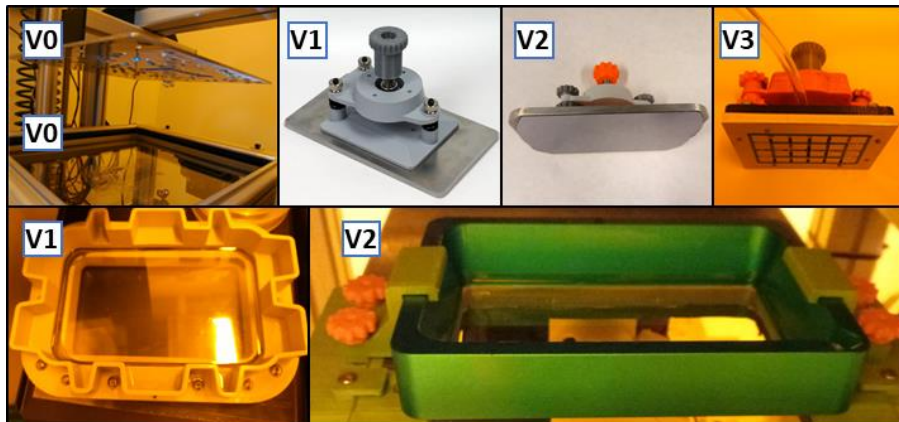


Figure 4-18. Different generation of build platforms and resin vats.

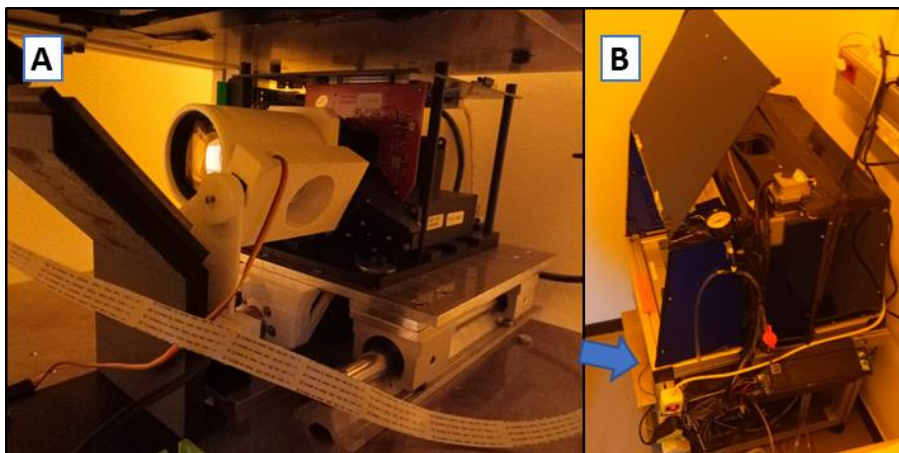


Figure 4-19. Final Printer setup. A) Detail the projector motorized focus system; B) General outlook of the printer.

Dimensions of all fabricated parts matched the original design and resulted in correct alignment. Vat size on V1 and V2 was effectively reduced.

After configuration and programming, UV projector functioned as required. Safety mechanism were tested successfully. UV projector focusing system (**Figure 4-19**) had theoretical movement resolution of $20\ \mu\text{m}$. UV projector irradiance curves are shown in **Figure 4-20**

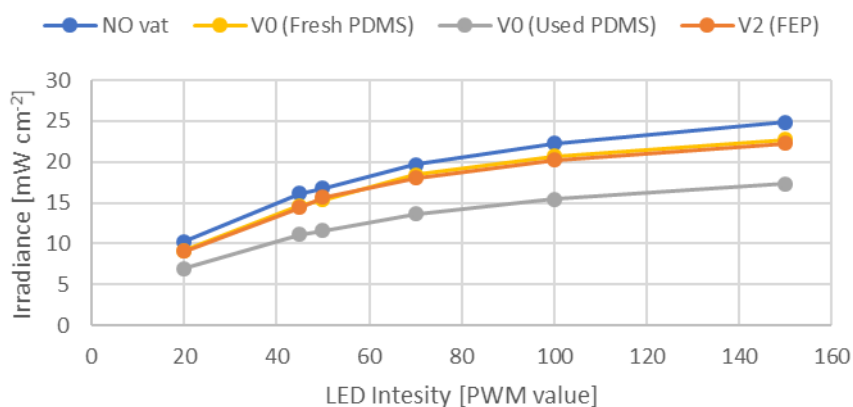


Figure 4-20. Projector irradiance profiles. V0 vat with PDMS shows a reduction of about 25 % due to ageing. V2 vat with FEP showed less than 1 % ageing reduction of irradiance for all the data points. Transmission efficiency of both systems freshly replaced is about 91 %.

. Both V2 (FEP) and V0 configuration with fresh PDMS show a mean irradiance reduction of about 9 % compared to the bare reading of the projector. Mean

difference between those two configurations was 1.07 %. PDMS V0 vat showed an extra mean reduction of 24.54 % due to aging after just a few prints (total mean reduction against no-vat readings: 30.98 %). V2 vat (not shown) after few prints showed mean difference of 0.78 %.

4.4.2 Calibration and resolution assessment

Measurement results of calibrations prints for feature resolution are reported in **Table 4-7**. XY mean error with final configuration was below pixel size and surface roughness was 1.12 μm .

Table 4-7. Feature resolution with different materials and configurations.

Resin used	Build Platform	Resin Vat	XY Mean error	XY error Standard Deviation	Z Mean error	Z error Standard Deviation
			$[\mu m]$	$[\mu m]$	$[\mu m]$	$[\mu m]$
Spot HT	V1	V0	410	49	57.1	49.8
Spot HT	V1	V1	59	18	24.7	28.8
Detax MP	V3	V2	13	23	8.3	1.12

Table 4-8. Channel array print success vs theoretical dimensions. Channels in green (✓) printed well and resulted in functional channels, channels in red (✗ ✗) were completely blocked by resin, channels in yellow (✗) showed some difficulties or were partially blocked. Letters inside some of the boxes refer to photos labeling in Figure 4-21.

Height\Width	1000	900	800	700	600	500	400	300
1000	✓	✓	✓	✓	✓	✓	✗	✗ c
800	✓	✓	✓	✗	✗	✗	✗ F	✗ ✗
600	✓ A,B	✗	✗	✗	✗	✗ D	✗ E	✗ ✗

After printing closed channel (cantilever) test model, only some of the channels were successfully cleared from residual resin during post-processing.

Table 4-8 resumes qualitatively overall printing results. Only two channels did not print at all, though not all the other could be completely cleaned from residual resin. Except for the two channels which did not print, lateral section images acquired with SEM were quantified to calculate mean and standard deviation values for width and height., reported in **Table 4-9**. **Figure 4-21** shows some of the acquired images. Particularly, different level of roughness can be observed between the roof (A), the bottom (B) and the lateral walls (C) of the channel.

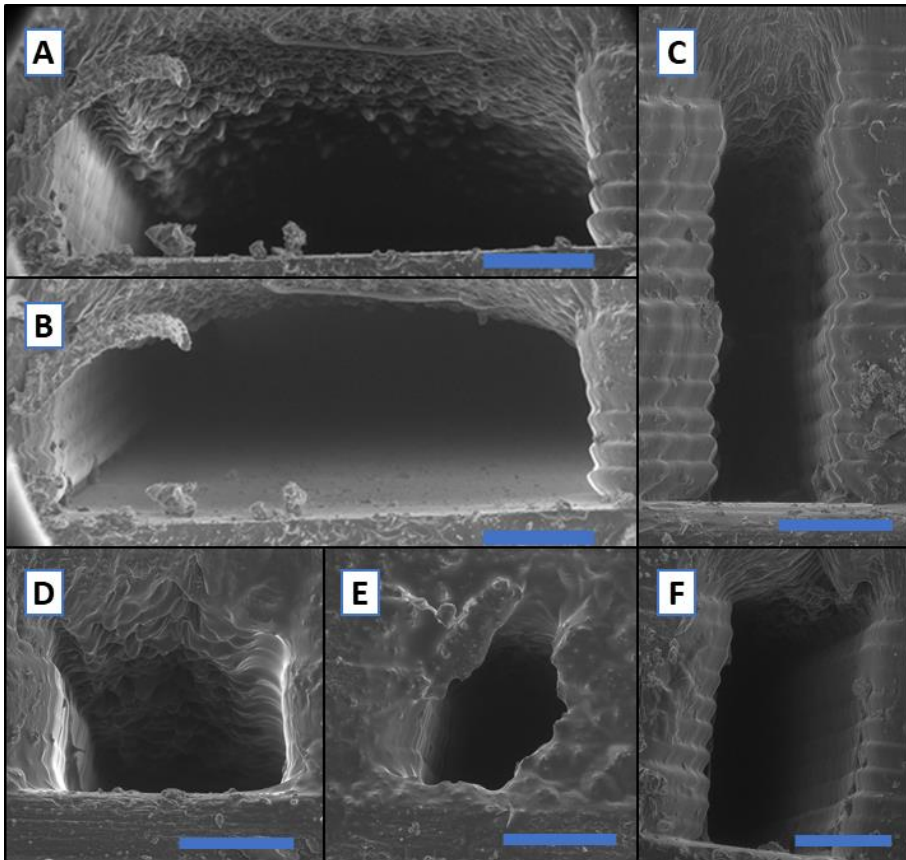


Figure 4-21. Closed channels printed using Spot HT resin and UV projector. A) Roof of a big channel (Dimensions: $976 \times 434 \mu\text{m}$) with visible surface roughness due to light filtering; B) Flat bottom of the same channel; C-F) Smallest channels measured. Dimensions: C) $209 \times 683 \mu\text{m}$ D) $390 \times 309 \mu\text{m}$; E) $237 \times 287 \mu\text{m}$ F) $318 \times 534 \mu\text{m}$. Scale bars are $200 \mu\text{m}$.

Table 4-9. Closed channel (cantilever) resolution assessment using Spot HT resin with UV projector, resin vat V2 and build platform V2.

Theoretical Height	Width mean error	Width error standard deviation	Height mean error	Height error Standard deviation
$[\mu m]$	$[\mu m]$	$[\mu m]$	$[\mu m]$	$[\mu m]$
1000	-21	32	-172	-63
800	-55	26	-208	67
600	-82	44	-234	48
OVERALL	-51	42	-203	65

4.4.3 Functional LOCs

Two different examples of functional LOC devices were printed successfully (**Figure 4-22**). Serpentine device was tested for laminar flow using two different ink solutions. Particle separation LOC was tested flowing microparticles. Quantification of cell separation efficiency is still in progress in the lab in another PhD thesis.

4.4.4 OOC applications

OOCv1-A membrane enclosed solution was successfully printed, assembled (**Figure 4-23-G**) and tested for leakage for 24 h at a flowrate of 2 mL min^{-1} .

OOCv1-B masters were successfully printed and replicated in PDMS (**Figure 4-23**). 3D print job of each layer took 20, 45 and 100 min for lower, middle and upper layer, respectively. Finally assembled device was successfully tested for leakage and hydrogels could be filled inside the chambers.

4.5 DISCUSSION

As illustrated in this chapter, before being able to start experimenting with novel OOC designs and ideas, lot of time was dedicated to improving the printer setup. All the improvements presented in this chapter were focused to improve printing process repeatability and accuracy, as well to unlock future possibilities for process expansion.

Switching resin vat from the old PDMS V0 brought many improvements. First, it enabled a more repeatable thickness of the first layer. Due to the spring-

loaded setup, the position of original V0 design used to vary each time the vat was removed (i.e. for cleaning or changing PDMS layer), introducing source of error. Both V1 and V2 version are secured directly to the printer structure while being easily removable for cleaning. Second, both V1 and V2 resin vat replaced PDMS with FEP film as release layer. As showed in **Figure 4-20**, aging of PDMS after few prints could result in 25 % reduction of light transmission, making this solution not desirable for a repeatable process with steady layer exposure. Inclusion of a glass bottom in V2 helped to avoid curved prints due to FEP film deformation. Finally, reduction of vat size helped reducing waste of resin material.

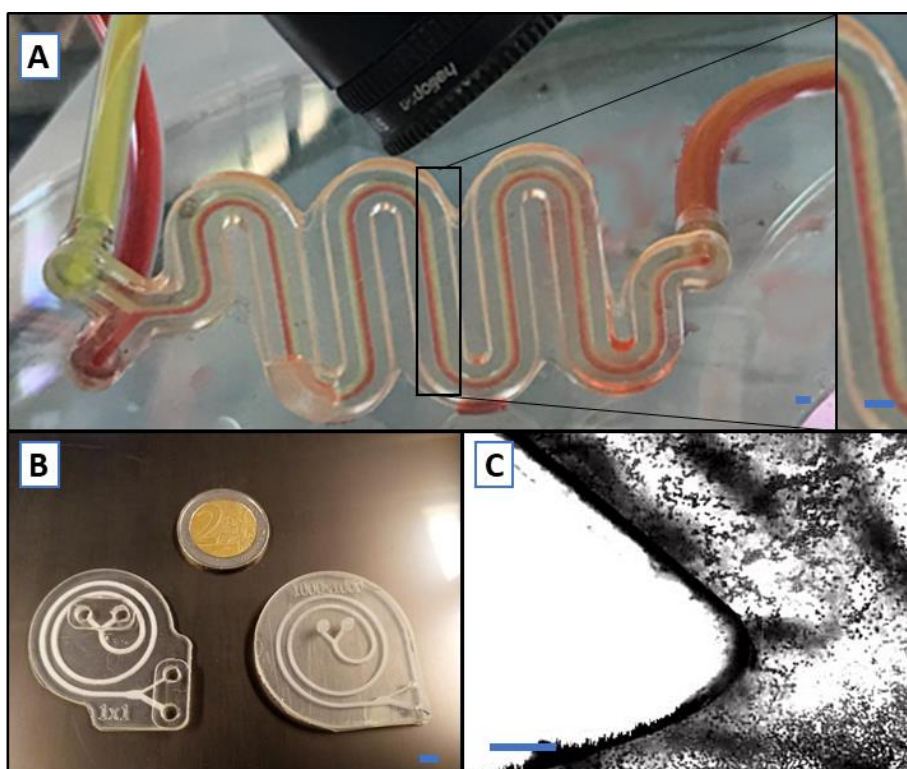


Figure 4-22. LOC devices printed with Spot HT resin and UV projector. A) Laminar flow serpentine (scale bars 1 mm); B) Particle separation LOC, both with (right) and without integrated connectors (left, scale bar 5 mm); C) Particle separation LOC microscope image during a test with microparticles (scale bar 200 μm).

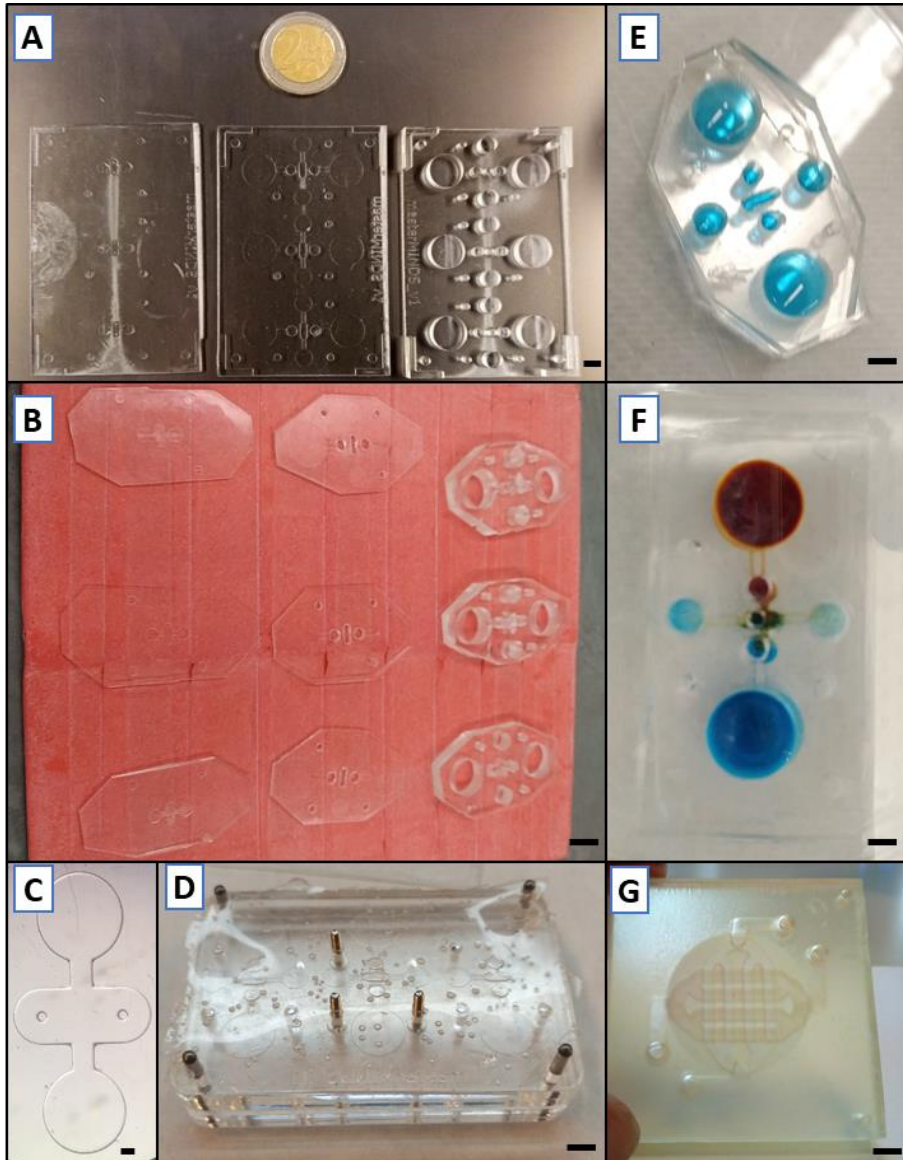


Figure 4-23. OOC devices fabricated using SL 3D printer. (Scale bars are 5 mm unless otherwise stated). A-F) Soft SL for multi-layered PDMS device fabrication; G) OOCv3 membrane embedded 3D printed device (Spot-HT). A) 3D-printed masters using Medicalprint transparent biocompatible resin; B) Several PDMS replicas (3 x layer) ready to assemble; C) Detail of layer 1 master (scale bar 500 μ m); D) Laser-cut support to simplify alignment of the different layers; E) Assembled device filled with ink solutions; F) Assembled device with Matrigel inside the chambers and filled with ink solution.

In parallel build platform iteration also brought important improvements. First, all designed solutions enabled easy alignment of build platform plane with the vat. Fast-release mechanism allowed for easy removal of the build platform while maintaining the alignment between the prints. Introducing flat and polished substrate (silicon wafer in V2 and glass slides in V3) allowed to incredibly reduce surface roughness of the print (see **Table 4-7** and **Figure 4-21-B**). Though results with silicon substrate (V2) had probably the best surface roughness, we finally opted for a more versatile solution where printing substrate could be easily replaced using a vacuum lock (V3). This, besides cutting down the cost per single substrate, enables a series of possible application reported in the future works section.

As can be observed in **Table 4-7**, build platform and vat modification resulted in improvement of the real resolution of the printer, as well as a decrease in surface roughness. Improvements to the projector also contributed, improving focus accuracy and reducing background exposure with a physical shutter. Like many entry-level printers in the market, to avoid exposure of the resin in the pause between layers the projector was simply switched to a black image before. To completely avoid lower intensity UV light to be still projected, a physical shutter is required.

Finally, the lower wavelength of the UV projector also benefits the resolution, especially when printing closed channels. Previous tests performed by our colleagues with Optoma projector never succeeded to print functional closed channels of $1 \times 1 \text{ mm}$ section or smaller. Lower wavelength (384 nm) resulted in smaller penetration depth across the resin, so we could achieve printing channels with measured hydraulic diameter down to $600 \mu\text{m}$ using the same resin (Spot HT) which had failed with the Optoma projector. Channels with measured hydraulic diameters in the $300\sim 600 \mu\text{m}$ range resulted in partial obstruction of the channels. It should be noted that the resolution error across Z-axis mainly arise from the problem of light penetrating across the resin when printing the roof of the channel. This hypothesis is confirmed by SEM imaging: **Figure 4-21** shows a huge difference in roughness between the roof (A) and the bottom of the channel (**Figure 4-21B**). Resin overexposure across layer resulted in a mean channel height error of $-203 \mu\text{m}$. Using resin optimized for 385-nm wavelength (like Detax Medicalprint used for OOCv3-B) should reduce light filtration, resulting in lower roughness and height error;

unfortunately, we had no time nor resin left to repeat the test with the new resin. Roughness could also impair microscopy observation; nonetheless, if low roughness is obtained at least in one side of the channel as well as in the corresponding outer wall of the print, microscope observation can be performed. That result was only possible upgrading the build platform with flat print substrates (V2, V3). Micro-scratches present in commercial build platforms were replicated by the resin, resulting in lower transparency of the printed models.

OOCv3-A demonstrate an example of possible DM hybrid strategies for fabrication of OOC devices. 3D printing the two layers enable separately enable to achieve low roughness on both upper and lower channel surfaces as well as simplifying post processing. Furthermore, printing the main structure enable to embed fluidic connectors into the device (i.e. Mini-Luer or $\frac{1}{4}$ -28 UNF female connectors). Sealing using pre-cut double-sided biocompatible adhesive enable easy integration of different kind of commercial membranes. A reprint using biocompatible resin and relative viability test of cell culture inside the device was not possible due to lack of available resin and time.

OOCv3-B demonstrate viability of SL as a tool for fabricating complex multi-layered PDMS microfluidic devices. SL has some advantages compared to traditional photolithography. Particularly, SL made possible to easy combine small microchannels (height $\sim 200 \mu m$) with taller reservoirs (few millimeters height), which would not have been possible with traditional soft lithography. Furthermore, SL drastically reduced both time and cost of masters fabrication. Print processes for OOCv3-B masters took between $20\sim 100 \text{ min}$ each, depending on master thickness, and the process was automated, requiring no user interaction during printing time. Post-processing time adds about 75 min per master, which might be reduced post-curing more masters at once. Additionally, post-processing time could be lowered to about 20 min per master using a professional curing unit, meaning the complete set of three masters might be printed and post-processed in less than four hours.

An actual limitation of SL compared to traditional photolithography for PDMS device fabrication is the current resolution of SL 3D printers. Just few UV 3D printers in the market can go below $50 \mu m$ pixel size and to which you should add the XY error (mean value $13 \mu m$ in our best configuration). Nonetheless, XY resolution of UV projectors has just started to be optimized and practically

every projector in the market depends on Texas Instruments DMD devices. We expect big improvements in SL resolution in the next coming years, due to improvements both in DLP projectors as well as in the materials.

4.6 CONCLUSIONS

In this chapter we have improved a SL 3D printer to enable its use for microfluidics application and we explored some possibilities for OOC fabrication through 3D printing.

Both XY and Z resolution of the printer where improved, achieving a mean dimensional error of $13\ \mu\text{m}$ in XY and $8.3\ \mu\text{m}$ in Z. Estimated roughness of flat printed surface was reduced to $1.12\ \mu\text{m}$.

We achieved optimal printing of closed channels down to hydraulic diameter of $600\ \mu\text{m}$ and partial obstruction in the range of $300\sim 600\ \mu\text{m}$. Same test with optimal resin is expected to further lower this value.

We demonstrated an easy solution for embedding commercial membranes in 3D printed OOC devices. Joining 3D printing with laser cut techniques, we were able to produce leakage-free device with embedded connectors.

We also demonstrated the viability of SL as an additional tool for PDMS multi-layered soft lithography. The proposed solution enables to fabricate device with diverse feature heights while drastically reducing costs, time and human interaction required for fabrication. To the best of our knowledge, there are no reported works of multilayered PDMS devices achieved by molding from SL-printed masters. Cell culture experiment on OOCv3-B are still ongoing.

4.7 REFERENCES

1. Bhattacharjee, N., Urrios, A., Kang, S. & Folch, A. The upcoming 3D-printing revolution in microfluidics. *Lab on a Chip* **16**, 1720–1742 (2016).
2. Wu, C., Yi, R., Liu, Y. J., He, Y. & Wang, C. C. L. Delta DLP 3D printing with large size. in *IEEE International Conference on Intelligent Robots and Systems 2016-Novem*, 2155–2160 (IEEE, 2016).
3. S. Scott Crump. Apparatus and method for creating three-dimensional objects. (1989).
4. Naderi, A., Bhattacharjee, N. & Folch, A. Digital Manufacturing for Microfluidics. *Annu. Rev. Biomed. Eng.* **21**, 325–364 (2019).
5. Waheed, S. *et al.* 3D printed microfluidic devices: Enablers and barriers. *Lab on a Chip* **16**, 1993–2013 (2016).
6. Hull, C. StereoLithography: Plastic prototypes from CAD data without tooling. *Mod. Cast.* (1988).
7. Andre, J.-C., Le Mehaute, A. & De Witte, O. Dispositif pour realiser un modele de piece industrielle. (1984).
8. Waldbaur, A., Rapp, H., Länge, K. & Rapp, B. E. Let there be chip - Towards rapid prototyping of microfluidic devices: One-step manufacturing processes. *Anal. Methods* **3**, 2681–2716 (2011).
9. Capel, A. J. *et al.* Design and additive manufacture for flow chemistry. *Lab Chip* (2013). doi:10.1039/c3lc50844g
10. Macdonald, N. P. *et al.* Comparing Microfluidic Performance of Three-Dimensional (3D) Printing Platforms. *Anal. Chem.* **89**, 3858–3866 (2017).
11. Au, A. K., Lee, W. & Folch, A. Mail-order microfluidics: evaluation of stereolithography for the production of microfluidic devices. *Lab Chip* **14**, 1294–1301 (2014).
12. Fang, N., Sun, C. & Zhang, X. Diffusion-limited photopolymerization in scanning micro-stereolithography. *Appl. Phys. A Mater. Sci. Process.* (2004). doi:10.1007/s00339-004-2938-x
13. Urrios, A. *et al.* 3D-printing of transparent bio-microfluidic devices in PEG-DA. *Lab Chip* **16**, 2287–2294 (2016).
14. Gong, H., Beauchamp, M., Perry, S., Woolley, A. T. & Nordin, G. P. Optical approach to resin formulation for 3D printed microfluidics. *RSC Adv.* **5**,

106621–106632 (2015).

15. Guo, Y., Ji, Z., Zhang, Y., Wang, X. & Zhou, F. Solvent-free and photocurable polyimide inks for 3D printing. *J. Mater. Chem. A* **5**, 16307–16314 (2017).
16. Cui, K.-J. *et al.* Blue laser diode-initiated photosensitive resins for 3D printing. *J. Mater. Chem. C* **5**, 12035–12038 (2017).
17. Bertsch, A., Heimgartner, S., Cousseau, P. & Renaud, P. Static micromixers based on large-scale industrial mixer geometry. *Lab Chip* (2001). doi:10.1039/b103848f
18. Miller, P. R. *et al.* Integrated carbon fiber electrodes within hollow polymer microneedles for transdermal electrochemical sensing. *Biomicrofluidics* (2011). doi:10.1063/1.3569945
19. Lee, W. *et al.* Ultrarapid Detection of Pathogenic Bacteria Using a 3D Immunomagnetic Flow Assay. *Anal. Chem.* **86**, 6683–6688 (2014).
20. Lee, W. *et al.* 3D-Printed Microfluidic Device for the Detection of Pathogenic Bacteria Using Size-based Separation in Helical Channel with Trapezoid Cross-Section. *Sci. Rep.* **5**, 7717 (2015).
21. Shallan, A. I., Smejkal, P., Corban, M., Guijt, R. M. & Breadmore, M. C. Cost-Effective Three-Dimensional Printing of Visibly Transparent Microchips within Minutes. *Anal. Chem.* **86**, 3124–3130 (2014).
22. Kanai, T. & Tsuchiya, M. Microfluidic devices fabricated using stereolithography for preparation of monodisperse double emulsions. *Chem. Eng. J.* **290**, 400–404 (2016).
23. Zhang, J. M., Li, E. Q., Aguirre-Pablo, A. A. & Thoroddsen, S. T. A simple and low-cost fully 3D-printed non-planar emulsion generator. *RSC Adv.* **6**, 2793–2799 (2016).
24. Femmer, T. *et al.* High-Throughput Generation of Emulsions and Microgels in Parallelized Microfluidic Drop-Makers Prepared by Rapid Prototyping. *ACS Appl. Mater. Interfaces* **7**, 12635–12638 (2015).
25. Patrick, W. G. *et al.* DNA assembly in 3D printed fluidics. *PLoS One* (2015). doi:10.1371/journal.pone.0143636
26. Brennan, M. D., Rexus-Hall, M. L. & Eddington, D. T. A 3D-printed oxygen control insert for a 24-well plate. *PLoS One* (2015). doi:10.1371/journal.pone.0137631
27. Robinson, C. D., Auchtung, J. M., Collins, J. & Britton, R. A. Epidemic

- Clostridium difficile strains demonstrate increased competitive fitness compared to nonepidemic isolates. *Infect. Immun.* (2014). doi:10.1128/IAI.01524-14
28. Chan, H. N. *et al.* Simple, Cost-Effective 3D Printed Microfluidic Components for Disposable, Point-of-Care Colorimetric Analysis. *ACS Sensors* (2016). doi:10.1021/acssensors.5b00100
 29. Lee, Y. S., Bhattacharjee, N. & Folch, A. 3D-printed Quake-style microvalves and micropumps. *Lab Chip* (2018). doi:10.1039/c8lc00001h
 30. Au, A. K., Bhattacharjee, N., Horowitz, L. F., Chang, T. C. & Folch, A. 3D-printed microfluidic automation. *Lab Chip* (2015). doi:10.1039/c5lc00126a
 31. Gong, H., Woolley, A. T. & Nordin, G. P. High density 3D printed microfluidic valves, pumps, and multiplexers. *Lab Chip* (2016). doi:10.1039/c6lc00565a
 32. Gong, H., Beauchamp, M., Perry, S., Woolley, A. T. & Nordin, G. P. Optical approach to resin formulation for 3D printed microfluidics. *RSC Adv.* (2015). doi:10.1039/c5ra23855b
 33. Rogers, C. I., Qaderi, K., Woolley, A. T. & Nordin, G. P. 3D printed microfluidic devices with integrated valves. *Biomicrofluidics* (2015). doi:10.1063/1.4905840
 34. Rogers, C. I. *et al.* Microfluidic valves made from polymerized polyethylene glycol diacrylate. *Sensors Actuators, B Chem.* (2014). doi:10.1016/j.snb.2013.10.008
 35. Gong, H., Woolley, A. T. & Nordin, G. P. 3D printed high density, reversible, chip-to-chip microfluidic interconnects. *Lab Chip* **16**, 1–218 (2018).
 36. Bhattacharjee, N., Parra-Cabrera, C., Kim, Y. T., Kuo, A. P. & Folch, A. Desktop-Stereolithography 3D-Printing of a Poly(dimethylsiloxane)-Based Material with Sylgard-184 Properties. *Adv. Mater.* **30**, 1–7 (2018).
 37. Kim, Y., Castro, K., Bhattacharjee, N. & Folch, A. Digital Manufacturing of Selective Porous Barriers in Microchannels Using Multi-Material Stereolithography. *Micromachines* **9**, 125 (2018).
 38. Kuo, A. P. *et al.* High-Precision Stereolithography of Biomicrofluidic Devices. *Adv. Mater. Technol.* **4**, 1800395 (2019).
 39. Kim, Y. T., Bohjanen, S., Bhattacharjee, N. & Folch, A. Partitioning of

- hydrogels in 3D-printed microchannels. *Lab Chip* **19**, 3086–3093 (2019).
40. Hwang, Y. *et al.* Capillary Flow in PDMS Cylindrical Microfluidic Channel Using 3-D Printed Mold. *J. Microelectromechanical Syst.* **25**, 238–240 (2016).
 41. Costa, P. F. *et al.* Mimicking arterial thrombosis in a 3D-printed microfluidic: In vitro vascular model based on computed tomography angiography data. *Lab Chip* **17**, 2785–2792 (2017).
 42. Glick, C. C. *et al.* Rapid assembly of multilayer microfluidic structures via 3D-printed transfer molding and bonding. *Microsystems Nanoeng.* **2**, 1–9 (2016).
 43. Raspberry Pi Foundation. Raspberry Pi®. Available at: <https://www.raspberrypi.org/>.
 44. Stallman, R. GNU General Public License 2.0. *Free Software Foundation* (1991). Available at: <https://www.gnu.org/licenses/old-licenses/gpl-2.0.en.html>.
 45. NanoDLP. Available at: www.nanodlp.com.
 46. Marlin firmware. Available at: www.marlinfw.org.
 47. Stallman, R. GNU General Public License 3.0. *Free Software Foundation* (2007). Available at: <https://www.gnu.org/licenses/gpl-3.0.html>.
 48. Mir-García, M. 3D-printed microfluidic devices inspired in a CTCs isolation technique. (Universitat de Barcelona, 20

5 Automating experimental set-up for OOC applications: integrating the chip into the lab

5.1	BACKGROUND	118
5.1.1	BOTTLENECKS TO A BROADER IMPACT	118
5.1.2	TEER ELECTRODES INTEGRATION AND ELECTRICAL CONNECTIONS.....	120
5.2	SPECIFIC OBJECTIVES OF THE CHAPTER.....	121
5.3	MATERIALS AND METHODS	122
5.3.1	MATERIALS AND FACILITIES	122
5.3.2	IMPROVING OOC DESIGN (OOC v2.1)	122
5.3.3	EMBEDDED FLOW CONTROL SYSTEM	124
5.3.4	INTEGRATED SENSORS FABRICATION (OOC v2.2)	126
5.4	RESULTS.....	129
5.4.1	IMPROVING OOC DESIGN	129
5.4.2	EMBEDDED FLOW CONTROL SYSTEM	129
5.4.3	INTEGRATED TEER SENSORS FABRICATION	131
5.5	DISCUSSION	132
5.6	CONCLUSIONS	133
5.7	REFERENCES	135

Previous chapters explored some DM and RP techniques for manufacturing of OOC devices. Between various benefits of DM techniques, chapters 3 and 4 evidenced the possibility to integrate standard connectors directly into the design. Integration is indeed a big potential for DM tools, which could simplify both fabrication and final user experience through smart choice during digital design. This chapter will focus on additional improvements to OOCv2.0. After an overview of the so-called “World-to-chip” problem, various improvements for previously developed device will be designed and manufactured.

Particularly, a set of integrated reservoirs and high-pressure connectors and an array of interdigitated electrodes for TEER measurement will be integrated into OOCv2.0 device and a complete, compact, low cost flow control system will be developed.

Results will be discussed before proceeding to the final part of the thesis where all developed technologies will be applied.

Collaborations: The work presented in this chapter was achieved in collaboration with PhD student Davide Di Giuseppe and his supervisor Prof. Eugenio Martinelli, from Sensors group of Rome Tor Vergata University.

5.1 BACKGROUND

5.1.1 Bottlenecks to a broader impact

Both OOC and LOC devices represents a very fast-moving field which is starting to shift from academic proof-of-concept studies to real-world solutions. As previously discussed, introducing DM and RP seems an important step to increase OOC impact and adoption in research, reducing time and costs associated with design and fabrication. In parallel some usability bottlenecks, often referred in the literature as the “chip-in-the-lab vs lab-on-chip” argument¹⁻³, should be addressed. **Figure 5-1** gives a straightforward idea of the usability problem: despite the promise of volumes reduction and automation, most published OOC works usually do not show the full picture. OOC devices end up being miniaturized chips in an expensive lab environment. Complex, costly and hard-to-reproduce experimental setups made of tubing, connections, pumps and cables often requires an engineering expertise which usually lacks in biomedical laboratories⁴. This affect usability and reproducibility of the results. Chip-in-a-lab problem can be addressed both by simplifying the interfacing to external setups as well as by integrating control systems or sensing functionality in simplified low-cost portable solutions.

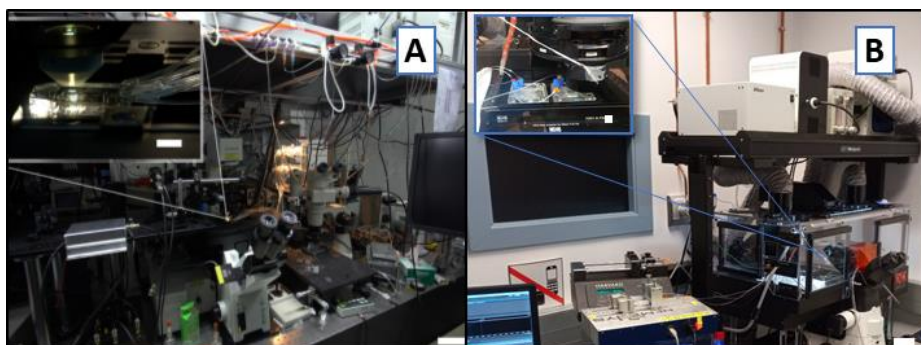


Figure 5-1. Chip in a lab. A) A microfluidic chip (inset) in a laboratory. The scale bars are 10 cm and 1 cm (inset). Reproduced with permission from [Streets, A. M. & Huang, Y., 2013](#)². B) Similar microfluidic setup in our lab and the microfluidic devices (inset).

5.1.1.1 World-to-chip connection

In the previous chapters we discussed various bonding techniques, because high quality sealing is one of the most important characteristics for a microfluidic device, and thus for any OOC. Nonetheless, high-quality sealing is worthless without a reliable fluidic interface between the chip and the “outer world” devices, such as pumps, tubing, etc. Those “world-to-chip” connections, often neglected in the microfluidics community, are typically the least reliable components of a microfluidic device, limiting its overall performance³. Furthermore, in long-term experiments involving cell culture, any leakage problem would result in a catastrophic outcome not only for experiment or sample involved, but also for the integrity of expensive microscopy setup involved. For an extensive review of microfluidic connectors solutions, we suggest reading of Temiz, Y. et al, 2015³, which classify published solutions into 4 categories: (1) reversible insertion of micro-needles or tubes into holes drilled or etched on the chip surface or edge, (2) reversible fluidic connection with direct contact to the surface of the device by compression sealing, (3) application of an adhesive to achieve a high strength and permanent interface, and (4) mono-lithic integration of microfluidic ports³. A more recent approach used 3D printing and ultrasonic welding to incorporate different type of connectors⁵.

5.1.1.2 Integrated control systems for microfluidics

In the scientific world nowadays, open source hardware and software are already considered “a giant’s shoulder”^{6,7} which can help reducing cost of microfluidic-related equipment. Lowering startup costs might encourage early adoption of OOC technologies in standard biomedical laboratories. Similar examples are already present in other fields of literature, from open source real-time polymerase chain reaction (PCR) kit (<https://openpcr.org/>) priced at 499\$⁸ to the “FlyPi”, a 100€ 3D printed open-source platform for fluorescence microscopy and optogenetics, including heat control of the measuring area⁹.

Most examples in the field of microfluidics mainly involve open-source control of fluidic system. Different approaches included open source syringe pumps^{10,11}, feedback-controlled syringe pressure pumps¹², programmable solenoid valves¹³ and pressure sources¹⁴ up to an all-in-one microfluidics control system¹⁵.

Though most design reduce costs and offer modularity, they still often do not achieve substantial size reduction. In that direction, we would like to remark one work which addressed size reduction with an approach similar to the one we followed in this chapter. The work, published in in October 2018¹⁶ during the final testing of our prototype, propose the usage of piezoelectric peristaltic micropumps controlled by a microcontroller.

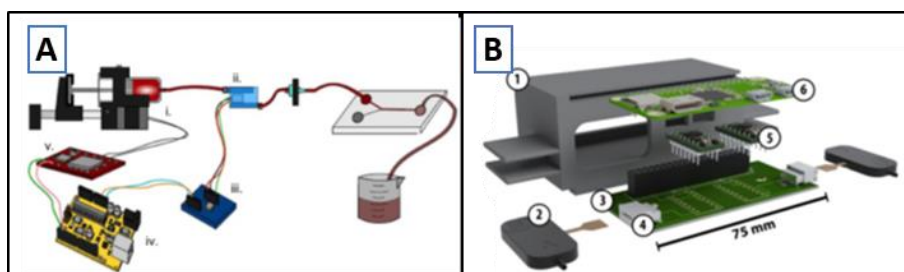


Figure 5-2. Integrated flow control systems for microfluidics. A) Low-cost feedback-controlled syringe pressure pump system (Reproduced from [Lake et al., 2017](#)¹²), including: i) a stepper motor; ii) a piezoresistive pressure sensor; iii) an instrumentation amplifier; iv) an Arduino Board; v) stepper motor driver; B) PiFlow, a low cost programmable flow system (Reproduced from [Kassis et al., 2018](#)¹⁶, under [Creative Commons Attribution-NonCommercial-No Derivatives License](#)), including: 1) 3D printed case; 2) commercial MP6 piezoelectric micropumps; 3) custom PCB; 4) pump connectors; 5) commercially available driving circuits; 6) commercially available Raspberry Pi Zero computer.

5.1.2 TEER electrodes integration and electrical connections

TEER is a valuable method for assaying in vitro barrier tissue integrity¹⁷. Epithelial cells form electrically tight barrier layers, whereby ‘electrically tight’ means that the tight junctions prevent the passage of ion currents along a paracellular pathway¹⁸. TEER measurement is a reliable indicator of the development of functional tight junctions¹⁹. Literature reports several solutions to enable on-chip TEER measurements, from insertion of small diameter electrodes inside the apical and basal channels^{20,21} to direct integration of electrodes into the device²²⁻²⁵.

Although various fabrication techniques are available for high-resolution patterning of electrodes on common substrates used in microfluidics (e.g. silicon, glass, plastics, PDMS, and paper), the necessity of electrical interfacing in addition to fluidic connections brings additional reliability issues, fabrication challenges, and packaging costs³. In many OOC applications, the chips are used only once to avoid cross-contamination between samples so electrical

connections, as well as fluidic connections, should preferably be non-permanent and easily pluggable³.

A few companies, including Micronit Microfluidics (The Netherlands)²⁶ and microLIQUID (Spain)²⁷, produce chip holders that provide both fluidic and electrical connections, but these are compatible with only a limited number of devices or applications³. Literature also reports examples of custom holders and card-edge sockets as non-permanent electrical connection solutions.

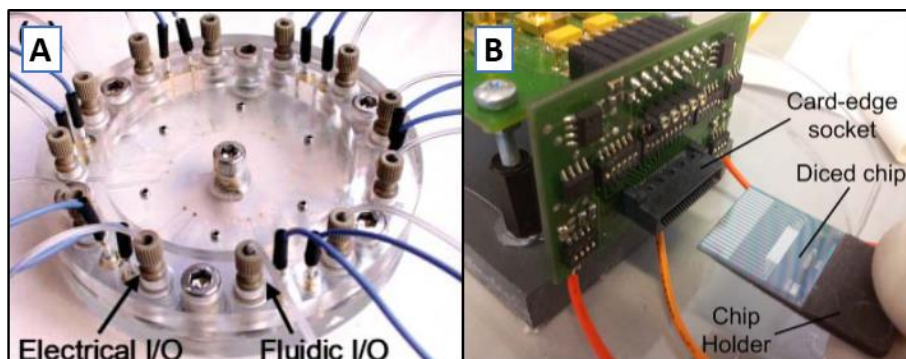


Figure 5-3. Non-permanent electrical connections for microfluidic devices. A) Custom holder solution integrating electrical and fluidic connections; Image reproduced from [Park et al., 2006](#)²⁸ by RSC permission; B) Card-edge connection solution²⁹; Image reproduced from [Temiz et al., 2012](#)²⁹ by RSC permission.

5.2 SPECIFIC OBJECTIVES OF THE CHAPTER

This chapter will focus on improving the previously developed OOCv2.0 device, enhancing its versatility. As overviewed in the introduction, there is no defined standard regarding world-to-chip connections. Furthermore, literature just shows few integrated solutions aimed to simplify microfluidics setups, which leaves room for improvements on that side.

In this chapter we will particularly address those specific objectives:

1. to address the fluidic world-to-chip interface problem with a versatile solution which is compatible with the DM process illustrated in Chapter 3;
2. to design and fabricate integrated electrodes for TEER measurements using a fabrication technique compatible with the original DM process and providing easy and non-permanent electrical interfacing solution;

3. to design and fabricate a portable fluidic setup which could be embedded in a portable platform, aimed to simplify laboratory setups and experimental procedures.

5.3 MATERIALS AND METHODS

5.3.1 Materials and Facilities

2-propanol (IPA, 99.8 %, ACS grade, 31090.1212), EtOH (96 %, ACS grade, 131085.1212) were purchased from PanReac – ITW reagents (Barcelona, Spain). Polycarbonate (PC) transparent membranes (Model 9100-4710, pore size $1\ \mu\text{m}$, thickness $10\ \mu\text{m}$, Whatman) were purchased from Sigma-Aldrich (St. Louis, MO USA). COP sheets (Zeonor® 1420R, thickness $180\ \mu\text{m}$) were purchased from Zeon Corporation (Tokyo, Japan). PMMA (clear, thicknesses 3, 6, 8 mm) was from Trotec Laser Inc. (Marchtrenk, Austria) Double sided biocompatible PSA (ARSeal® 8026) was supplied from Adhesive Research, Inc. (Glen Rock, PA USA). 467MP PSA was purchased from 3M™ (Maplewood, MN USA). Molex Zero Injection Force (ZIF) standard connectors (52271-1679) were purchased from Molex (Lisle, IL USA). TFA etchant was purchased from Transene Co Inc (Danvers, MA USA). AZ® 5214-E photoresist, AZ® 400K Developer and AZ® 100 Remover were purchased from Microchemicals GmbH (Ulm, Germany). Mini-Luer® connectors were purchased from ChipShop (Jena, Germany). Tygon tubing (Tygon ND-100-80, ID: $0.51\ \text{mm}$, OD: $1.59\ \text{mm}$) was from Cole Parmer (Vernon Hills, IL USA). Piezoelectric micropumps MP6 and respective MP6-OEM drivers were purchased from Bartels Mikrotechnik GmbH (Dortmund, Germany).

Photolithographic processes described in this chapter were performed both the IBEC MicroFabSpace and at the clean room facility of the Institute for Photonics and Nanotechnologies (IFN), Italian National Research Center (CNR), in Rome. Except if otherwise specified, all laser processing was performed at Department of Electronic Engineering, University of Rome Tor Vergata.

5.3.2 Improving OOC design (OOC v2.1)

Starting from OOC V2.0, we designed a series of added features to improve device versatility for different kind of experiments.

5.3.2.1 Adding threaded connector

We designed an extra layer of PMMA with four ¼-28 Unified National Fine (UNF) threaded female connectors aligned with inlet/outlets. 467MP PSA was laminated on top of PMMA layer and laser cut to size. ¼-28 UNF threads are formed using a threading plug tap. Threaded layer is aligned to preassembled OOC v2.0 using the previously described aluminum aligner and pressed using $2 \cdot 10^6$ kg for 30 s. Silicone O-rings (ID: 2.6 mm, OD: 5 mm, thickness: 1.2 mm) can be added in each cavity to improve sealing.

5.3.2.2 Adding media reservoirs

Starting from previous design, we designed a second extra layer of PMMA featuring 4 open reservoirs (one for each inlet/outlet) which enables static culture. Through CAD, reservoirs were carefully designed to not add material in the central membrane area interested to microscope observation and not to hinder the connection of ¼-28 UNF connectors. An optional PMMA lid (thickness 3 mm) was also designed, in order to prevent evaporation and contamination of the medium.

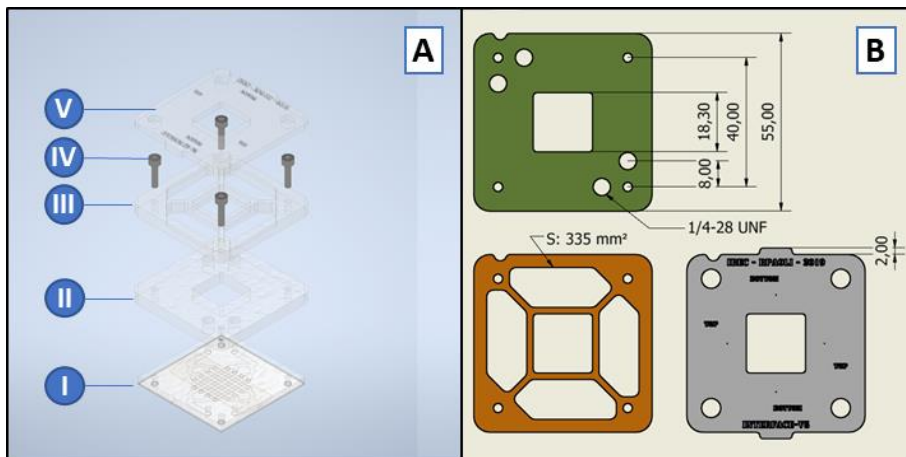


Figure 5-4. OOC Design v2.1. A) Exploded view of the assembly: I) OOC v2.0 device; II) ¼-28 threaded connectors layer (PMMA); III) Media reservoirs layer (PMMA); IV) Metric Socket head screws; V) Top lid (PMMA) used to close the reservoirs; B) Main dimensions of the added layers in OOC v2.1.

5.3.2.3 Custom microscope holders

Custom OOC holders with tight tolerances were designed using Autodesk Inventor to fit our microscope incubators and to secure the OOC for repeatable positioning in time-lapse imaging using computer controlled XYZ stage.

Holders were printed on a Fused Deposition Modeling (FDM) 3D printer using PLA (Z resolution 300 μm , nozzle diameter 400 μm).

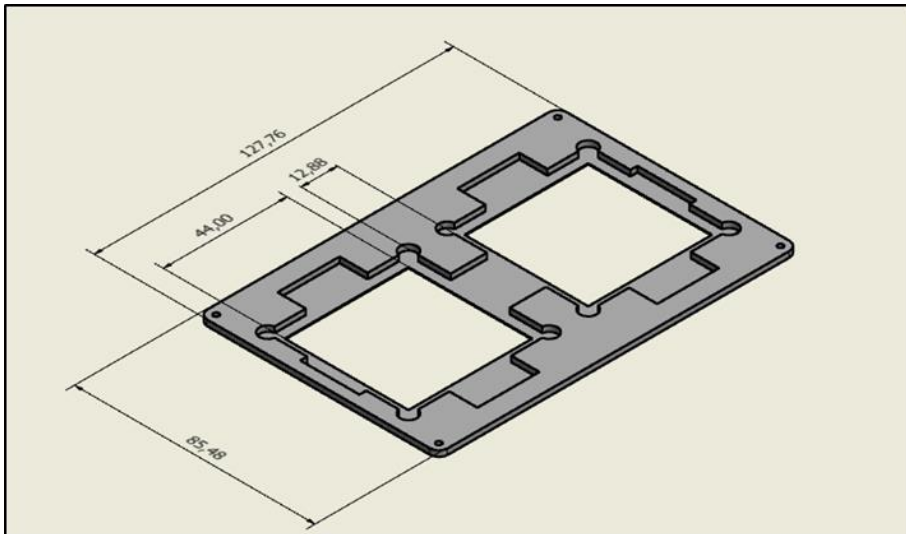


Figure 5-5. Custom microscope holder sized to standard microtiter plate dimensions.

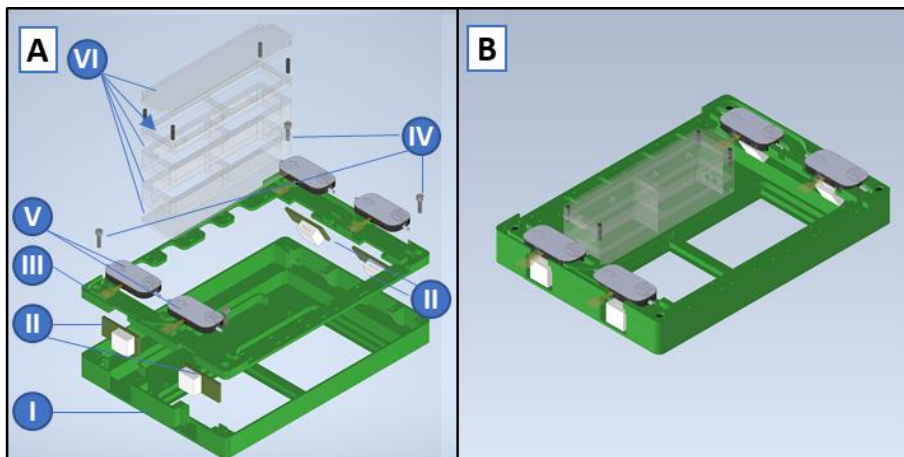


Figure 5-6. Design concept of the Embedded flow control system. A) Exploded view of the experimental block, including a base block (I), micropumps connectors (II) embedded under the top cover (III), which is secured with screws (IV). Micropumps (V) can be later connected and secured on top thanks to tight tolerance embossed shapes. A preassembled PMMA media reservoir (VI) is also secured to base block thanks to recessed profile. B) Assembled device.

5.3.3 Embedded flow control system

We designed a complete experimental setup with embedded flow control system to fit into our microscope mini-incubator. The system consists of a

compact experimental unit, which fits into the mini-incubator (**Figure 5-6**), and an external electronic control system.

5.3.3.1 Portable experimental unit

The portable experimental unit consists of a system holder which hosts two OOC devices, 4 removable MP6 micropumps, MP6 pumps electrical connectors, cable routing to a single connector, PMMA media reservoirs for recirculating flow and recessed guides for tubing in order to avoid changes in pressure due to tubing displacement.

PMMA reservoirs were made stacking together precut hollow layers to a flat base (thickness 3 mm). PSA was applied to PMMA, layers were cut to shape and pressed together. Holes for Tygon tubing were drilled into the walls using an electric drill.

System holder was designed in Autodesk Inventor based on OOC model, connectors and incubator dimensions, and was 3D printed in PLA (Z resolution 300 μm , nozzle diameter 400 μm).

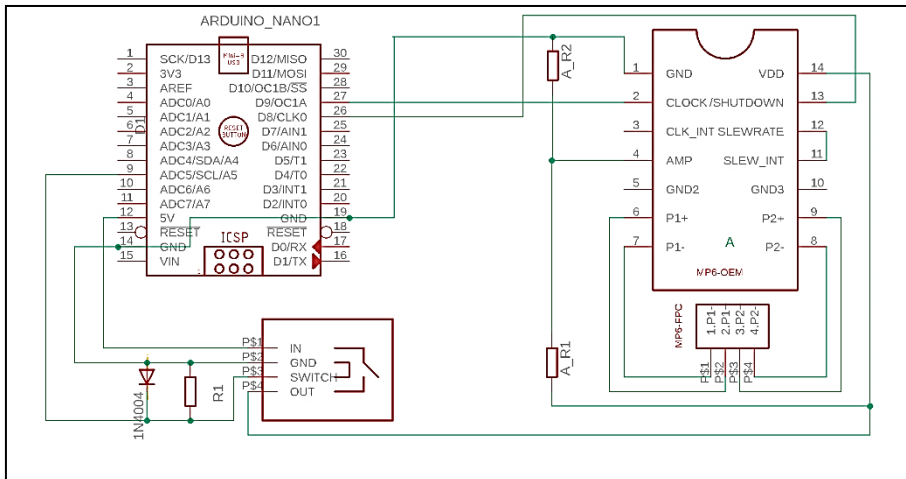


Figure 5-7. Basic schematic of the electronic flow control system for one pump. Arduino controls the MP6-OEM driver through PWM port; Full circuit consist of four MP6-OEM.

5.3.3.2 Small footprint external flow control

An external flow control electronic circuit based on Arduino Nano was designed and tested with solderless breadboard (**Figure 5-7**). MP6-OEM driver modules from Bartels® enable to drive the pump regulating stroke amplitude and frequency parameters. Amplitude is set using the AMPLITUDE pin, setting

the pin voltage. Frequency is set using the CLOCK pin, with a PWM signal. Arduino® Nano³⁰ allow control of PWM output values in response to commands received through the serial interface. We designed a shield with this purpose. Amplitude is fixed (independently) for each channel using a separate voltage divider.

A preliminary prototype of the circuit was fabricated hand-soldering components to a prototype board. Finally, the design was implemented in Autodesk Eagle, traces were routed and Printed Circuit Board (PCB) layers were exported and sent to an online service for final fabrication. Components were hand-soldered to the PCB. The board fits the Arduino® Nano³⁰ and 4 MP6-OEM modules in removable sockets and 4 MP6 connectors in a $50 \times 50 \text{ mm}$ footprint. Flexible flat cables were used to interface with the experimental block.

The device can be attached to a computer through a USB cable, identifying as a virtual serial port. Sending commands through the serial port, flow through the 4 pumps can be controlled. MP6 pumps stoke amplitude is fixed by the choice of the onboard resistors, and two different pumping frequencies can be controlled through the Arduino. The actual PCB design enable to drive 4 semi-independent flows configuration.

5.3.4 Integrated sensors fabrication (OOC v2.2)

5.3.4.1 OOC v2.2 sensor design

An array of concentric interdigitated electrodes for TEER was designed in Autodesk Inventor (**Figure 5-8**) and exported to DXF format. Each of the 16 channel intersections features two pairs of electrodes, one on the roof of the upper channel and one on the floor of the bottom channel. Interdigitated electrodes have $25 \mu\text{m}$ concentric fingers, radially spaced by $25 \mu\text{m}$. Inner circle diameter is $100 \mu\text{m}$, outer circumference diameter is 1.6 mm . Electrodes are routed to two opposite external flaps which protrude from the final assembly and are sized according to industry standard 1 mm pitch ZIF connectors. Taking advantage of a clever design, routing traces are insulated using the channel layers, without need for extra passivation procedures.

5.3.4.2 OOC v2.2 manufacturing

Chrome mask was fabricated by Direct Write Laser at IBEC MicroFabSpace.

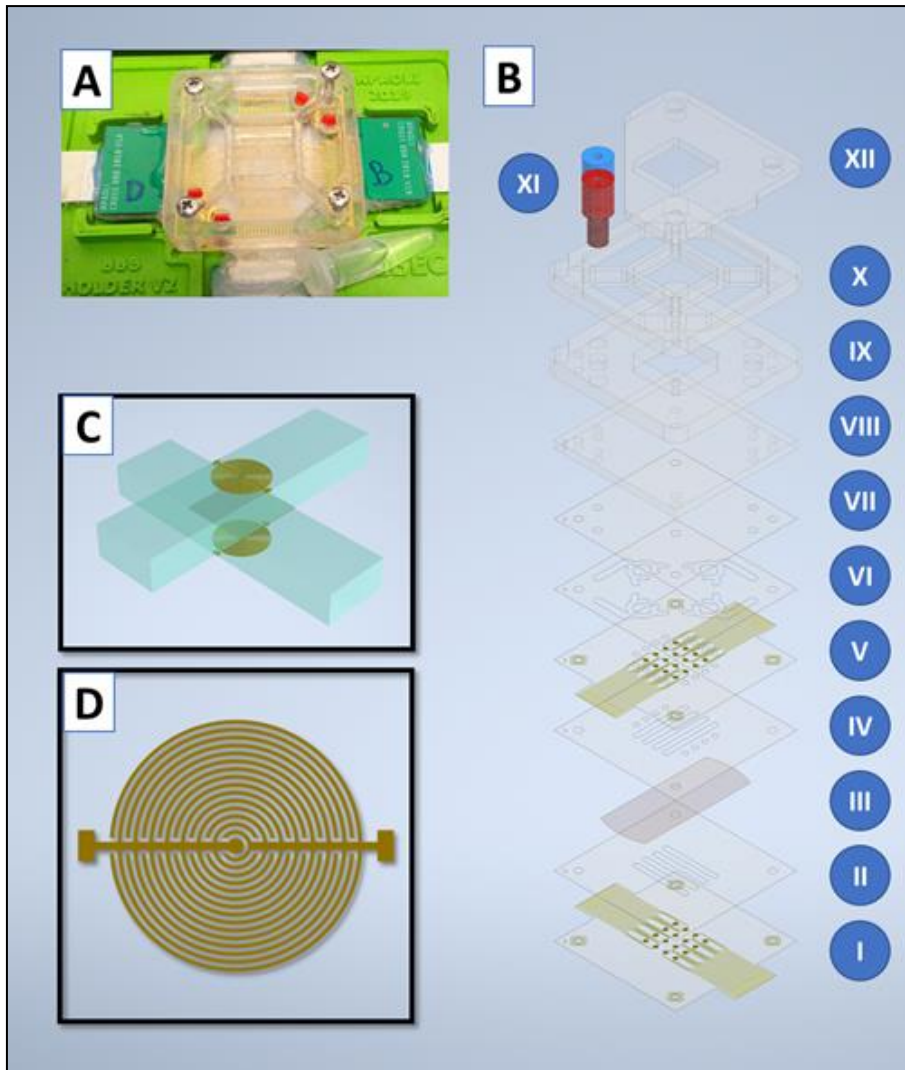


Figure 5-8. OOC v2.2 with embedded electrodes for TEER measurements. A) Assembled device inside the custom microscope holder, with attached connectors; B) Exploded view of the device: I) bottom layer with electrodes (COP, Au); II) lower channels (COP); III) PC membrane (COP); IV) upper channels (COP); V) upper electrodes layer with holes for flow routing (COP, Au); VI) fluidic splitter channel (COP); VII) inlets/outlets (COP); VIII) Luer-Lock connector layer (PMMA, 3 mm); IX) ¼-28 UNF threaded connectors layer (PMMA 6 mm); X) media reservoir layer (PMMA, 6 mm); XI) ¼-28 Fluidic male connectors; XII) removable media reservoir lid (PMMA, 3 mm); C) Detail of one of the 16 measurement spots located at each of the 16 channels intersection; D) Detail of the interdigitated electrodes design.

Layers were fabricated by laser cutting as described in the previous chapters. After cutting, COP electrodes layers were cleaned with EtOH and sputtered with 100 nm of gold. A 2- μm thick layer of AZ[®] 5214-E was spun on the substrate (2000 rpm, 30 s) and baked at 95 °C on a hotplate.

Substrate was aligned with chrome mask in a manual MJB4 mask aligner (SÜSS Microtec, Germany), exposed with UV light (Energy: 200 mJ cm⁻²) and developed for 30 s using a 1:4 dilution of AZ[®] 400K Developer in DI water. Gold was wet etched using TFA etchant for 40s. Finally, photoresist was lift off by washing in AZ 100 Remover for 60 s.

Assembly was performed using the same conditions described in Chapter 3, following the layer order shown in **Figure 5-8-B**.

5.3.4.3 Custom holder and adapters

A custom holder was designed into Autodesk Inventor to fit inside the microscope OKO-Lab H301T incubator and to secure OOC V2.2 (**Figure 5-9**). The holder was 3D printed in PLA using FDM (Z resolution 0.3 mm, nozzle diameter 0.4 mm).

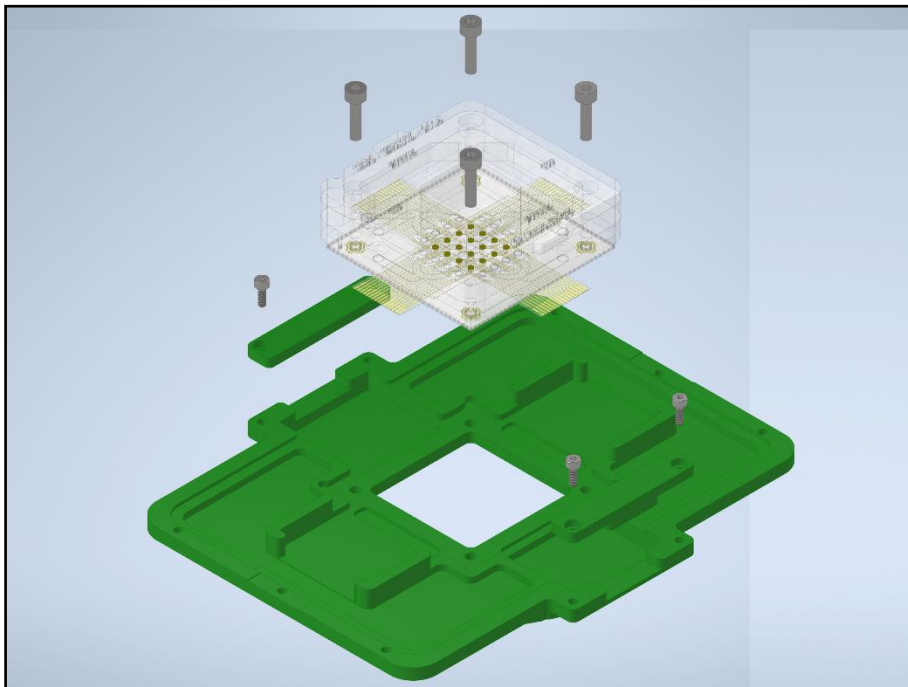


Figure 5-9. OKO-Lab incubator adapter for OOC v2.2

5.4 RESULTS

5.4.1 Improving OOC design

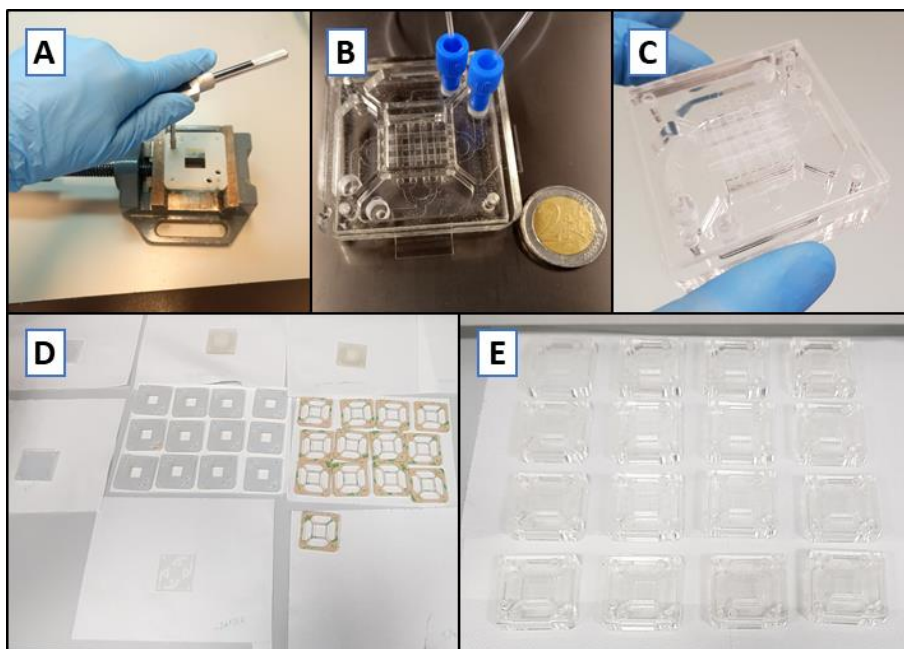


Figure 5-10. OOC v2.1 fabrication. A) Adding 1/4-28 UNF threads to laser cut holes; B) Top view of final assembled OOC v2.1 (2 Euro coin for scale comparison); C) Bottom view of assembled OOC v2.1; D) Freshly cut layers for batch fabrication of 20 devices and E) the respective assembled devices.

We fabricated add-in layers for previously fabricated OOC v2.0. Alignment with preexisting inlet was correct. Connectors and reservoirs showed no leakage. We further fabricated 20 new OOC v2.1 devices. Overall fabrication time for the complete batch (including material preparation, cutting, thread-making and assembly) took 8 hours.

5.4.2 Embedded flow control system

5.4.2.1 Small footprint flow control system

We developed, soldered, debugged and tested a first prototype of the flow control system. Final prototype PCB fits $50 \times 50 \text{ mm}$ and can control up to 4 micropumps. Serial commands make possible to enable/disable each pump independently and to control flow through selection of peristaltic frequency. Due to Arduino Board characteristics, a total of two independent frequencies can be selected, driving 2 pumps each.

5.4.2.2 Portable experimental unit

A portable experimental unit was designed and fabricated. Dimensions tolerances were adjusted for a tight fit of the components. External PMMA media reservoirs were successfully fabricated using laser cutting. System was extensively tested for leakage for 48 h. Current configuration enabled flowrates in the range of $0.15\sim 5\text{ mL min}^{-1}$, though additional tuning could be achieved using different resistor values in the schematic.

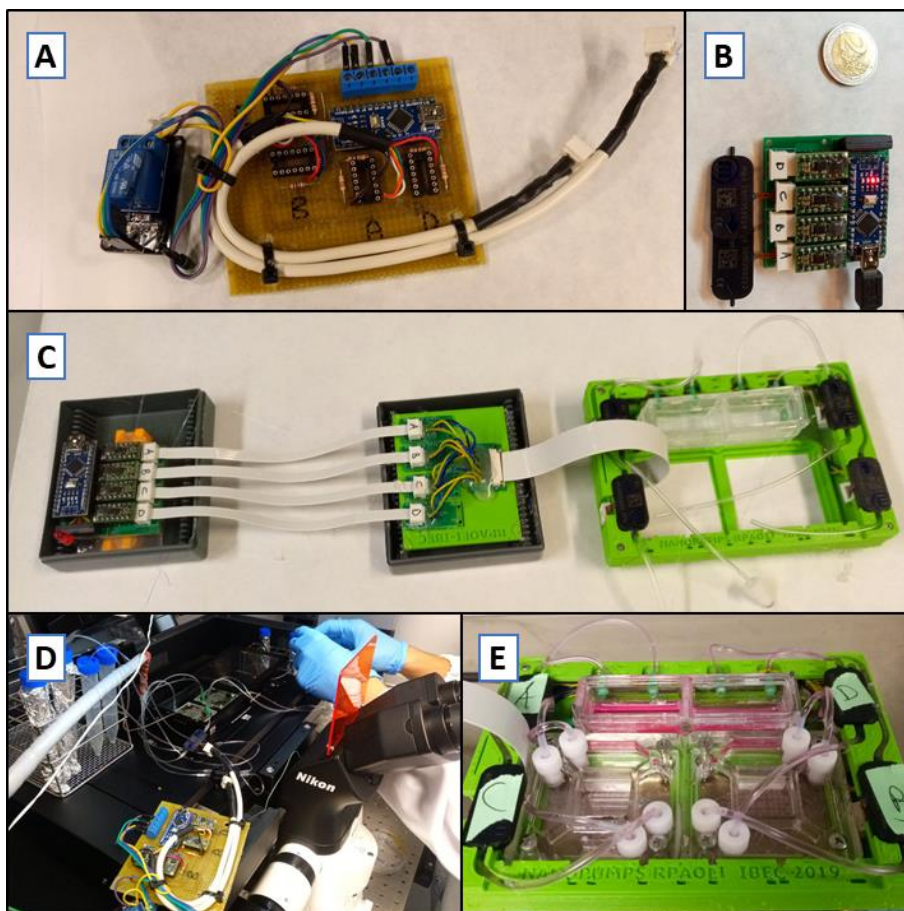


Figure 5-11. Embedded flow control system. A) First prototype of the external flow control; B) Smaller footprint final prototype and 2 Euro coin for size comparison; C) Complete system including (left to right): flow control system; Flat extension cables interface; experimental block; D) Testing the first prototype; E) Testing the final prototype.

Estimated cost of the prototype – not including OOCs and $\frac{1}{4}$ -28 UNF connectors – is 295€ (reported with details in **Table 5-1**). We estimate the cost

could be easily scaled down close to 200€ with few improvements in the design and a modest quantity usage.

Table 5-1. Compact experimental unit cost detail. *Notice that MP6 micropumps and MP6 drivers can be reduced purchasing in quantity. **3D printed cost is estimated using external printing services; cost can be reduced drastically owning a 3D printer.

Parts	Unit Price	Quantity	Cost
Arduino Nano (clone)	2-3€	1	2-3€
MP6 micropump	25€*	4	100€*
MP6 driver	40€*	4	160€*
PCB	~1€	1	~1€
Other components	3-5€	1	3-5€
3D Printed parts	20€**	1	20€**
PMMA Reservoirs	~3€	1	3€
Tubing	~1€	2 m	2€
TOTAL			295€

5.4.3 Integrated TEER sensors fabrication

6 pairs of electrodes layers were fabricated in COP according to the described protocol (2 pairs at IBEC facilities and 1 pair at CNR facilities, respectively). Photolithography results were checked both using a multimeter to test for short-circuits and under microscope for defects. Electrodes were later assembled into final OOC v2.2 version.

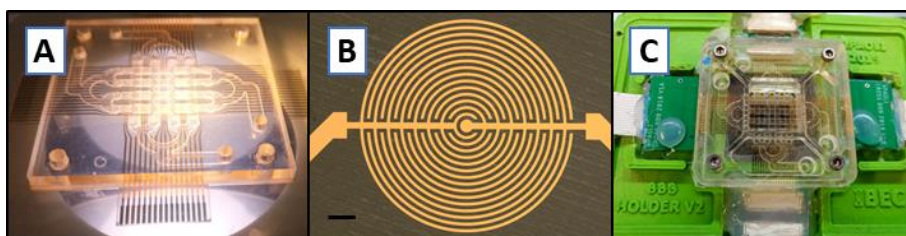


Figure 5-12. Fabricated OOC v2.2. A) Assembled device without threaded connectors and reservoirs; B) Microscope image of a single pair of interdigitated electrodes (Scale bar: 200 µm); C) Assembled device with threaded connectors and reservoirs in the custom microscope adapter, with electrical connections.

5.5 DISCUSSION

In this chapter we explored various upgrades to the OOC v2.0 design to improve usability, versatility and to add new features.

OOC v2.1 introduces two kind of enhancements. On the one hand, threaded connectors added an extra layer of robustness to microfluidic connections. Female $\frac{1}{4}$ -28 UNF connections can withstand higher pressure than Mini-Luer connectors and are much less prone to wear out after repeated mating cycles. Furthermore, tubing connection to the respective male plug appear to be more stable. On the other hand, the inclusion of fluidic reservoirs enables easier maintaining of static control cell-cultures, ensuring extra stock of culture media to ensure presence of enough nutrients without need of frequent maintenance. Additional lid also limit evaporation from the reservoirs while providing an extra barrier against contamination of the cell culture.

Batch fabrication of 20 devices was achieved in 8 hours. We consider this result remarkable, particularly considering the relatively low automation level of the assembly steps in our facility. Layers were manually inserted and removed into the alignment block and manually pressed one-by-one, leaving great margin of throughput improvement by automating these steps.

In addition to the novelty evidenced in Chapter 3 discussion and to the best of our knowledge, it is the first time an optically clear membrane-embedded OOC device, fabricated in COP using laser cut, features embedded PMMA media reservoirs and auto-aligning standard threaded connectors.

Our proposed embedded flow system provides a compact solution to enable experiments with recirculating flow on two devices at the same time. The system can select 2 independent frequencies to drive 4 pumps. As flowrate is a combination of amplitude and frequency, depending on the resistors choice for each channel we can control up to 4 different semi-independent flowrates. Limitation of 2 frequencies might be overcome in future models using a different microcontroller.

The experimental unit, once fluidically connected, has the additional benefit of enabling translation from cell-culture cabinet to the incubator and to the microscopy setup without the need to move or disconnect complex setups and without worries about contaminations (thanks to on-chip and external

reservoirs lids). The electronic control system can be easily disconnected and reconnected to the experimental block using a single ZIF connector and the single flat cable do not hamper the closing of the microscope microincubator. The electronic control system is compatible with any computer through USB connection and a serial port terminal. Electronic control system can be easily controlled and programmed by the same computer operating the microscope or by an external one. Use of remote desktop connection software or similar solutions can be used to enable remote control of the setup. A small-sized embedded computer (i.e. Raspberry Pi) might be added to the setup to avoid the need for an external computer, as suggested by the similar PiFlow implementation¹⁶. In the same way, wireless control could be implemented. A manual interface (buttons, display) might also be easily added to enable hybrid control (programmatic and by manual input). Compared to PiFlow, we find our Embedded system has the additional benefit integrating the pumps in the same physical unit with OOC devices and reservoirs, avoiding accidental changes in pressure due to relative displacement or accidental pulling of tubing and connections. Furthermore, integrating the whole system inside the microscope incubator we avoid extra setup complexity for live imaging and guarantee the same experimental conditions (i.e. temperature and gas concentration) to reservoirs, tubing and OOC devices.

Finally, OOC v2.2 showed the compatibility of the DM process illustrated in Chapter 3 with electrodes embedding. Electrodes can be fabricated on top of COP material after laser cutting and before the assembly. Use of external flaps enabled the use of ZIF connector so simplify connection of the device to the measurement setup. Use of CAD software enabled the fabrication of custom 3D printed adapters to secure devices and connectors with a perfect fit, ensuring an easier and more solid assembly of the setup environment.

To the best of our knowledge, it is the first time an optically-clear membrane-embedded OOC device, fabricated in COP using laser ablation, features embedded electrodes for TEER measurements with standard ZIF connectors.

5.6 CONCLUSIONS

In this chapter we modified the previous OOC v2.0 and designed new tools to improve usability and versatility of the device, as well as to add new

functionalities. All improvements were designed to maintain compatibility with the DM techniques chosen.

With design v2.1, we added both a more robust microfluidic interface to the device as well as a low maintenance solution for static culture. OOC v2.1 improves versatility of the device, allowing the use of both standard Mini Luer and more robust ¼-28 UNF connectors, while adding the possibility to easily maintain cell cultures in static conditions thanks to on-chip reservoirs. Also, the potential for scalability of the manufacturing process was proven achieving the fabrication of a full batch of 20 devices in less than 8 hours, despite the room for throughput improvement of the assembly process.

With design v2.2 we demonstrated the compatibility of the DM process illustrated in chapter 3 with the integration electrodes. We successfully integrated 16 double pairs interdigitated electrodes for TEER measurements and took advantage of the material characteristics to include easy-to-handle standard ZIF connectors.

Both v2.1 and v2.2 designs took advantage of DM, which made easier to design additional parts perfectly aligned with the previous design. Both improvements also are compatible with the previous DM process. To the best of our knowledge, it is the first time an optically-clear membrane-embedded OOC device, fabricated in COP using laser ablation, which features both embedded electrodes for TEER measurements with standard ZIF connectors and embedded auto-aligning PMMA threaded connectors and on-chip media reservoirs.

Taking advantage of CAD and DM, we designed and fabricated a compact embedded flow system as a complete solution for recirculating flow experiments on two devices at the same time. The developed experimental unit is a complete portable system which simplifies usability and fits a complete microfluidic setup inside a microscope microincubator. External driving circuit can be easily connected/disconnected and used to drive the pumps with a flowrate of $0.15\sim 5\text{ ml min}^{-1}$.

5.7 REFERENCES

1. Mohammed, M. I., Haswell, S. & Gibson, I. Lab-on-a-chip or Chip-in-a-lab: Challenges of Commercialization Lost in Translation. *Procedia Technol.* **20**, 54–59 (2015).
2. Streets, A. M. & Huang, Y. Chip in a lab: Microfluidics for next generation life science research. *Biomicrofluidics* **7**, 011302 (2013).
3. Temiz, Y., Lovchik, R. D., Kaigala, G. V. & Delamarche, E. Lab-on-a-chip devices: How to close and plug the lab? *Microelectron. Eng.* **132**, 156–175 (2015).
4. Bhattacharjee, N., Urrios, A., Kang, S. & Folch, A. The upcoming 3D-printing revolution in microfluidics. *Lab on a Chip* **16**, 1720–1742 (2016).
5. Finkbeiner, T., Soergel, H. L., Koschitzky, M. P., Ahrens, R. & Guber, A. E. Ultrasonic welding for the rapid integration of fluidic connectors into microfluidic chips. *J. Micromechanics Microengineering* **29**, (2019).
6. Dryden, M. D. M., Fobel, R., Fobel, C. & Wheeler, A. R. Upon the Shoulders of Giants: Open-Source Hardware and Software in Analytical Chemistry. *Anal. Chem.* **89**, 4330–4338 (2017).
7. Nguyen, T., Zoëga Andreasen, S., Wolff, A. & Duong Bang, D. From Lab on a Chip to Point of Care Devices: The Role of Open Source Microcontrollers. *Micromachines* **9**, 403 (2018).
8. Lim, G. S. *et al.* A lab-on-a-chip system integrating tissue sample preparation and multiplex RT-qPCR for gene expression analysis in point-of-care hepatotoxicity assessment. *Lab Chip* (2015). doi:10.1039/c5lc00798d
9. Maia Chagas, A., Prieto-Godino, L. L., Arrenberg, A. B. & Baden, T. The €100 lab: A 3D-printable open-source platform for fluorescence microscopy, optogenetics, and accurate temperature control during behaviour of zebrafish, *Drosophila*, and *Caenorhabditis elegans*. *PLOS Biol.* **15**, e2002702 (2017).
10. Akash, K., Kumar, M. P., Venkatesan, N. & Venkatesan, M. A single acting syringe pump based on Raspberry Pi - SOC. *2015 IEEE Int. Conf. Comput. Intell. Comput. Res. ICCIC 2015* 1–3 (2016). doi:10.1109/ICCIC.2015.7435694
11. Garcia, V. E., Liu, J. & DeRisi, J. L. Low-cost touchscreen driven programmable dual syringe pump for life science applications. *HardwareX* **4**, (2018).

12. Lake, J. R., Heyde, K. C. & Ruder, W. C. Low-cost feedback-controlled syringe pressure pumps for microfluidics applications. *PLoS One* **12**, 1–12 (2017).
13. da Costa, E. T. *et al.* Getting started with open-hardware: Development and control of microfluidic devices. *Electrophoresis* **35**, 2370–2377 (2014).
14. Frank, P., Haefner, S., Elstner, M. & Richter, A. Fully-Programmable, Low-Cost, “Do-It-Yourself” Pressure Source for General Purpose Use in the Microfluidic Laboratory. *Inventions* **1**, 13 (2016).
15. Watson, C. & Senyo, S. All-in-one automated microfluidics control system. *HardwareX* **5**, e00063 (2019).
16. Kassis, T. *et al.* PiFlow: A biocompatible low-cost programmable dynamic flow pumping system utilizing a Raspberry Pi Zero and commercial piezoelectric pumps. *HardwareX* **4**, (2018).
17. Hickman, J. Transepithelial/endothelial Electrical Resistance (TEER) theory and applications for microfluidic body-on-a-chip devices. *J. Rare Dis. Res. Treat.* **1**, 46–52 (2018).
18. Thuenauer, R., Rodriguez-Boulan, E. & Rümer, W. Microfluidic approaches for epithelial cell layer culture and characterisation. *Analyst* **139**, 3206–3218 (2014).
19. Thuenauer, R., Rodriguez-Boulan, E. & Römer, W. Microfluidic approaches for epithelial cell layer culture and characterisation. *Analyst* **139**, 3206–18 (2014).
20. Herland, A. *et al.* Distinct Contributions of Astrocytes and Pericytes to Neuroinflammation Identified in a 3D Human Blood-Brain Barrier on a Chip. *PLoS One* **11**, e0150360 (2016).
21. Partyka, P. P. *et al.* Mechanical stress regulates transport in a compliant 3D model of the blood-brain barrier. *Biomaterials* **115**, 30–39 (2017).
22. Ferrell, N. *et al.* A microfluidic bioreactor with integrated transepithelial electrical resistance (TEER) measurement electrodes for evaluation of renal epithelial cells. *Biotechnol. Bioeng.* **107**, 707–716 (2010).
23. Booth, R. & Kim, H. Characterization of a microfluidic in vitro model of the blood-brain barrier (μ BBB). *Lab Chip* **12**, 1784 (2012).
24. Hediger, S., Sayah, A., Horisberger, J. D. & Gijs, M. A. M. Modular microsystem for epithelial cell culture and electrical characterisation. *Biosens. Bioelectron.* **16**, 689–694 (2001).

25. Sun, T. *et al.* On-chip epithelial barrier function assays using electrical impedance spectroscopy. *Lab Chip* **10**, 1611–1617 (2010).
26. Micronit Microfluidics. Available at: www.micronit.com. (Accessed: 24th July 2019)
27. microLIQUID. Available at: www.microliquid.com. (Accessed: 24th July 2019)
28. Park, J. J. *et al.* Chitosan-mediated in situ biomolecule assembly in completely packaged microfluidic devices. *Lab Chip* **6**, 1315–1321 (2006).
29. Temiz, Y., Ferretti, A., Leblebici, Y. & Guiducci, C. A comparative study on fabrication techniques for on-chip microelectrodes. *Lab Chip* **12**, 4920–4928 (2012).
30. Arduino. Available at: www.arduino.cc. (Accessed: 24th July 2019)

6 OOC for Kidney tubular applications

6.1	BACKGROUND	140
6.1.1	THE KIDNEY	140
6.1.2	KIDNEY-ON-CHIP STATE OF ART	143
6.2	MATERIALS AND METHODS	149
6.2.0	MATERIALS AND GENERAL CELLS SEEDING PROTOCOLS	149
6.2.1	TUBULAR KIDNEY EXPERIMENTS ON OOCv1.....	151
6.2.2	TUBULAR KIDNEY EXPERIMENTS ON OOCv2.1.....	153
6.3	RESULTS.....	155
6.3.1	TUBULAR KIDNEY EXPERIMENTS ON OOCv1.....	155
6.3.2	TUBULAR KIDNEY EXPERIMENTS ON OOCv2.1.....	156
6.4	DISCUSSION	158
6.5	CONCLUSIONS	159
6.6	REFERENCES	161

After exposing all technological achievement in the previous part of the thesis, in this chapter we start presenting their applications to biological problems. Particularly, we will apply OOCv1-A, OOCv2.1 and the compact experimental module with embedded flow control to the study of diabetic dysfunctions of the tubular kidney.

The reader will be first introduced to some required knowledge about kidney and nephron physiology, the role of fatty acid mechanism in diabetic kidney disease, as well as to review of the state of art of kidney-mimicking OOC devices.

Experiments involves culturing of renal proximal tubular cells (RPTCs) extracted from kidney organoids generated from human embryonic stem cells (hESC). Cells from organoid cultured under oscillatory (diabetogenic) and physiological glucose level conditions were exposed to fatty acid to evaluate its accumulation inside the cells. Results are finally exposed and discussed.

Collaborations: the work presented in this chapter was achieved in collaboration with the Dr. Elena Garreta Bahima, Dr. Carmen Hurtado and ICREA researcher Dr. Nuria Montserrat Pulido from Lab Pluripotency for organ regeneration.

6.1 BACKGROUND

6.1.1 The Kidney

6.1.1.1 Kidney structure and physiological values

The kidneys are bean-shaped paired organs that lie on the posterior wall of the abdomen¹. In the adult human, each kidney weights between 115 and 170 g and is approximately 11 cm long, 6 cm wide and 3 cm thick¹, constituting together approximately 0.5 % of body weight.

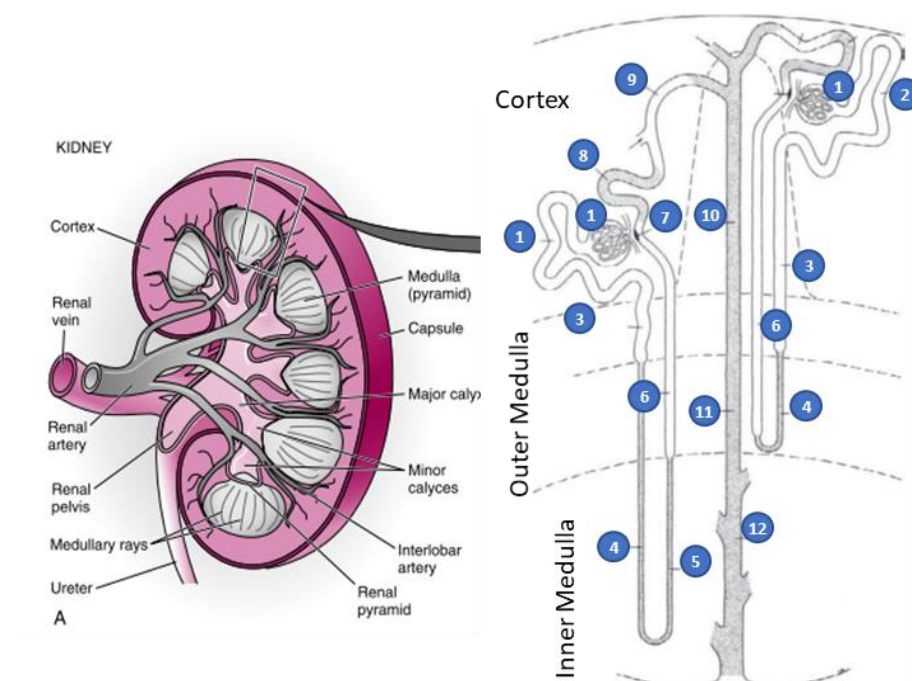


Figure 6-1. The kidney (left) and the nephron structure (right). The renal corpuscle (1), also referred as the Glomerulus, consists of glomerular capillaries and Bowman's capsule. The proximal tubule initially forms several coils (2, *pars convoluta*), followed by a straight part descending toward the medulla (3, *pars recta*)². The intermediate tubule is a thinner structure formed by the descending thin limb (4) and the ascending thin limb (5, only in nephrons with long loops of Henle)². The distal tubule is formed by a straight part, the thick ascending limb (6, *pars recta*) and the convoluted distal tubule (8). The whole U-shaped part, including proximal straight tubule (3), intermediate tubule (4-5) and distal straight tubule (6) is also referred as Loop of Henle. Near the end, the nephron passes between the afferent and efferent arterioles of the same nephron. This short segment of the thick ascending limb that touches the glomerulus is called the macula densa (7). Finally, a short connecting tubule (9) joins the nephron with the collecting duct system (10-12).² Images reproduced/adapted by permission of Elsevier from: A) Joeppen et al, 2012¹; B) Alpern et al., 2013².

Cutting the kidney across the coronal/frontal plane (**Figure 6-1**, left), we can easily distinguish two regions: the outer one (in dark pink), called the cortex, and the inner one, called medulla.

The specific structural and functional unit of the kidney is the nephron (**Figure 6-1**, right). Each kidney is formed by 800000 to 1200000 nephrons^{1,2}, each of them located across the cortex and the medulla. Nephrons consist of a renal corpuscle connected to a complicated and twisted hollow tube composed of a single cell layer, consisting of 3 more sections: proximal tubule, intermediate tubule, distal tubule^{1,2}. The tube ends in the collecting duct system. When they reach the inner medulla, tubules from different nephrons fuse together. In the human kidney, an average of eight fusions has been found³ a number that may also be a good approximation for other species².

The basic vascular pattern of the kidney is preserved across mammalian species². As reported in **Table 6-1**, smaller vessels in rats are in the order of few tens of microns. Coherently, other publications estimate the diameter of the tubule to be in the range of 22~50 μm ⁴⁻⁶. The fluid shear stress within the renal tubule system was estimated in the range of 0.02~2 Pa^{6,7}.

Table 6-1. Analysis of rat diameter and radius values distribution across rat kidney blood network, as reported by Nordsletten et al., 2006⁸. Diameter decreases moving from the feeding artery toward the glomeruli afferent arteriole, while segment length has no special correlation.

Vessel type	Ramification order	Number of elements	Mean radius [μm]	Mean length [mm]
Feeding renal artery	0	2	603.77 \pm 94.52	0.185
Interlobar arteries	1	4	428.05 \pm 80.95	1.440 \pm 0.647
	2	9	285.63 \pm 52.86	8.975 \pm 1.331
Arcuate arteries	3	38	205.41 \pm 4.38	2.516 \pm 2.053
	4	139	175.07 \pm 23.35	1.031 \pm 0.674
Interlobular arteries	5	418	123.99 \pm 21.35	0.511 \pm 0.000
	6	1210	71.42 \pm 16.34	1.001 \pm 0.216
	7	2926	46.46 \pm 14.32	0.656 \pm 0.286
	8	9258	26.02 \pm 9.51	0.404 \pm 0.390
Afferent arterioles	9	30659	14.72 \pm 4.05	0.423 \pm 0.283
	10	68564	10.79 \pm 2.41	0.312 \pm 0.285

6.1.1.2 The kidney as a target for new OOC models

The kidneys have crucial role in maintaining our body homeostasis. Their main activity is filtering waste material and extra water from our blood, producing urine, while also helping to control blood pressure and produce hormones.

Kidneys have a natural appeal for OOC application both for drugs testing as well as illnesses research. Nephrotoxicity accounts for only 2% of drug development failures in pre-clinical studies, this number rises to 19% of failures in Phase 3, and 20% of acute renal failure in community and hospital settings^{9,10}. Given the societal cost of nephrotoxicity and the insensitivity of current methods to detect it, sensitive methods for prediction of toxicity in preclinical studies and identification of injury in humans are extremely important for patient safety in clinical practice and in all stages of the drug-development process.

On the other hand, the incidence rates of end-stage renal disease (ESRD) have increased steadily internationally since 1989¹¹. ESRD is the final stage of chronic kidney disease (CKD). Diabetic kidney disease (DKD) develops in approximately 40% of patients who are diabetic and is the leading cause of CKD worldwide¹². Although ESRD may be the most recognizable consequence of diabetic kidney disease, most patients actually die from cardiovascular diseases and infections before needing kidney replacement therapy¹². Metabolic changes associated with diabetes lead to glomerular hypertrophy, glomerulosclerosis, and tubulointerstitial inflammation and fibrosis¹².

6.1.1.3 The role of mitochondrial fatty acid β -oxidation (FAO) in DKD

Glucose, fatty acids and amino acids are the three substrates used by our organism to generate energy, as well as to synthesize macromolecules¹³. In the case of fatty acid, the prime pathway for their degradation is mitochondrial fatty acid β -oxidation (FAO). FAO is an anaerobic catabolic process which takes place into the mitochondria of eukaryotic cells and breaks down fatty acid to extract energy.

FAO is the preferred energy source for highly metabolic cells such as cardiac myocytes, as oxidation of fatty acids generates more adenosine triphosphate (ATP) per molecule than does oxidation of glucose¹⁴. Tubular epithelial cells are one of the cell types with the highest energy demands in the body. Renal proximal tubular cells (RPTCs), which have high levels of baseline energy

consumption and a copious supply of mitochondria, have also been found to primarily rely on FAO as their energy source^{14,15}.

Disruption of FAO mechanism has been previously linked to DKD and CKD. Renal fibrosis shows almost identical manifestation in all progressive forms of CKD, suggesting it is a final common pathway in this condition^{14,16,17}. Previous research showed that reduction of FAO alone was sufficient to reprogram RPTCs into a profibrotic phenotype¹⁴.

Diabetes results in mitochondrial dysfunction, which leads to impaired β -oxidation of fatty acids and oxidative phosphorylation defect, contributing to the development of CKD^{18,19}. Particularly, as β -oxidation also takes place in the mitochondria, it has also been suggested that reduced FAO could be just one manifestation of a broader mitochondrial dysfunction and/or oxidative phosphorylation defect¹⁴. Link between glucose levels fluctuations and induced mitochondrial dysfunction had been demonstrated in hepatic cell²⁰.

Based on urine metabolomics and kidney biopsy studies, human DKD is characterized by reduced mitochondrial function²¹. A recent study demonstrated that stimulation of mitochondrial structure and function via activation of AMP-activated protein led to an increase in superoxide production and a reduction in parameters of diabetic kidney disease¹⁹. The study suggests that in addition to glycemic and blood pressure control, restoration of mitochondrial structure, function, and signaling may be novel ways to improve diabetic kidney disease and prevent the decline in organ function¹⁹.

6.1.2 Kidney-on-chip state of art

Although kidney is the major site of organ damage caused by drug toxicity, few engineered human kidney models have been developed that recapitulate responses to toxic drugs in vitro²². First attempt at studying the effect of shear stress on renal tubular cells dates back to 2001, when *Essig and colleagues* cultured proximal tubule from C57Bl/6 mice and from LLC-PK1 Bovine cell line under flow conditions²³. The device, consisting of a parallel plate chamber ($20 \times 70 \times 0.5 \text{ mm}$) assembled using two glass slides, is almost in the range of milli-fluidics. Nonetheless, the system enabled the first study of shear stress effects applying laminar flows of $1\sim 5 \text{ mL min}^{-1}$ ($0.016\sim 0.08 \text{ Pa}$ shear stress)

In 2007 *Baoudin and colleagues* used a PDMS device with microchambers interconnected by a microfluidic network to allow continuous renal tubular cell feeding²⁴. PDMS microchambers ($400 \times 400 \times 100 \mu\text{m}$) were seeded with Madin Darby Canine Kidney (MDCK) distal tubule cells at different initial concentrations ($2.5 \sim 5 \times 10^5 \text{ cells} \cdot \text{cm}^{-2}$). Flow rates used ($0, 10, 25, 50 \mu\text{L} \cdot \text{min}^{-1}$) generated a shear stress of $0, 0.002, 0.006, 0.01 \text{ Pa}$. Results showed increased proliferation under dynamic culture ($10 \mu\text{l min}^{-1}$, 0.002 Pa). Chronic toxicity assessment adding ammonium chloride (5 mM and 10 mM) to culture media resulted in important reduction of proliferation.

Borenstein group developed in 2008 a computational design of an ideal nephron OOC device composed by three different steps, reproducing respectively the glomerular, tubular and Henle's loop functions^{25,26}. The design uses physiological dimensions for the channels in each step and computed flowrates are also coherent with physiological values^{25,26}. Nonetheless, the study is limited to numerical simulations of urea reabsorption and no further practical application of this design can be found in the literature²⁶.

In 2010, another work studied effects of flow on renal cell culture, including for the first time a porous membrane (diameter $0.4 \mu\text{m}$)²⁷. The PDMS device consisted of a microfluidic channel ($1 \text{ mm} \times 1 \text{ cm} \times 100 \mu\text{m}$) and a PDMS well ($2 \text{ mm} \times 0.6 \text{ cm} \times 1 \sim 2 \text{ mm}$), separated by the membrane. Bonding of the different layers was achieved using O_2 plasma treatment (**Figure 6-2**). Both experimental and control devices, realized bonding PDMS channels to a glass substrate, were functionalized with fibronectin ($10 \mu\text{g mL}^{-1}$ for 1 h) to improve cell attachment. Primary rat inner medullary collecting duct (IMCD) cells were seeded and cultured statically in the device for 3 days up to confluency; later, cells were exposed to a fluid shear stress of 0.1 Pa for 5 h while provided nutrients from the static compartment resembling outer tubular fluid²⁶.

Fluid shear stress resulted in 3-fold increase of cell height and better resistance to oxidative stress. Also, thanks to fluid shear stress, IMCD cells were able to recognize their apical and basolateral surfaces within the device and polarize accordingly. Furthermore, functionality of molecular transport (water and Na uptake by Aquaporin 2) was tested and found to be responsive to hormone stimulations (Vasopressin, Aldosterone).

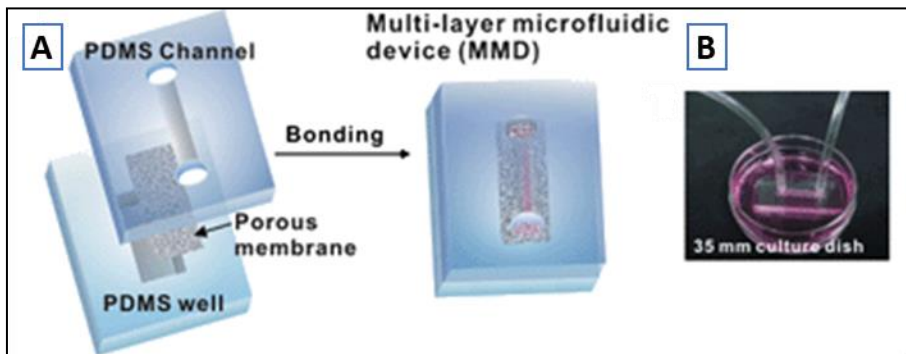


Figure 6-2. Fabrication and operation of a multi-layer microfluidic device (MMD). (a) The MMD is a sandwich assembly of polydimethylsiloxane (PDMS) channel, polyester membrane, and PDMS reservoir bonded with plasma treatment. (b) Photograph showing the operation of MMD that is connected to a syringe pump with silicone tubes. The MMD is placed on a culture dish containing an outside tubular fluid (OF). - Reproduced by RSC permission from [Jang et al, 2010](#)²⁷.

The first approach of an human proximal tubule-on-a-chip was published by *Ingber's* group in 2013 (**Figure 6-3**)²⁸. The device is a slightly modified version of the previous²⁷, featuring the same membrane and microfluidic channel, with a slightly deeper PDMS well ($1.1\text{ mm} \times 1.1\text{ cm} \times 3\text{ mm}$). Primary Human endothelial RPTCs were seeded on the membrane ($2 \cdot 10^5\text{ cells cm}^{-2}$) on static conditions and cultured under moderate flow shear stress (0.02 Pa). Control cells were plated on similar ECM-coated porous polyester membranes and cultured in traditional Transwell inserts under static conditions. Cells cultured under flow conditions resulted in enhanced differentiation after 3 days, by means of increased primary cilium formation, alkaline phosphatase activity, albumin transport and glucose reabsorption. Furthermore, testing for drug-induced (cisplatin) toxicity response showed a more specific response of cells cultured in «proximal tubule-on-a-chip».

Other works tried to model specific renal pathologic conditions, as autosomal dominant polycystic kidney disease (ADPKD)²⁹, renal fibrosis³⁰ or kidney stones formation³¹. These works are not attempting to reproduce the whole organ functional unit but specific parts or disease condition²⁶.

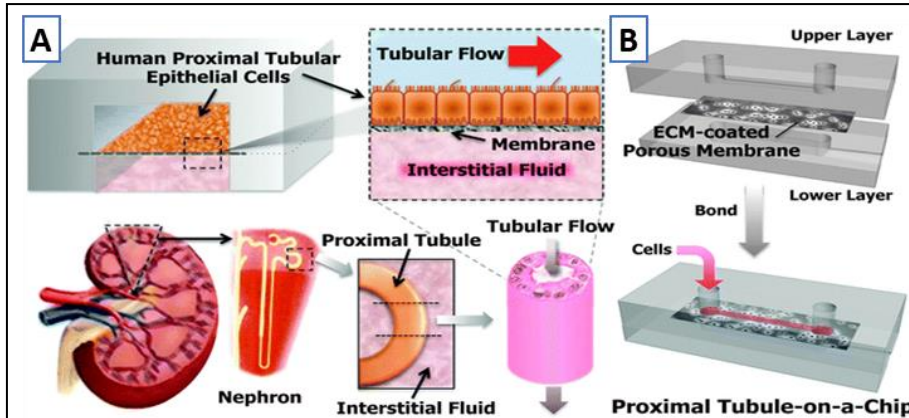


Figure 6-3. Design for the human kidney proximal tubule-on-a-chip. A) The microfluidic device consists of an apical channel (intraluminal channel) separated from a bottom reservoir (interstitial space) by an ECM-coated porous membrane upon which primary human proximal tubule epithelial cells are cultured in the presence of a physiological level of apical fluid shear stress. The basolateral compartment is accessible for fluid sampling and addition of test compounds to study active and passive epithelial transport. This design mimics the natural architecture, tissue–tissue interface and dynamically active mechanical microenvironment of the kidney proximal tubule; B) Device assembly: the upper layer, polyester porous membrane, and lower layer are bonded together through surface plasma treatment. Human primary proximal tubular epithelial cells are seeded through device inlet onto the porous ECM-coated membrane - Reproduced by RSC permission from [Janq et al, 2013](#)²⁸

Jansson and colleagues cultured primary kidney epithelial cells isolated from cysts of ADPKD to study the role of ouabain in the evolution of the disease²⁹. *Moll and colleagues* studied the role of immortalized human RPTCs (HK-2) in renal fibrosis, culturing renal cells on top of human dermal fibroblasts. Aim of the research work was to investigate how interactions between the two cell types contribute to cisplatin-induced kidney injury. *Wei and colleagues* used a 400 μm cylindrical PDMS microfluidic channel to study kidney stones formation (**Figure 6-5**)³¹. Proximal tubule epithelial cell from immortalized line HK-2 were seeded in the device after functionalizing it with fibronectin. In situ formation of calcium phosphate stones was observed in real time using Raman spectroscopy after injection of CaCl_2 and Na_3PO_4 .

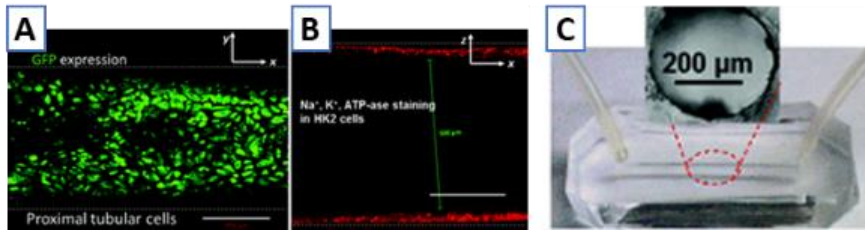


Figure 6-4. Renal proximal tubules generated in 3D. A) GFP expression; B) Na⁺, K⁺, ATP-ase; C) photograph of the device with circular cross-section. All scale bars are 200 μm. Reproduced by RSC permission from [Wei et al, 2012](#)³¹

Another approach for kidney-on-chip development used a dialysis-like hollow fiber membrane embedded inside a PDMS device³². PDMS apical and basal chamber were assembled together with the hollow fiber (Outer diameter, $OD = 780 \mu\text{m}$, Inner diameter, $ID = 490 \mu\text{m}$) on a microscope slide (**Figure 6-5**). After sterilization with ethanol and functionalization (5 mg mL^{-1} bovine fibrinogen, 50 U mL^{-1} bovine thrombin), the device was seeded 4 times with RPTCs. Cells were cultured under flow condition for 7 days. Successive fluorescent immunostaining and electron microscopy revealed a confluent RPTC monolayer with polarized expression of proximal tubule and ion transport markers, as well as the formation of microvilli on the apical side^{26,32}. Tubular reabsorption studies suggested reabsorption might be mediated by active transport.

A different approach in 2013 was an interface point between dialyzer miniaturization and OOC device³³. Microfluidic titanium layers with a serpentine channel (1 mm wide, 500 μm height) were assembled together, separated by different dialysis porous membranes (Polyethersulfone - PES, Mixed Cellulose Ester - MCE, Regenerated Cellulose - RC). The device was modular, so the total interchange surface could be increased by adding layers to increase the. Two types of immortalized cells were cultured in different layers: HK-2 cell line and human umbilical vein endothelial cells (HUVEC). Results showed a 2-fold improvement in cell proliferation when exposed to flow stimulation. Using 6-layers chip, urea nitrogen and B12 vitamin filtering clearance as well as ammoniogenesis values were found at physiological levels.

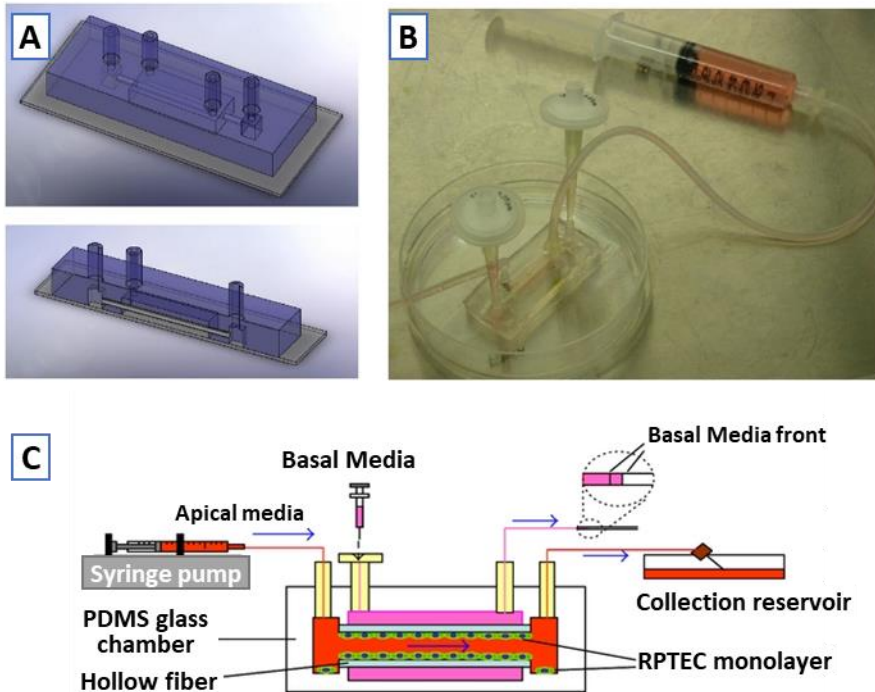


Figure 6-5. A Fibrin-Based Tissue-Engineered Renal Proximal Tubule for Bioartificial Kidney Devices: Development, Characterization and In Vitro Transport Study (2013). (a) Schematic and (b) image of the “lab-on-a-chip” hollow-fiber bioreactor. Set-up for (c) inulin recovery perfusion studies. Reproduced from [Ng et al, 2013](#)³².

A different approach in 2013 was an interface point between dialyzer miniaturization and OOC device³³. Microfluidic titanium layers with a serpentine channel (1 mm wide, 500 μm height) were assembled together, separated by different dialysis porous membranes (Polyethersulfone - PES, Mixed Cellulose Ester - MCE, Regenerated Cellulose - RC). The device was modular, so the total interchange surface could be increased by adding layers to increase the. Two types of immortalized cells were cultured in different layers: HK-2 cell line and human umbilical vein endothelial cells (HUVEC). Results showed a 2-fold improvement in cell proliferation when exposed to flow stimulation. Using 6-layers chip, urea nitrogen and B12 vitamin filtering clearance as well as ammoniogenesis values were found at physiological levels.

6.2 MATERIALS AND METHODS

6.2.0 Materials and general cells seeding protocols

This subsection reports detailed information about all the materials used in the biological experiments, the facilities used and the general seeding protocols for OOC devices. Seeding cells in microfluidics devices require a series of additional steps which depends on the device used. In order to avoid repetition in the methods section of this and the following chapter, general protocols for seeding in OOCv1 and OOCv2.1-2 are reported here in detail for further reference. Experiment-specific parameters will be reported in each experimental protocol (i.e. cell types used, seeding densities, functionalization solution, etc.). Also, the protocol for organoids culture and cell isolation, common to all experiment in this chapter, is reported in this section.

6.2.0.1 Materials

Tygon® tubing (ND-100-80, ID: 0.51 mm, OD: 1.59 mm, Cole Parmer) was from VWR (Radnor, PA USA). Diamidino-2-phenylindole (DAPI, 62248), BODIPY™ FL C16 (4,4-Difluoro-5,7-Dimethyl-4-Bora-3a,4a-Diaza-s-Indacene-3-Hexadecanoic Acid, Invitrogen™ D3821), MitoTracker™ Red CMXRos (Invitrogen™ M7512) were from ThermoFisher Scientific (Waltham, MA USA). Anti-VE Cadherin antibody (ab33168) was from Abcam (Cambridge, UK).

6.2.0.2 Facilities

All culture experiments were performed at Institute of Bioengineering of Catalonia, Barcelona, Spain. Confocal microscopy imaging was performed at the Advanced Microscopy Facilities of Institute for Research in Biomedicine (IRB), Barcelona, Spain.

6.2.0.3 OOCv1 general cells seeding protocol

After final assembly according to methods exposed in Chapter 2, OOCv1 device was sterilized by autoclave (121 °C, 20 min) and activated using UVO₃ treatment for 10 minutes. OOCv1 device was connected to Harvard PHD2000 syringe pump and freshly prepared functionalization solution was perfused through the device at controlled flowrate. After overnight incubation at 37 °C 5.0 % carbon dioxide (CO₂), the device was infused with sterile phosphate buffer saline (PBS) and cell culture media (10 min each, 30 μL min⁻¹) before proceeding to cell seeding. Cells were trypsinized and resuspended in the required seeding density. A 1-mL disposable syringe was

loaded with approximately 50 μL of cell suspension per device and connected to the desired channel. Seeding is performed manually, with gentle, very slow and steady pushing. Cell seeding density is verified under a microscope and incubated for 2 h at 37 °C.

6.2.0.4 OOCv2.1 and OOC v2.2 cells seeding protocol

After final assembly according to methods in Chapter 5, each device was activated using Bioforce UVO₃ tip cleaner (20 min) under fume hood. The device was interfaced with 10 mL disposable syringe using Luer 23G flat needles, Tygon® tubing and ¼-28 UNF fluidic connectors. All the materials had been sterilized in advance. The device was placed on top of a hotplate in order to maintain the temperature as close to 37 °C as possible during the whole process to avoid the introduction of dissolved bubble. After connecting syringes to lower and upper channel outlets, inlet reservoir was filled with EtOH 70 % solution and the device was infused manually by negative pressure induced flow. Subsequently both syringes were connected to a PHD 2000 Syringe Pump (Harvard Apparatus, Massachusetts, USA). Inlet reservoir was emptied using an aspiration pipette, refilled with 2 mL PBS and pump started in refill mode (Volume: 1000 μL , Flowrate: 200 $\mu\text{L} \cdot \text{min}^{-1}$) to flush both channels. Flush operation was repeated twice.

Coating and seeding can be performed on upper channel, on lower channel or on both. When both channels had to be seeded and two different functionalizations were required, we started with the solution requiring longer incubation time. To functionalize a channel, we plugged the opposite channel using Mini-Luer® plugs. Unplugged inlet reservoir was filled with 500 μL of coating solution and the pump was started in refill mode (Volume: 200 μL , Flowrate: $-200 \mu\text{L} \text{ min}^{-1}$). Afterwards, the remaining ports were plugged with Mini-Luer® plugs to prevent evaporation and the device was incubated for the required time at 37 °C. If two functionalizations were required, the procedure was repeated after reconnecting both channels and flushing them with sterile PBS.

After all the incubation had completed, both channels were infused again with culture medium before seeding. When seeding of both channels was required, we always started from the lower channel.

To seed a channel, we filled the respective inlet reservoir with 500 μL of cell suspension at required density and started flow immediately after (Volume: 200 μL , Flowrate: $-50 \mu\text{L min}^{-1}$). After flow had finished, device was subsequently plugged and inspected under a microscope to check seeding homogeneity before incubating for 2 h at 37 °C. When seeding lower channel, the device must be incubated upside-down. If both channels had to be seeded, the procedure was then repeated for the upper channel after previously seeded cells adhesion.

6.2.0.5 Organoids culture and cell isolation

From day 16 of differentiation kidney organoids were maintained under hyperglycemia condition (5~25 mM oscillatory) or control condition (5mM glucose) with Dulbecco's Modified Eagle Medium (DMEM), changing medium every day until day 23. The oscillatory treatment has been reported to have more deleterious effects than constant high glucose exposure.

On day 23, kidney organoids were incubated with fluorescein-conjugated Lotus tetragonolobus lectin (LTL, Vector Laboratories) (1:500) overnight to obtain the population of RPTCs from differentiated hESCs kidney organoids. Fluorescence-activated cell sorting Aria Fusion Instrument (BD Biosciences) was used for cell sorting, obtaining LTL+ cells (RPTCs). After sorting, cells were plated in 6 multi-well plates and expanded for 1-2 months under tubular medium (DMEM supplemented with 1 % Penicillin-Streptomycin, 5 % FBS (ThermoFisher), ITS 1X, 5mM Glucose).

6.2.1 Tubular kidney experiments on OOCv1

6.2.1.1 Rationale

Tubular kidney experiments in OOCv1 were oriented at investigating the absorption of C16 fatty acids under open-loop flow conditions in cells extracted from organoids cultured both under physiological and diabetogenic conditions. We seeded two OOCv1 devices accordingly, as resumed in **Table 6-2**.

Table 6-2. Experimental conditions overview for tubular kidney cultures on OOCv1.

Condition	Control	Diabetogenic
Organoids culture glucose concentration	Physiological 5 mM	Oscillating 5 mM / 25 mM
Flowrate [$\mu\text{L min}^{-1}$]	2.8	2.8

6.2.1.2 Tubular cells seeding in OOCv1 devices

Two OOCv1 devices were seeded according to the general protocol reported in section 6.2.0.3. Functionalization was performed flowing fibronectin solution ($0.15 \mu\text{g mL}^{-1}$, 30 min, $20 \mu\text{L min}^{-1}$) and incubating overnight. Tubular medium described in section 6.2.0.5 was used as culture medium. RPTCs had been previously extracted from kidney organoids generated from hESC as reported in section 6.2.0.5. Both devices were seeded in the upper channel at a density of $7.5 \text{ M cells mL}^{-1}$. One device (control condition) was seeded with RPTCs from hESC derived kidney organoids cultured under physiological 5 mM glucose concentration. The other device (diabetogenic condition) was seeded with RPTCs from hESC derived organoids which had been exposed to oscillatory high glucose concentration of glucose (5~25 mM).

6.2.1.3 Open-loop flow experiment

After cell adhesion, each OOCv1 device was connected to two 10-mL disposable syringes (one per inlet) and two waste reservoirs. Both devices were perfused at $2.5 \mu\text{L min}^{-1}$ for 48 h with renal culture supplemented with fluorescently labelled C16 fatty acid (BODIPY FL C16, 50 nM). The whole experiment was performed at 37 °C, 5.0 % CO₂ concentration.

6.2.1.4 Cell fixation and imaging

After 48 h, cells fixation inside the devices was performed by flowing in sequence PBS (1X, $150 \mu\text{L}$, $2.5 \mu\text{L min}^{-1}$, 1 h), Paraformaldehyde (PFA, 2.5 %, $600 \mu\text{L}$, $2.5 \mu\text{L min}^{-1}$, 4 h) and PBS (1X, $150 \mu\text{L}$, $2.5 \mu\text{L min}^{-1}$, 1 h). Quantities are per single channel.

Confocal fluorescence images were acquired using inverted confocal Leica SP5 microscope. Fluorescence has been quantified after selecting as region of

interest (ROI) the area with cell presence and normalizing against mean value of background pixels.

6.2.2 Tubular kidney experiments on OOCv2.1

6.2.2.1 Rationale

Tubular kidney experiments in OOCv2.1 were aimed to expand the study performed in OOCv1. Taking advantage of the portable flow control we designed, we decided to study the system with closed-loop recirculating flow.

As in OOCv1 experiments, we compared culturing of cells extracted from organoids previously culture under different conditions. Furthermore, taking advantage of the improvements in OOCv2.1, we added two static on-chip replicas, one for each condition, as a baseline to compare the effect of flow and shear stress.

Table 6-3. Experimental conditions overview for tubular kidney cultures on OOCv2.1

Condition		Control	Diabetogenic
Organoids culture glucose concentration		Physiological 5 mM	Oscillating 5 mM / 25 mM
Replicas per Flow condition	300 $\mu\text{L min}^{-1}$	2	2
	Static	1	1

6.2.2.2 Tubular cells seeding in OOCv2.1 devices

Six OOCv2.1 devices were seeded according to the general protocol reported in section 6.2.0.4. Functionalization was performed flowing fibronectin solution ($0.15 \mu\text{g mL}^{-1}$, 30 min, $20 \mu\text{L min}^{-1}$) and incubating for 1 h at 37°C . Tubular medium described in section 6.2.0.5 was used as culture medium. RPTCs had been previously extracted from kidney organoids generated from hESC as reported in section 6.2.0.5. Both devices were seeded in the upper channel at a density of $1.7 \text{ M cells mL}^{-1}$. One device (control condition) was seeded with RPTCs from hESC derived kidney organoids cultured under physiological 5 mM glucose concentration. The other device (diabetogenic condition) was seeded with RPTCs from hESC derived organoids which had been exposed to oscillatory high glucose concentration under 25 mM of glucose.

6.2.2.3 *Recirculating flow experiment*

Four OOCv2.1 devices were selected for recirculating flow experiments (2 devices for each condition). Experimental unit and PMMA reservoirs were cleansed with EtOH 70 % and dried using filtered N₂ gas stream. After cell attachment, the two OOCv2.1 device were inserted into the experimental unit. PMMA reservoirs were connected to MP6 micropumps and ¼-28 UNF microfluidic connectors using Tygon® tubing. PMMA reservoirs were filled with 4 mL of tubular media supplemented with labelled C16 fatty acid (BODIPY™ FL C16, 50 nM) and closed using their lid. Outlets and inlets of the devices were finally connected to the flow system after priming the circuit. On-chip reservoirs were washed with sterile PBS and aspirated using a pipette.

Experimental unit was reintroduced into the incubator (37 °C, 5.0 % CO₂) together with the flow control system and flow was started at 300 μL min⁻¹.

6.2.2.4 *Static controls*

Two static controls (one for 5 mM condition and one for fluctuating 5~25 mM condition) were also performed. After seeding, the on-chip reservoirs were filled using tubular media supplemented with labelled C16 fatty acid (BODIPY™ FL C16, 50 nM), covered using the OOCv2.1 lid and reintroduced into the incubator (37 °C, 5.0 % CO₂) for 24 h.

6.2.2.5 *Cell fixation, staining and imaging*

After 24h experiment, cells fixation and staining were performed for all the six devices at room temperature, using a negative flowrate of -50 μL min⁻¹. At each step, indicated volumes were perfused through each channel after aspirating and replacing the liquid in the reservoir at each step.

The channels were perfused with Mitotracker™ (50 nM, 0.75 mL), washed twice with PBS (1X, 0.5 mL) and fixed with PFA (4 %, 0.75 mL). After fixation, the channels were washed again twice using PBS (1X, 0.5 mL), perfused with DAPI (1:5000, 0.5 mL) and washed twice with PBS (1X, 0.75 mL, twice) before storing at 4 °C until performing the imaging.

Confocal fluorescence images were acquired using inverted confocal Leica SP5 microscope. Fluorescence has been quantified after selecting as ROI the area with cell presence and normalizing against mean value of background pixels and cell number.

6.3 RESULTS

6.3.1 Tubular kidney experiments on OOCv1

Cells successfully seeded and cultured on the device for 48h. Fluorescence imaging show accumulation of C16 fatty acid inside the cells (**Figure 6-6**). Mean fluorescence intensity was increased in diabetogenic samples (**Figure 6-7**).

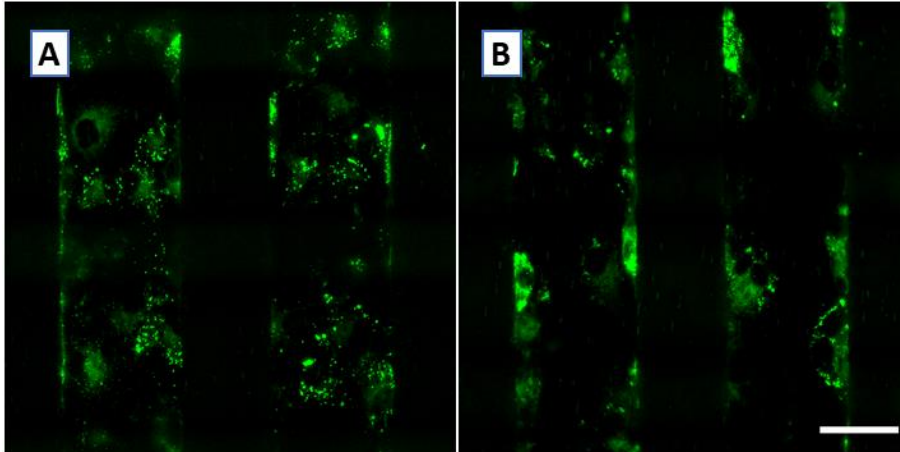


Figure 6-6. Fluorescence Imaging of Kidney Tubular cells on OOCv1.0-B. A) Cells from organoids cultured under tubular conditions; B) Cells from organoids cultured under diabetogenic oscillatory conditions (5~25 mM). Scale bars are 40 μm .

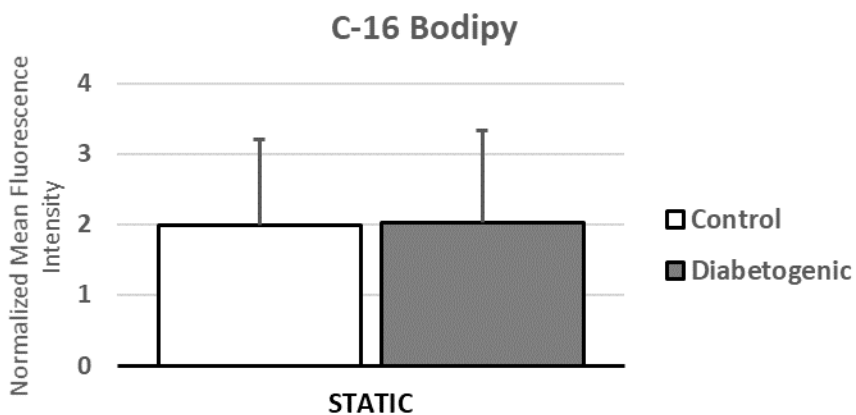


Figure 6-7. Mean C16 intensity comparison on fluorescence images of OOCv1-B, normalized by background intensity.

6.3.2 Tubular kidney experiments on OOCv2.1

Cells were successfully seeded and maintained under recirculating flow for 24 hours. Fluorescence imaging showed accumulation of C16 fatty acid inside the cells, as well as mitochondrial activity. Mitochondrial activity was higher in cells under recirculating flow conditions.

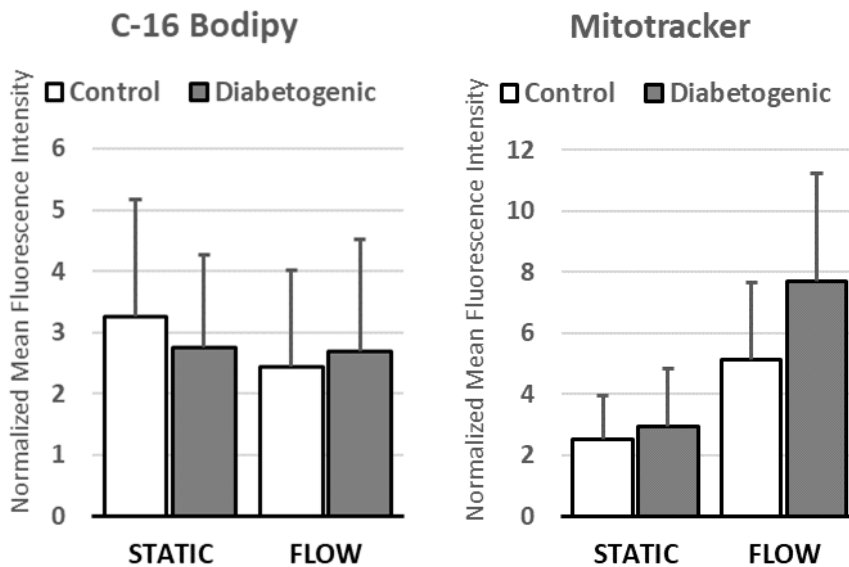


Figure 6-8. Fluorescence intensity of C16 and mitochondrial markers in renal tubular experiments in OOCv2.1, normalized by background intensity.

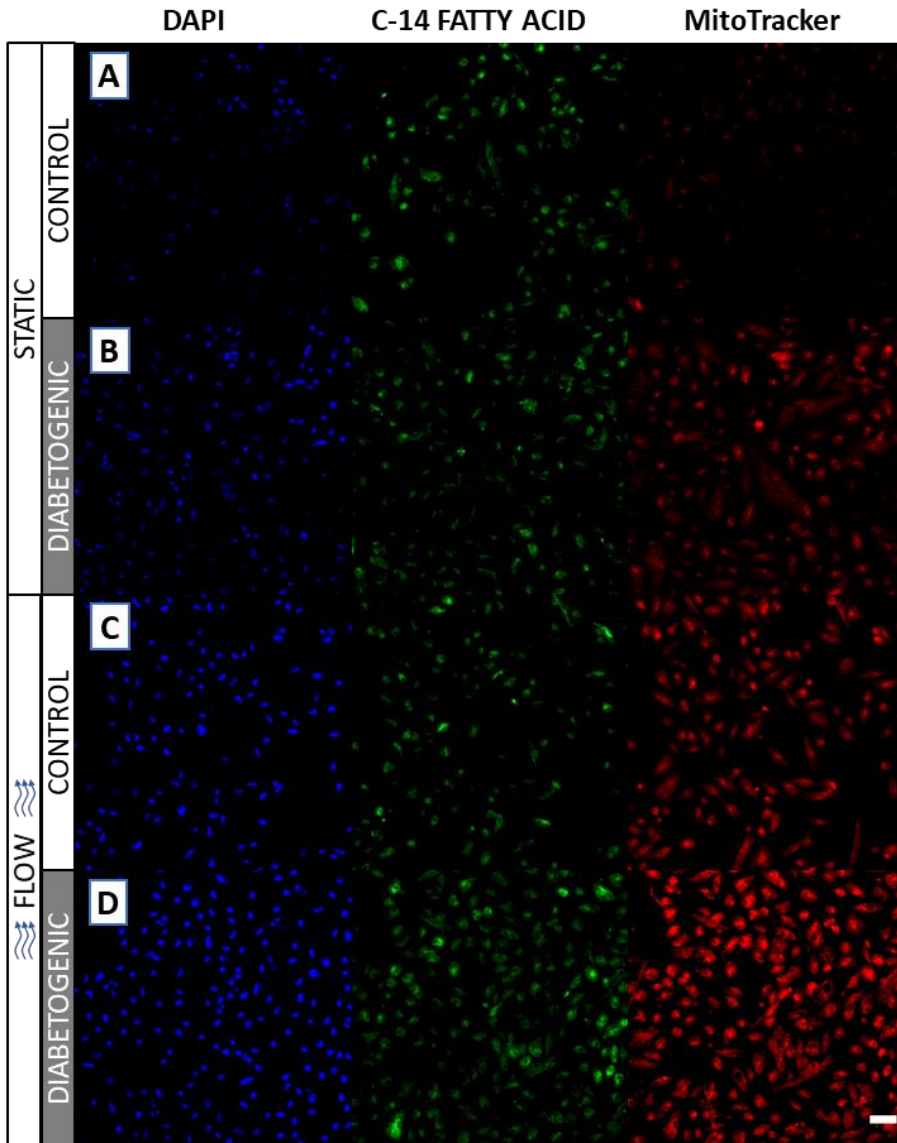


Figure 6-9. Fluorescence imaging of tubular kidney cells in OOCv2.1. A) Static conditions, control; B) Static condition, Diabetogenic; C) Recirculating flow condition, control; D) Recirculating flow condition, diabetogenic. Nuclei stained in blue (left column), C16 fatty acid stained in green (center column) and mitochondria stained in red (right column). Scale bar: 50 μm .

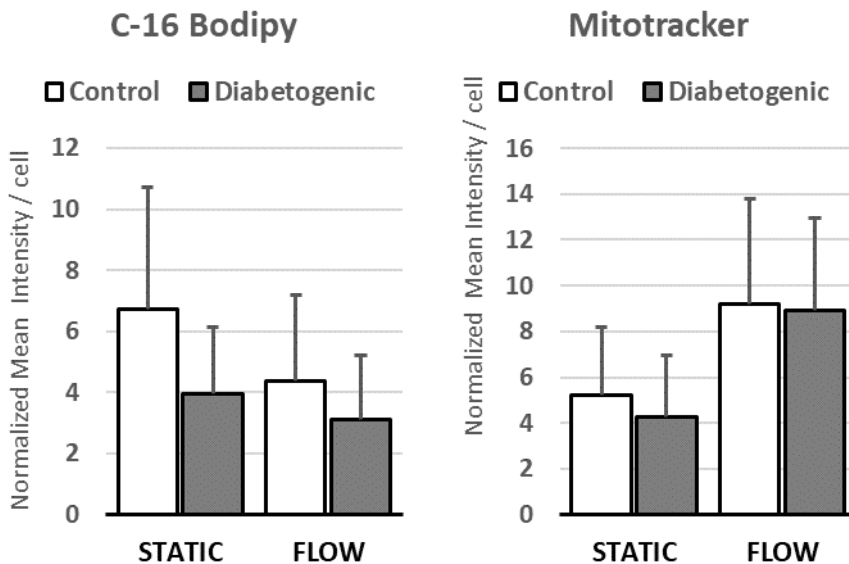


Figure 6-10: Fluorescence intensity C16 and mitochondrial markers in renal tubular experiments in OOCv2.1, normalized by background intensity and cell number.

6.4 DISCUSSION

Tubular kidney experiments resulted in accumulation of C16 fatty acid inside the cells. In open-loop flow experiments on OOCv1-B, normalized mean intensity of C16 fluorescent marker showed little difference between conditions, though accumulation in diabetogenic sample appear more homogeneously diffused across the whole cell compared to control.

On the contrary (**Figure 6-10**), experiments on OOCv2.1 showed a decrease in mean intensity of C16 fluorescent marker between control and diabetogenic conditions on both static and recirculating flow samples. Overall, C16 marker intensity is reduced under flow conditions, particularly in control condition. Apparent contradictory previous result from experiments on OOCv1-A device might be related to the lack of normalization per cell number in the previous analysis, due to absence of nuclei staining.

Staining with MitoTracker in static experiments showed a decrease in normalized intensity in static condition, which is less evident under flow conditions. This, together with the overall increase in MitoTracker signal moving from static to flow condition, possibly suggests a higher number of active mitochondria.

A more precise quantification of C16 accumulation would be suggested, considering the presence of background signal due to partial accumulation of the marker on the membrane during the experiment. Also, higher C16 accumulation should be expected in recirculating flow conditions, as more molecules are expected to interact with the cells when transported by active flow compared to diffusion only in static condition.

More precise quantification of fatty acid absorption from recirculating media could be achieved measuring C16 concentration in residual reservoir media after the experiment. Samples from reported experiments had already been stored at $-20\text{ }^{\circ}\text{C}$ for future quantification, after completing more replicas of the experiment.

Awaiting further data, we suggest the increase in MitoTracker signal under recirculating flow might be connected with corresponding overall reduction of C16 signal, possibly evidencing the beneficial effect of fluidic shear stress. As suggested by recent studies, restoration of mitochondrial structure, function, and signaling might be a novel way to prevent the decline in organ function and improve diabetic kidney disease¹⁹, which appear connected to impaired FAO and oxidative phosphorylation defect¹⁴. Other studies have demonstrated beneficial effect of shear stress on mitochondrial activity of endothelial cells^{34,35}, which are also physiologically subjected to fluid flow.

6.5 CONCLUSIONS

We demonstrated viability of OOCv1-B and OOCv2.1 devices for culturing of RPTCs previously extracted from kidney organoids generated from hESC.

Renal experiments showed accumulations of C16 fatty acid in tubular renal cells. Experiments in OOCv1-B with open-loop flow showed minimum increase of mean intensity of C16 marker in cells obtained from organoids cultured under diabetogenic conditions. On the contrary, fluorescence quantification of experiments on OOCv2.1 with media recirculation showed inverted trend, possibly because the impossibility to objectively normalize the previous data by number of cells. A more precise quantification of C16 accumulation should anyway be performed by quantifying media samples of OOCv2.1 experiments.

MitoTracker intensity analysis suggested a possible increase in mitochondrial activity due to beneficial effect of shear stress, which would confirm existing studies on the subject.

Renal experiments in OOCv2.1 also demonstrated the functionality of embedded flow control system detailed in Chapter 5. The flow system simplified the setup complexity.

6.6 REFERENCES

1. Koeppen, B. M. & Stanton, B. A. *Renal Physiology*. (Mosby, 2012).
2. Alpern, R. J., Moe, O. W. & Caplan, M. *Seldin and Giebisch's The Kidney - Physiology & Pathophysiology*. (Academic Press, 2013).
3. Oliver, J., MacDowell, M. & Fund, C. Nephrons and kidneys: a quantitative study of developmental and evolutionary mammalian renal architectonics. (1968).
4. Chou, C. L., Sands, J. M., Nonoguchi, H. & Knepper, M. A. Concentration dependence of urea and thiourea transport in rat inner medullary collecting duct. *Am. J. Physiol. - Ren. Fluid Electrolyte Physiol.* (1990).
5. DiGiovanni, S. R., Nielsen, S., Christensen, E. I. & Knepper, M. A. Regulation of collecting duct water channel expression by vasopressin in Brattleboro rat. *Proc. Natl. Acad. Sci. U. S. A.* (1994). doi:10.1073/pnas.91.19.8984
6. Cai, Z., Xin, J., Pollock, D. M. & Pollock, J. S. Shear stress-mediated NO production in inner medullary collecting duct cells. *Am. J. Physiol. - Ren. Physiol.* **279**, 270–274 (2000).
7. Jang, K.-J. *et al.* Fluid-shear-stress-induced translocation of aquaporin-2 and reorganization of actin cytoskeleton in renal tubular epithelial cells. *Integr. Biol. (Camb)*. **3**, 134–41 (2011).
8. Nordsletten, D. A., Blackett, S., Bentley, M. D., Ritman, E. L. & Smith, N. P. Structural morphology of renal vasculature. *Am. J. Physiol. Heart Circ. Physiol.* **291**, H296-309 (2006).
9. Naughton, C. A. Drug-induced nephrotoxicity. *American Family Physician* **78**, 743–750 (2008).
10. Redfern, W. S. *et al.* Impact and prevalence of safety pharmacology-related toxicities throughout the pharmaceutical life cycle. *J. Pharmacol. Toxicol. Methods* **62**, e29 (2010).
11. Carpi, A., Donadio, C. & Tramonti, G. *Progress in Hemodialysis - From Emergent Biotechnology to Clinical Practice*. (InTech, 2011). doi:10.5772/878
12. Alicic, R. Z., Rooney, M. T. & Tuttle, K. R. Diabetic kidney disease: Challenges, progress, and possibilities. *Clin. J. Am. Soc. Nephrol.* **12**, 2032–2045 (2017).
13. Houten, S. M. & Wanders, R. J. A. A general introduction to the biochemistry of mitochondrial fatty acid β -oxidation. *J. Inherit. Metab. Dis.* **33**, 469–477 (2010).
14. Kang, H. M. *et al.* Defective fatty acid oxidation in renal tubular epithelial cells has a key role in kidney fibrosis development. *Nat. Med.* **21**, 37–46 (2015).
15. Meyer, C., Nadkarni, V., Stumvoll, M. & Gerich, J. Human kidney free fatty acid and glucose uptake: evidence for a renal glucose-fatty acid cycle. *Am. J.*

Physiol. Metab. **273**, E650 (2017).

16. O'Brien, P. D., Sakowski, S. A. & Feldman, E. L. Mouse models of diabetic neuropathy. *ILAR J.* **54**, 259–272 (2014).
17. Nath, K. A., Salahudeen, A. K., Clark, E. C., Hostetter, M. K. & Hostetter, T. H. Role of cellular metabolites in progressive renal injury. *Kidney Int. Suppl.* **38**, S109-13 (1992).
18. Chen, D. Q. *et al.* The link between phenotype and fatty acid metabolism in advanced chronic kidney disease. *Nephrol. Dial. Transplant.* **32**, 1154–1166 (2017).
19. Dugan, L. L. *et al.* AMPK dysregulation promotes diabetes-related reduction of superoxide and mitochondrial function. *J. Clin. Invest.* **123**, 4888–4899 (2013).
20. Yin, X. *et al.* Glucose fluctuation increased hepatocyte apoptosis under lipotoxicity and the involvement of mitochondrial permeability transition opening. *J. Mol. Endocrinol.* **55**, 169–181 (2015).
21. Sharma, K. *et al.* Metabolomics reveals signature of mitochondrial dysfunction in diabetic kidney disease. *J. Am. Soc. Nephrol.* **24**, 1901–1912 (2013).
22. Benam, K. H. *et al.* Engineered In Vitro Disease Models. *Annu. Rev. Pathol.* **10**, 195–262 (2015).
23. Essig, M., Terzi, F., Burtin, M. & Friedlander, G. Mechanical strains induced by tubular flow affect the phenotype of proximal tubular cells. *Am J Physiol Ren. Physiol* **281**, F751-762 (2001).
24. Baudoin, R., Griscom, L., Monge, M., Legallais, C. & Leclerc, E. Development of a renal microchip for in vitro distal tubule models. *Biotechnol. Prog.* **23**, 1245–53 (2007).
25. Weinberg, E., Kaazempur-Mofrad, M. & Borenstein, J. Concept and computational design for a bioartificial nephron-on-a-chip. *Int. J. Artif. Organs* **31**, 508–14 (2008).
26. Paoli, R. & Samitier, J. Mimicking the kidney: A key role in organ-on-chip development. *Micromachines* **7**, (2016).
27. Jang, K.-J. & Suh, K.-Y. A multi-layer microfluidic device for efficient culture and analysis of renal tubular cells. *Lab Chip* **10**, 36–42 (2010).
28. Jang, K.-J. *et al.* Human kidney proximal tubule-on-a-chip for drug transport and nephrotoxicity assessment. *Integr. Biol.* **5**, 1119 (2013).
29. Jansson, K. *et al.* Endogenous concentrations of ouabain act as a cofactor to stimulate fluid secretion and cyst growth of in vitro ADPKD models via cAMP and EGFR-Src-MEK pathways. *AJP Ren. Physiol.* **303**, F982–F990 (2012).
30. Moll, S. *et al.* Epithelial cells as active player in fibrosis: findings from an in vitro

model. *PLoS One* **8**, e56575 (2013).

31. Wei, Z., Amponsah, P. K., Al-Shatti, M., Nie, Z. & Bandyopadhyay, B. C. Engineering of polarized tubular structures in a microfluidic device to study calcium phosphate stone formation. *Lab Chip* **12**, 4037–40 (2012).
32. Ng, C. P., Zhuang, Y., Lin, A. W. H. & Teo, J. C. M. A Fibrin-Based Tissue-Engineered Renal Proximal Tubule for Bioartificial Kidney Devices: Development, Characterization and In Vitro Transport Study. *Int. J. Tissue Eng.* **2013**, 1–10 (2013).
33. Zhu, W., Li, J. & Liu, J. The cell engineering construction and function evaluation of multi-layer biochip dialyzer. *Biomed. Microdevices* **15**, 781–91 (2013).
34. Bretón-Romero, R. *et al.* Laminar shear stress regulates mitochondrial dynamics, bioenergetics responses and PRX3 activation in endothelial cells. *Biochim. Biophys. Acta - Mol. Cell Res.* (2014). doi:10.1016/j.bbamcr.2014.07.003
35. Wu, L. H., Chang, H. C., Ting, P. C. & Wang, D. L. Laminar shear stress promotes mitochondrial homeostasis in endothelial cells. *J. Cell. Physiol.* (2018). doi:10.1002/jcp.26375

7 OOC for BBB applications

7.1	BACKGROUND	166
7.1.1	BBB PHYSIOLOGY	166
7.1.2	BBB-ON-CHIP STATE OF ART.....	167
7.2	SPECIFIC OBJECTIVES OF THE CHAPTER	170
7.3	MATERIALS AND METHODS	171
7.3.0	MATERIALS AND GENERAL CELLS SEEDING PROTOCOLS	171
7.3.1	BBB EXPERIMENTS	171
7.4	RESULTS	176
7.4.1	PHASE CONTRAST TIME-LAPSE	176
7.4.2	IMMUNOSTAINING	176
7.4.3	ELECTRICAL IMPEDANCE SPECTROSCOPY (EIS)	184
7.5	DISCUSSION	187
7.6	CONCLUSIONS	190

In this chapter we will continue the application of developed technologies to biological problem. Particularly, co-culturing of two different cell types will be performed both on OOCv2.1 and OOCv2.2 to investigate the Blood Brain Barrier (BBB) formation and disruption.

After introducing the reader to BBB physiology and the role of junctional complexes in barrier integrity, a brief review of current OOC models will be exposed.

Through different kind of experiments described in the methods section, involving live phase contrast imaging, immunostaining, and electrical impedance spectroscopy, formation and integrity of the barrier will be assessed.

Results are discussed, proposing a new model able to classify electrical impedance spectroscopy (EIS) measurements from different timepoints with high accuracy.

Collaborations: The work presented in this chapter was achieved in collaboration with PhD student Davide Di Giuseppe and his supervisor Prof. Eugenio Martinelli, from Sensors group of Rome Tor Vergata University, and PhD student Maider Badiola Mateos, from Nanobioengineering group of IBEC.

7.1 BACKGROUND

7.1.1 BBB physiology

The BBB is a physical, metabolic and transport barrier localized at the central nervous system micro vessels. It is a physical dynamic barrier constituted by a single layer of non-fenestrated endothelial cells (ECs), surrounded by a basal membrane, the end-feet of perivascular cells (astrocytes and pericytes or smooth muscle in the case of larger vessels), microglia and neurons, that collectively form the neurovascular unit (NVU)¹. Surrounding the BBB, macrophages, and other immune cells interact with the BBB regulating its permeability through inter- or intra-cellular signaling, forming together the extended NVU² (**Figure 7-1**). The BBB is an interesting tissue-tissue interface to study as its selectivity is determinant in the development of new drug delivery systems.

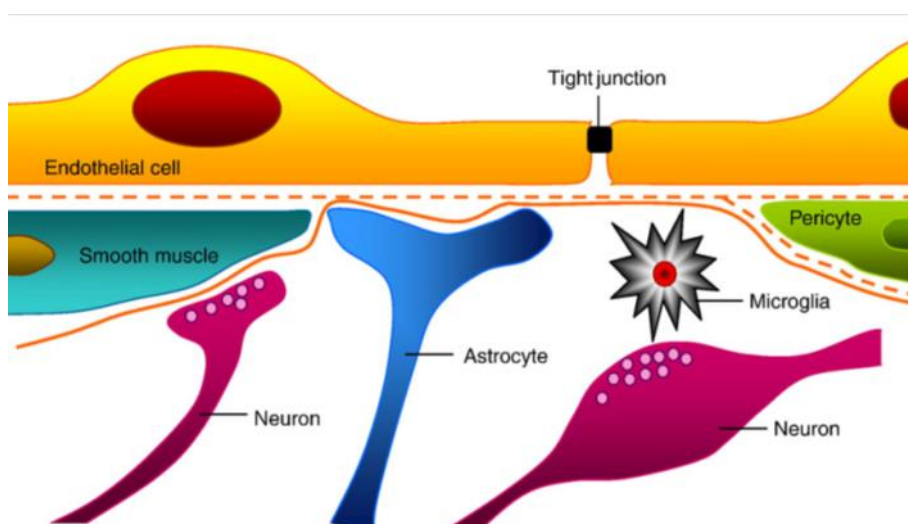


Figure 7-1. BBB structure. The cerebral endothelial cells form tight junctions at their margins which seal the aqueous paracellular diffusional pathway between the cells¹. Pericytes are distributed discontinuously along the length of the cerebral capillaries and partially surround the endothelium¹. Both the cerebral endothelial cells and the pericytes are enclosed by, and contribute to, the local basement membrane which forms a distinct perivascular extracellular matrix¹. Image reproduced from [Abbot et al, 2010](#)¹.

7.1.1.1 The role of Tight Junctions (TJ) and Adherens Junctions (AJ) in BBB integrity

The BBB is responsible for mediating brain supply of nutrients, waste efflux and inhibiting paracellular diffusion, forcing the transport of each kind of molecule

through different transcellular mechanisms, as previously reviewed¹. Its selectivity is vital for the central nervous system, which is protected from toxins, ion fluctuations, interferences with neurotransmitters released in the peripheral nervous system, inflammation, and macromolecules³.

BBB integrity and selectivity is maintained thanks to its junctional complexes (TJ, AJ and gap junctions)⁴⁻⁶. These complexes are intertwined nets of proteins that have a role in controlling the passage of substances. Gap junctions are essential for intercellular communication^{7,8}. TJ can finely regulate barrier permeability by sealing the membrane and forming dynamic size- or charge-selective channels^{9,10}. However, barrier integrity and dynamics are regulated by both TJ and AJ^{4,11}. In brain ECs, the major transmembrane AJ protein is VE-cadherin¹². VE-cadherin based AJ are regulated by Zonula occludens 1 (ZO-1), one of the most relevant components of the TJ, essential for the endothelial barrier formation¹³. Previous studies simulated disruption of these junctions using drugs (i.e. Mannitol, $C_6H_{14}O_6$)^{14,15}.

Mannitol induces the following cascade of events recently reviewed by Linville *et al.*¹⁶: **1)** first of all, it induces the shrinkage of endothelial cells, increasing tensile forces on TJs; **2)** the weakest TJ between adjacent cells fail first, generating transient focal leaks (subcellular randomly distributed disruptions in the endothelium of 1-2 μm); **3)** paracellular permeability increases almost instantaneously, not altering the transcellular permeability or the global TJ network; **4)** micro vessel diameter decreases and endothelial cells present vacuolation in a dose-dependent manner; **5)** endothelial cell apoptosis and lost also occurs in a dose-dependent manner, probably as a result of vacuolation¹⁷; **6)** transient BBB opening is reversed and the barrier function is re-established in a period of time inversely proportional to the dose; **7)** accumulated hyperosmotic stress still presents inconsistent barrier function after 48h.

7.1.2 BBB-on-chip state of art

The three conventional approaches to study transfer across the BBB are parallel artificial membrane permeability assays (PAMPA), cell-based transwell assays, and animal models¹⁸. Advances in microfluidics devices and integrated sensors microfabrication have resulted in a new generation of in vitro OOC BBB models¹⁸. Furthermore, these microfluidic devices are usually suitable for co-culturing various types of cells, allowing for high-resolution imaging, and monitoring intracellular and

extracellular responses. Most importantly, OOC BBB devices can incorporate shear stress.

7.1.2.1 Design approaches

Design solutions for BBB OOC usually follow 4 main approaches: sandwich design, parallel design, 3D tubular design and vasculogenesis design¹⁸.

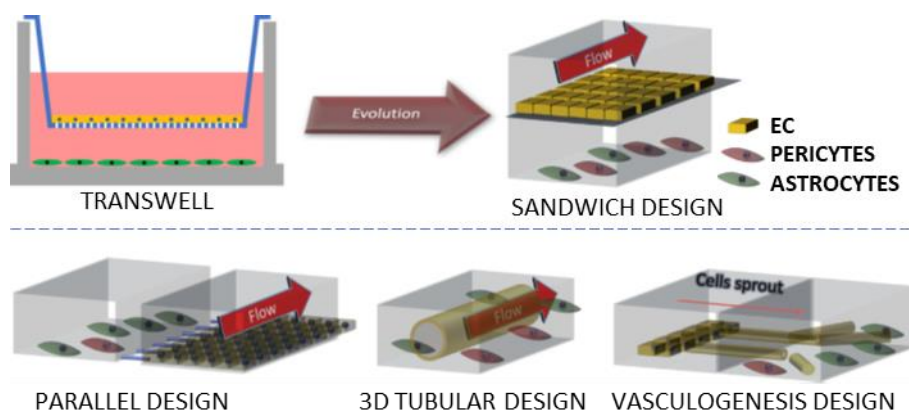


Figure 7-2. Design strategies for BBB OOC models. Image reproduced from [Abbot et al, 2019](#)¹⁹.

Sandwich design approach features two layers of channels (usually PDMS) separated by a porous membrane^{20–24}. Polycarbonate membranes ($0.2\sim 3\ \mu\text{m}$ pore diameter) are commonly used in these devices, similar to the Transwell system¹⁸. Usually ECs are seeded in the upper channel, while pericytes, astrocytes, or other brain cells are cultured in the lower channel, though cell-cell signaling appear to be inhibited by vertical separation¹⁸. Interestingly, in a recent publication reversing the cell seeding configuration, with ECs cultured in 3D vessel-like structure in the lower channel and pericytes and astrocytes seeded in the upper channel, cell–cell contacts can be observed^{18,25}.

Parallel design approach achieve a similar configuration where two parallel channels placed in the same horizontal plane are separated by an array of PDMS microchannels^{26–28} or by an hydrogel^{29,30}. For example, an array of micropillars with $3\text{-}\mu\text{m}$ gaps was reported to separate the blood and brain compartments²⁶ and was then utilized for co-culture with astrocytes²⁷ or brain tumor cells^{18,28}. Though imaging capabilities are improved, PDMS microchannels results in a barrier thickness which is not comparable with the physiological basal membrane¹⁸. Hydrogel-approach

enabled development of a four-channel BBB OOC where hydrogel was premixed with cells (astrocytes or neurons) and loaded into the respective channel²⁹. Collagen gel is also a popular material to form barrier in BBB OOC devices, leading to similar results^{18,30}.

3D tubular design approach aims at fabricating systems with cylindrical channels, which benefits from a more homogenous WSS across the inner surface compared to rectangular-section channels^{18,31}. For example, a collagen gel-based 3D microvascular tube structure has been constructed by using microneedles of different diameters (75~150 μm)³², and such tubular structure was later applied in OOC BBB devices³³. Nonetheless, gel-based 3D tubular OOC devices have a limitation over the difficulty to electrical measurement due to the cylindrical chip design^{18,34}

Finally, vasculogenesis is a less common yet interesting approach which aims to recreate micro vessels *de novo*, without a predetermined scaffold. Introducing a collagen matrix into a microfluidic device in close proximity to ECs, cells sprouted to form new blood microvessels³⁵. The approach consisted of a device with dual channels for ECs and neuronal cells separated by a fibrin hydrogel^{18,36}. Despite probably achieving the best mimicking, the generated micro vessels have irregular branching which limits experimental reproducibility and electrical measurements.

7.1.2.2 *Electrical barrier assessments*

Permeability of the BBB can be assessed, among other methods, by non-invasive electrical measurements. TEER is a widely accepted measurement technique to assess biological barrier integrity which consists in applying an Alternate Current (AC) electrical signal across electrodes placed on both sides of a cellular monolayer and measuring voltage and current to calculate the electrical impedance of the barrier³⁷. As most common TEER measurement approaches, it involves applying low frequency signal close to Direct Current (DC) in order to estimate the value of electrical resistance. This approach is the most common^{27,38-45}, often using commercial dedicated measuring systems like the EVOM2 (World Precision Instruments, Inc., Sarasota, FL USA). We will instead use the term Electrical Impedance Spectroscopy (EIS) to differentiate when the analysis is performed on a broader range including higher frequency of the spectra. Both scenarios consist on measurements across two electrodes, one situated in the brain side and one in the blood side of the BBB.

Most approaches incorporate simple wire electrodes inside the device after assembly^{46–48} or use single pair of embedded electrodes^{20,43}. A recently published approach included an array of simple micro-electrodes⁴⁵. Just few works performed real EIS measurements, with applied signal in the 0.1 Hz~3 MHz frequency range^{21,22,47,48}.

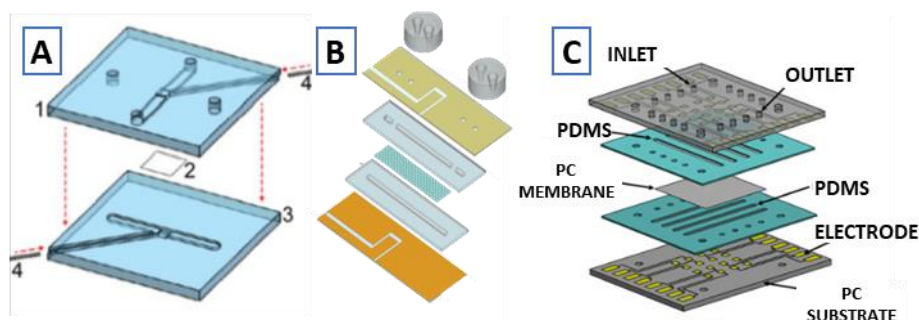


Figure 7-3. BBB TEER-EIS experimental set-ups. A) Schematic representation of the device, with (1) the top part, (2) Transwell membrane and (3) the bottom part of the BBB chip, with side-channels to incorporate the (4) Pt electrodes (Reprinted by permission of Springer Nature from [Griep et al, 2013](#)⁴⁶); B) Structural assembly of device from [Walter et al, 2016](#)²⁴; PDMS reservoirs (gray) holding the inlet and outlet tubes are fixed to the top of the chip. The porous cell culture membrane (dotted sheet) is situated between the upper and the lower channels made of PDMS (light blue); C) 3D illustration showing the multi-layer structure of the BBB chip; © 2018 IEEE. Reprinted, with permission, from [Jeong et al, 2018](#)⁴⁵.

7.2 SPECIFIC OBJECTIVES OF THE CHAPTER

Specific objectives of chapter 7 are:

- 7.1. to verify the viability of fabricated device (OOCv2.1, OOCv2.2) for co-culturing of different cells under flow condition;
- 7.2. to verify repeatability of electrical measurements using electrodes in OOCv2.2;
- 7.3. to adapt immunostaining protocols “on-chip”;
- 7.4. to assess BBB formation and recovery after a disruptive treatment using various techniques;

7.3 MATERIALS AND METHODS

7.3.1 Materials and general cells seeding protocols

This subsection reports detailed information about all the materials used in the biological experiments, the facilities used and the general seeding protocols for OOC devices. Cell seeding and culture protocols are based on general protocols described in the previous chapter.

7.3.1.1 *Materials*

Tygon[®] tubing (ND-100-80, *ID*: 0.51 mm, *OD*: 1.59 mm, Cole Parmer) was from VWR. ZO-1 Monoclonal Antibody (ZO-1-1A12, Alexa Fluor 488, 339188), Goat anti-Rabbit IgG (H+L) Highly Cross-Adsorbed Secondary Antibody (Alexa Fluor 568, A11036), Hoechst 33342, Trihydrochloride, Trihydrate (10 mg/mL in Water, Invitrogen[™] H3570) were from ThermoFisher Scientific (Waltham, MA USA). Anti-VE Cadherin antibody (ab33168) was from Abcam (Cambridge, UK). Human BBB hCMEC/D3 EC line (SCC066) was from Merck Millipore (Burlington, MA USA).

7.3.1.2 *Facilities*

All culture experiments were performed at Institute of Bioengineering of Catalonia, Barcelona, Spain. Confocal microscopy imaging was performed at the Advanced Microscopy Facilities of Institute for Research in Biomedicine (IRB), Barcelona, Spain.







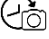

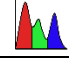
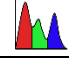
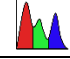
7.3.2 BBB experiments

7.3.2.1 *Rationale*

The following experiments were aimed to mimic the BBB formation, co-culturing two different kind of cells, and its disruption after administering D-Mannitol. To achieve that, we performed two different kind of experiments, using hCMEC/D3 human brain EC line and bovine pericytes to mimic the barrier. On the one hand, we used OOCv2.1 devices to study the phenomena using phase-contrast live microscopy time-lapse and fluorescence imaging after immunostaining. Immunostaining controls were performed using traditional Petri dish cultures. On the other hand, we used OOCv2.2 device to study EIS through impedance spectroscopy. **Table 7-1** resumes the experimental condition of all OOC samples. The timepoints of representative events (seeding, mannitol, fixation) are normalized against the timepoint when confluency was reached (DoC, day of confluence), as there were variations in the effective

density observed after seeding. This was a measure to assure that mannitol treatment was applied on confluent monolayers, in equivalent conditions.

Table 7-1. Experimental conditions overview for BBB experiments. DIV: days in vitro.

Sample abbreviation	BBB1	BBB2	CTRL	BBBE
Description	1 cell type Flow and mannitol	2 cells types, Flow and mannitol	2 cells types Static, No Mannitol	2 cells types, Flow, Mannitol, EIS
OOc version used	2.1	2.1	2.1	2.2
Cells type	hCMEC/D3 only	hCMEC/D3 + Pericytes	hCMEC/D3 + Pericytes	hCMEC/D3 + Pericytes
D-Mannitol			-	
Flow			-	
Assays	Time-lapse			-
	Fluorescence			
	EIS	-	-	-
Events	Confluence (DoC)	3 DIV	3 DIV	3 DIV
	DoC+2	Mannitol	Mannitol	Fixation
	DoC+3	Fixation	Fixation	-

7.3.2.2 BBB cells seeding in OOC v2.1 and OOC v2.2

All four OOCv2.1 devices were seeded according to the general seeding protocol in section 6.2.0.4. Three devices (BBB2, CTRL, BBBE) were seeded on both channels, whereas the fourth device (BBB1) was seeded only in the upper channel. Lower channels were functionalized using a dilution of Collagen, Type I Solution, from rat tail in PBS (1:20, 1 h) and seeded with hCMEC/D3 cells suspension ($2.8 \text{ M cells mL}^{-1}$). Upper channel was functionalized using Gelatin from Porcine

Skin (2 mg mL^{-1} , 10 min) and seeded with bovine pericytes suspension ($2 \text{ M cells mL}^{-1}$).

7.3.2.3 Time-lapse experiments

After 3 DIV, two devices (BBB1, BBB2) were fitted inside the microscope incubator and a third one (CTRL) was cultured under static condition inside standard incubator. Phase contrast time-lapse 10X images were captured every minute for both BBB1 and BBB2 devices using a Nikon Eclipse Ti2 microscope. Additional higher resolution images were captured though a 9MP camera (MU900, AmScope, California, USA) which we had previously attached to the microscope auxiliary optical port and connected to an external PC. Secondary camera acquisition trigger and focus offset adjustment for the second device was managed through a custom Nikon Macro Script we developed.

Media in flow devices (BBB1, BBB2) was changed daily by flowing 2 mL at a flowrate of $50 \mu\text{L min}^{-1}$. Static device (CTRL) media change was performed replacing media inside the on-chip reservoirs. Additional permeability assay was performed daily on BBB1 and BBB2. After 5 DIV, CTRL was fixed, while BBB1 and BBB2 were exposed to D-Mannitol (0.3 M conc, 45 min) and washed using cell culture medium. After 6 DIV, BBB1 and BBB2 were fixed and prepared for immunostaining.

7.3.2.4 Petri Dish Controls

As experimental controls of the device compartmentalized co-culture, hCMEC/D3 ($500 \text{ cells mm}^{-2}$) and pericytes ($360 \text{ cells mm}^{-2}$) were seeded independently in Petri dishes following the same procedures. In all cases, cells were kept in culture for a total of 6 days, changing the medium daily.

7.3.2.5 Electrical Impedance Spectroscopy (EIS) experiment

After cells attached, BBBE device was fitted into the custom incubator adapter and electrical connections were secured. The incubator was maintained at $37 \text{ }^\circ\text{C}$, 95 % Humidity, 5 % CO_2 , 10 % O_2 . Culture medium was changed daily, flowing 1 mL with negative flow of $-50 \mu\text{L min}^{-1}$ and temperature was left stabilizing before starting measurements. After 4 DIV, cells were exposed to D-Mannitol (0.3 M con, 45 min). After 5 DIV, cells in the device were fixed. EIS measurements were performed using an Agilent 4294A precision impedance analyzer (Agilent Technologies, Santa Clara, CA, USA). After selecting 6 channels intersection over 16 available on the device, we

performed measurements using a 3-terminals plus guard configuration. The three-terminal (3T) configuration employs coaxial cables with outer shielding connected to the guard terminal to reduce the effects of stray capacitance extending the typical impedance range above 100 k Ω . From 1 *DIV* to 5 *DIV* included (timepoints *TP1*~*TP5*), using a custom MATLAB interface we acquired 100 spectra every 24h for each selected location (6 locations total, labelled A-F, **Figure 7-4**). Each spectrum was acquired in a frequency range between 100 *Hz* and 10 *MHz*, spanning 300 points in a logarithmic scaling, enabling DC isolation and oscillator voltage of 0.7 *V*.

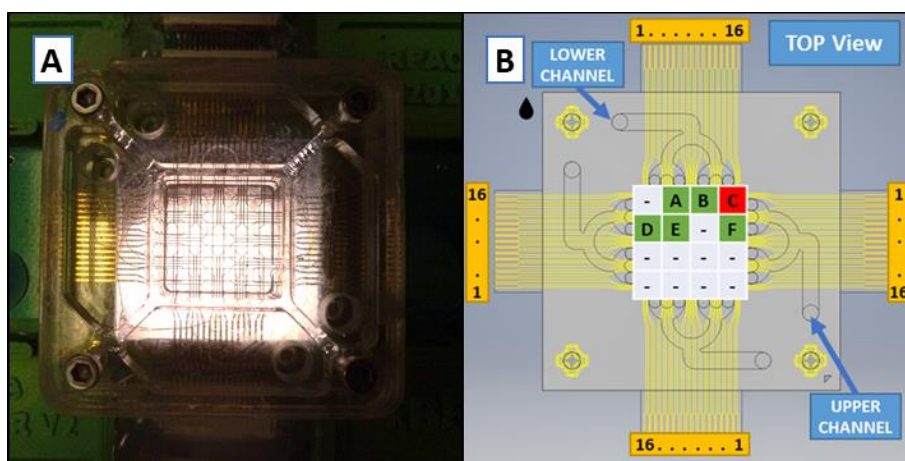


Figure 7-4. BBBE1 measuring configuration. A) OOCv2.2 device mounted on the adapter for BBBE1 experiment. B) Measuring locations configuration; location C (red) was later removed from data due to an experimental error.

7.3.2.6 Cell fixation, staining and imaging

After the end of experiment, cells fixation and staining were performed for BBB1, BBB2 and CTRL devices using a negative flowrate of $-50 \mu\text{L min}^{-1}$. All steps were performed at room temperature, unless otherwise specified. All solutions were prepared in PBS 1X. At each step, indicated volumes were perfused through each channel after aspirating and replacing the liquid in the reservoir.

Devices were washed twice with PBS (1X, 0.5 mL) and fixed using PFA (4%, 0.75 mL). After washing again twice with PBS (1X, 0.75 mL), cells were permeabilized with PBS-Triton (0.1 %, 1 mL). Blocking solution (0.5 mL, 10 % Fetal Bovine Serum [FBS], 0.1 % Triton) was flowed and left in incubation for 2 h. After washing with PBS-triton (0.1 %, 1 mL), primary antibody solution (0.5 mL, 5 % FBS, 0.1 % Triton, sodium azide 0.01 %, 1:1000 VE-Cadherin antibody) was flowed

through the device and left in incubation overnight at 4 °C. Channels were washed again with PBS-triton (0.1 %, 1.5 mL) before applying secondary antibody solution (0.5 mL, 1 h incubation, 5 % FBS, 0.1 % Triton, 0.01 % sodium azide, 1: 1000 Alexa Fluor® 568 donkey anti rabbit). From that point, devices were protected from light. After washing again with PBS-triton, ZO-1 monoclonal antibody solution was applied (0.5 mL, 5 % FBS, 0.01 % sodium azide, 1: 100 ZO-1-1A12, Alexa Fluor® 488, 3 h incubation). Channels were washed again using PBS (1X, 1.25 mL) before applying Hoechst-PBS solution (32.4 μM, 0.5 mL) and finally washed with PBS-azide (1.5 mL, 0.02 %).

Confocal fluorescence images of BBB1, BBB2, CTRL devices and Petri dishes controls were acquired using inverted confocal Leica SP5 microscope.

7.3.2.7 EIS Data Analysis

The acquired dataset consisted of 3000 total measurements by 300 spectral line features matrix. We considered impedance module $|Z|(f)$ defined as

$$|Z|(f) = \sqrt{R(f)^2 + X(f)^2} \quad (7-1)$$

where R is the resistance and X is the reactance at given frequency f , which together give the complex impedance Z

$$Z = R + jX \quad (7-2)$$

To evaluate the measurements repeatability, the fluctuation between measurements was calculated as following:

$$Fluctuation(f)[\%] = \frac{\sigma_{|Z|}(f)}{\mu_{|Z|}(f)} * 100 \quad (7-3)$$

where $\sigma_{|Z|}(f)$ and $\mu_{|Z|}(f)$ are respectively the standard deviation and the mean value of the spectrum at given frequency across all the measurements done at a specific timepoint and in a specific location.

All the data analysis has been performed in MATLAB r2019a environment (MathWorks, US) using a classification toolbox provided by Milano Chemometrics⁴⁹.

Unsupervised and supervised classification of timepoints was performed and evaluated using a 5 groups venetian-blinds cross-validation. Unsupervised classification was performed using a Principal Component Analysis. Supervised

classification was tested using a principal component analysis – linear discriminant analysis (PCA-LDA) model trained with data from positions C, D, E, F (2000 measurements) and tested with data from A and B data (1000 measurements). Finally, after removing data related to a measurement error, LDA model was trained using data from positions D, E, F (1500 measurements) and tested with data from A and B.

7.4 RESULTS

We tested a total of 4 conditions, BBB1, BBB2, CTRL and BBBE. After reaching confluence, at 5 *DIV* BBB1 and BBB2 were treated with D-mannitol, while CTRL device was fixed. BBB1 and BBB2 were left recovering for 24 *h* and then fixed. All devices were immunostained and imaged by confocal microscope. BBB1 and BBB2 were also live imaged along the experiment using phase-contrast time-lapse. BBBE experiment also administered D-mannitol and EIS was characterized across the whole experiment.

7.4.1 Phase contrast time-lapse

Phase contrast frames from time-lapse acquisition from the bottom channel of both devices BBB1 and BBB2 are shown in **Figure 7-5**. Images from BBB1 experiment (ECs only seeded in the device) show loss of confluency after mannitol administration (DoC+2) and no significant recovery after 24 h (DoC+3). Images from BBB2 (both cell types seeded in the device) shows less damage after mannitol administration (DoC+2) and better recovery after 24 h (DoC+3).

7.4.2 Immunostaining

ECs monoculture in a Petri dish (**Figure 7-7**) presented high levels of ZO-1 expression, although not localized in the cell membrane. The exposure of cells to mannitol 0.3 *M* led to an abrupt apoptosis and mostly nuclear localization of the ZO-1, although it was recovered 24 *h* later. VE-cadherin expression, however, was severely affected with the treatment and not fully recovered after.

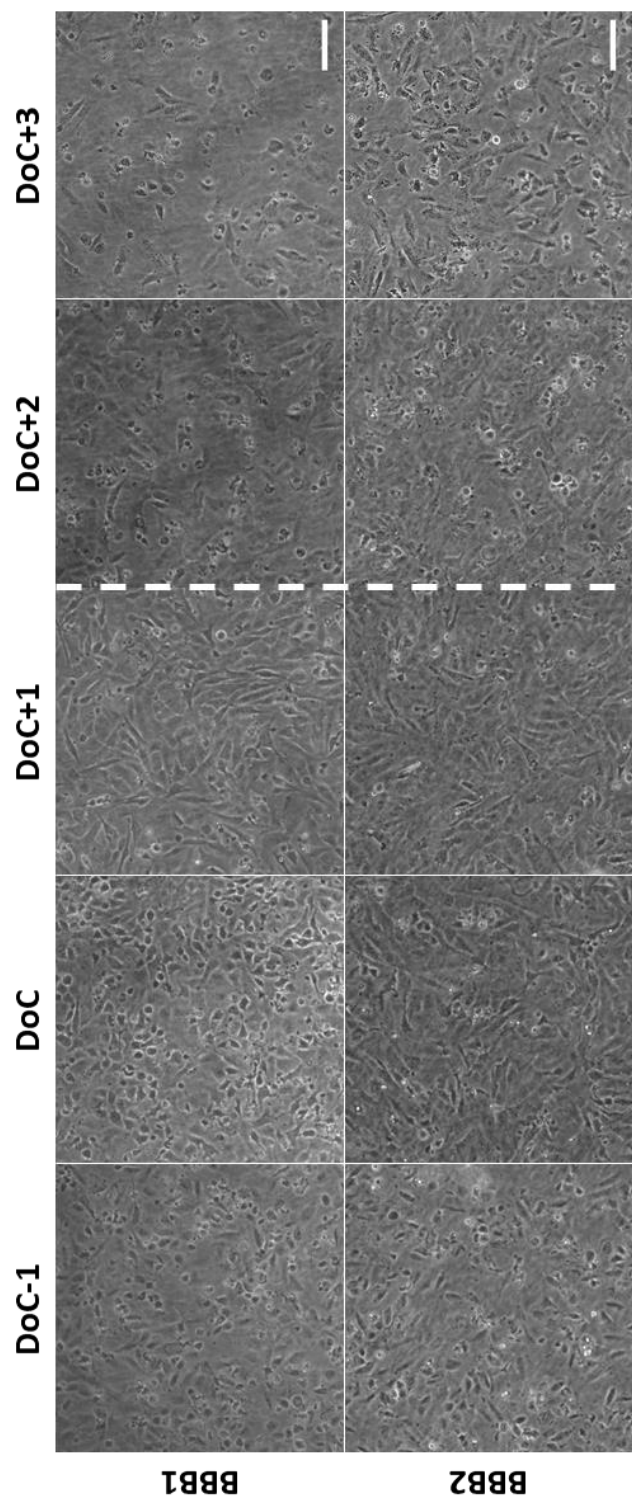


Figure 7-5. Bright field live imaging of the bottom channel of BBB1 and BBB2 experiments. White dashed line represents the moment when mannitol was administered. BBB1 (only ECs) shows higher detrimental effect after mannitol treatment. BBB2 (both cell types) shows better recovery at DoC+3. Scale bar 100 μm .

Pericytes monoculture in a Petri dish (**Figure 7-8**) presented high levels of ZO-1 expression, not exclusively in the cell membrane. When cells were exposed to mannitol, ZO-1 signal decreased slightly and, as a result of apoptosis, some pores appeared on the monolayer. Membrane integrity, in regard to TJ, was restored normally 24h after the mannitol damage. However, it was not restored the VE-cadherin signal.

In OOC devices, where ECs were cultured (bottom of the membrane) with pericytes (top of the membrane) similar variations of marker expression could be observed. Comparison of relevant TJ and AJ markers expression related to confluency before and 24 h after mannitol treatment are shown in **Figure 7-9** and **Figure 7-10**.

On the OOC membrane (**Figure 7-9**), where both ECs and pericytes are interacting at each side of the membrane, similar levels of ZO-1 can be observed in samples fixed before and 24 h after mannitol treatment. VE-cadherin expression is almost absent.

At the bottom of the device (**Figure 7-10**), where only ECs are cultured, severe damages on the ZO-1 and VE-cadherin expression can be observed after mannitol treatment, related with the high apoptosis levels (as observed with the nuclear staining). The corresponding Petri dish controls (**Figure 7-7-A, C**) show higher levels of confluency in both samples.

Results from the membrane of BBB1 (ECs only, **Figure 7-6**) showed as well high levels of damage, apoptosis and barrier disruption when ECs were cultured alone and exposed to mannitol.

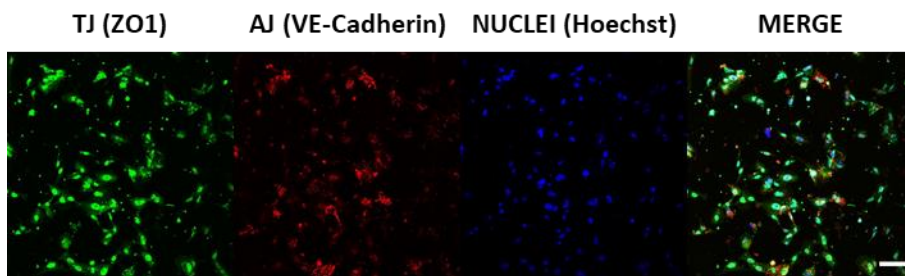


Figure 7-6. Immunostaining results of BBB1 (ECs only), 24 h after mannitol treatment. ZO-1 tight junctions are stained in green. VE-cadherin adherens junctions are stained in red. Nuclei are stained in blue. Scale bar 100 μ m.

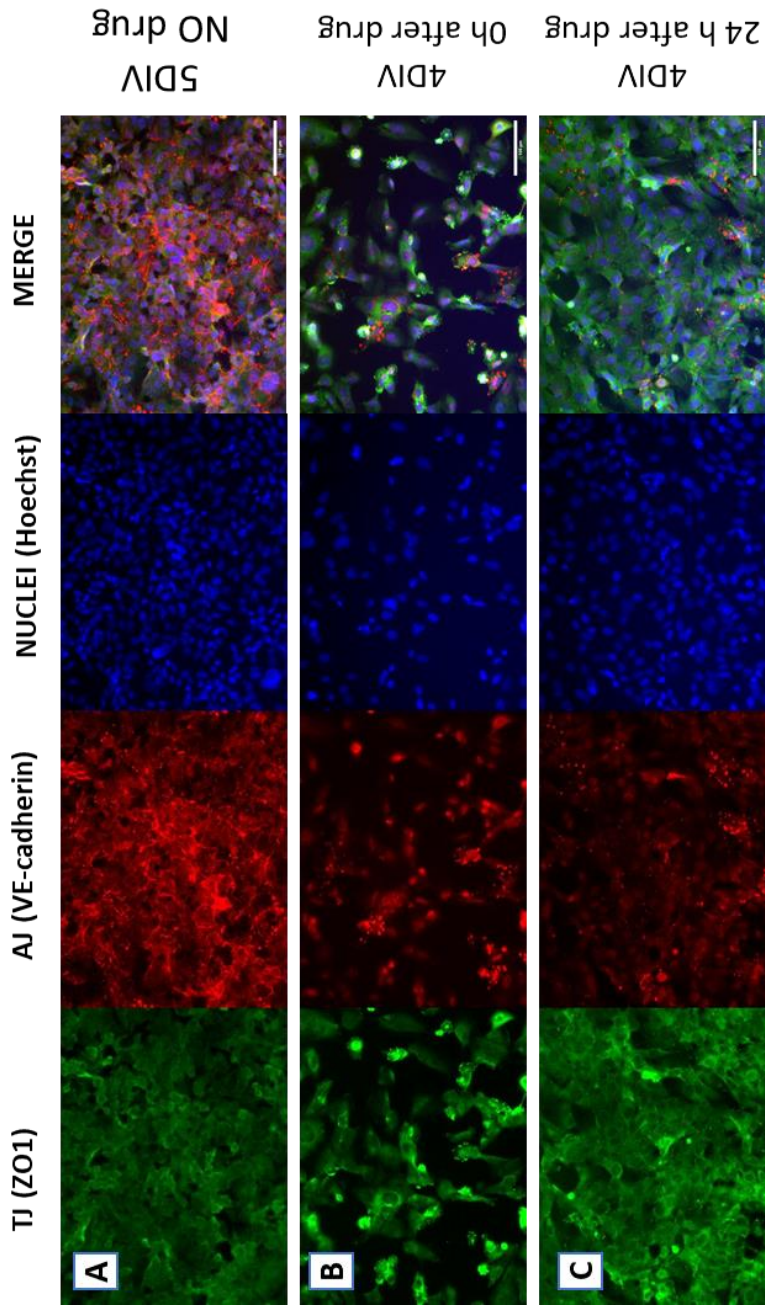


Figure 7-7. Fluorescence images of ECs control culture in Petri dishes. ZO-1 tight junctions are stained in green. VE-cadherin adherens junctions are stained in red. Nuclei are stained in blue. Images show barrier integrity in controls non exposed to mannitol (A), in samples right after mannitol treatment (B) and 24h after the treatment (C). Scale bar 100 μm .

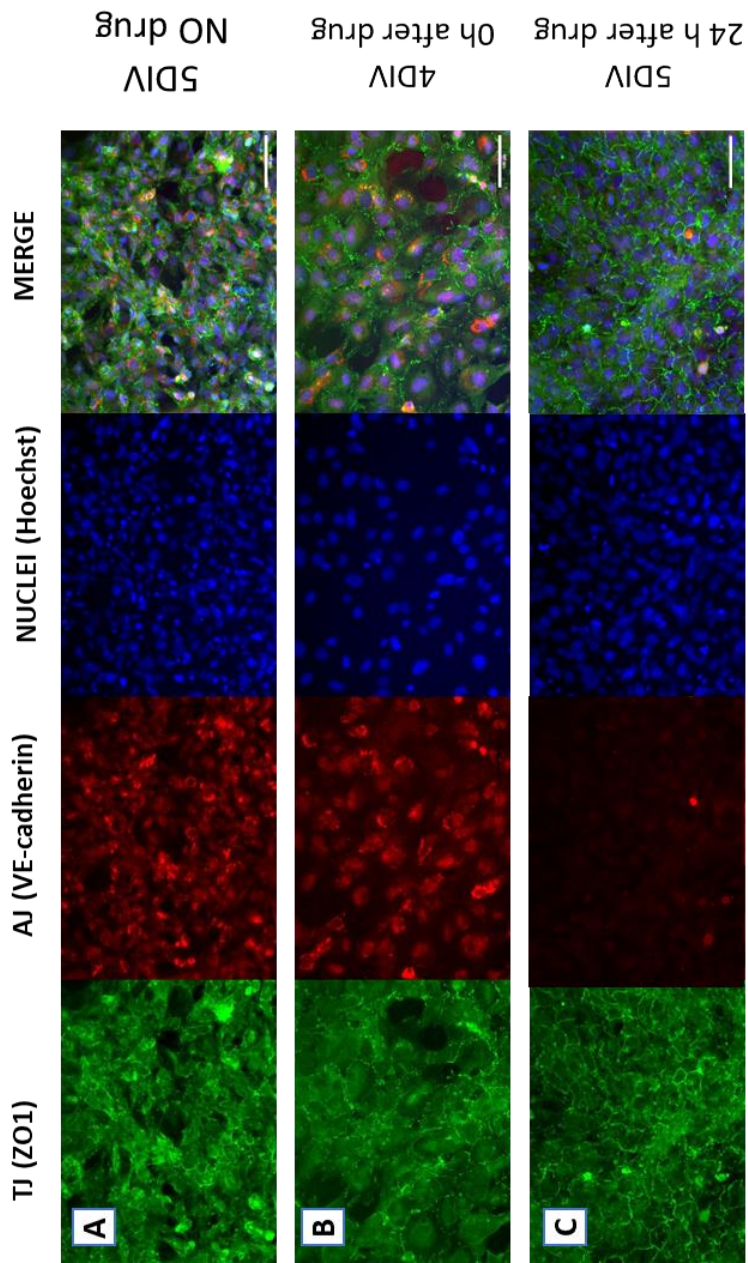


Figure 7-8. Fluorescence images of pericytes control culture in Petri dishes. ZO-1 tight junctions are stained in green. VE-cadherin adherens junctions are stained in red. Nuclei are stained in blue. Images show barrier integrity in controls non exposed to mannitol (A), in samples right after mannitol treatment (B) and 24h after the treatment (C). Scale bar 100µm.

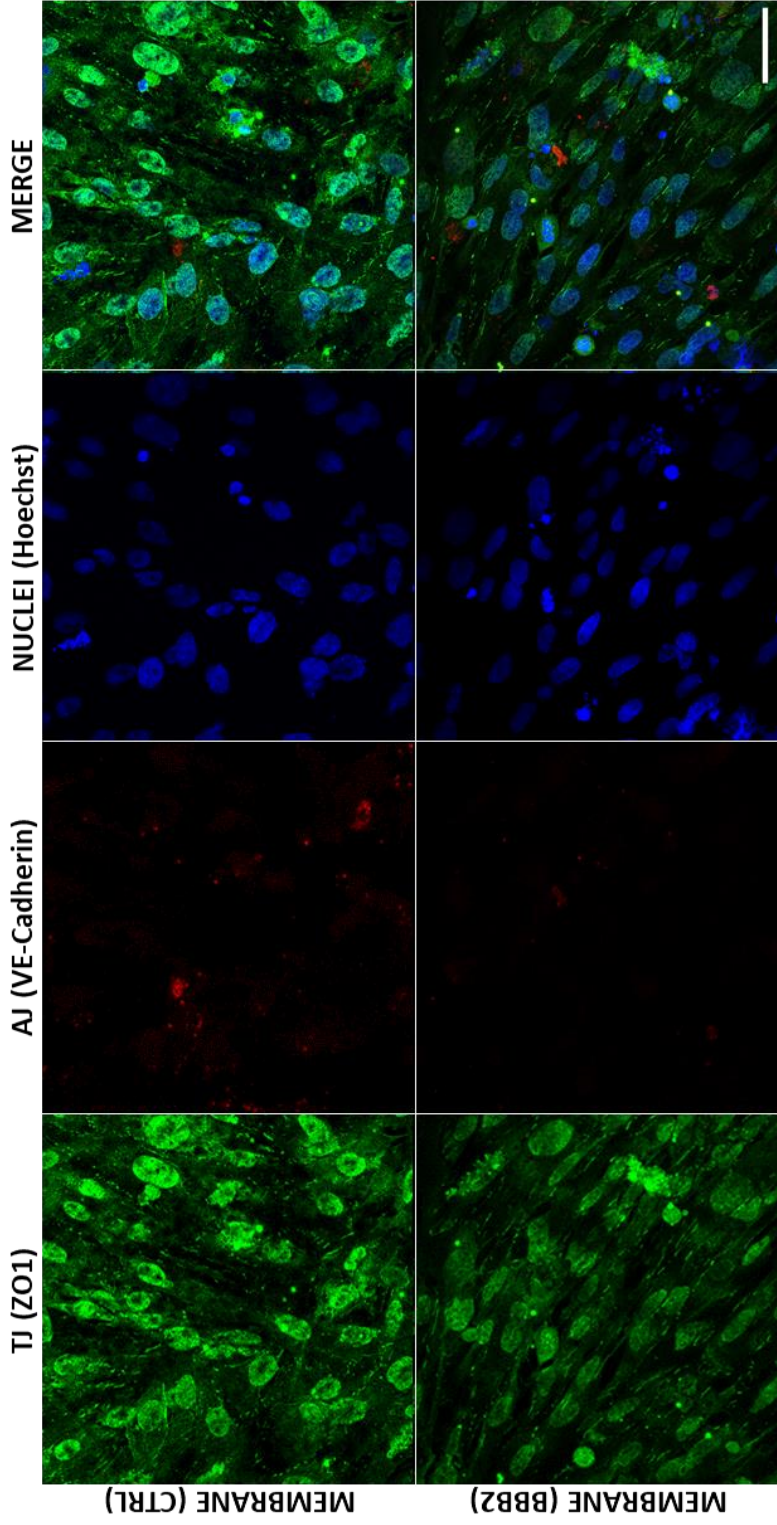


Figure 7-9. Immunostaining of the membrane, where both cell types are present on each side, before (CTRL) and 24-h after mannitol treatment (BBB2). ZO-1 tight junctions are stained in green. VE-cadherin adherens junctions are stained in red. Nuclei are stained in blue. Scale bar 50 μm .

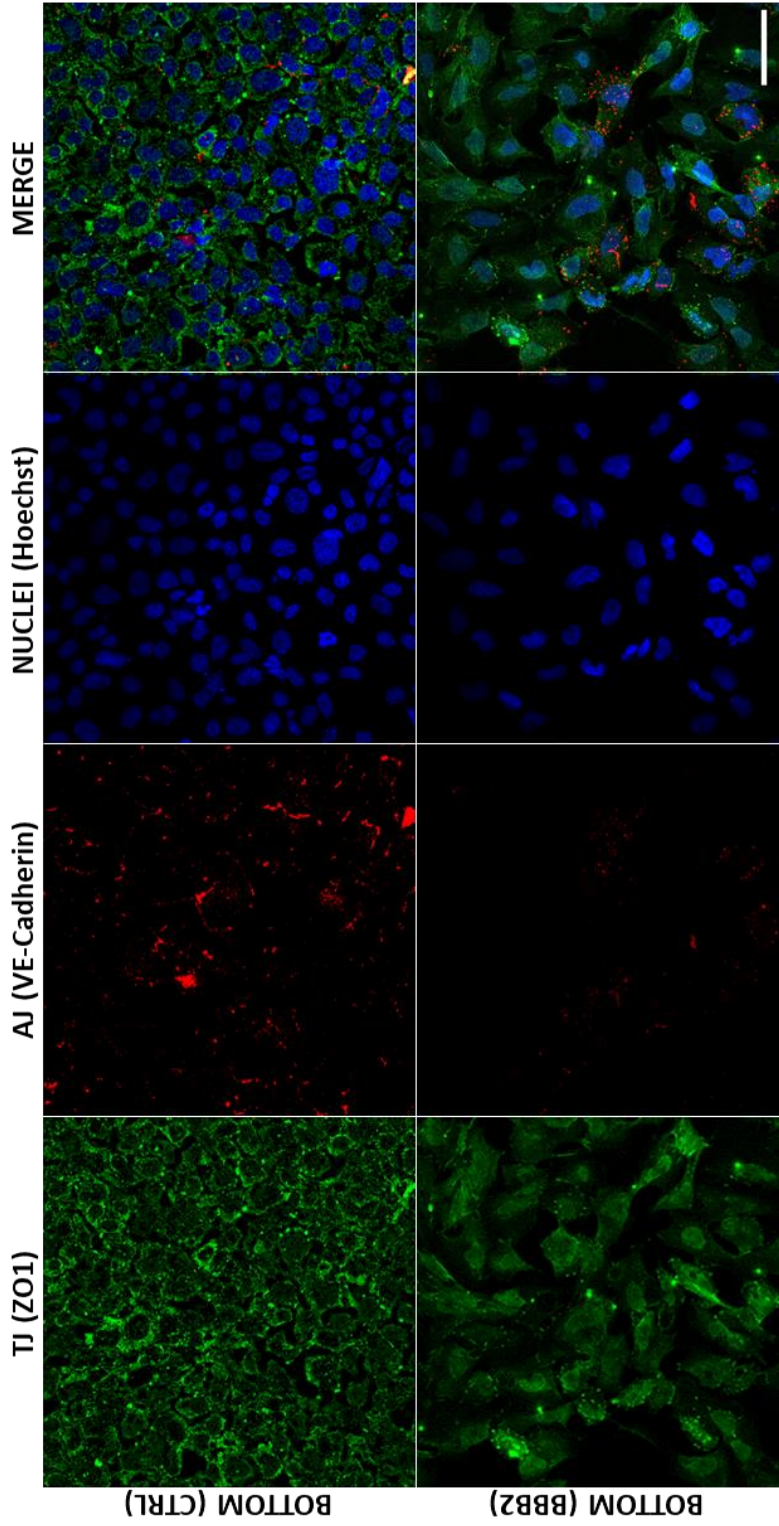


Figure 7-10. Immunostaining of the bottom of the channels (ECs only) before (CTRL) and 24-h after mannitol treatment (BBB2). ZO-1 tight junctions are stained in green. VE-cadherin adherens junctions are stained in red. Nuclei are stained in blue. Scale bar 50 μm .

7.4.3 Electrical impedance spectroscopy (EIS)

The acquired dataset consists in 3000 total measurements by 300 spectral line features matrix. The developed classification method, based on the impedance measurements, can recognize the cell status corresponding to each timepoint.

Typical impedance spectrum at a specific location for each timepoint is shown in **Figure 7-11**. Maximum measurement fluctuation across the whole dataset was 2.5 %.

The PCA has been performed considering 8 PCs explaining more than 99 % of total variance (**Figure 7-12-A**). Supervised PCA-LDA model cross-validation resulted in 97% accuracy in training and 80 % accuracy in testing (**Table 7-2**). Reduction in accuracy was related to misclassification of the samples belonging to DoC and DoC+3. Clear distinction between measurements acquired on different positions can be observed in **Figure 7-12-B**, particularly for DoC-1 (marked with an arrow).

After identifying a measurement error occurred at DoC+2 on location C (-B), the removal of measurements related to location C resulted in improved accuracy both in training (100 %) and in testing (90 %) (**Figure 7-13-B, Table 7-3**).

Table 7-2. Confusion matrix of PCA-LDA model on the whole dataset.

<i>Real/Predicted</i>	DoC-1	DoC	DoC+1	DoC+2	DoC+3
DoC-1	200	0	0	0	0
DoC	0	200	0	0	0
DoC+1	0	0	100	100	0
DoC+2	0	0	0	200	0
DoC+3	0	100	0	0	100

Table 7-3. Confusion matrix of LDA model after excluding location C.

<i>Real/Predicted</i>	DoC-1	DoC	DoC+1	DoC+2	DoC+3
DoC-1	200	0	0	0	0
DoC	0	200	0	0	0
DoC+1	0	0	200	0	0
DoC+2	0	0	0	200	0
DoC+3	0	100	0	0	100

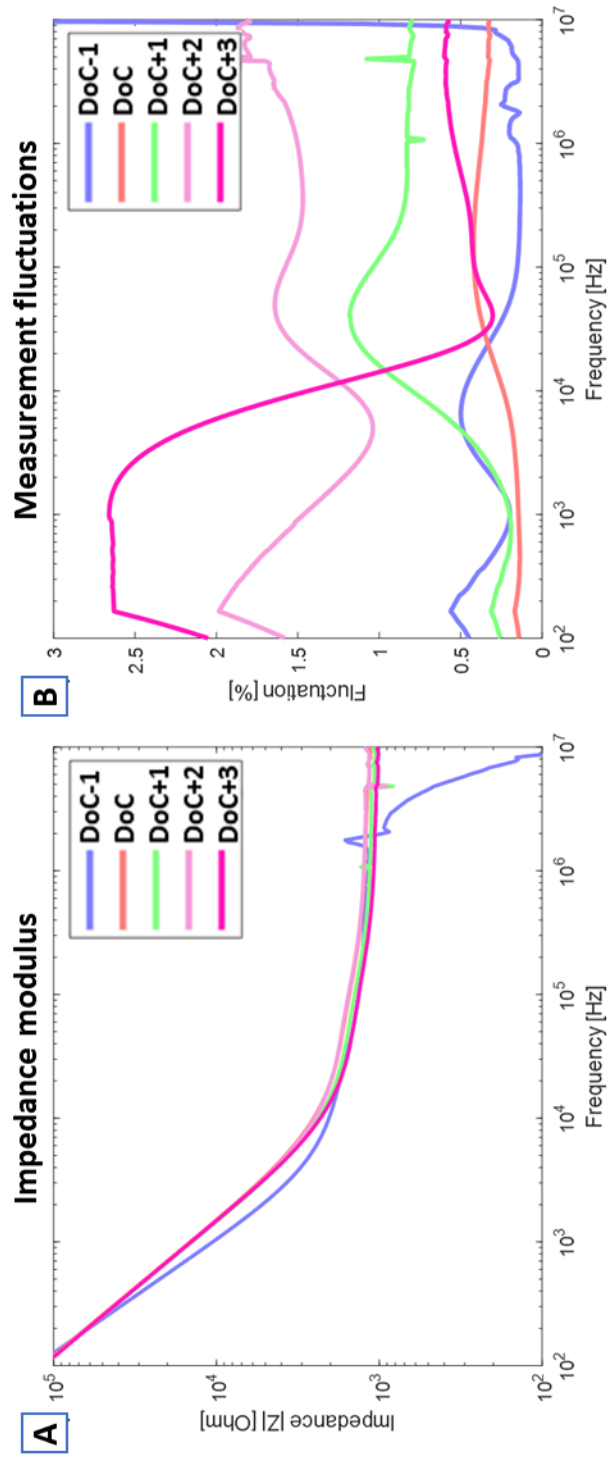


Figure 7-11. Typical measured impedance spectra across different timepoints. A) Impedance modulus spectrum across all timepoints of a single location; B) Measurements fluctuations across all timepoints of a single location.

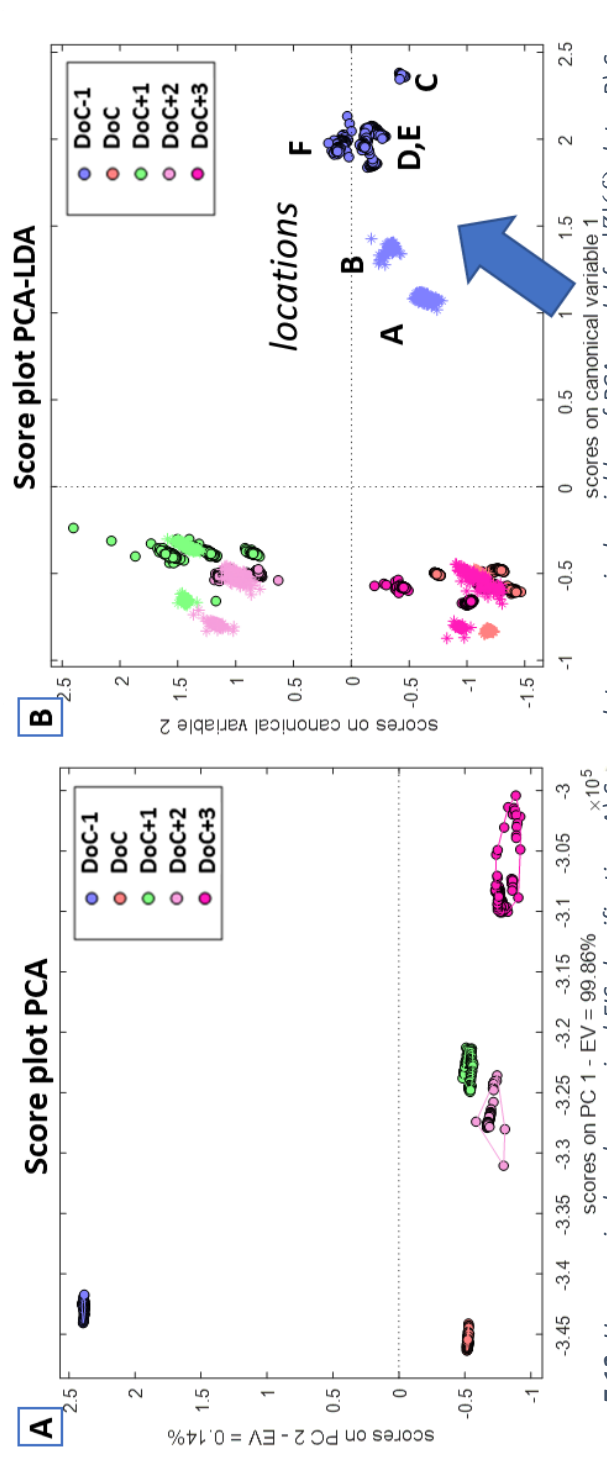


Figure 7-12. Unsupervised and supervised EIS classification. A) Score plot on canonical variables of PCA model for $|Z|(f)$ data; B) Score plot on canonical variables of PCA -LDA model for $|Z|(f)$ data. Dots represent training data; asterisks represent test data. Distinction between measurements acquired on different positions is particularly evident for DOC-1 data (arrow).

7.5 DISCUSSION

Both live phase-contrast imaging and confocal imaging showed greater cells viability and recovery in experiments involving both cell types (BBB2, CTRL) (**Figure 7-5-BBB2, Figure 7-9, Figure 7-10,**) compared to ECs only (BBB1) (**Figure 7-6 and Figure 7-5-BBB1**). This result suggests an active role of the pericytes in the integrity of the BBB and in the recovery from a hyperosmotic transient opening. The result is coherent with previous works in the literature which evidenced the critical role of pericytes in the development, maintenance, and regulation of BBB^{50,51}.

In CTRL experiments, ZO-1 staining shows formation of TJ both on the membrane (both cell types) (**Figure 7-9-CTRL**) and at the bottom (ECs only) (**Figure 7-10-CTRL**). At the membrane, where we had lower confluency levels, ZO-1 expression was also lower and more localized on the nuclei. Based on previous reports that suggested that ZO-1 localization on the cell is related to the maturity and extent of cell-cell contacts⁵², we can conclude that we did not have a fully mature barrier on the membrane whereas it was higher but still not fully mature at the bottom. VE-cadherin staining results support as well that conclusion. We saw the formation of AJ on the bottom of the lower channel, where only ECs are present (**Figure 7-10-CTRL**). On the contrary, imaging of the membrane separating the channels (**Figure 7-9-CTRL**), with both cell types cultured on the respective side, showed negative AJ signal. In comparison, VE-cadherin and ZO-1 levels were higher in the corresponding controls of ECs in Petri dishes (**Figure 7-7-No drug**) and pericytes in Petri dishes (**Figure 7-8-No drug**). This is directly related with the maturity of the barrier formation and with the crosstalk required between TJ complex proteins and AJ complex proteins during barrier development^{4,13}.

After exposing our devices to mannitol treatment, more drastic effects were observed at the bottom of the channel (**Figure 7-10-BBB2**) than on the membrane (**Figure 7-9-BBB2**). Considering that the barrier was not fully mature in any of the two sides, we can conclude that this difference in the mannitol effect is, once more, directly related to the direct contact of pericytes on the other side of the membrane, which contribute on maintaining the integrity of the BBB and recovering it^{50,51}. They have previously been reported to play an essential role on the BBB regulating the

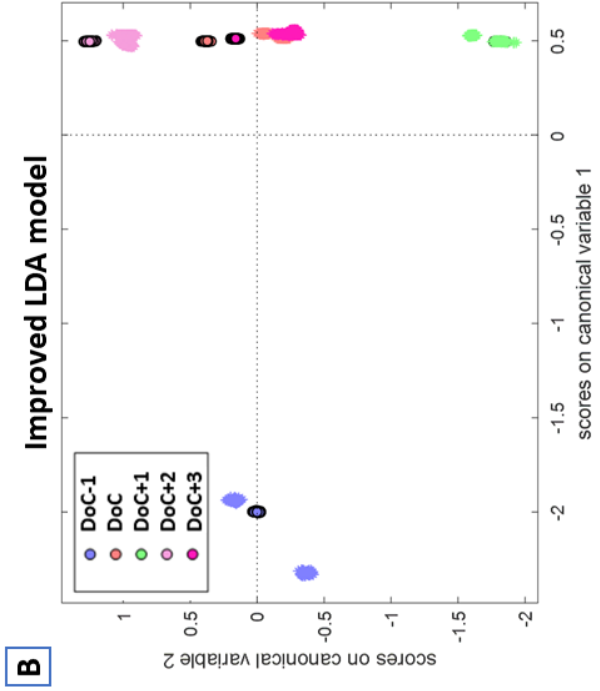
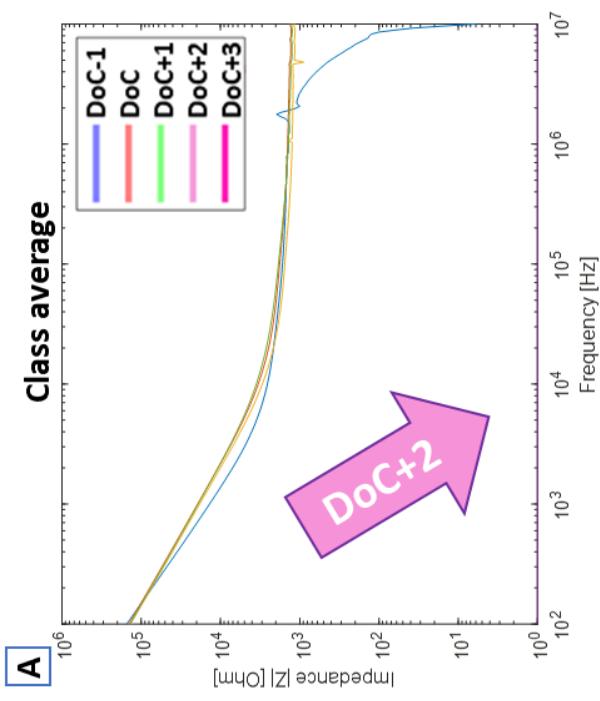


Figure 7-13. Improved EIS supervised classification. A) Impedance spectrum average across all timepoints of measurements performed on location C, showing measurement error on DoC+2 (arrow); B) Score plot on canonical variables of LDA model for $|Z|(f)$ dataset, excluding location C.

transcytosis of ECs, the integrity (as measured through TEER), the synthesis of basal membrane compounds (that contribute to the membrane tightness), the expression of efflux pumps, the inhibition of immune cell trafficking and the permeation of agents that promote vascular permeability⁵³.

Petri dishes controls showed higher formation of AJ in ECs (**Figure 7-7**), while TJ were more defined in pericytes (**Figure 7-8**). This could explain higher presence of both TJ and AJ on the membrane when co-cultured (**Figure 7-9**), as compared to BBB1 (**Figure 7-6**). Also, higher confluency of Petri dish controls may be related to a small error in the effective seeding density in OOC devices. While proportional volumetric densities had been correctly calculated, seeding of the devices is still one of the most delicate steps of the experimental procedure. Moreover, lower recovery of confluency and TJ and AJ signal in OOC devices after the treatment might be related to the same reason. The more confluent the cells are, the more likely they form a mature and stronger barrier, needing higher mannitol doses to cause disruption. It has been previously reported that the treatment dose that we used requires up to 4 days to obtain a full recovery of the integrity status when the drug was applied³³. Some studies have also reported that that barrier integrity, measured through TEER, is highly affected by the seeding density of ECs⁵⁴.

At last an LDA model based on impedance module $|Z|(f)$ was developed which is able to separate measurements from different timepoints with an accuracy of 90/100 % (training/testing). Some considerations can be done about different timepoints. According to LDA model, DoC-1 measurement represents the class with most separation against the others. On the contrary, EIS Measurements from DoC and DoC+3 are really close to each other. 24 h after administration of mannitol (DoC+3), cells had started to recover, reaching confluence levels similar to DoC (**Figure 7-5**), while AJ and TJ are not yet fully recovered (**Figure 7-9** and **Figure 7-10**). Then, misclassification between measurements from DoC and DoC+3 might have a biological meaning, as a consequence of the restoration of a biological stage (confluency and barrier integrity levels) similar to DoC (**Figure 7-14**). The separation of DoC+2 can be related to biological phenomena of cell shrinkage, vacuolation and apoptosis caused by mannitol treatment. Similarly, DoC-1 separation from the all the other classes has a biological explanation, as cell confluency is still very low and cells with short time in vitro are not yet stable.

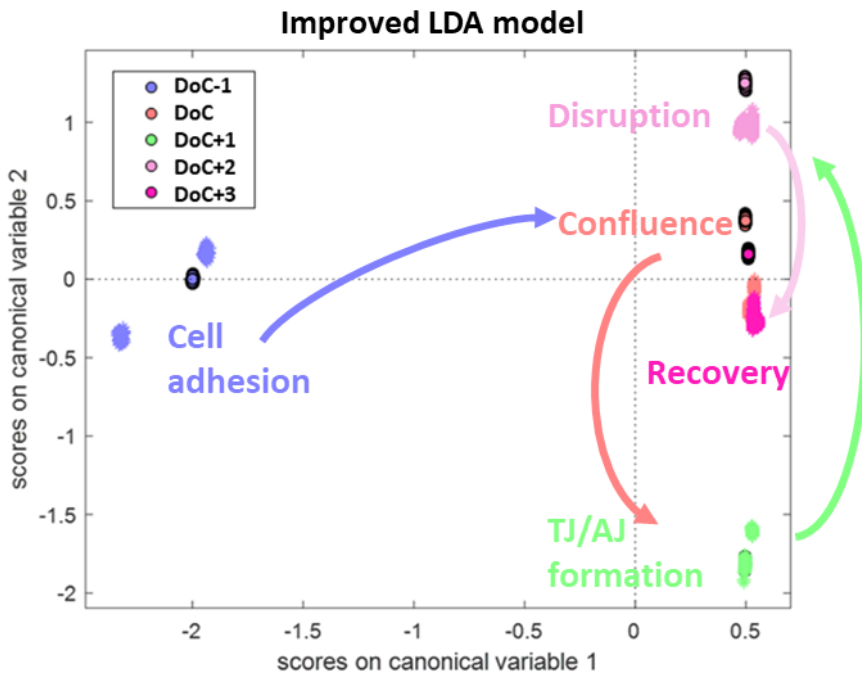


Figure 7-14. Improved EIS model with overlay of biological data interpretation.

7.6 CONCLUSIONS

BBB experiments showed viability of both OOCv2.1 and OOCv2.2 for co-culturing of different types of cells. To mimic the BBB, ECs and pericytes were cultured inside the devices. After 4 DIV, formation of AJ and TJ could be observed. Administering Mannitol resulted in an impairment of the barrier, affecting cells confluence and formation of junctional complexes. Co-culturing of both cell types (BBB2) resulted in better recovery after mannitol administering compared to only brain ECs (BBB1). Results suggest a critical role of pericytes in the development, maintenance, and regulation of BBB, in accordance with the literature.

EIS measurements for assessing barrier formation were performed on 6 different location of the device. An LDA model for classification of measurements from different timepoints was developed. After removal of data related to a measurement error, the model resulted in 100 % accuracy in training and 90 % accuracy in testing. Misclassification only occurred between timepoints DoC and DoC+3, which might be justified by a similar biological stage of confluency and barrier integrity levels.

7.7 REFERENCES

1. Abbott, N. J., Patabendige, A. A. K., Dolman, D. E. M., Yusof, S. R. & Begley, D. J. Structure and function of the blood–brain barrier. *Neurobiol. Dis.* **37**, 13–25 (2010).
2. Neuwelt, E. A. *et al.* Engaging neuroscience to advance translational research in brain barrier biology. *Nat. Rev. Neurosci.* **12**, 169–182 (2011).
3. Abbott, N. J. Blood–brain barrier structure and function and the challenges for CNS drug delivery. *J. Inherit. Metab. Dis.* **36**, 437–449 (2013).
4. Tietz, S. & Engelhardt, B. Brain barriers: Crosstalk between complex tight junctions and adherens junctions. *J. Cell Biol.* **209**, 493–506 (2015).
5. Stamatovic, S. M., Johnson, A. M., Keep, R. F. & Andjelkovic, A. V. Junctional proteins of the blood–brain barrier: New insights into function and dysfunction. *Tissue Barriers* **4**, e1154641 (2016).
6. Keep, R. F. *et al.* Brain endothelial cell junctions after cerebral hemorrhage: changes, mechanisms and therapeutic targets. *J. Cereb. Blood Flow Metab.* **38**, 1255–1275 (2018).
7. Bader, A. *et al.* Adenosine receptors regulate gap junction coupling of the human cerebral microvascular endothelial cells hCMEC/D3 by Ca²⁺ influx through cyclic nucleotide-gated channels. *J. Physiol.* **595**, 2497–2517 (2017).
8. Meşe, G., Richard, G. & White, T. W. Gap Junctions: Basic Structure and Function. *J. Invest. Dermatol.* **127**, 2516–2524 (2007).
9. Anderson, J. M. & Van Itallie, C. M. Physiology and Function of the Tight Junction. *Cold Spring Harb. Perspect. Biol.* **1**, a002584–a002584 (2009).
10. Steed, E., Balda, M. S. & Matter, K. Dynamics and functions of tight junctions. *Trends Cell Biol.* **20**, 142–149 (2010).
11. Shigetomi, K., Ono, Y., Inai, T. & Ikenouchi, J. Adherens junctions influence tight junction formation via changes in membrane lipid composition. *J. Cell Biol.* **217**, 2373–2381 (2018).
12. Li, W., Chen, Z., Chin, I., Chen, Z. & Dai, H. The Role of VE-cadherin in Blood-brain Barrier Integrity Under Central Nervous System Pathological Conditions. *Curr. Neuropharmacol.* **16**, 1375–1384 (2018).
13. Tornavaca, O. *et al.* ZO-1 controls endothelial adherens junctions, cell–cell tension, angiogenesis, and barrier formation. *J. Cell Biol.* **208**, 821–838 (2015).
14. Kim, J. A. *et al.* Collagen-based brain microvasculature model in vitro using three-dimensional printed template. *Biomicrofluidics* **9**, 1–16 (2015).
15. Chen, R., Zhao, X. & Hu, K. *Physically open BBB. Brain Targeted Drug Delivery System* (Elsevier Ltd., 2019). doi:10.1016/b978-0-12-814001-7.00009-3
16. Linville, R. M. *et al.* Modeling hyperosmotic blood–brain barrier opening within

- human tissue-engineered in vitro brain microvessels. *J. Cereb. Blood Flow Metab.* 0271678X1986798 (2019). doi:10.1177/0271678X19867980
17. Shubin, A. V, Demidyuk, I. V, Komissarov, A. A., Rafieva, L. M. & Kostrov, S. V. Cytoplasmic vacuolization in cell death and survival. *Oncotarget* **7**, 55863–55889 (2016).
 18. Oddo, A. *et al.* Advances in Microfluidic Blood–Brain Barrier (BBB) Models. *Trends Biotechnol.* (2019). doi:10.1016/j.tibtech.2019.04.006
 19. Oddo, A. *et al.* Advances in Microfluidic Blood–Brain Barrier (BBB) Models. *Trends Biotechnol.* (2019). doi:10.1016/j.tibtech.2019.04.006
 20. Booth, R. & Kim, H. Characterization of a microfluidic in vitro model of the blood-brain barrier (μ BBB). *Lab Chip* **12**, 1784 (2012).
 21. Griep, L. M. *et al.* BBB on CHIP: Microfluidic platform to mechanically and biochemically modulate blood-brain barrier function. *Biomed. Microdevices* **15**, 145–150 (2013).
 22. Brown, J. A. *et al.* Recreating blood-brain barrier physiology and structure on chip: A novel neurovascular microfluidic bioreactor. *Biomicrofluidics* **9**, (2015).
 23. Sellgren, K. L., Hawkins, B. T. & Grego, S. An optically transparent membrane supports shear stress studies in a three-dimensional microfluidic neurovascular unit model. *Biomicrofluidics* **9**, (2015).
 24. Walter, F. R. *et al.* A versatile lab-on-a-chip tool for modeling biological barriers. *Sensors Actuators B Chem.* **222**, 1209–1219 (2016).
 25. Maoz, B. M. *et al.* A linked organ-on-chip model of the human neurovascular unit reveals the metabolic coupling of endothelial and neuronal cells. *Nat. Biotechnol.* **36**, 865–874 (2018).
 26. Prabhakarbandian, B. *et al.* SyM-BBB: a microfluidic blood brain barrier model. *Lab Chip* **13**, 1093 (2013).
 27. Deosarkar, S. P. *et al.* A novel dynamic neonatal blood-brain barrier on a chip. *PLoS One* **10**, 1–21 (2015).
 28. Terrell-Hall, T. B., Ammer, A. G., Griffith, J. I. G. & Lockman, P. R. Permeability across a novel microfluidic blood-tumor barrier model. *Fluids Barriers CNS* **14**, 1–10 (2017).
 29. Adriani, G., Ma, D., Pavesi, A., Kamm, R. D. & Goh, E. L. K. A 3D neurovascular microfluidic model consisting of neurons, astrocytes and cerebral endothelial cells as a blood–brain barrier. *Lab Chip* **17**, 448–459 (2017).
 30. Xu, H. *et al.* A dynamic in vivo-like organotypic blood-brain barrier model to probe metastatic brain tumors. *Sci. Rep.* **6**, 36670 (2016).
 31. van der Helm, M. W., van der Meer, A. D., Eijkel, J. C. T., van den Berg, A. & Segerink, L. I. Microfluidic organ-on-chip technology for blood-brain barrier research. *Tissue*

Barriers **4**, (2016).

32. Chrobak, K. M., Potter, D. R. & Tien, J. Formation of perfused, functional microvascular tubes in vitro. *Microvasc. Res.* **71**, 185–196 (2006).
33. Kim, J. A. *et al.* Collagen-based brain microvasculature model in vitro using three-dimensional printed template. *Biomicrofluidics* **9**, 024115 (2015).
34. Herland, A. *et al.* Distinct Contributions of Astrocytes and Pericytes to Neuroinflammation Identified in a 3D Human Blood-Brain Barrier on a Chip. *PLoS One* **11**, e0150360 (2016).
35. Song, J. W. & Munn, L. L. Fluid forces control endothelial sprouting. *Proc. Natl. Acad. Sci. U. S. A.* **108**, 15342–15347 (2011).
36. Bang, S. *et al.* A Low Permeability Microfluidic Blood-Brain Barrier Platform with Direct Contact between Perfusable Vascular Network and Astrocytes. *Sci. Rep.* **7**, 8083 (2017).
37. Hickman, J. Transepithelial/endothelial Electrical Resistance (TEER) theory and applications for microfluidic body-on-a-chip devices. *J. Rare Dis. Res. Treat.* **1**, 46–52 (2018).
38. Papademetriou, I., Vedula, E., Charest, J. & Porter, T. Effect of flow on targeting and penetration of angiopep-decorated nanoparticles in a microfluidic model blood-brain barrier. *PLoS One* **13**, 1–18 (2018).
39. Partyka, P. P. *et al.* Mechanical stress regulates transport in a compliant 3D model of the blood-brain barrier. *Biomaterials* **115**, 30–39 (2017).
40. Wang, Y. I., Abaci, H. E. & Shuler, M. L. Microfluidic blood–brain barrier model provides in vivo-like barrier properties for drug permeability screening. *Biotechnol. Bioeng.* **114**, 184–194 (2017).
41. Xu, H. *et al.* A dynamic in vivo-like organotypic blood-brain barrier model to probe metastatic brain tumors. *Sci. Rep.* **6**, 36670 (2016).
42. Herland, A. *et al.* Distinct Contributions of Astrocytes and Pericytes to Neuroinflammation Identified in a 3D Human Blood-Brain Barrier on a Chip. *PLoS One* **11**, e0150360 (2016).
43. Walter, F. R. *et al.* A versatile lab-on-a-chip tool for modeling biological barriers. *Sensors Actuators, B Chem.* **222**, 1209–1219 (2016).
44. Booth, R. & Kim, H. Characterization of a microfluidic in vitro model of the blood-brain barrier (μ BBB). *Lab Chip* **12**, 1784–1792 (2012).
45. Jeong, S. *et al.* A Three-Dimensional Arrayed Microfluidic Blood–Brain Barrier Model With Integrated Electrical Sensor Array. *IEEE Trans. Biomed. Eng.* **65**, 431–439 (2018).
46. Griep, L. M. *et al.* BBB on CHIP: Microfluidic platform to mechanically and biochemically modulate blood-brain barrier function. *Biomed. Microdevices* **15**, 145–150 (2013).

47. van der Helm, M. W. *et al.* Direct quantification of transendothelial electrical resistance in organs-on-chips. *Biosens. Bioelectron.* **85**, 924–929 (2016).
48. Falanga, A. P. *et al.* Shuttle-mediated nanoparticle transport across an in vitro brain endothelium under flow conditions. *Biotechnol. Bioeng.* **114**, 1087–1095 (2017).
49. Ballabio, D. A MATLAB toolbox for Principal Component Analysis and unsupervised exploration of data structure. *Chemom. Intell. Lab. Syst.* (2015). doi:10.1016/j.chemolab.2015.10.003
50. Lai, C. H. & Kuo, K. H. The critical component to establish in vitro BBB model: Pericyte. *Brain Res. Rev.* **50**, 258–265 (2005).
51. Blanchette, M. & Daneman, R. Formation and maintenance of the BBB. *Mech. Dev.* **138**, 8–16 (2015).
52. Gottardi, C. J., Arpin, M., Fanning, A. S. & Louvard, D. The junction-associated protein, zonula occludens-1, localizes to the nucleus before the maturation and during the remodeling of cell-cell contacts. *Proc. Natl. Acad. Sci.* **93**, 10779–10784 (1996).
53. Moura, R. P., Almeida, A. & Sarmento, B. The role of non-endothelial cells on the penetration of nanoparticles through the blood brain barrier. *Prog. Neurobiol.* **159**, 39–49 (2017).
54. Eigenmann, D. E. *et al.* Comparative study of four immortalized human brain capillary endothelial cell lines, hCMEC/D3, hBMEC, TY10, and BB19, and optimization of culture conditions, for an in vitro blood–brain barrier model for drug permeability studies. *Fluids Barriers CNS* **10**, 33 (2013).

8 General Conclusions

In this thesis different microfluidic devices with cell culture interfaces for OOC applications were successfully designed, fabricated and tested. Improved fabrication techniques have been tested and applied, moving from standard PDMS soft lithography to more recent DM techniques, like LOM (with laser cut and xurography) and SL 3D printing.

Using traditional PDMS soft-lithography techniques, a first multilayer organ-on-chip device with embedded commercial membrane (OOCv1) was successfully designed considering generalized Hess-Murray law. Optimized fabrication protocols enabled to achieve low-profile devices for high resolution imaging. Computer simulations of WSS confirmed a decreasing distribution toward the center of the device to promote cell adhesion and increase residence time inside the membrane area.

Using LOM techniques, two different DM RP protocols were developed for the fabrication of OOCv2 biocompatible device in COP with embedded commercial membrane. Both protocols, respectively involving cutting plotter and laser cutter machine, allowed mask-less fabrication and assembly of final COP devices with embedded Mini Luer® connectors in PMMA in less than 1~2 hours. The developed process is rapid, low cost and enables easy modifications of the design, connectors embedding and scalability.

The designs were easily modified by adding extra features like standard ¼-28 UNF threaded connectors and on-chip medium reservoirs (OOCv2.1) or electrodes for TEER measurement (OOCv2.2). OOCv2.1 design improved fluidic connections and versatility of OOC2.0 device. Also, OOCv2.1 proved the potential for process scalability by achieving the fabrication of a full batch of 20 devices in less than 8 hours, with yet lot of room for throughput improvements by automating the assembly process. OOCv2.2 demonstrated the compatibility of the same DM process with the integration of 16 double pairs interdigitated gold electrodes, featuring easy-to-handle standard ZIF connectors. Both contributions were also aimed at simplifying the “world-to-chip” problem of microfluidics, which inherently affects OOC.

A low-cost compact experimental set-up with embedded flow control was also developed. The experimental unit is a complete portable system which simplifies

OOO experimental setup and usability. Fitting a complete microfluidic setup inside a small microscope microincubator, it aims to encourage early adoption of OOO technologies in standard biomedical laboratories by reducing startup costs and setup complexity.

We have implemented and improved a technological process based on SL 3D printing technology for the fabrication of microfluidic devices. A commercial SL printer was first modified, through different design iterations, to enable high resolution printing of transparent resins. Both XY- and Z-resolution were improved, as well as surface roughness which is determinant to achieve transparent devices. Functional example LOC device have been printed and complete channels with hydraulic diameter down to $600\ \mu\text{m}$ were successfully printed, though better results are expected using high definition UV resins. Two possible strategies for RP of OOO devices were demonstrated. On the one hand, an easy solution for embedding commercial membranes in 3D printed OOO device was established mixing 3D printing and laser cut techniques. In addition, SL viability as tool for PDMS multi-layered soft lithography was demonstrated. To the best of our knowledge, it is the first time SL is used for RP of PDMS multi-layered devices.

Finally, all the OOO technology developed was tested in biological applications. Tubular kidney experiments demonstrated the viability of OOCv1-B and OOCv2.1 devices for cell culture Renal experiments showed accumulations of C16 fatty acid in tubular renal cells cultured inside the device, though more precise quantification though other techniques is suggested to infer solid conclusions on differences between samples. On the contrary, MitoTracker intensity analysis suggested a clear increase in mitochondrial activity due to beneficial effect of shear stress, which would confirm existing studies on the subject. Experiments with OOCv2.1 also demonstrated the functionality of the compact experimental system for recirculating flow conditions. The system contributes to simplify the overall fluidic setup and improve user experience.

Biological experiments on the BBB proved viability of OOCv2.1 and OOCv2.2 for compartmentalized co-culture of two different types of cells to mimic the barrier. Administering Mannitol resulted in an impairment of the barrier, affecting cells confluence and formation of junctional complexes Co-culture of pericytes and ECs achieved better results in BBB formation and recovery capacity after disruption treatment compared to ECs only, both in terms of cell confluency and formation of

junctional complexes. Results suggest a critical role of pericytes in the development, maintenance, and regulation of BBB, in accordance with the literature. Analysis of EIS measurements performed on OOCv2.2 demonstrated measurement repeatability. A new LDA model for classification of measurements acquired from different timepoints was developed. After removal of data related to a measurement error, the model resulted in 100 % accuracy in training and 90 % accuracy in testing. This result has been confirmed by imaging data. Thanks to its high distinction between classes, the proposed model has potential applications as non-invasive label-free assessment of barrier integrity.